Phase transformations and microstructure - mechanical properties relations in Complex Phase high strength steels

Christophe Mesplont

Ingénieur Ecole Universitaire Des Ingénieurs de Lille

DEA Science des Matériaux, Université de Lille

UNIVERSITEIT
GENT

FACULTEIT TOEGEPASTE WETENSCHAPPEN
VAKGROEP METALLURGIE EN MATERIAALKUNDE

Laboratorium voor Algemene Metallurgie, Siderurgie en Fysische Metaalkunde

Proefschrift ingediend tot het behalen van de graad van Doctor in de Toegepaste Wetenschappen, richting Materiaalkunde promotor : Prof. dr. ir. B.C. De Cooman

Acknowledgements / Dankwoord / Remerciements

Christophe

Table of Contents

Chapter I   Design of high strength multiphase steels

Chapter II   Experimental procedure

Chapter III   Improved method to study multistep phase transformations kinetics from dilatometric data

Chapter IV   Experimental study of multistep phase transformations kinetics during continuous cooling C-Mn steels

Chapter X   General Conclusions

Appendix   Use of the dilatometer to study magnetic transformations in steels

List of Symbols

α: Ferrite

α_B: Ferritic bainite

α': Martensite

β: Hydrostatic pressure sensitivity of the austenite stability

ΔG^{ch}: Chemical driving force

ΔG^{σ}: Mechanical driving force

ε: True strain

$\varepsilon_1, \varepsilon_2, \varepsilon_3$: Principal strains

ε_{eng}: Engineering strain

ε_{eq}: Equivalent strain

γ: Austenite

γ_{res}: Residual austenite after intercritical annealing

γ_{ret}: Retained austenite in the final microstructure

γ_C: Activity coefficient of C

θ: Cementite

ρ_{disl}: Dislocation density

σ: True stress

σ_{eng}: Engineering stress

a_{α}: Ferrite lattice parameter

a_{γ}: Austenite lattice parameter

a_C: Activity of carbon

a_M: Martensite lattice parameter

A_{c1}: Temperature at which austenite formation starts during heating

A_{e1}: Equilibrium temperature for the lower boundary of the $\alpha+\gamma$ range

A_{r1}: Temperature at which austenite disappears during cooling

A_{c3}: Temperature at which austenite formation is completed during heating

A_{e3}: Equilibrium temperature for the upper boundary of the $\alpha+\gamma$ range

List of Symbols

A_{r3}: Temperature at which austenite starts to transform to ferrite during cooling

B_S: Bainitic start temperature

C_α: Ferrite C content [wt%] in the final microstructure

$C_{\alpha B}$: Bainitic ferrite C content [wt%] in the final microstructure

$C_{\gamma IA}$: Austenite C content [wt%] at intercritical annealing stage

$C_{\gamma ret}$: Austenite C content [wt%] in the final microstructure

C_{Fe3C}: Cementite C content [wt%] in the final microstructure

c_M: Martensite lattice parameter

C_{tot}: Total carbon content [wt%]

f: Transformed fraction of austenite to bainite (α_B); 0 = start of bainite transformation, 1 = end of bainite transformation

f_α: Ferrite fraction in the final microstructure

$f_{\alpha B}$: Bainitic ferrite fraction in the final microstructure

f_γ: Austenite volume fraction

$f_{\gamma IA}$: Austenite volume fraction at intercritical annealing stage

$f_{\gamma ret}$: Austenite volume fraction in the final microstructure

f_{Fe3C}: Cementite volume fraction in the final microstructure

f_M: Transformed fraction of austenite to martensite (α_M); 0 = start of martensite transformation, 1 = end of martensite transformation

G_α: Free energy of ferrite

G_γ: Free energy of austenite

I_{hkl}: Intensity of a diffraction peak

M_d: Temperature above which austenite is stable and no deformation induced transformation to martensite takes place

M_d30: Temperature at which 30 % tensile deformation induces a transformation of 50 % of the austenite to martensite

M_f: End of martensitic transformation

M_S: Martensitic start temperature

M_S^σ: Temperature at which the mode of transformation of austenite to martensite changes from stress-assisted to strain-induced

M^S_{ref}: Saturation magnetization of a fully ferromagnetic reference sample

M^S_{TRIP}: Saturation magnetization of a specimen

n: Strain hardening coefficient

P: Hydrostatic pressure

$R_{p0.2}$: Stress at 0.2 % plastic strain

$V_{\alpha B}$: Bainitic ferrite fraction in percentage in the final microstructure

$V_{\gamma IA}$: Austenite volume fraction in percentage at intercritical annealing stage

$V_{\gamma ret}$: Austenite volume fraction in percentage in the final microstructure

List of Abbreviations

AFM   Atomic Force Microscopy

B   Bain

Bcc   Body centered cubic

Bct   Body centered tetragonal

BH   Bake Hardening

CE   Carbon equivalent

CI   Confidence index

CPS   Counts Per Second

DDQ   Deep Drawing Quality

DP   Dual Phase

EBSD   Electron Back Scattering Diffraction

ELC   Extra low carbon

Fcc   Face centered cubic

FWHM   Full width half maximum

HSLA   High Strength Low Alloyed

IBT   Isothermal Bainitic Transformation

IF   Internal friction

ILS   Invariant Line Strain

IPS   Invariant Plane Strain

IQ   Image quality

JMA   Johnson-Mehl-Avrami

KS   Kurdjumov-Sachs

LOM   Light Optical Microscopy

ND   Normal direction

NW   Nishiyama-Wasserman

ODF   Orientation Distribution Function

PTMC   Phenomenological Theory of Martensite Crystallography

RD   Rolling direction

ReX   Recrystallization

RT   Room Temperature

SEM   Scanning Electron Microscopy

TD   Transverse direction

TE   Total Elongation

TEM   Transmission Electron Microscopy

TRIP   TRansformation Induced Plasticity

TTT   Time Temperature Transformation

UE   Uniform Elongation

ULC   Ultra low carbon

UTS   Ultimate Tensile Strength

XRD   X Ray Diffraction

YPE   Yield point elongation

YS   Yield stress

WH   Work Hardening

wt%   Weight percent

CHAPTER I

Design of high strength multiphase steels

I.1 Introduction

There is an increasing need for high strength formable sheet steels for automotive applications, in order to reduce the body-in-white (BIW) weight. For this reason, a large part of current sheet steel research is focussed on the development of high strength flat rolled steels combining a high tensile strength with an adequate elongation. This combination of tensile strength and elongation is particularly difficult to achieve as most engineering materials experience a loss of formability at higher strength. The choice of alloying elements is very important due to their influence on the microstructure and the strength. The largest contribution of the steel composition is related to the effect of alloying elements on the microstructure, which determines most of the mechanical properties of the final product. For example, martensitic tool steels posses a very high strength, but have a brittle behaviour. At the other end of the strength scale, the soft low alloy ferritic steels can undergo large deformations, but are not very resistant to rupture. For decades, steelmakers favoured a pearlitic microstructure when strength was required, in particular for rails, which had also a reasonable elongation and a good wear resistance. Today, the tendency is to form bainitic structures that give the best compromise in term of mechanical properties. The choice of the composition is very important in the development of high strength bainitic steels. Alloying elements will indeed favour one or the other transformation product by controlling the kinetics of their formation and can thus lead to markedly different microstructures. Figure I.1 summarises the methods of investigation used to develop high strength bainitic steels in the present work. The different steps leading to the industrial implementation of these new steels was developed separately.

In this introduction, a critical review is made on the choice of a composition leading to the development of new bainitic sheet steel. First, a survey of the current development in high strength multiphase steels is made. As this doctoral dissertation focuses on multiphase steels with bainite as the major constituent, the main characteristics of the bainitic transformation and in particular the different bainite morphologies are emphasized. Compositions that lead to microstructures with mainly bainite are selected by means of simulations using empirical formulae based on the composition. Microstructures are predicted using theoretical TTT (Time, Temperature, Transformation) and CCT (Continuous Cooling Transformation) diagrams.

A rough prediction of the tensile strength using empirical models based on the steel composition is helpful to design new steels. A new empirical formula had to be developed for high strength bainitic steels. The improved equation for the tensile strength was developed based on models taking into account the final microstructure. The strength of separate phases was estimated by taking into account the contributions of the dislocation density, the amount

of interstitial and substitutional hardening, and the austenite grain size. Hardness measurements performed on dilatometer samples gave indications on the ability of the tested composition to reach the desired strength level.
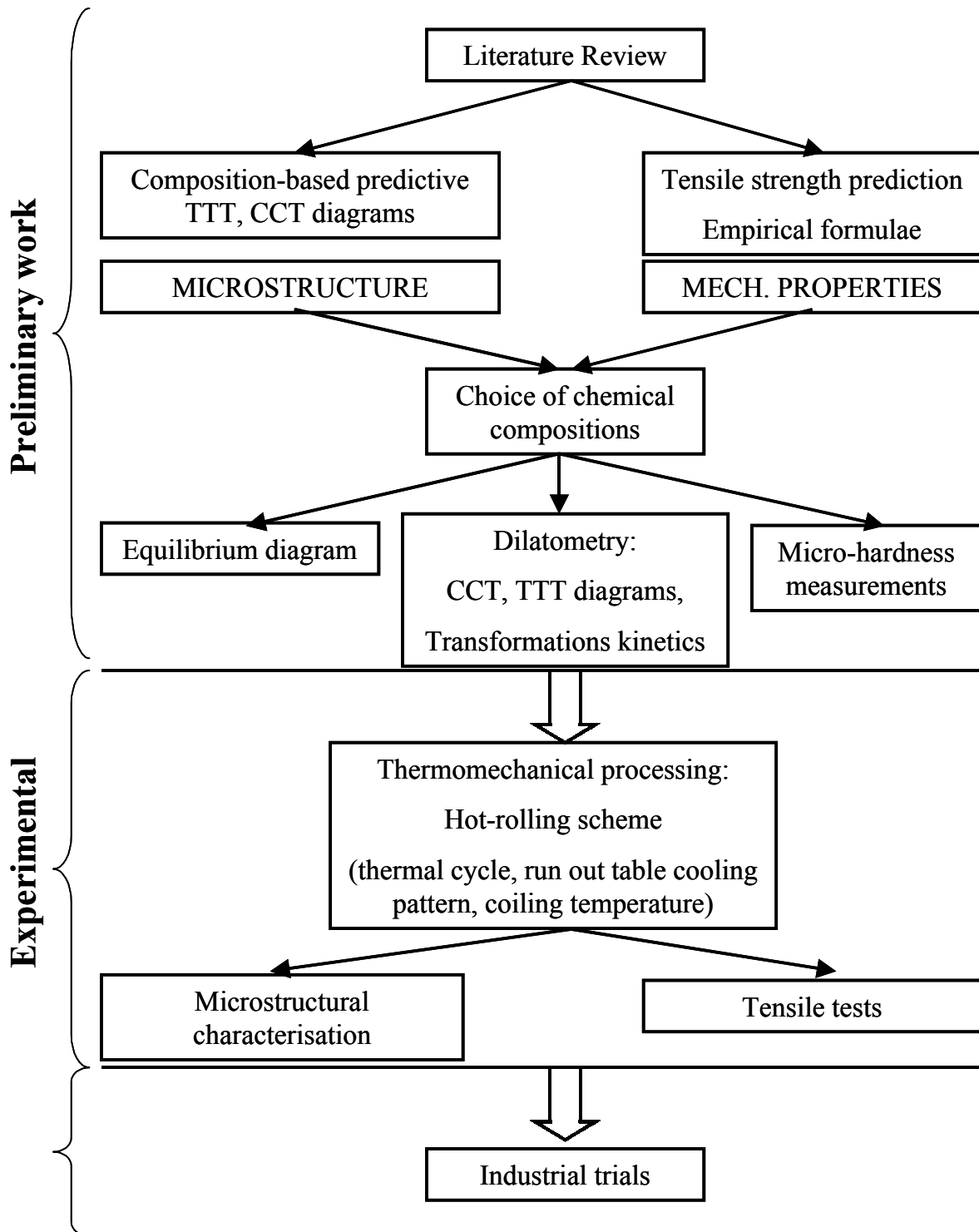
Figure I.1: Development of bainitic steels: method of investigation used for the present work.

A thermomechanical processing was based on the laboratory simulation results. Hot-rolling simulations, microstructure evaluation and tensile properties were tested before industrial scale trials were attempted.

Several steels compositions were designed using the proposed method to develop ultra high strength bainitic steel. Some of the compositions were used for a fundamental approach of the relevant phase transformations, while others were designed specifically to obtain bainitic steels with 1000 MPa tensile strength and 10 % total elongation. The latter industrial target was reached with a number of compositions. One steel composition was chosen and complex phase steel with a bainite-martensite-austenite microstructure was obtained as both hot-rolled and cold-rolled sheet.[1]

I.2 High strength multiphase steels for automotive applications

In recent years, reducing the weight of vehicles to improve the fuel efficiency has become a priority for the automotive industry. The Ultra Light Steel Auto Body (ULSAB) project was initiated in 1994 under the leadership of Porsche Engineering Services, Inc. and rapidly became a consortium regrouping 35 steel companies in 18 countries over 5 continents.[2] The ULSAB-AVC (Advanced Vehicle Concept) is the most recent addition to the global steel industries series of initiatives offering steel solutions to the challenges facing automakers around the world to increase the fuel efficiency of automobiles, improve safety and performance and lower costs. The AVC body structures are composed of 100 % high strength steels (HSS), with ~ 80 % of the steels being advanced high strength steels. These steels include dual phase (DP), transformation induced plasticity (TRIP), complex phase (CP) and martensitic steels.[3]

Figure I.2 shows the properties of different categories of hot-rolled high strength steels being developed currently at LISm (Laboratory for Iron and Steelmaking of Ghent University).[4]
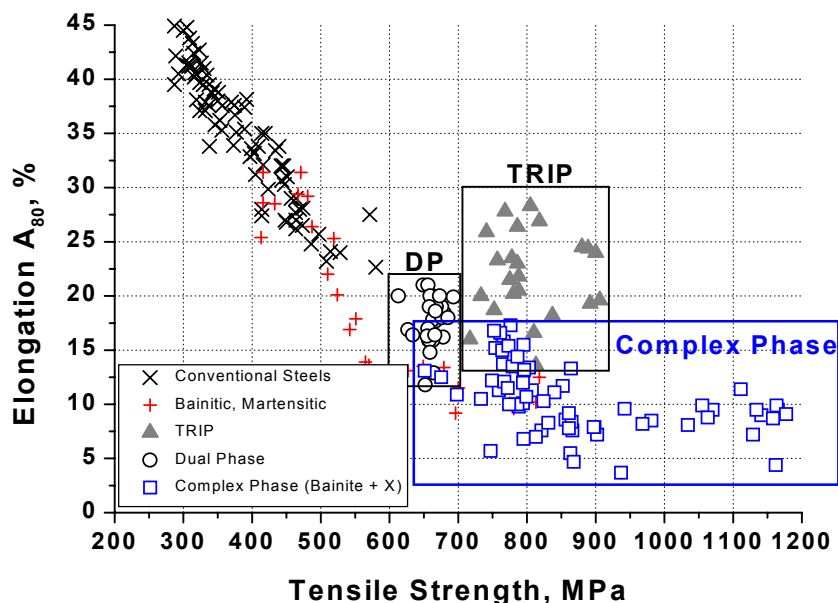
Figure I.2: Tensile properties of hot-rolled high strength steels.

Conventional steels include bake hardenable (BH) steels, carbon-manganese (CMn) steels, micro-alloyed High Strength Low Alloyed (HSLA) steels, which make use of precipitation hardening, rephosphorized steels and high strength interstitial free (IF) steels, which use solid solution hardening. Those steels typically offer modest formability at tensile strengths higher than 450 MPa.[5] Flat rolled sheet steel products such as DP steels and TRIP steels, which combine high strength and adequate elongation, are very attractive for the automotive industry. Both these multiphase steels are known to have an excellent fatigue resistance and can therefore be used for wheel discs where a high resistance to fatigue is important. TRIP steels can be used in parts of the body that need to absorb energy in case of a crash, such as reinforcements, in view of their particular strain hardening behaviour. These high strength steels have a complex microstructure, which is in all cases a mixture of two or more phases. Microstructures combining the bainite constituent and other phases such as ferrite (FB steels) or martensite (Bainite-Martensite steels) can lead to higher levels of strength with adequate elongation. Ferrite-bainite steels have a high tensile strength and both an adequate elongation and an excellent hole-expansion performance, which ensure a good formability. Potential applications for high strength bainitic steels include critical parts related to passenger safety: anti-intrusion frames of automotive structures. Complex Phase (CP) steels are defined as steels having a microstructure consisting in ferrite, bainite and martensite, plus possibly a small amount of retained austenite. It must be noted that to obtain multiphase steels the precise control of the thermomechanical processing is of fundamental importance. Indeed, while alloying elements can help to obtain a desired microstructure by the effect they have on the phase transformations kinetics, their contribution may also be a strengthening effect. The main characteristics of these advanced high strength steels are described in the next paragraphs.

I.2.1   Dual Phase (DP) steels

The microstructure of standard DP steels consists of a soft ferrite (α) and about 10 vol.% of lath martensite (α'). Figure I.3 shows the microstructure of cold rolled dual phase steel containing 56 % ferrite (grey) and 44 % martensite (bright phase). The mechanical properties of this steel are 600 MPa yield strength (YS) and 1200 MPa tensile strength (TS). The very low YS/TS ratio of 0.5 is the key to the good formability of that steel.

In lower strength dual phase steels, the soft ferrite phase is generally continuous, giving these steels excellent ductility. When these steels deform, however, strain is concentrated in the lower strength ferrite phase, creating a high work hardening rate. The DP steels exhibit higher initial work hardening rate, uniform and total elongation, ultimate tensile strength, and lower YS/TS ratio than conventional HSLA steels with comparable tensile strength. The bake hardening effect (BH), which is the increase in yield strength resulting from a combination prestraining and a low temperature aging can increase the yield strength considerably. This BH effect is commonly used as automotive sheet steel is always deformed and aged during the low temperature (< 200 °C) paint baking cycle after the application of the paint layers.

Conventional bake hardening effects, of BH steels for example, remain somewhat constant after prestrains of about 2 %. The extent of the bake hardening effect in advanced high

strength steels depends on the specific chemistry and thermal histories of the steels. DP steels are usually designed to provide ultimate tensile strengths of up to 1000 MPa.
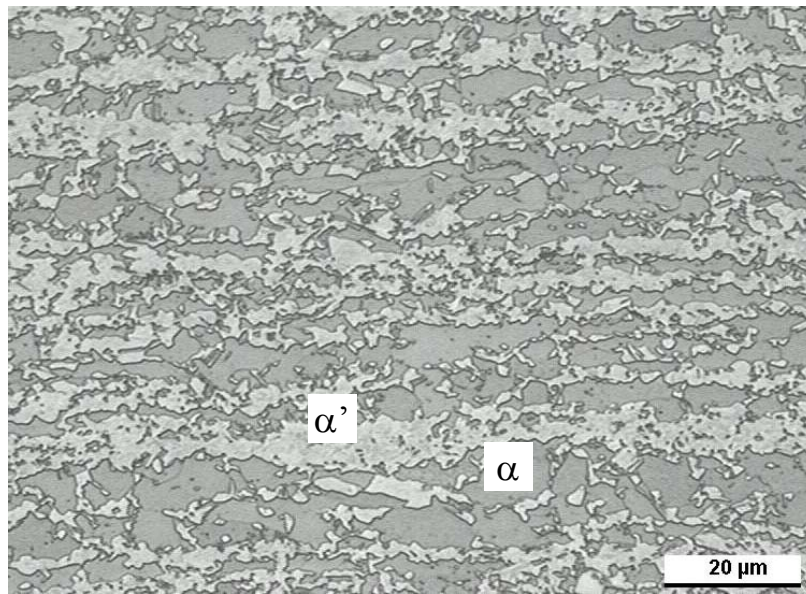
Figure I.3: LOM Microstructure of dual phase steel. Etchant: LePera. [6]

In DP steels, carbon favours the formation of martensite at practical cooling rates. That is, it increases the hardenability of the steel. Manganese, chromium, molybdenum, vanadium and nickel added individually or in combination also increase hardenability. Carbon strengthens the martensite as a ferrite solute strengthener. Silicon and phosphorus are very effective substitutional solid solution strengthening elements. Silicon also strengthens the martensite by causing the partitioning of carbon to the austenite thus increasing its hardenability and the strength of the resulting martensite phase. These additions are carefully balanced, not only to produce the required mechanical properties, but also to avoid difficulties with resistance spot welding.

I.2.2   Transformation Induced Plasticity (TRIP) steels

The TRIP steel microstructure shown in Figure I.4 consists of a ferrite matrix, α (grey) containing a dispersion of retained austenite, γ (bright) and bainite, α_b (dark).

During the deformation of TRIP steels, the retained austenite also transforms to martensite with increasing strain, which results in an increase of the work hardening rate at higher strain.

Silicon, aluminium or a combination of Si and Al must be present to suppress the carbide precipitation during the bainitic transformation. The strain level at which retained austenite begins to transform to martensite is controlled by the carbon content in the retained austenite. At low carbon levels, the retained austenite transforms almost immediately upon deformation, increasing work hardening rate and formability during the stamping process. At high carbon contents, the retained austenite is more stable and begins to transform only at strain levels beyond those produced during stamping and forming, and the retained austenite is still present in the final part. It can then transform to martensite during a crash, and thereby provide greater crash energy absorption. TRIP steels can provide either (a) excellent formability for

stamping complex parts or (b) exhibit high work hardening during crash deformation and provide excellent crash energy absorption.
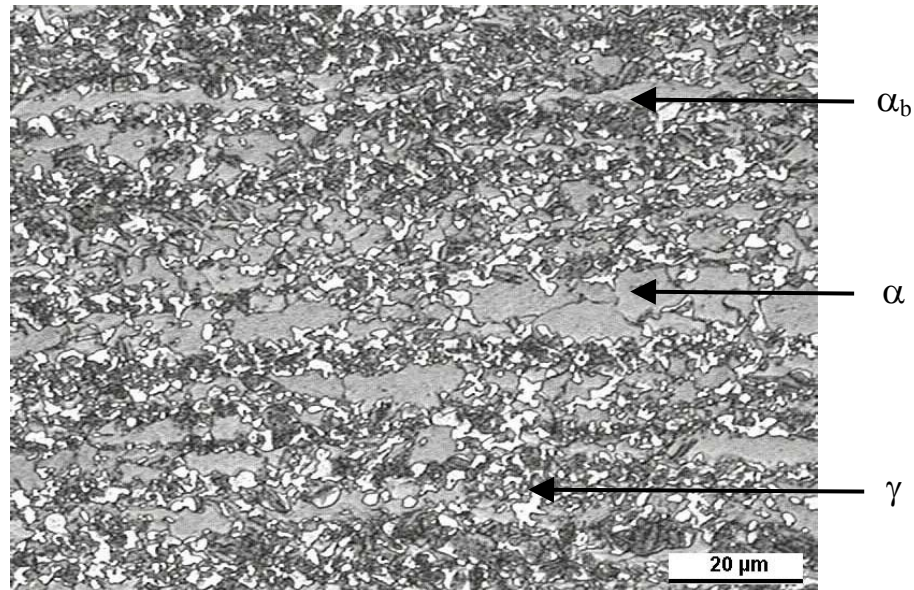
Figure I.4: Typical microstructure for a TRIP steel. Etchant: LePera.

I.2.3   Complex Phase (CP) steels

Very high ultimate tensile strengths can be achieved with complex phase steel. CP steel consists of a fine microstructure of ferrite and a higher volume fraction of hard phases that can be strengthened by fine precipitates. The same alloying elements found in DP and TRIP steels are used for CP steels. In addition, small quantities of niobium, titanium and/or vanadium are used to form small strengthening precipitates. Complex phase steels provide tensile strengths of at least 800 MPa.

Figure I.5 shows the microstructure of a hot rolled CP steel consisting of bainite and martensite. This steel has an ultimate tensile strength superior to 1000 MPa. Complex phase steels are characterized by formability, high-energy absorption, and high residual deformation capacity.
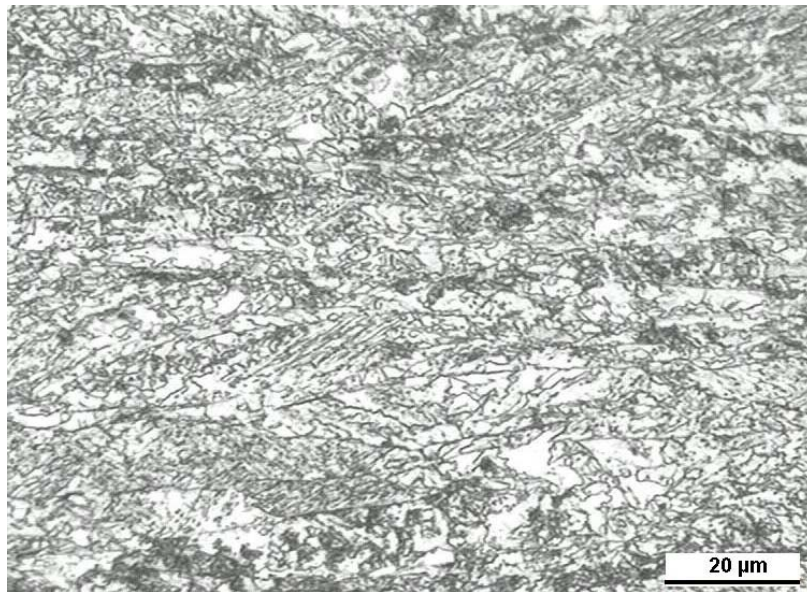
Figure I.5: Microstructure of a CP steel, mainly bainite/martensite. Etchant: Nital.

Potential applications for CP steels in automotive manufacturing include parts requiring high-energy absorption capacity in the elastic and low-plastic range, such as bumper and B-pillar reinforcements.

I.2.4 *Martensitic steels*

In martensitic steels, the austenite that exists during hot rolling or annealing is transformed almost entirely into martensite during quenching on the run-out table for hot rolled steels or in the cooling section of the annealing line in case of cold rolled steel. The microstructure of martensitic steel contains mostly lath martensite as shown in Figure I.6. Martensitic sheet steel provide currently the highest strengths, up to 1500 MPa ultimate tensile strengths. Martensitic steels are often subjected to post-quench tempering to improve ductility. This provides formability even at very high strengths. Carbon is added to martensitic steels to increase hardenability and strengthen the martensite. Manganese, silicon, chromium, molybdenum, boron, vanadium, and nickel are also used in various combinations to increase hardenability.
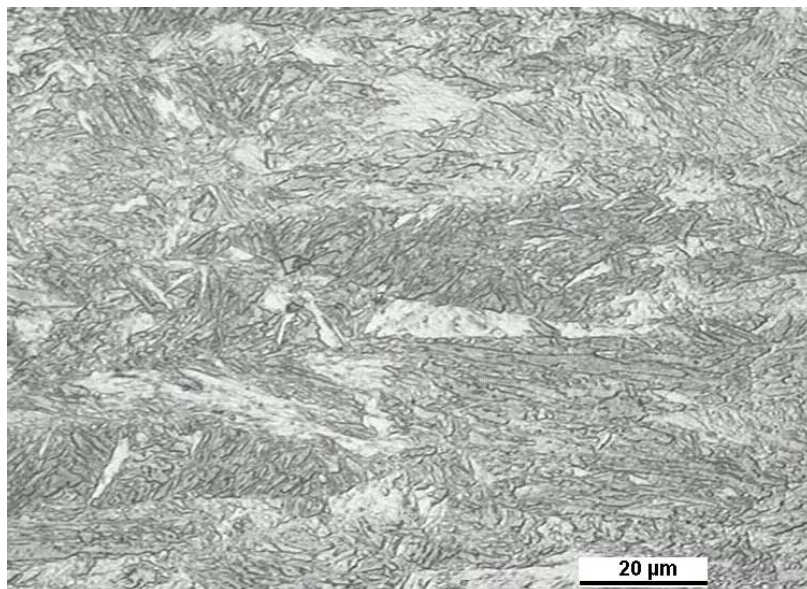
Figure I.6: Microstructure of martensitic steel. Etchant: Nital.

I.2.5   Properties and applications

Table I.1 gives an overview of typical tensile properties of the steel grades proposed in the ULSAB-AVC body structure concept.

Their potential practical applications are shown in Figure I.7 for the C-class body. Approximately 85 % of the steels used are high strength steels. A clear majority of components was designed using DP steels.

Table I.1: Sheet steel properties of selected steel grades.

Steel Grade	YS (MPa)	UTS (MPa)	Total EL (%)	n-value (5-15 %)	$\bar{r}$
BH 210/340	210	340	34-39	0.18	1.8
BH 260/370	260	370	29-34	0.13	1.6
DP 280/600	280	600	30-34	0.21	1.0
IF 300/420	300	420	29-36	0.20	1.6
DP 300/500	300	500	30-34	0.16	1.0
HSLA 350/450	350	450	23-27	0.14	1.1
DP 350/600	350	600	24-30	0.14	1.0
DP 400/700	400	700	19-25	0.14	1.0
TRIP 450/800	450	800	26-32	0.24	0.9
DP 500/800	500	800	14-20	0.14	1.0
CP 700/800	700	800	10-15	0.13	1.0
DP 700/1000	700	1000	12-17	0.09	0.9
Mart 950/1200	950	1200	5-7	0.07	0.9
Mart 1250/1520	1250	1520	4-6	0.065	0.9

■ **Dual Phase**
■ **BH**
■ **Mart**
■ **TRIP**
■ **IF**
■ **HSLA**
■ **CP**
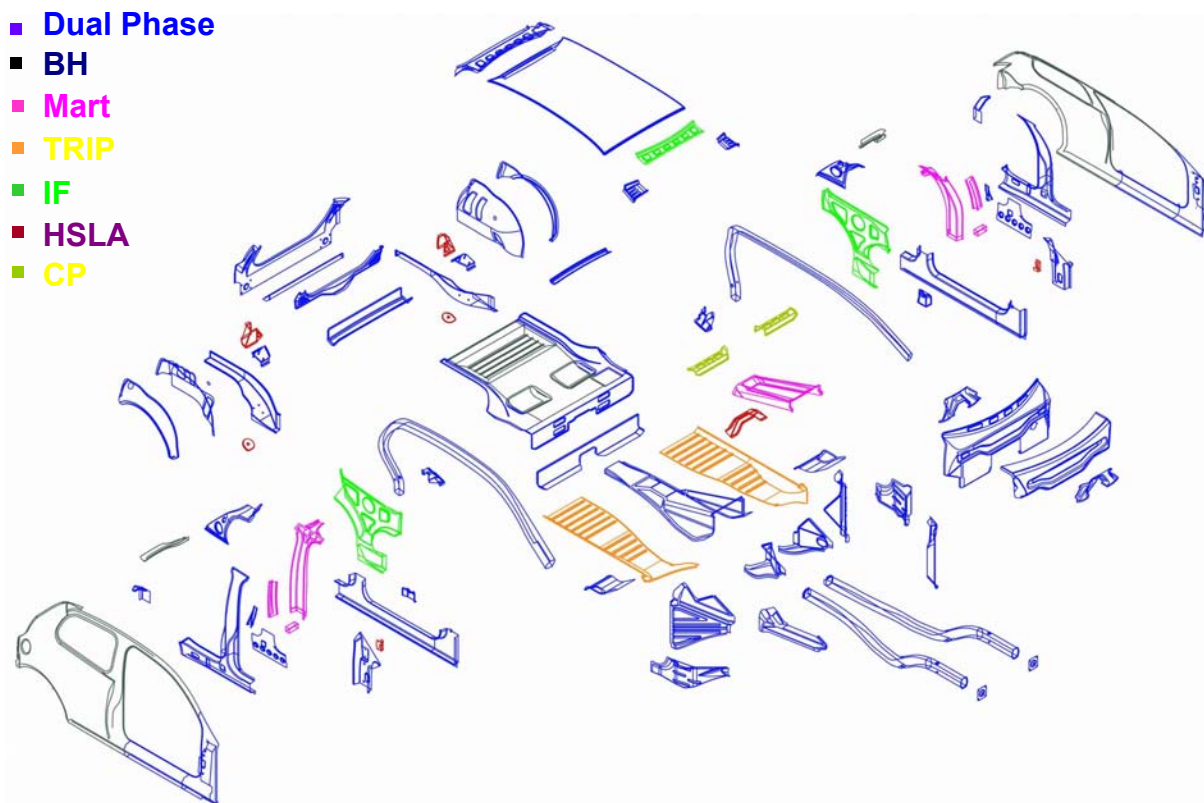
Figure I.7: Exploded view of final ULSAB-AVC C-Class concept design, showing steel types selected for individual parts.[3]

I.3 The bainite transformation

I.3.1   Main features

In medium and low C steels, the pearlite reaction occurs isothermally between 550 °C and 720 °C. The cooperative growth of ferrite and cementite implies a diffusive transformation mechanism. At low transformation temperatures, martensite is formed by a displacive transformation mechanism, as there is insufficient time for the eutectoid diffusion-controlled decomposition process to occur. The majority of carbon atoms in the fcc (face centered cubic) γ-Fe remain in solution in the α-Fe phase. As a result, the bcc (body centered cubic) lattice is distorted to bct (body centered tetragonal). Between the two, there is a temperature range in which fine aggregates of ferrite plates (or laths) and cementite particles are formed. These intermediate structures are called bainite. The bainite has a different morphology as the transformation temperature changes. The bainitic reaction presents characteristics of both diffusive and displacive transformations. The proposed mechanisms intervening in the bainite transformation are still quite controversial. As an intermediate phase between pearlite and martensite, it was envisioned that bainite could be related to one of the mechanisms intervening in each phase change, (i) diffusive phase transformation for pearlite, involving a complete reconstruction of the new crystallographic lattice by the uncoordinated migration of atoms; or (ii) displacive formation of martensite without any diffusion but only a lattice change by the coordinated movements of the iron and substitutional atoms[7].

Although it is generally accepted that the bainite transformation exhibits many features common to the martensitic transformation most of the early works felt uneasy about the fact that the bainite reaction proceeded at an easily observable rate, whereas the martensite growth rate was known to be limited only by the nucleation rate of martensite nuclei as the very high mobility of the transformation interface made it virtually growth-rate independent.[8,9] The bainite formation associates features characteristic of the martensitic transformation and features similar to the austenite decomposition to pearlite. The latter pearlite reaction is characterized by carbon diffusion and its redistribution between the ferrite and the θ-carbide (Fe_3C). The bainite transformation is now generally divided in 2 distinct stages: a stage of growth of ferrite followed by a stage of C-redistribution, which can lead to the precipitation of carbides.[10]

I.3.2   Morphologies of bainite

Bainite is a complex aggregate of ferrite and carbides with a particular morphology described as acicular or 'in sheaves'.[11] These sheaves consist of thin lenticular platelets or laths called "sub-units" of ferrite separated by regions of either untransformed austenite or martensite or carbide formed after the growth of bainitic ferrite. Furthermore, the platelets tend to adopt almost the same crystallographic orientation within a given sheaf. The ferrite laths have the Kurdjumov-Sachs (KS) crystallographic orientation relationship with the parent austenite: $\{111\}_\gamma//\{011\}_\alpha$ and $<011>_\gamma//<110>_\alpha$.[12] The growth of each sub-unit is accompanied by a shape change with a large shear component. This shape strain causes plastic deformation of austenite that seems responsible for the fact that each sub-unit grows to a limited size usually smaller than the parent austenite grain size. Consequently, the sheaf as a whole grows by the repeated appearance of new sub-units, which nucleate mostly near the tips of the already existing sub-units, where the local C content is the lowest, and thus the M_s temperature is the highest.

A distinction is usually made between upper bainite and lower bainite depending on the place where carbide precipitation occurs. The bainite transformation is accompanied by a carbon redistribution following the formation of bainitic ferrite. At relatively high temperatures, upper bainite is formed. It consists of sheaves of ferrite platelets with cementite particles trapped between the platelets. As a consequence of the transformation mechanism, the austenite that is trapped between platelets becomes enriched in carbon so that cementite precipitation occurs adjacently to the ferrite platelets. At a lower temperature, lower bainite is formed. It also consists of a non-lamellar aggregate of ferrite and carbides. The lower bainite usually contains a fine dispersion of carbides within the lenticular ferrite plates and carbides precipitates from the enriched austenite between the bainitic ferrite platelets.

Depending on the thermal treatment, bainite has many different morphologies. This often leads to confusing microstructural characterizations. Different bainitic microstructures have been classified in a microstructural atlas for bainitic microstructures[13], and some authors have proposed their own alternative classification. An elegant classification scheme has been proposed by Bramfitt and Speer.[14] The three general classes of bainite microstructure are represented in Figure I.8 together with their description.
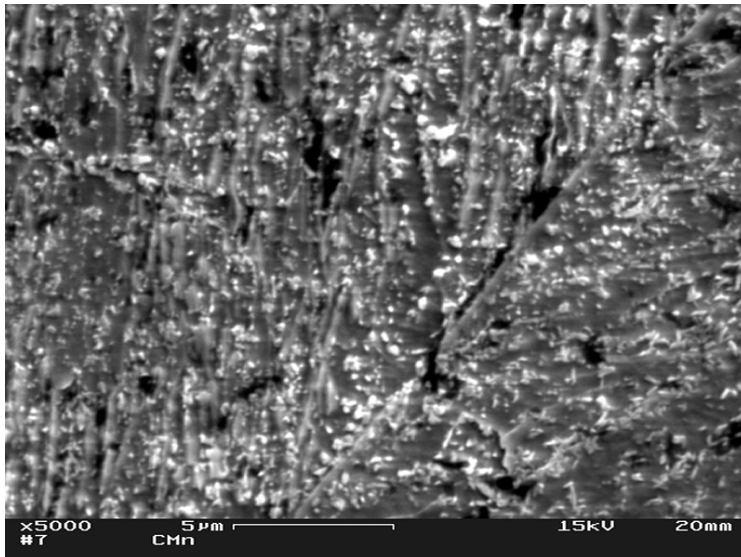
B$_1$

Acicular ferrite with intralath (plate) precipitation

cementite (B$_1^c$)

epsilon carbide (B$_1^\varepsilon$)

B$_2$

Acicular ferrite with interlath (plate) particles or films

cementite (B$_2^c$)

austenite (B$_2^a$)

martensite (B$_2^m$)

B$_3$
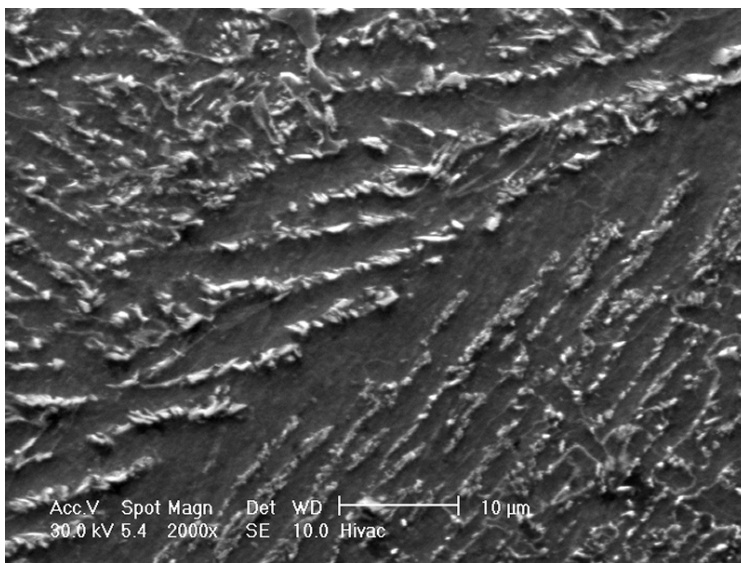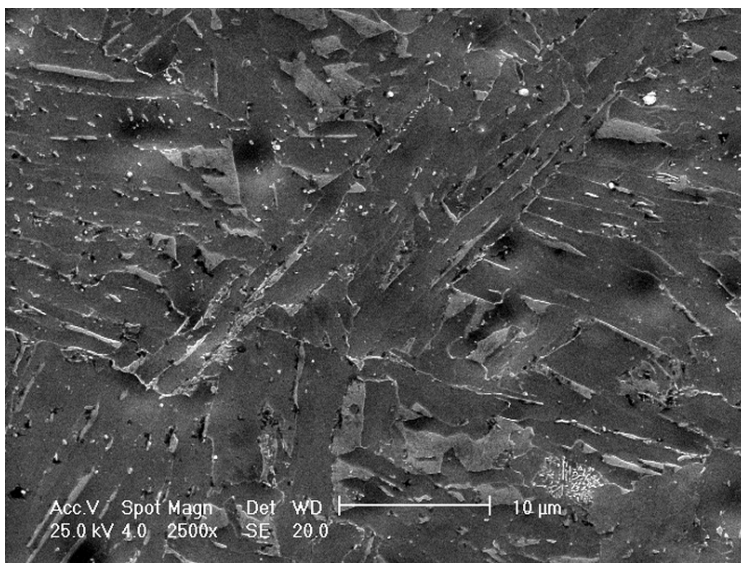
Acicular ferrite with "discrete-island" constituent

austenite (B$_3^a$)

martensite (B$_3^m$)

pearlite (B$_3^p$)

Figure I.8: SEM microstructures showing the 3 Bramfitt-Speer[14] classes of bainite, B$_1$, B$_2$ and B$_3$ (from top to bottom).

I.3.3   Mechanisms of the bainitic transformation

The bainite transformation can be considered as a slow transformation involving a number of successive or competitive events.

1. $\gamma \mid \gamma$

Plastic deformation

α

Supersaturated ferrite lath growth,
α and γ have the K-S orientation relationship:
$\{111\}_{\gamma} \,/\!/\, \{011\}_{\alpha}$ and $<011>_{\gamma} \,/\!/\, <110>_{\alpha}$

2.

α

C   C
C   C

C rejection to γ

3.

α

Low C area, M_s is higher,
Nucleation of ferrite lath at the tip

4.   No Si

Sheaf

carbides

Si-added

Sheaf

High C γ_{ret} $\quad \gamma_{ret} \rightarrow \alpha'$
$\quad\quad\quad\quad\quad \gamma_{ret}$
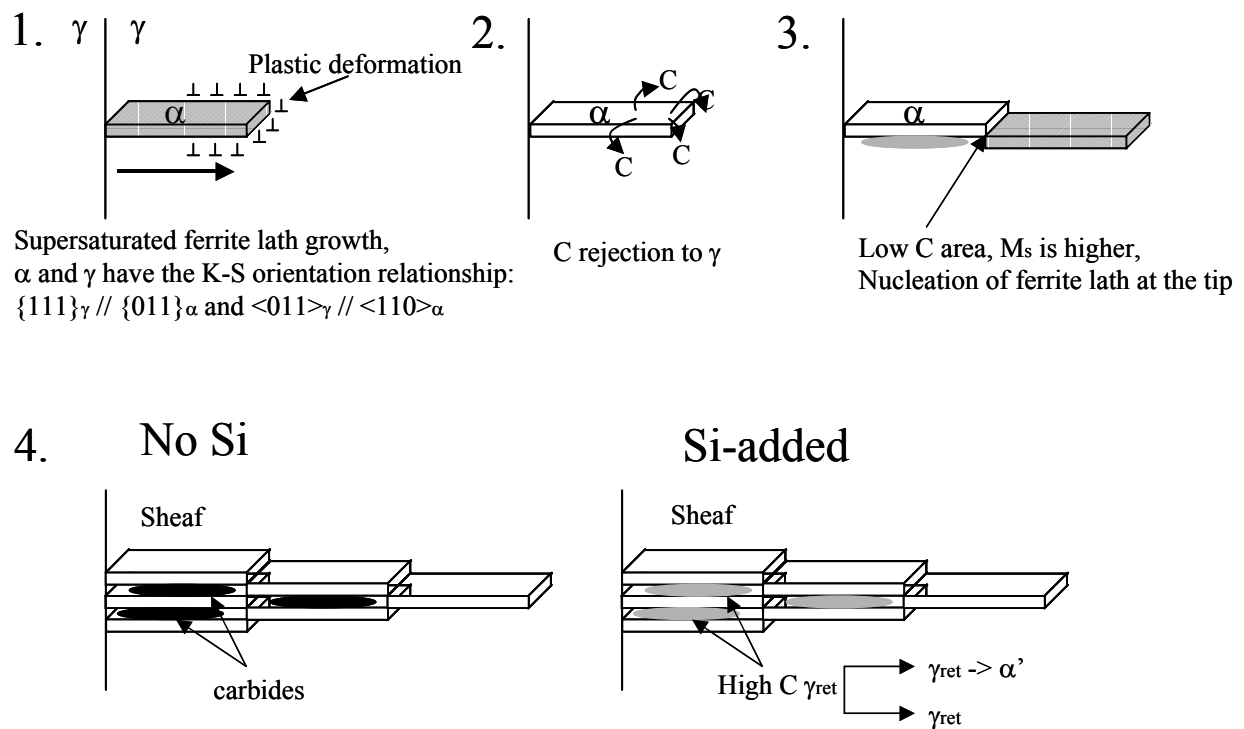
Figure I.9: Schematic representation of the development of a sheaf of upper bainite.

Figure I.9 represents schematically how a sheaf of upper bainite propagates through an austenite grain. A lenticular platelet of ferrite nucleates at an austenite grain boundary and lengthens towards the grain interior until its further growth is prevented by the plastic deformation of surrounding austenite. A second plate then nucleates at the tip of the first and a sheaf of bainite propagates through the austenite grain by this process of successive nucleation and growth of sub-units.[8] Note that the growth rate of platelets is much faster than the growth rate of the sheaf as a consequence of these repeated nucleation events intervening as the rate-controlling process.

The bainitic sub-units are formed by a displacive phase transformation. There is no redistribution of substitutional or interstitial alloying elements. The temperature at which bainite transformation occurs allows the excess carbon in the sub-unit to diffuse from ferrite to the surrounding austenite, because of the much lower solubility of C in α than in γ. The carbon content of bainitic ferrite decreases while residual austenite from which the next ferrite platelets have to grow shows an increase of carbon content until the cementite precipitation starts. In steels alloyed with sufficient amounts of elements suppressing the carbide precipitation, such as Si, the bainite consists of ferrite sub-units with high C residual austenite. That residual austenite may transform to martensite if its C content is such that M_s > RT.

The distinction between upper bainite and lower bainite can be understood by comparison of the time required for the C to diffuse out of the bainitic ferrite platelets with the time required to precipitate cementite.

Figure I.10 schematically represents both cases. If carbon redistribution is fast because it occurs at high temperatures, *i.e.* if the C diffusion process dominates, the cementite does not precipitate within ferrite platelets and upper bainite is formed.

In the case of a relatively rapid carbide precipitation within ferrite or of a high carbon supersaturation, all the carbon cannot be easily rejected from ferrite, which leads to the formation of lower bainite.

Formation of a supersaturated Sub-Unit

Carbon diffusion
into austenite

Carbon diffusion
into austenite and
carbide precipitation
in ferrite

Carbide precipitation
From austenite

Upper Bainite
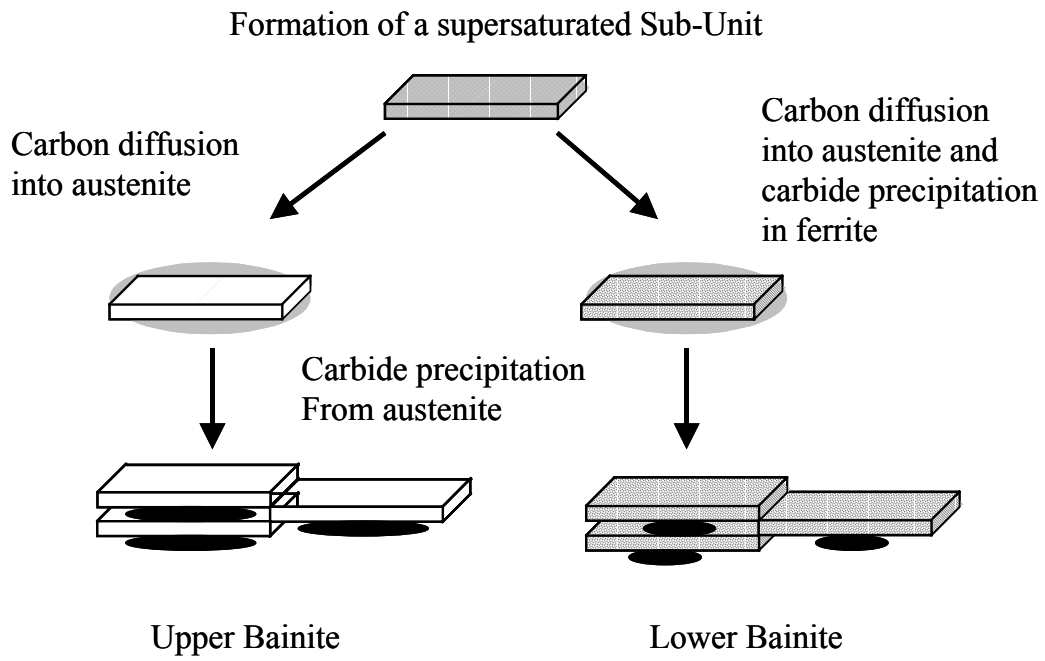
Lower Bainite

Figure I.10: Schematic illustrating the differences between upper bainite and lower bainite.[10]

I.3.4 *TEM microstructure of bainite in hot-rolled CP steel*

Thin foils were prepared from hot-rolled complex phase steel coiled at 550 °C. That Nb-microalloyed CMnMoCrB steel contained a mixture of bainite (~60 vol.%), martensite (~30 vol.%) and retained austenite. The microstructure was observed using a Philips EM 420 Transmission Electron Microscope (TEM) operating at 120 kV. Figure I.11 is a general view of a bainitic ferrite lath showing its dimensions. The measured thickness of 0.5 μm is in the range of 0.2 – 2 μm reported previously for a Fe-0.22 wt.% C steel. The lath width depends on its isothermal bainitic transformation temperature.[15]
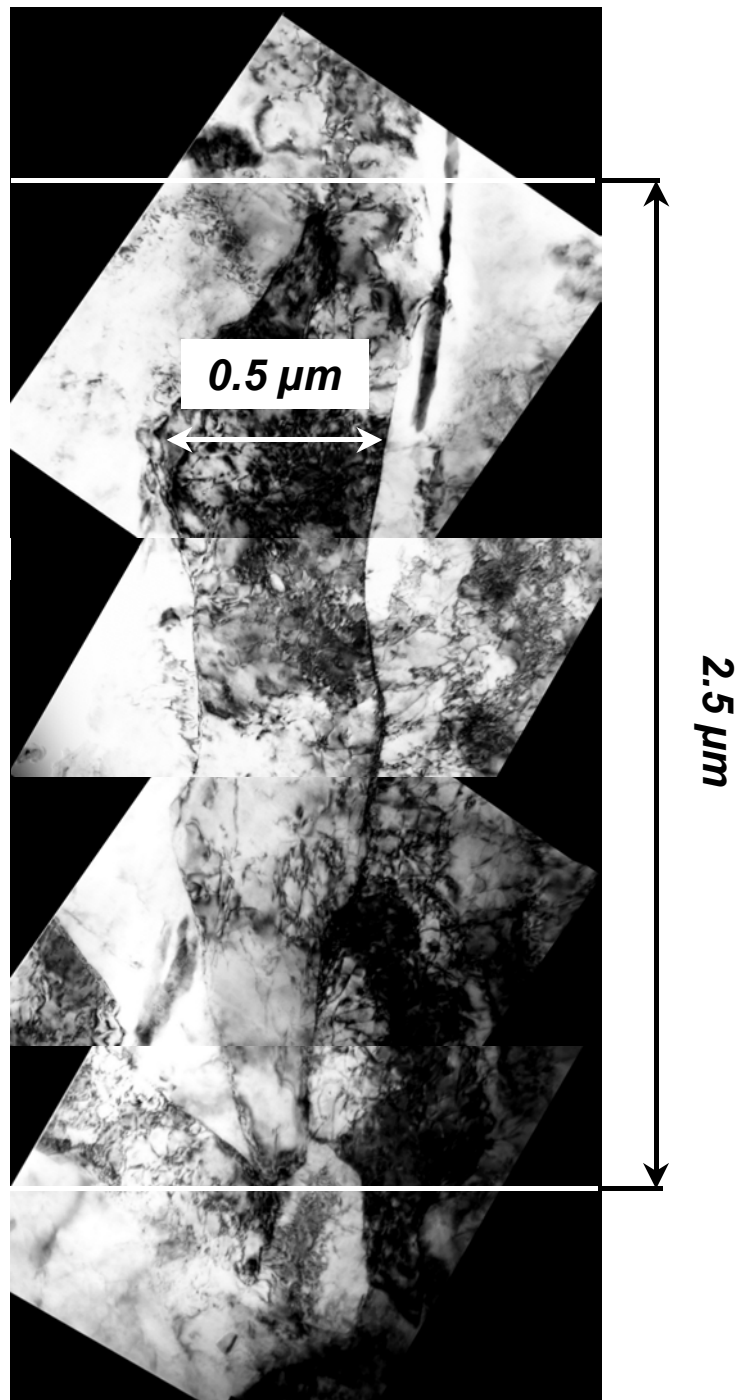
Figure I.11: TEM micrograph of a bainitic ferrite lath in hot-rolled CP steel.

Figure I.12 shows other bainitic ferrite laths of similar dimensions. It can be clearly seen that intralath precipitation of carbides occurred during the bainite formation. As suggested in the schematic representation of Figure I.9 the presence of many dislocations is observed at the interface between a bainitic ferrite lath and a second phase, likely martensite. Due to its chemical composition responsible for low kinetics of phase transformations, the presence of both upper bainite and lower bainite is possible in the CP steel coiled at 550 °C. In addition, it can be seen that the bainitic ferrite contains a very high dislocations density.
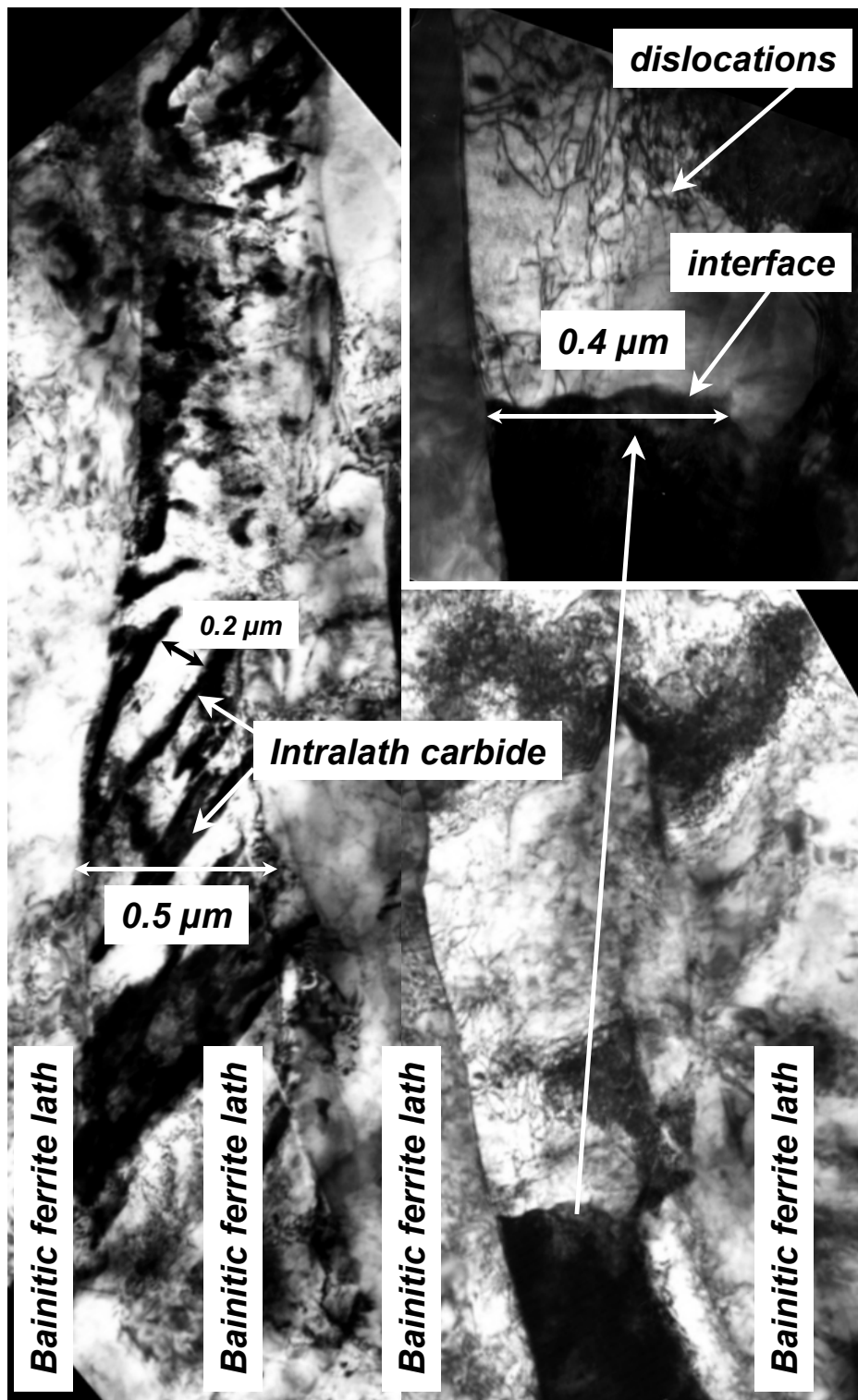
Figure I.12: TEM microstructure of lower bainite with intralath precipitation of carbides.

Figure I.13a is a general view of ferritic bainite in the hot-rolled CP steel. A very high density of dislocations is observed, and some carbides are present. It is difficult to determine whether they precipitated inside a bainitic ferrite lath or between laths, due to the orientation of the TEM sample. It is remarkable that, as seen in Figure I.13b no interlath carbides were present between the examined bainitic ferrite laths. It must be noted that the central bainitic ferrite lath contains many dislocations but was oriented in such a manner that the dislocations were out of contrast, allowing for an unobstructed view of the interfaces.
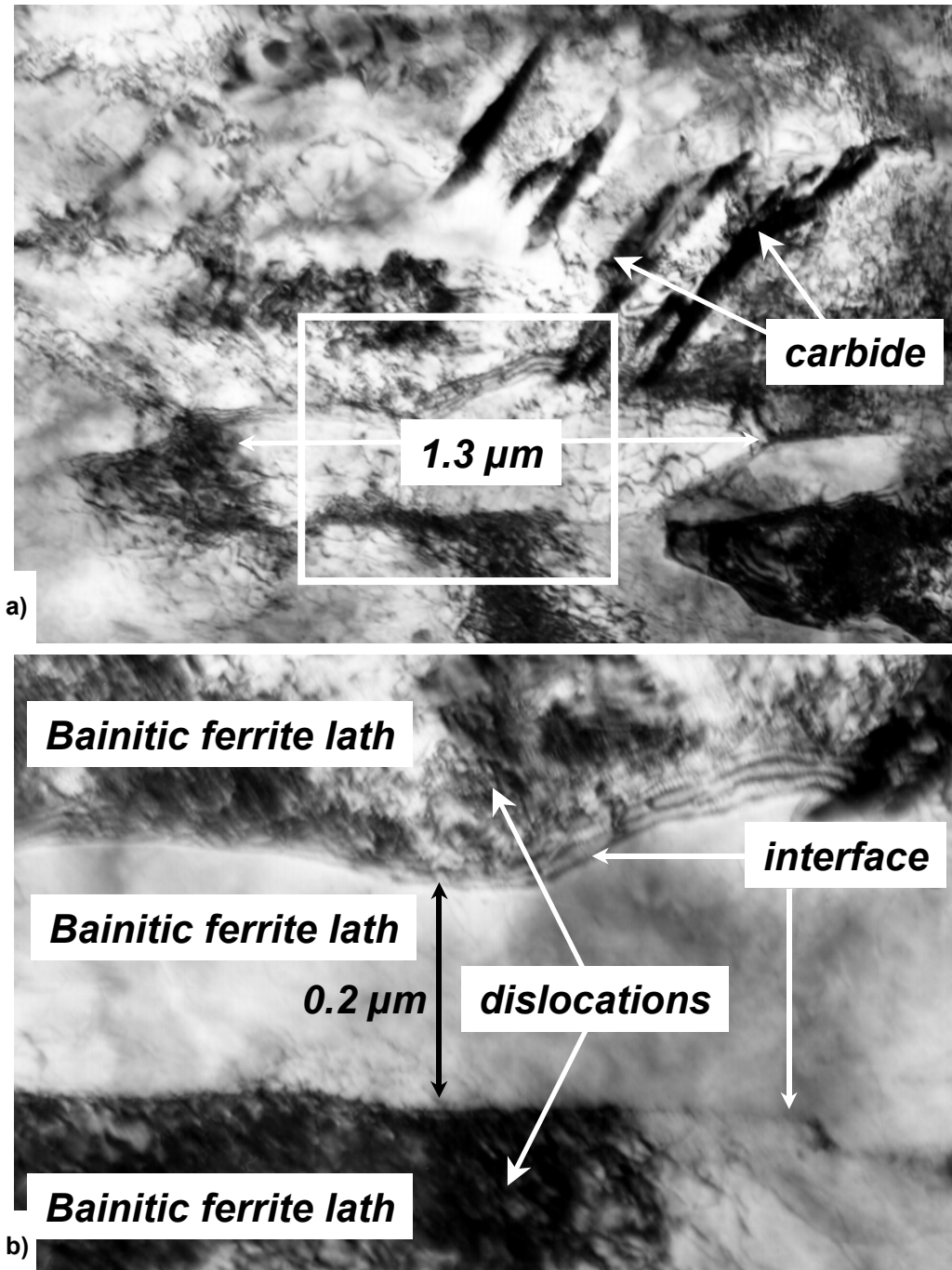
Figure I.13: a) TEM micrograph of bainitic ferrite containing dislocations and intralath carbides. Note the absence of interlath carbides in the enlargement of the rectangular region indicated. The interfaces between the bainitic ferrite laths are low angle boundaries.

Figure I.14, however, shows clear evidence of interlath carbide precipitation in the same TEM sample. This morphology, typical for upper bainite, was also found in tempered martensite in which multi-variant carbide precipitation occurred.[16]
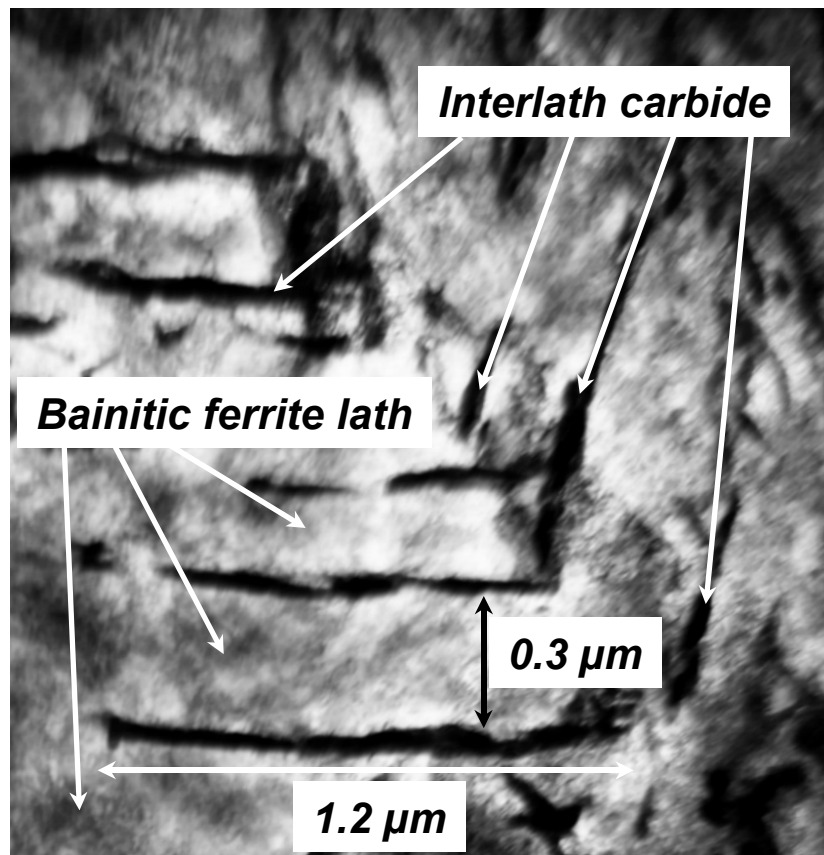
Figure I.14: TEM micrograph of the upper bainite microstructure showing the presence of interlath carbide precipitation with 2 different crystallographic variants.

In the hot-rolled CP steel, upper bainite formed in the first period of coiling at 550 °C, then lower bainite appeared, finally martensite formed in the remaining austenitic regions. In such regions, TEM observations showed evidence for the presence of high C, twinned martensite present at the interface between bainitic ferrite laths. The parallel lines observed in Figure I.15 are due to twin interfaces in the plate martensite. The diffraction pattern obtained from this microstructure showed clear twin spots. During the bainite formation, the untransformed austenite enriched in C. Due to the C concentration profile in those regions, not all the austenite transformed to martensite. At the interphase boundaries, the C content was high enough to prevent the martensitic transformation of austenite at room temperature, as the M_s temperature, decreased by the high C content, was below RT. The surrounding phase is thus retained austenite as illustrated in Figure I.15.
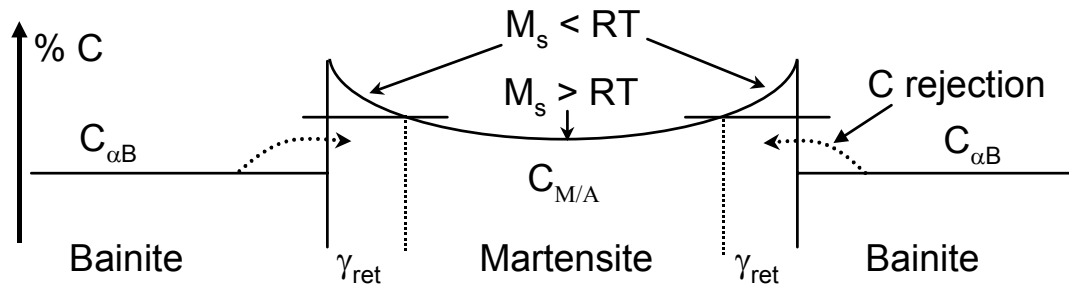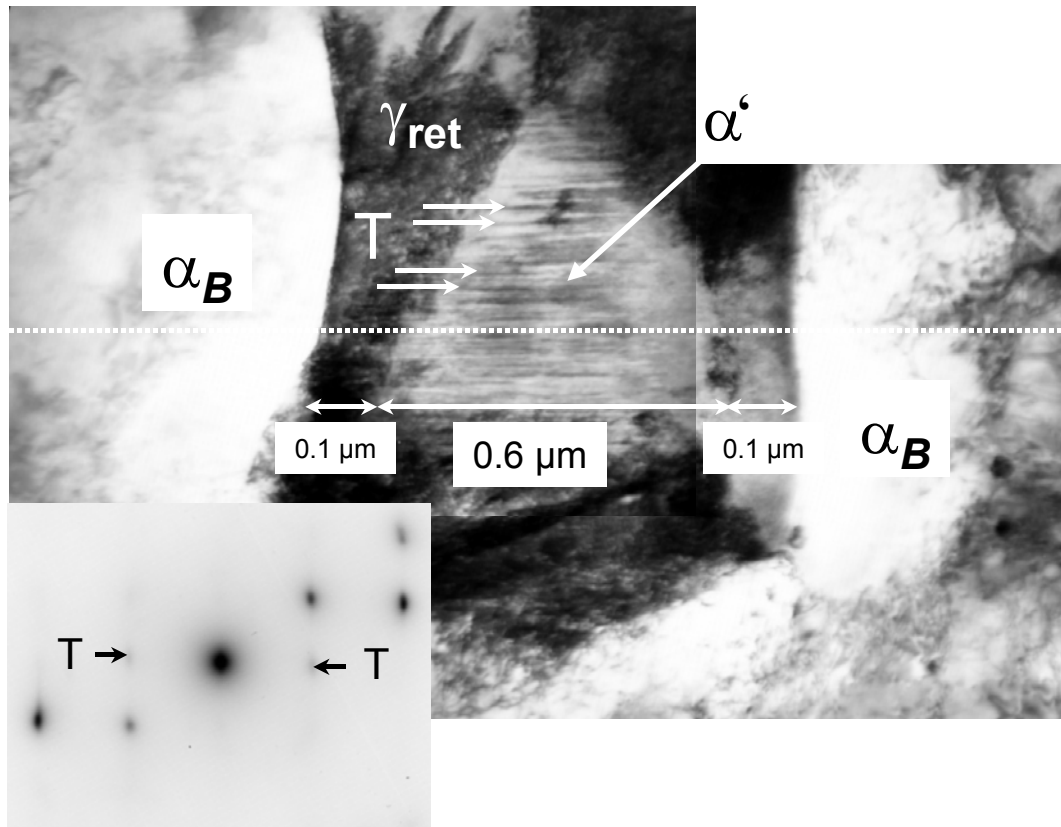
Figure I.15: TEM microstructure of CP steel showing the complex bainite-martensite-austenite mixture (inset: diffraction pattern showing weak twin-related diffraction spots at T) and schematic of its C concentration profile along the dotted white line on the TEM micrograph.

I.4 General considerations on micro-alloying elements

I.4.1 Global definitions [17]

The behaviour of the individual micro alloying elements classifies them in two groups: (a) the mildly carbide-forming elements, or the elements that do not form carbides, and (b) the strong carbide-forming elements. Generally, the non-carbide forming elements are also γ stabilizers, *i.e.* they expand the γ field, and the carbide-formers are α stabilizers, *i.e.* they reduce the γ phase field. Any of the elements in solid solution in α strengthen the ferrite matrix in steel. They contribute differently to hardening, and differ also in the extent to which they reduce plasticity in adding a certain increment to strength. P, Si, Mn, Ni, Mo, V, W and Cr, by order of importance, increase hardness of pure Fe. The non-carbide-forming elements in steel are almost wholly dissolved in the ferrite either in pearlitic steels or in the structures of tempered martensite. Ni, Si, Al and much of Mn in steel are dissolved in the ferrite regardless of the C content. The carbide-forming elements are to be found extensively in ferrite only when the C content is insufficient to combine with them. The excess C required to substantially withdraw the element from ferrite is less, the stronger the carbide-forming tendency. The mildly carbide-forming elements Cr and Mn are generally divided between carbide and ferrite, even with relatively high C content. The principle of partition of these carbide-forming elements follows the same general trend when the steel is heated to form austenite, except that the solubility of these elements may be high in austenite and, since the C itself is often largely dissolved, there is frequently no carbide phase left. Only with the stronger carbide-forming elements or in high-C steels are persistently insoluble carbide particles left at high heating temperatures. V, Nb and Ti stabilise C even at relatively low concentration. A classification of substitutional micro alloying elements according to their carbide-forming tendency and their effect on the γ field is made in Table I.2.

Table I.2: General trends of substitutional elements in the Fe-C binary system.

	α-stabilizers	γ-stabilizers
Carbide formers	Mo, Cr, V, W, Ti, Nb, Zr	Mn, Co
Non carbide formers	Si, P, Al	Ni, Cu

I.4.2 Influence on the formation of bainite [18]

C influences the range of temperatures over which upper and lower bainite occur. The B_s temperature is depressed by many alloying elements but C has the most pronounced influence, as indicated by the following empirical equation for the B_s temperature:[19]

$$B_s(°C) = 830 - 270C - 90Mn - 37Ni - 70Cr - 83Mo \qquad \text{(I.1)}$$

where the alloy concentrations are all in wt.%. C has a much larger solubility in the austenite than in the ferrite, and is very strong austenite stabilizer.

This leads to a general retardation of reaction kinetics. The fraction of carbides to be found in the final microstructure increases in proportion to the C concentration so that the concentration must be kept below about 0.4 wt.% to ensure reliable mechanical properties.

In plain carbon steels, the bainitic reaction is kinetically shielded by the ferrite and pearlite reactions, which start at higher temperatures and shorter times, so that in continuously cooled samples bainitic structures are difficult to obtain. The addition of metallic alloying elements usually results in the retardation of the ferrite and pearlite reactions. In addition, the bainite reaction is depressed to lower temperatures. This often leads to a greater separation of the reactions, and the TTT curves for many alloy steels show much more clearly separate C-shaped curves for the pearlite and bainitic reactions. However, it is still difficult to obtain a fully bainitic microstructure because of its proximity to the martensite reaction. A very effective mean of isolating the bainite reaction in low C steels consists of adding about 0.002 wt.% solute boron to a 0.5 wt.% Mo steel.[20] In a Mo-added steel the bainite reaction is promoted. The boron additions markedly retard the ferrite reaction. The effect of B is probably due to the preferential segregation of B to the prior austenite boundaries. This permits the bainite reaction to occur at shorter times. At the same time, the bainite C-shaped curve is hardly affected by the B addition, so that martensite formation is not enhanced. This B-Mo effect has been clearly observed in a 0.17 wt.% C-1.6 wt.% Mn steel containing 25 ppm soluble B and 0.2 wt.% Mo. The continuous cooling transformation (CCT) diagram of Figure I.16 shows that a fully bainitic microstructure is obtained for a wide range of cooling rates.
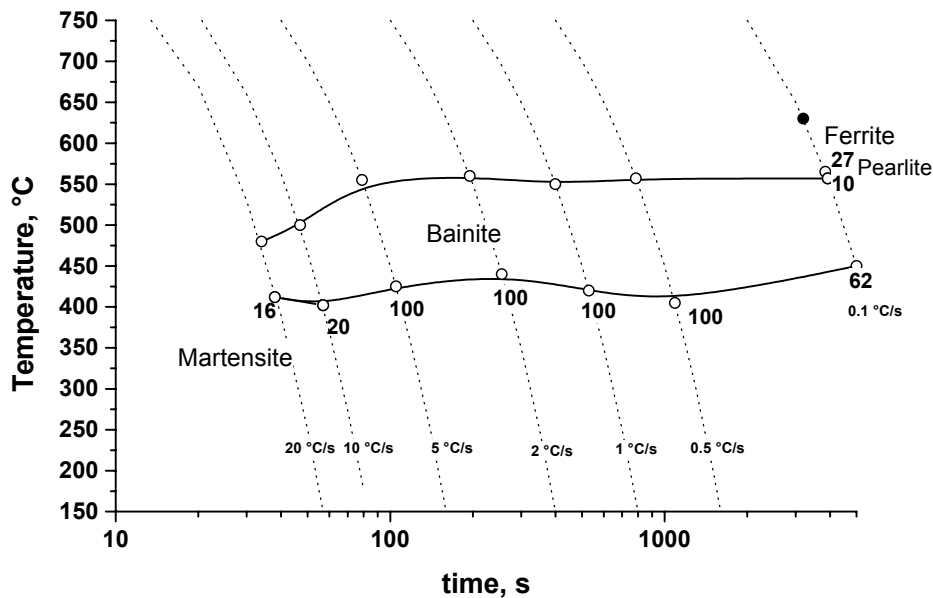
Figure I.16: CCT diagram for 0.17 C-1.6 Mn-0.2 Mo steel with 25 ppm soluble B.

A study on bainitic rail steels has shown, using the computer program SteCal 2™ that Mo is present to cause a distinct bainite nose and the Mn and Cr delay both pearlite and bainite transformation.[21] Increased Si stabilizes untransformed austenite by delaying the precipitation of carbide from bainite containing regions of metastable austenite. B has no effect on the transformation temperatures. B does however have an influence on the austenite decomposition kinetics in that it greatly reduces ferrite nucleation.

A fully bainitic steel having a tensile strength > 750 MPa and an A_{80} elongation > 10 % was developed.[22] The following principles were taken into considerations to determine the adequate chemical composition:

-The C concentration must be low enough to avoid martensite formation;

-The Mn concentration must be high enough to avoid ferrite formation. It increases incubation time and decreases the temperature of $\gamma - \alpha$ transformation;

-Si additions increase the rate of carbon redistribution in austenite and slow the austenite decomposition. It suppresses carbide formation. It also results in a substitutional strengthening. The silicon content was fixed to 0.25 wt.% to have an incubation time maximal for ferrite and minimal for bainite;

-Other alloying elements are needed to increase the strength. B, Ti, Nb and Mo were considered:

- B segregates to austenitic grain boundaries and interacts with dislocation networks. The nose of ferrite is thus driven back to the right on CCT diagrams, *i.e.* the incubation time is increased. The B effect is only observed when B is present in solution;

- Ti is added to keep the B in solution by forming TiN and avoiding the formation of BN precipitates. The Ti content must be at least 3.4 N to fully stabilise the N. Ti also contributes to the strengthening;

- Nb causes a strengthening due to NbC or Nb(C,N) precipitate formation. It also retards the recrystallisation and the grain growth by forming fine carbides. This results in finer grains. In combination with B, the growth of large $Fe_{23}(CB)_6$ precipitates at γ grain boundaries is avoided;

- Mo is a ferrite stabilizer. It reduces the diffusivity of C in γ. Mo is responsible for a pronounced solute drag like effect (SDLE) due to its segregation to the $\alpha-\gamma$ interface, therefore decreasing the mobility of the $\alpha-\gamma$ interface. Mo retards the ferrite and pearlite formations greatly but does not influence the bainite formation. It is also a solid solution strengthening element.

Four compositions summarized in Table I.3, were chosen to evaluate the influence of these different alloying elements.

Table I.3: Tested steel compositions, in wt.%.

Composition	C	Mn	Nb	Ti	B	Si	Mo
1.CMn	0.08	1.6	-	-	-	-	-
2.CMnNb	0.08	1.6	0.02	-	-	-	-
3.CMnNbB	0.08	1.6	0.04	0.02	0.002	0.25	-
4.CMnNbBMo	0.08	1.6	0.04	0.02	0.002	0.25	0.2

The target in terms of mechanical properties was reached with composition 4. A fully bainitic structure with desired properties was obtained for specific thermo-mechanical treatments. This study showed that adding 200 ppm Nb increased the strength by 80 MPa. A small 20 ppm B addition in combination with 200 ppm Nb gave more than 100 MPa additional strength. The 0.2 wt.% Mo addition resulted in an 80 MPa higher strength. Whatever the alloying element, the elongation was always reduced.

Larger amount of alloying elements were used to increase the strength level even further. Table I.4 shows some high strength bainitic steel compositions as reported in the recent literature. The tensile strength levels ranged from 950 – 1250 MPa.

Table I.4. Nominal compositions of experimental bainitic rail steels.[23]

	C	Mn	Si	Cr	Mo	V	Ti	B	Nb
Krupp	0.07	4.5	-	-	0.50	-			-
	0.30	-	-	2.70	0.20	-			-
Thyssen Stahl	0.40	1.50	0.70	1.10	0.80	0.10	-	-	-
AAR (J6)	0.25	2.00	1.80	1.95	0.45	-	0.035	0.003	-
British steel	0.50	2.00	1.50	-	-	-	-	-	-
	0.23	1.30	0.40	0.30	0.30	0.04	0.022	0.002	-
Nippon Steel	0.31	1.31	0.31	1.32	0.26	-	-	-	-
	0.29	1.16	0.35	2.21	-	-	-	-	0.04
	0.35	0.74	1.98	2.41	-	-	0.032	-	-
	0.32	0.41	0.29	2.81	0.59	-	-	-	-

I.5 Microstructure prediction

I.5.1   Continuous Cooling Transformation (CCT) diagrams

Maynier *et al.*[24] developed a model to estimate critical cooling rates to obtain martensite (V_1), bainite (V_2) or ferrite (V_3). These cooling rates depend on an austenitization parameter (P_a), which is calculated on the basis of the time and temperature of the austenitization, and on the composition of the steel:

$$P_a = \left(\frac{1}{T} - \frac{nR}{\Delta H} \log \frac{t}{t_0} \right)^{-1}$$ (I.2)

where T is the temperature in K, t the time, t_0 corresponds to one unit of time, n is a constant equal to ln(10), R is the perfect gas constant (8.3144 J K^{-1} mol^{-1}) and ΔH is the activation energy for grain growth ($\sim$ 460 kJ/mol). This equation is derived from the Arrhenius rate equation:

$$rate \propto \exp\left(\frac{-\Delta H}{RT} \right)$$ (I.3)

In the case of austenite grain growth, it is considered that two thermal cycles $T(t)$, $T_0(t_0)$ during which only diffusion intervenes will have the same effects if the concentration gradient along the diffusion line is constant:

$$Dt = D_0 t_0$$ (I.4)

If the activation energy for diffusion ΔH is constant, one obtains:

$$t \exp\left(\frac{-\Delta H}{RT} \right) = t_0 \exp\left(\frac{-\Delta H}{RT_0} \right)$$ (I.5)

The austenitization parameter P_a is equal to the temperature T_0, and is related to the austenite grain size, as increasing P_a increases the austenitization time and/or temperature, leading to coarser grains. The equation (I.2) is the logarithmic form of the equation (I.5).

The initial cooling rates are given by:

$$Log V_r = K_0 - \sum (K_P, P_a)$$ (I.6)

with K_0 the constant and K_p coefficients with p = C, Mn, Si, Ni, Cr, Mo, V in wt.% and P_a in °C.

The different values of coefficients are given in Table I.5.

Table I.5: Constants for cooling rates.

	K_0	C	Mn	Ni	Cr	Mo	P_a(°C,1h)
log V_1	9.81	4.62	1.05	0.54	0.5	0.66	0.00183
log V_1 (90)	8.76	4.04	0.96	0.49	0.58	0.97	0.001
log V_1 (50)	8.5	4.13	0.86	0.57	0.41	0.94	0.0012
log V_2	10.17	3.8	1.07	0.7	0.57	1.58	0.0032
log V_2 (90)	10.55	3.65	1.08	0.77	0.61	1.49	0.004
log V_2 (50)	8.74	2.23	0.86	0.56	0.59	1.6	0.0032
log V_3 (90)	7.51	1.38	0.35	0.93	0.11	2.31	0.0033

It was possible, using this model, to estimate the cooling rate ranges for different phases transformations. V_r being the cooling rate, if $V_r > V_1$, only martensite is formed. If $V_1 > V_r > V_2$ bainite and martensite are formed. If $V_2 > V_r > V_3$ bainite and ferrite/pearlite will be present in the final microstructure. If $V_r < V_3$ the steel will contain ferrite and pearlite.

I.5.2   Time Temperature Transformation (TTT) diagrams

Li *et al.*[25] recently improved a model by Kirkaldy[26] to predict isothermal reaction incubation times according to the initial steel composition. The general forms of the TTT diagrams in this model are described by the following equations:

$$\tau(X,T) = \frac{F(C,Mn,Si,Ni,Cr,Mo,G)}{\Delta T^n \exp(-Q/RT)} S(X) \tag{I.7}$$

where *F* is a function of the steel content in C, Mn, Si, Ni, Cr and Mo in wt.%, *G* is the prior austenite grain size (ASTM number), ΔT is the undercooling, and *Q* is the activation energy of the diffusional reaction. The exponent of undercooling *n* is an empirical constant determined by the effective diffusion mechanism. For example *n*=2 for volume diffusion and *n*=3 for boundary diffusion. *S(X)* is the reaction rate term, which is an approximation to the sigmoidal time-dependance of phase transformations:

$$S(X) = \int_0^X \frac{dX}{X^{0,4(1-X)}(1-X)^{0,4X}} \tag{I.8}$$

In this model, the Ae_3 and Ae_1 temperatures are calculated using a thermodynamic model. Ae_3 can also be calculated using Andrews formula valuable for steels containing less than 0.6 wt.% carbon and a sum of alloys inferior to 5 wt.%:[27]

$$Ae_3(°C) = 910 - 203C^{1/2} - 15.2Ni - 30Mn + 44.7Si + 104V + 31.5Mo + 13.1W \tag{I.9}$$

Physically, Ae_1 represents the asymptote of pearlite start curve in a TTT diagram. Andrews has published an empirical equation for Ae_1:[27]

$$Ae_1(°C) = 727 - 10.7Mn - 16.9Ni + 29.1Si + 16.9Cr + 6.38W + 290As \qquad (I.10)$$

The asymptote of the bainite start curve in TTT diagrams was used to calculate the undercooling for bainite reaction. When compared with the data presented in the isothermal transformation diagrams in the U.S. Steel Atlas, it was found that the original equation for estimating the bainite start temperature, B_s, in the Kirkaldy model overestimated the suppressing effect of Si. Li *et al.* thus modified this equation by normalizing the coefficient of Si at Si = 0.25 wt.%. The modified B_s equation is given by:[25]

$$B_s(°C) = 637 - 58C - 35Mn - 15Ni - 34Cr - 41Mo \qquad (I.11)$$

The M_s (martensite start) formula proposed by Kung and Rayment[28] based on a modification of the original linear formula by Andrews was adopted in this model:

$$M_s(°C) = 539 - 423C - 30.4Mn - 17.7Ni - 12.1Cr - 7.5Mo + 10Co - 7.5Si \qquad (I.12)$$

Figure I.17 shows the TTT diagram predicted for a 0.15C-1.6Mn-0.5Cr-0.2Mo steel using the formulas presented before. Ae_1 and Ae_3 correspond respectively to the critical temperatures at which hypoeutectoid steel is fully ferritic and fully austenitic at equilibrium, respectively.
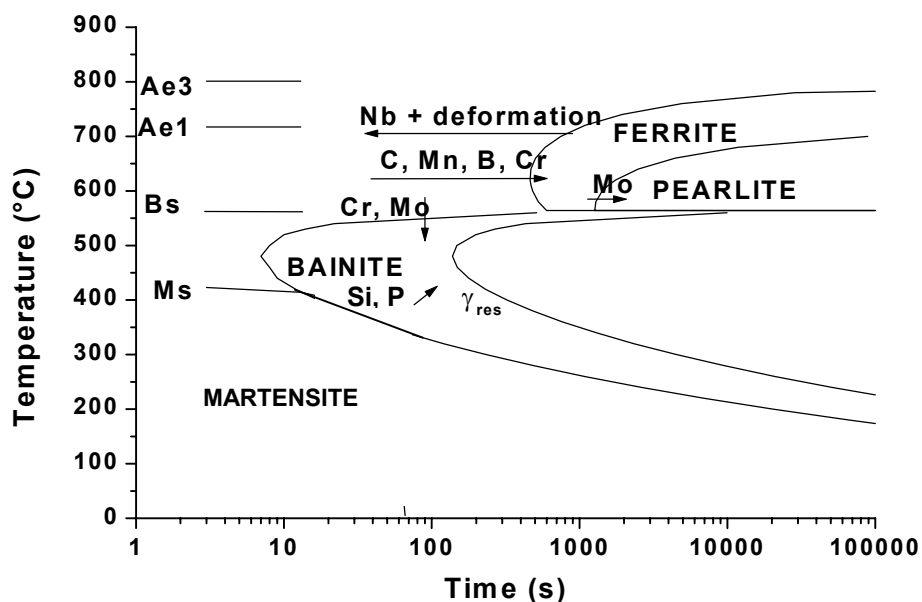
Figure I.17: TTT diagram predicted for 0.15C-1.6Mn-0.5Cr-0.2Mo steel. The effects of some alloying elements on the different phase transformations are indicated.

Those temperatures are usually affected by the heating or cooling rate. The index "c" stands for transformations during heating ("chauffage" in French), *i.e.* between Ac_1 and Ac_3 the α→γ transformation occurs, while the index "r" stands for tansformations during cooling ("refroidissement" in French).

Carbon is the alloying element that has the stronger influence on the phase transformations temperatures. Its effect and the effects of other alloying elements on the phase transformations temperatures are indicated on Figure I.17. Table I.6 regroups some of the most often used empirical formulas to predict the transformation temperatures, applicable to steels with C < 0.6 wt.% (except formulas from Zhao applicable to steels with C > 0.8 wt.%) .

Table I.6: Empirical formulas to predict transformation temperatures, in °C, based on the steel composition.

Temperature	Authors	Formula
Ar_3, Ac_3	Andrews[27]	$Ac_3(°C) = 910 – 203C^{1/2}$ - 15.2Ni - 30Mn + 44.7Si + 104V + 31.5Mo + 13.1W.
	Sekine[29]	$Ar_3(°C) = 868 - 396C - 68Mn + 25Si.$
	Okamoto[30]	$Ar_3(°C) = 901 - 325C - 92Mn + 33Si + 287P + 40Al.$
	Leysen[31]	$Ar_3(°C) = 901 - 830C - 61Mn + 71Si + 362P.$
Ac_1	Andrews[27]	$Ac_1(°C) = 727 – 10.7Mn – 16.9Ni + 29.1Si + 16.9Cr + 6.38W + 290As.$
B_s	Stevens and Haynes[19]	$B_s(°C) = 830 - 270C - 90Mn - 37Ni - 70Cr - 83Mo.$
	Li et al[25]	$B_s(°C) = 637 - 58C - 35Mn - 15Ni - 34Cr - 41Mo.$
		$B_s'(°C) = 720 - 585C + 126C² - 66Ni +6Ni² -32 Cr$
	Zhao[37]	$+2.17Cr² - 92Mn + 8Mn² - 42Mo – 36Cu.$
M_s	Payson and Savage[32]	$M_s(°C) = 499 - 308C - 32.4Mn - 16.2Ni - 27Cr - 10.8Mo - 10.8Si – 10.8W + (10Co).$
	Carapella[33]	$M_s(°C) = 496$ x $(1 – 0.62C)(1 – 0.092Mn)(1 – 0.033Si)(1 – 0.045Ni)(1 – 0.07Cr)(1 – 0.029Mo)(1 – 0.018W)(1 + 0.012).$
	Nehrenberg [34]	$M_s(°C) = 499 - 292C – 32.4Mn – 16.2Ni - 22Cr – 10.8Mo – 10.8Si + 10Co.$
	Rowland and Lyle[35]	$M_s(°C) = 499 - 324C – 32.4Mn – 16.2Ni - 27Cr – 10.8Mo – 10.8Si – 10.8W + 10Co.$
	Grange and Stewart[36]	$M_s(°C) = 538 - 350C – 37.7Mn – 18.9Ni – 37.7Cr - 27Mo + 10Co.$
	Stevens and Haynes[19]	$M_s(°C) = 561 - 474C - 33Mn - 17Ni - 17Cr - 21Mo + 10Co – 7.5Si.$
	Andrews[27]	$M_s(°C) = 539 - 423C - 30.4Mn - 17.7Ni - 12.1Cr - 7.5Mo - 11Si.$
	Kung and Rayment[28]	$M_s(°C) = 539 - 423C - 30.4Mn - 17.7Ni - 12.1Cr - 7.5Mo + 10Co - 7.5Si.$
		$M_s(°C) = 420 – 208.33C – 72.65N – 43.36N² - 16Ni + 0.7817Ni² - 0.02464 Ni³ - 2.473Cr – 33.428Mn + 1.296Mn² - 0.02167Mn³ + 30Mo + 12.86Co – 0.2654Co² + 0.001547Co³ - 7.18Cu – 16.28Ru + 1.72Ru² - 0.08117Ru³.$
	Zhao[37]	$M_s(°C) = 539 – 423C - 30.4Mn - 7.5Si + 30Al.$

Mahieu[38]

I.6 Strength prediction

I.6.1 *Empirical models based on the steel composition*

Alloying elements contribute to the strength of the final product. Many attempts have been made to link the final product tensile strength to its chemical composition. Many empirical formulas exist but each equation is adapted to a limited range of composition and does not take into account the thermal history of the steel. Nevertheless, such formulas are useful to approximate the final product strength when designing new steel. For bainitic steels, few formulas exist. For instance, the tensile strength of low carbon (< 0.25 wt.%) bainite formed by air cooling has been related directly to the chemical composition by Pickering:[39]

$$TS(MPa) = 243 + 1900C + 228(Cr + Mn) + 228Mo$$
$$+ 91W + 22Ni + 61Cu + 380(Ti + V)$$

(I.13)

Note that no contribution to strength is attributed to silicon. More recently, De Boer *et al.* proposed the following relation between the steel composition and its tensile strength for high strength bainitic steels by means of regression analysis:[40]

$$TS(MPa) = 430 + 688C + 81Si + 196Mn + 202Cr + 80Mo + 400V$$

(I.14)

Equation (I.14) was obtained by analysis of steels with approximately 0.4 wt.% C and 1.5 wt.% Si, and by varying alloying element concentrations within specific limits. The influence of Mn (0.70 to 1.30 wt.%), Cr (0.15 to 1.50 wt.%), Mo (0.20 to 0.80 wt.%) and V (0 to 0.10 wt.%) was tested.

I.6.2 *Improved equation for hot-rolled bainitic steels*

Equation (I.14) was applied to hot-rolled bainitic steels using a large range of compositions, reported by different authors. The calculated tensile strength is plotted in Figure I.18 as a function of the measured tensile strength for 164 steels of various compositions.[22,41-40] The agreement between the calculated and measured tensile strength was rather poor when equation (I.14) was used.

It is clear that more elements needed to be considered and the multiplying factors representing the contributions of each element to strength had to be adjusted. By means of multilinear regression calculations, we derived the following improved equation:

$$TS(MPa) = 288 + 803C + 83Mn + 178Si + 122Cr + 320Mo$$
$$+ 60Cu + 180Ti + 1326P + 2500Nb + 36000B$$

(I.15)

The application of that equation to the 164 steels is shown in Figure I.19.
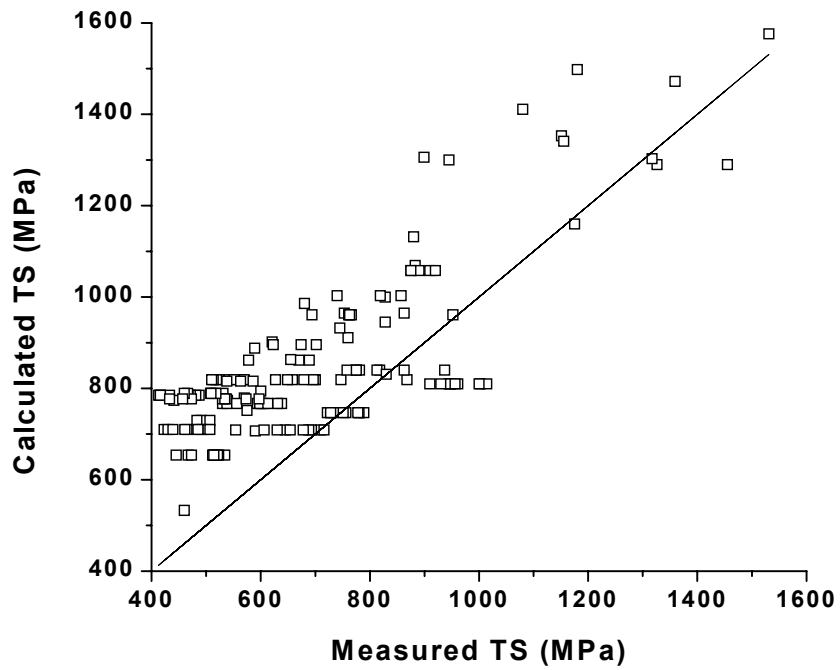
Figure I.18: Comparison between calculated (using equation I.14) and measured tensile strength for 164 steels.
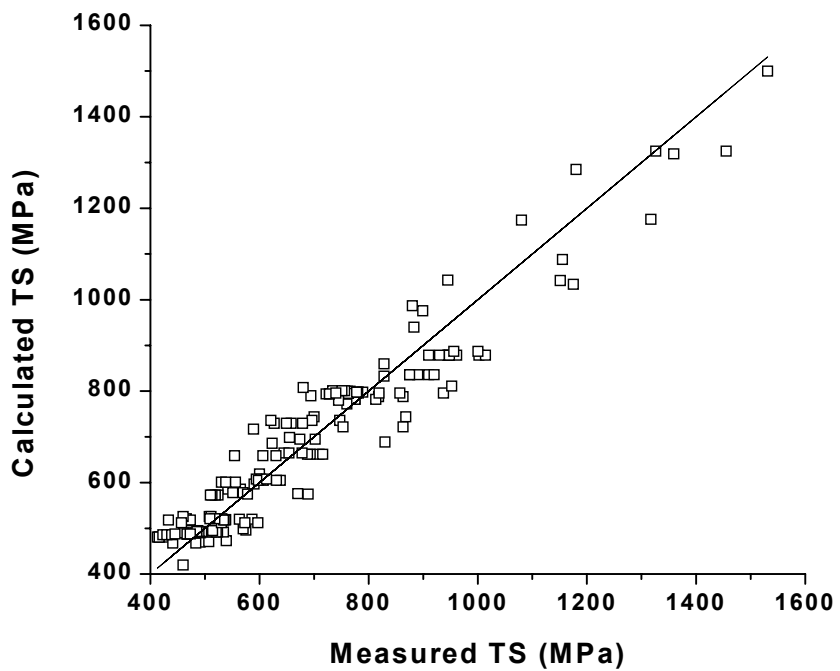
Figure I.19: Prediction of the tensile strength with equation (I.15).

The equation (I.15) is suitable for high strength bainitic steels with C content below 0.8 wt.% and the following range of compositions: Mn < 2 wt.%, Si < 1.8 wt.%, Cr < 2 wt.%, Mo < 0.8 wt.%, Cu < 1.6 wt.%, Ti < 500 ppm, P < 700 ppm, Nb < 800 ppm and B < 30 ppm.

It has been used to design hot-rolled bainitic steels[52], and was found to be also suitable for the lower strength TRIP steels if the base strength constant of 288 MPa is replaced by 238 MPa.[53]

I.6.3 Microstructure-based models

In the previous paragraph, the tensile strength of steels was estimated using empirical models based only on composition. Some models that predict the strength σ_i of each phase according to grain size, dislocation density, substitutional and interstitial elements content are also available.

The total strength σ_{total} can be estimated if the volume fractions V_i and strengths σ_i of each phase is known:

$$\sigma_{total} = \sum_i \sigma_i V_i = \sigma_{ferrite} V_{ferrite} + \sigma_{pearlite} V_{pearlite} + \sigma_{bainite} V_{bainite} + \sigma_{martensite} V_{martensite} \quad (I.16)$$

The strength of separate phases σ_i can be estimated by means of Swift's equation[54] describing the shape of stress (σ) – strain (ε_p) curves in the continuum plastic theory:

$$\sigma_i = a_i (b_i + \varepsilon_{pi})^{N_i}, \quad \varepsilon_i = \varepsilon_{pi} + \frac{\sigma_i}{E} \quad (I.17)$$

Hüper *et al.*[55] reported the materials constants *a*, *b* and *N* of Swift's equation for ferrite, pearlite, bainite and martensite in function of their composition, the ASTM grain size, *d*, and the lamellar spacing of pearlite in μm, S_0. Those constants are summarized in Table I.7.

Table I.7: Summary of materials constants (*a,b,N*) of Swift's equation in unit microstructures.[55]

Microstructure	*a* (MPa)	*b*	*N*
Ferrite	$109Si + 54.9P + 62.7Mn + 10.8d^{-1/2} + 373$	0.002	$-0.037Si + 0.35P - 0.024Mn + 1.07 \times 5/(10 + d^{-1/2}) - 0.12$
Pearlite	$189S_0^{-1/2} + 1140$	0.002	$-2.795 \times 10^{-2} Si - 1.11 \times 10^{-2} Mn + 0.219d^{-1/2} + 0.202$
Bainite	$2560C + 311Mn + 271$	0.002	$0.109C + 0.0133Mn + 0.072$
Martensite	$8590C + 1830$	0.0001	$0.763C + 0.153$

Other approaches to calculate the strength of separate phases are described below.

I.6.3.1 Strength of ferrite

The yield strength of pure iron is temperature dependent and the intrinsic strength of ferrite is typically 64 MPa at 273 K, as measured by *e.g.* Kimura.[56] Substitutional alloying elements have a strengthening effect. According to Pickering (alloy contents in wt.%):[57]

$$\sigma_{ss}(MPa) = 680P + 83Si + 32Mn + 38Cu + 33Ni \tag{I.18}$$

Interstitial elements C and N have both a strengthening effect of 5000 MPa/wt.%. In microalloyed steels, the maximum C solubility in ferrite is 0.02 wt.%, which gives C a contribution of 100 MPa to strengthening in ferrite.

The ferritic grain size has also a strengthening effect. This effect is described by the Hall-Petch equation:[58,59]

$$\sigma_{gs} = \sigma_0 + \frac{K}{\sqrt{d}} \tag{I.19}$$

In commercial quality steels, the values of σ_0 and K have been determined to 30 MPa and 21.8 MPa.mm$^{1/2}$, respectively.[60] With *e.g.* a grain of diameter $d = 20$ μm, the strengthening is 184 MPa.

The total strength of ferrite is usually between 300 and 600 MPa.

I.6.3.2 Strength of bainite

The strength of bainite consists of a number of strengthening mechanisms:

$$\sigma = \sigma_{Fe} + \sum_i x_i \sigma_{SSi} + \sigma_C + K_L(\overline{L})^{-1} + K_D \rho_D^{0.5} \tag{I.20}$$

where x_i is the concentration of a substitutional solute which is represented by a subscript i.
K_L coefficient for strengthening due to lath size, 115 MN m^{-1}
K_D coefficient for strengthening due to dislocations, 7.34 x 10^{-6} MN m^{-1}
σ_{Fe} strength of pure, annealed iron, 219 MN m^{-2} at 300 K
σ_{SSi} substitutional solute (i) strengthening
σ_C solid solution strengthening due to carbon
ρ_D dislocation density, typically 10^{16} m^{-2}
$\overline{L}$ measure of ferrite lath apparent thickness, typically 0.2 μm

The strength increment due to dissolved carbon should vary with the square root of the carbon concentration according to solid-solution theory:

$$\sigma_c = 1722.5C^{1/2} \tag{I.21}$$

where the strength is in MN m^{-2} and the C concentration is in wt.%.

Honeycombe and Bhadeshia assume that the maximum carbon content in ferritic bainite is 0.02 wt.%.[61] This value is currently subject of many discussions and some researchers recently reported 0.2 wt.% carbon in bainite using convergent beam Kikuchi line diffraction patterns.[62] The very high dislocation density ($\sim 10^{13}$ cm^{-2}) in the bainitic phase in TRIP steels was assumed to effectively trap high levels of interstitial C, and up to 0.24 wt.% C was measured in the bainitic phase.[63] For the present example, however, a value of 0.02 wt.% was used.

Alloying elements also contribute to the strength of the final microstructure. Substitutional solutes do not partition during the displacive growth of either martensite or bainite, so that their concentrations are fixed by the composition of steel as a whole. Solid solution strengthening contributions, σ_{Ssi} can be estimated as a function of temperature and strain rate from published data.

Table I.8: Strength (MN m^{-2}) of pure iron as a function of temperature and solid solution strengthening terms for ferrite, for 1wt.% of solute. The data are for a strain rate of 0.0025 s^{-1}.

	200°C	**100°C**	**Room T (23°C)**	**-40°C**	**-60°C**
Fe	215	215	219	355	534
Si	78	95	105	70	-44
Mn	37	41	45	8	-57
Ni	19	23	37	-2	-41
Mo	-	-	18	-	-
Cr	7.8	5.9	5.8	7.4	15.5
V	-	-	4.5	-	-
Co	1.0	1.8	4.9	9.1	5.8

Table I.8 shows that whereas the strength of pure iron increases as the temperature is reduced, strengthening due to substitutional solutes often goes through a maximum as a function of temperature. Indeed, there is some solution softening at low temperatures because the presence of a foreign atom locally assists a dislocation to overcome the Peierls barrier at low temperatures.

When martensite or bainite form at high temperatures, the shape change due to shear transformation causes plastic deformation, and hence the accumulation of dislocations in both the parent and product phases. The extent of the plasticity depends on the yield strength, and hence on the temperature. Takahashi and Bhadeshia have therefore suggested that the dislocation density of both martensite and bainite can be represented empirically as a function of temperature alone, for the temperature range 570-920 K:[64]

$$\log_{10}\{\rho_D\} = 9.2840 + \frac{6881}{T} - \frac{1780360}{T^2} \qquad (I.22)$$

where T is the transformation temperature in Kelvin, and ρ_D is stated in units of m^{-2}.

The strengthening σ_ρ (MN m^{-2}) due to dislocations is given by:

$$\sigma_\rho = 0.38\mu b(\rho_D)^{0.5} \cong 7.34 \times 10^{-6}(\rho_D)^{0.5} \tag{I.23}$$

where μ is the shear modulus and b is the magnitude of the Burgers vector. Figure I.20 shows a plot of equation (I.23).
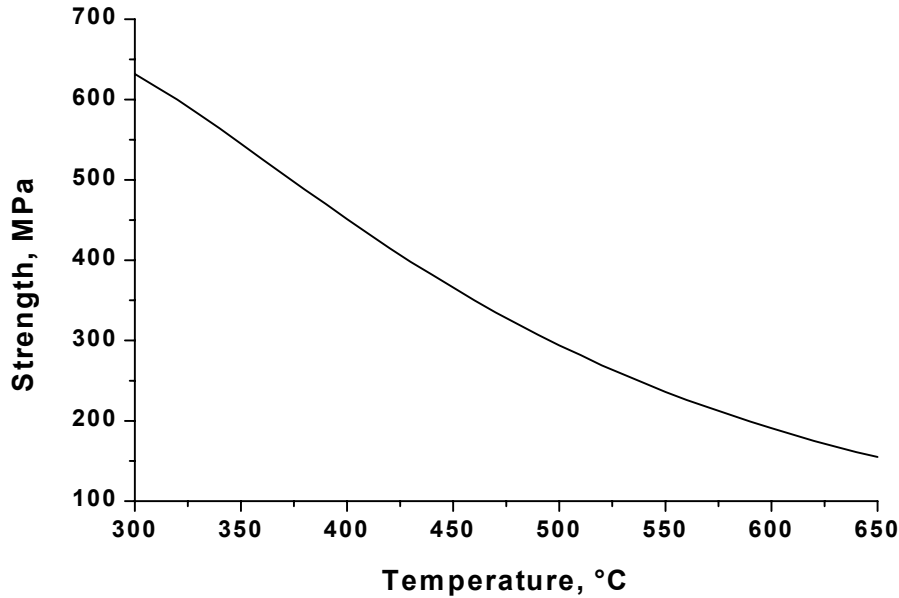
Figure I.20: Contribution of dislocation density to the strength of bainite and martensite, as a function of transformation temperature.

Martensite and bainite grow in the form of very fine plates or laths. The resulting grain size strengthening is defined as:

$$\sigma_{gs} \cong 115\overline{L}^{-1} \text{ MN m}^{-2} \tag{I.24}$$

where $\overline{L}$ is the mean intercept measured on random sections. In such sections, the ferrite plates appear approximately parallel-side, and the thickness is then measured in a direction normal to the long edges of the plates. The average value of the measurements is taken to represent a "grain size", which is really an apparent plate thickness. The procedure is useful in characterizing any quantitative trends in microstructure but obviously ignore stereological considerations. For example, if a platelet is represented as a disc of radius r, and thickness t, with r>>t, then the mean intercept length is given by $\overline{L} = 2t$, and the mean intercept area is given by $A = 2rt$.

There is some uncertainty about the influence of carbon on the grain size of bainite. The apparent thickness of bainite is, in general, found to increase with transformation temperature from about 0.2 to 2 μm when the transformation temperature changes from 425 °C to 570 °C, respectively, for a Fe-0.22 wt.% C commercial steel.

I.6.3.3   Strength of martensite

The main contribution to the strength of martensite is due to the solid solution strengthening by carbon. As other phases are formed before the martensite, the carbon content in untransformed austenite has increased. To estimate the carbon content a simple mass balance equation is used:

$$\bar{x} = x_\gamma V_\gamma + x_\alpha V_\alpha + x_{\alpha_b} V_{\alpha_b}$$ (I.25)

where $\bar{x}$ is the carbon content of the steel,
x_i are the carbon content in austenite, ferrite and bainite,
V_i are the volume fraction of respective phases.

The new carbon content in austenite has an influence on martensite start temperature. Its new value is calculated using the following equation derived from the equation (I.12):

$$M_s' = M_{s0} - 539(x_\gamma - x_0)$$ (I.26)

With M_{s0} the initial temperature of martensitic transformation,
x_γ the carbon content in austenite just before martensitic transformation,
x_0 the initial carbon content in austenite.

Dislocations contribution is calculated at this new temperature using the equations (I.22) and (I.23).

The lath size contribution is estimated to be 75 MPa, as in the case of bainite.

I.6.3.4   Strength of austenite

The yield strength of residual austenite in Si-TRIP steels is expressed by Young and Bhadeshia as:[65]

$$\sigma_\gamma (MPa) = (1 - 0.26.10^{-2} T_r + 0.47.10^{-5} T_r^2 - 0.26.10^{-8} T_r^3) \times 15.4$$
$$\times (4.4 + 23C + 1.3Si + 0.24Cr + 0.94Mo + 32N)$$ (I.27)

where $T_r = T - 25$, T being the temperature in °C. Concentrations are in wt.%.

I.6.3.5   Application

A number of complex phase steels with a bainite-martensite-austenite microstructure were studied in the course of the present work. One composition in particular was chosen for a more in depth study of the phase transformations. This Nb-B-Mo-Cr microalloyed CMn steel contained 0.16 wt.% C, 1.6 wt.% Mn, 0.25 wt.% Si, 0.5 wt.% Cr, 0.2 wt.% Mo and B, Ti and Nb additions. The tensile strength calculated by means of the improved equation (I.15) is 995 MPa. According to dilatometric measurements and metallographic observations, the microstructure of that steel cooled at the rate 5 °C/s from 1200 °C consists of about 60 vol.% bainite and 30 vol.% martensite, leaving 10 vol.% of untransformed austenite.

The contributions to strength of separate phases were calculated and the results are shown in Table I.9. The results of the empirical strength calculation and the microstructure-based method are remarkably close to the actual, measured strength.

Table I.9: Strength prediction for 0.6Bainite-0.3Martensite-0.1Austenite CP steel (in MPa).

	Iron contribution	64	
	Carbon contribution	244	with 0.02 wt.% C
BAINITE	Substitutional strengthening	106	
	Dislocations	236	at 550 °C
	Lath size	75	
	Total strength of bainite	725	
	Iron contribution	64	
	Carbon contribution	1051	with 0.37 wt.% C
MARTENSITE	Substitutional strengthening	106	
	Dislocations	653	at 284 °C
	Lath size	75	
	Total strength of martensite	1950	
AUSTENITE	Total strength of austenite	131	at 25 °C
0.6B+ 0.3M+ 0.1A	**Total strength of steel**	**1033**	
	Calculated strength using (I.15)	**995**	
	Measured strength	**1060**	

The steel was laboratory hot rolled and coiled at 550 °C to produce the required CP microstructure. The tensile strength was 1060 MPa, which is close to the predicted tensile strength. Note that in the previous calculation the possible strengthening resulting from the Ti and Nb microalloying was not taken into account. The additional strengthening may be of the order of 100 Mpa, *i.e.* increasing the total strength of about 10 % in a fully ferritic steel. There is currently no theory for the effect of Nb microalloying addition on the mechanical properties of bainite and martensite.

I.6.4   Hardness

The hardness of the steel may be divided into hardness of different phases using the rule of mixture:

$$Hv = X_m Hv_m + X_b Hv_b + (X_f + X_p)Hv_{f+p}$$ (I.28)

where Hv is the hardness in Vickers; X_m, X_b, X_f and X_p are the volume fraction of martensite, bainite, ferrite and pearlite, respectively; and Hv_m, Hv_b, Hv_{f+p} are the hardness of martensite, bainite, and the mixture of ferrite and pearlite, respectively.

Empirically based formulas developed by Maynier *et al.* were used for the calculation of Hv_m, Hv_b, and Hv_{f+p} taking into account the steel composition and the cooling rate:[66]

$$Hv_m = 127 + 949C + 27Si + 11Mn + 8Ni + 16Cr + 21\log V_r \tag{I.29}$$

$$Hv_b = -323 + 185C + 330Si + 153Mn + 65Ni + 144Cr + 191Mo \\ + (89 + 53C - 55Si - 22Mn - 10Ni - 20Cr - 33Mo)\log V_r \tag{I.30}$$

$$Hv_{f+p} = 42 + 223C + 53Si + 30Mn + 12.6Ni + 7Cr + 19Mo \\ + (10 - 19Si + 4Ni + 8Cr + 130V)\log V_r \tag{I.31}$$

where V_r is the cooling rate at 700 °C in °C/h.

Knowing the volume fraction of different phases, determined by dilatometry and metallographic observations, or estimated by means of proposed models, the hardness may be predicted. The hardness value can be converted to tensile strength in MPa using the following empirical relationship:[67]

$$TS(MPa) = 80 + 2.57Hv \tag{I.32}$$

I.7 Processing of complex phase steels

In previous paragraphs, it was shown that alloying elements contribute to the strength of the final product, and can also play a crucial role in determining the final microstructure. In paragraph I.2, it was shown that very different kinds of microstructures could be obtained when starting from the same steel composition. Therefore, it is necessary to control the microstructure formation by means of the appropriate thermal cycles.

I.7.1 Hot rolled complex phase steels

Complex Phase (CP) steels are defined as steels having a microstructure consisting in ferrite, bainite and martensite, plus eventually a small amount of retained austenite. In comparison to Dual Phase (DP) steels, the presence of the microconstituent bainite in CP steels provides higher strength levels. Using small additions of elements retarding the austenite to ferrite transformation, hot rolled steels with a Bainite-Martensite-Austenite microstructure were produced. These steels had a continuous stress-strain curve similar to that of dual phase steel, a strength level of 1200 MPa and an elongation of 10 %. The hot rolling scheme used to produce hot rolled CP steels from a Nb-alloyed CMnMoCrB steel composition is shown in Figure I.21a.
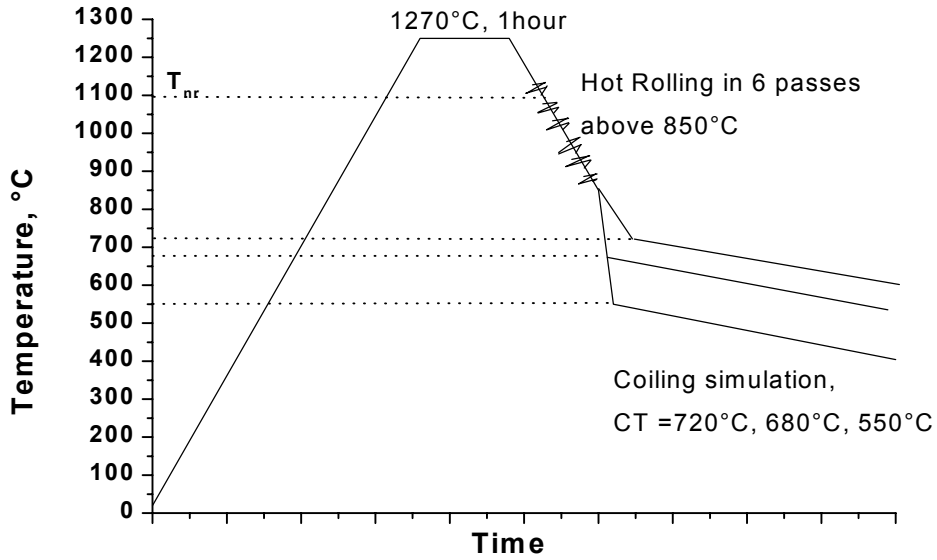
a)
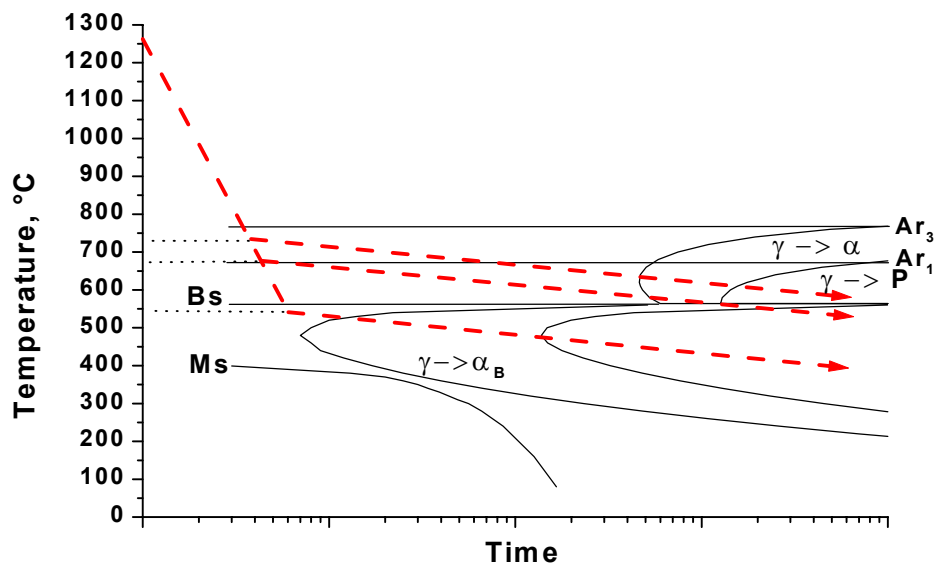
b)

Figure I.21. a) Hot-rolling scheme and b) schematic TTT diagram for the studied steel composition.

The most important parameter is the coiling temperature (CT), which determines the type of transformation that will occur. The schematic Time-Temperature-Transformation (TTT) diagram of Figure I.21b illustrates clearly that coiling at different temperatures will result in different transformation products.

I.7.2   Cold rolled complex phase steels

Annealing cycles consisting of a reheating to an intercritical temperature between Ac_1 and Ac_3 followed by a cooling and an isothermal holding at a temperature above the martensite start temperature (M_s), were performed to produce a CP microstructure after cold rolling. It can be seen on the pseudo Fe-C diagram of Figure I.22 that the ferrite volume fraction and its carbon content is controlled by the intercritical annealing (IA) temperature and time of annealing. During the cooling and holding, part of the intercritical austenite transforms to bainite. The volume fraction of bainite is a function of the IA temperature, which determines the carbon content in the austenite and hence the bainite start (B_s) temperature, and of the isothermal bainite transformation (IBT) temperature and time. During the subsequent cooling to room temperature, martensite is formed, and some austenite may remain untransformed.
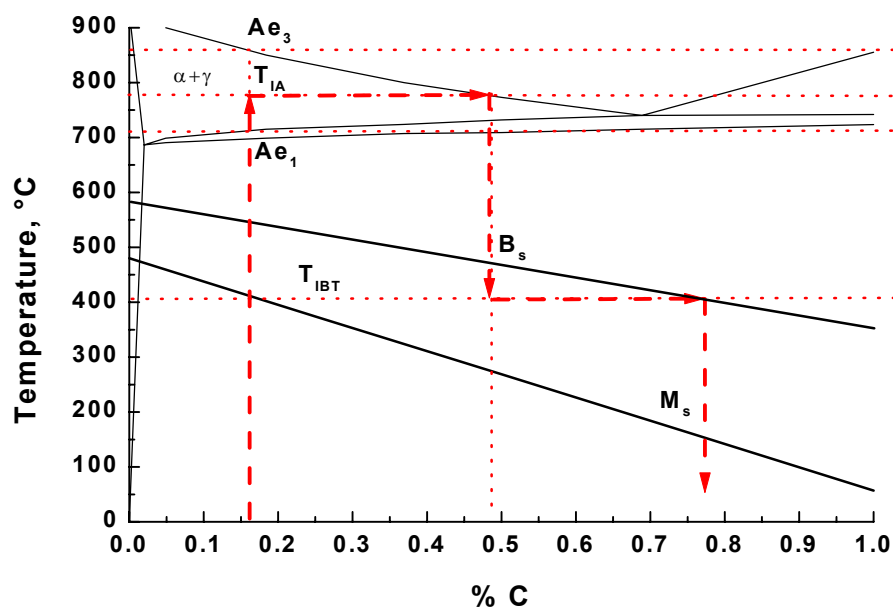
Figure I.22: Pseudo Fe-C diagram showing the variation of C in the austenite during an IA cycle.

The annealing cycles are schematically shown in Figure I.23a, and the time-temperature-transformation (TTT) diagram in Figure I.23b illustrates what is happening during the cooling following the annealing. Continuous annealing simulations were done on cold rolled sheet steels. Complex phase microstructures consisting in ferrite, bainite and martensite were obtained.
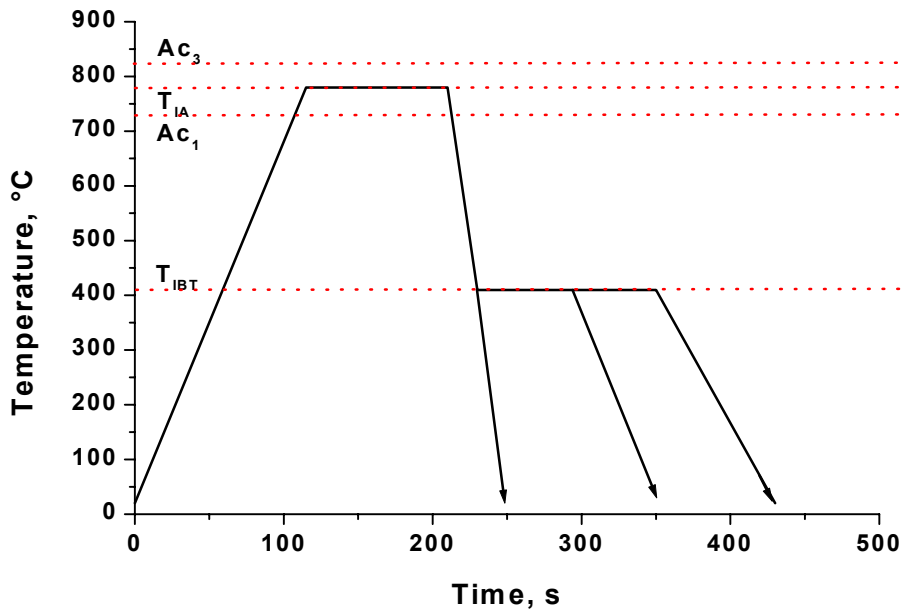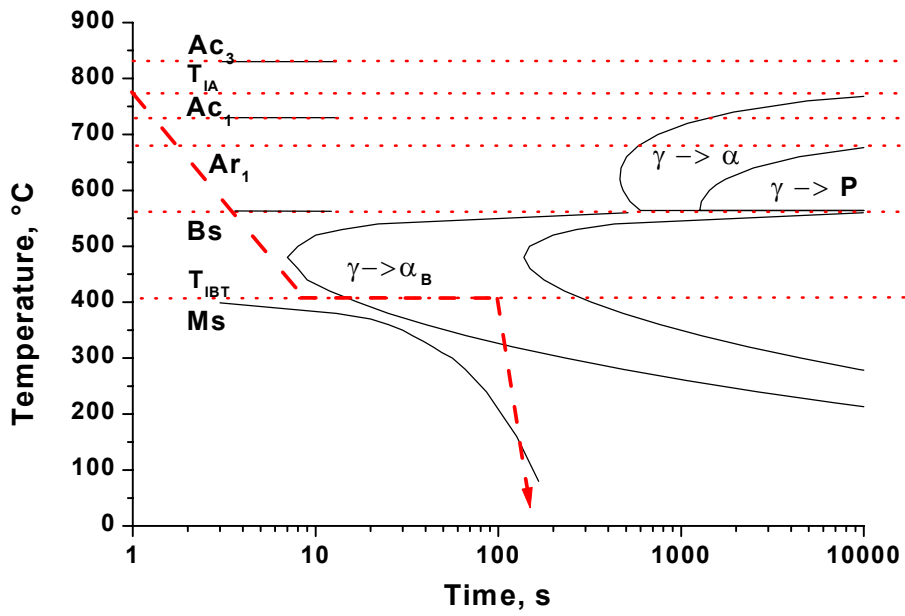
Figure I.23: a) Annealing cycles and b) corresponding TTT diagram.

I.8 Aims and scope of the present work

The scope of the current work was to develop hot rolled and cold rolled high strength complex phase steel using a physical metallurgy approach. The present work is divided in 10 chapters. After the introduction in *Chapter I*, the experimental details are described in *Chapter II*. In *Chapter III* a model accounting for the carbon partitioning during the austenite decomposition is developed for multiphase transformations. The practical application of the model to various phase transformations in CMn steels is presented in *Chapter IV*. The effects of small additions of soluble Boron on the austenite decomposition in a CMn steel are reported in detail in *Chapter V*. *Chapter VI* reviews the effects of micro alloying with combinations of Mo, Cr and soluble B in CMn steels on the austenite decomposition. *Chapter VII* involves the texture measurements of a hot rolled complex phase steel coiled at different coiling temperatures. The effect of the austenite deformation state is shown to affect the crystallographic orientation of the product phases. *Chapter VIII* is a review on the effects of microalloying elements Cr, Mo, B and Nb on the microstructure formation in hot rolled multiphase high strength steels. A classification of the final mechanical properties is done in function of the microstructure. In *Chapter IX* the intercritical annealing process after cold rolling complex phase steel is studied in detail to predict the final microstructure. The process parameters were varied to produce different multiphase microstructures and link those microstructures and their tensile properties. Finally, *Chapter X* summarizes the main conclusions of this work and contains suggestions for further work.

References

[1] European patent application No 01870186.2, 2001.

[2] http://www.ulsab.org/public/overview/consortium.htm

[3] ULSAB-AVC Consortium. Technical Transfer Dispatch #6, May 2001. www.ULSAB-AVC.org.

[4] C. Mesplont, S. Vandeputte, B.C. De Cooman: 43rd MWSP Conf. Proc., ISS, Vol.39, 2001, p.359.

[5] B.C.DeCooman, M.DeMeyer, T.Waterschoot, C.Mesplont, J.Mahieu, U.Meers: Proceedings High Strength Steels: Processing and Applications (HISPA) '99, April, Ranchi, p.8.

[6] F.S. LePera: Journal of Metals, March 1980, p.38.

[7] R. F. Hehemann: Phase Transformations, ASM, Metals Park, Ohio, 1970, p.397.

[8] H.K.D.H. Bhadeshia: Bainite in Steels, Second Edition, The Institute of Metals, London, 2001, p.19.

[9] H.K.D.H. Bhadeshia: Bainite in Steels, Second Edition, The Institute of Metals, London, 2001, p.63.

[10] H.K.D.H. Bhadeshia: Bainite in Steels, Second Edition, The Institute of Metals, London, 2001, p.129.

[11] M. Takahashi, H.K.D.H. Bhadeshia: Mater. Trans. JIM, 1991, vol. 32, p.689.

[12] G. Kurdjumov, G. Sachs, Z. Phys., 1930, Vol. 64, p. 225.

[13] Bainite Committee of Iron and Steel Institute of Japan: Atlas for Bainitic Microstructures vol.1, ISIJ, 1992.

[14] B.L. Bramfitt, J.G. Speer: Metallurgical Transactions A, vol. 21A, april 1990, p.817.

[15] H.K.D.H. Bhadeshia: Bainite in steels. The Institute of Materials, eds. 1992, p.27.

[16] H.K.D.H. Bhadeshia: Bainite in steels. The Institute of Materials, eds. 1992, p.65.

[17] E.C. Bain, H.W. Paxton: Alloying elements in steel. Second edition, 1961. American Society for Metals. P. 62.

[18] R W K Honeycombe, H K D H Bhadeshia: Steels, Microstructure and properties. Second edition, Edward Arnold (Ed.), 1995, p.133.

[19] W. Steven, A.G. Haynes: J. of the Iron and Steel Institute 183, 1956, p.349.

[20] L.J. Habraken, M. Economopoulos: Transformation and Hardenability in Steels, Symposium, 27-28 February 1967, Climax Molybdenum Co. of Michigan / University of Michigan, p.69.

[21] R.K. Steele: 39th MWSP Conf. Proc., Iss, Vol. XXXV, 1998, p.997.

[22] L. Vandoorne: Engineering Degree Thesis, Ghent University, 1998.

[23] B.L. Bramfitt: 39th MWSP Conf. Proc., Iss, Vol. XXXV, 1998, p.989.

[24] Ph. Maynier, J. Dollet, P. Bastien: <u>Revue de Métallurgie</u>, Avril 1970, p.343.

[25] M.V. Li, D.V. Niebuhr, L.L. Meekisho, D.G. Atteridge: <u>Metallurgical and Materials Transactions B</u>, Vol.29B, june 1998, p.661.

[26] J.S. Kirkaldy, D. Venugopalan: Phase Transformations in Ferrous Alloys, D.A.R. Marder and J.I. Goldstein, eds., AIME, New York, NY, 1983, p.128.

[27] K.W. Andrews: <u>JISI</u>, vol. 203, 1965, p.721.

[28] C.Y. Kung, J.J Rayment: <u>Metall. Trans. A</u>, 1982, vol. 13A, p.328.

[29] I. Tamura, H. Sekine, T. Tanaka, C. Ouchi : Thermomechanical processing of HSLA steels, Butterworths, 1988.

[30] T. Nakamura, K. Esaka : Thermec 1988, p. 645.

[31] F. Leysen, C. Standaert, U. Meers, J. Dilewijns: Proc. 3rd Int. Conf. On recrystallization and related phenomena, Monterey, California (USA), 21-24 october 1996, p. 437.

[32] P. Payson, C.H. Savage : <u>Trans. ASM</u>, 33, 1994, p.261.

[33] L.A. Carapella: <u>Metals Progress</u>, vol. 46, 1944, p.108.

[34] A.E. Nehrenberg, <u>Trans. AIME</u> 167, 1946, p.494.

[35] E.S. Rowland, S.R. Lyle: <u>Trans. AIME</u>, vol. 37, 1946, p.27.

[36] R.A. Grange, H.M. Stewart: <u>Trans. AIME</u>, vol.167, 1946, p.467.

[37] J. Zhao: <u>Materials Science and Technology</u>, November 1992, vol. 8, p.997.

[38] J. Mahieu, J. Maki, B.C. De Cooman, S. Claessens : <u>Metallurgical and Materials Transactions A</u>, vol. 33A, 2002, *in press*.

[39] F.B. Pickering: Transformation and Hardenability in Steels, Symposium, 27-28 February 1967, Climax Molybdenum Co. of Michigan / University of Michigan, p.109.

[40] H. de Boer, S. R. Datta, H-J. Kaiser, S.O. Lundgreen, B. Müsgen, H. Schmedders, K. Wick: <u>Stahl und Eisen</u> 115, Nr.2, 1995, p.93.

[41] S.C. Wang, F.J. Chiu: Proceedings from Materials Solutions '97 on Accelerated Cooling/Direct Quenching Steels. 15-18 September 1997, Indianapolis, Indiana, p.77.

[42] P. Teracher, G. Marron: High Strength Steels for Automotive Symposium Proceedings, 1994, p.27.

[43] A. Kern, H. Schmedders, A. Zimmermann: 39th MWSP Conf. Proc., Iss, Vol. XXXV, 1998, p.1015.

[44] A. Bodin, A.B.C. Edelman, P.M. Hekker: High Strength Steels for Automotive Symposium Proceedings, 1994, p.17.

[45] E.M. Focht: Proceedings from Materials Solutions '97 on Accelerated Cooling/Direct Quenching Steels, 15-18 September 1997, Indianapolis, Indiana, p.23.

[46] A.Tamminen: Thermomechanical Processing in Theory, Modelling and Practice. Proceedings of an International Conference Organized in Celebration of the 75th Anniversary of The Swedish Society for Materials Technology. 4-6 September 1996, Stockholm, Sweden, p.357.

[47] K. Sawley, M. Scholl: 39th MWSP Conf. Proc., Iss, Vol. XXXV, 1998, p.1007.

[48] P.E. Repas, G.A. Dries, D.J. Wincko: Thermomechanical Processing in Theory, Modelling and Practice. Proceedings of an International Conference Organized in Celebration of the 75th Anniversary of The Swedish Society for Materials Technology, 4-6 September 1996, Stockholm, Sweden, p.330.

[49] Y. Shan, Y. Wang, Z. Liu, B. Qian, A. Li: Proceedings from Materials Solutions '97 on Accelerated Cooling/Direct Quenching Steels, 15-18 September 1997, Indianapolis, Indiana, p.101.

[50] M.A. Linaza, J.L. Romero, J.M. Rodriguez-Ibabe, J.J. Urcola: Thermomechanical Processing in Theory, Modelling and Practice. Proceedings of an International Conference Organised in Celebration of the 75th Anniversary of The Swedish Society for Materials Technology. 4-6 September 1996, Stockholm, Sweden, p.351.

[51] A.M. Hall. Introduction to Today's Ultrahigh-Strength Structural Steels. Issued under the auspices of American Society for Testing and Materials and the Defence Metals Information Centre. 1971.

[52] C. Mesplont, T. Waterschoot, S. Vandeputte, D. Vanderschueren, B.C. De Cooman: Thermomechanical Processing of Steels Conference Proceedings, IOM Communications, UK, May 2000, p.495.

[53] B. Mintz: Galvatech' 2001, Stahl und Eisen, Marcel Lamberights (Ed), 2001, p.551.

[54] H.W. Swift: Journal of the Mechanics and Physics of Solids, vol. 1, 1952, p.1.

[55] T. Hüper, S. Endo, N. Ishikawa, K. Osawa: ISIJ International, vol.39, No.3, 1999, p.288.

[56] H. Kimura: Materials Transactions, JIM, vol. 40, No. 10, 1999, p.1025.

[57] H. Adrian, F.B.Pickering, Materials Science and Technology, Vol.7, 2, 1991, p.176.

[58] E.O. Hall, Proc. Phys. Soc. (Lond.) 64B, 1951, p.747.

[59] N.J. Petch, J. Iron Steel Inst. 174, 1953, p.25.

[60] B.Engl, K. Polteschmidt: <u>Stahl u. Eisen</u>, 114, n°7 ,1994, p.47.

[61] R.W.K. Honeycombe, H.K.D.H. Bhadeshia: Steels, Microstructure and Properties, Second edition, 1995, Edward Arnold, p. 311.

[62] M.-X.Zhang, P.M.Kelly: <u>Materials Characterization</u> 40, 1998, p.159.

[63] M. De Meyer, A.K. De, L. Tosal-Martinez, B.C. De Cooman: 43rd MWSP Conf. Proc., Iss, Vol. XXXIX, Charlotte, NC, 2001, p.349.

[64] M. Takahashi, H.K.D.H. Bhadeshia: <u>Materials Science and Technology</u> 6, 1990, p.592.

[65] C.H.Young, H.K.D.H.Bhadeshia, <u>Mater. Sci. Technol</u>. 10, 1994, p.209.

[66] P. Maynier, J. Dollet, P. Bastien: Hardenability Concepts with Applications to Steels, D.V. Doane and J.S. Kirkaldy, eds., AIME, New York, NY, 1978, p.518.

[67] B.Donnay, J.C. Herman, V. Leroy, U. Lotter, R. Grossterlinden, H. Pircher: 2nd Int. Conf. on Modelling of Metal Rolling Processes. London, 9-11 december 1996, p.113.

Experimental procedure

II.1   Introduction

This chapter gives an overview of the materials, equipment and characterization techniques used in the cause of the research work reported in the present doctoral dissertation. For the sake of clarity, some experimental details may also be present at the start of each chapter.

II.2   Material preparation

The laboratory castings were prepared at the Laboratory for Iron and Steelmaking (LISm) as 100 kg ingots in a Pfeiffer VSG100 induction furnace operating under argon gas protective atmosphere. Varied steel compositions were cast for different purposes. At first, based on microstructure and tensile predictions presented in chapter I, different steels aiming at high tensile strength and adequate elongation were cast in order to select the best appropriate composition for industrial development. Only part of those steels designed for rolling simulation was used for the present work. The compositions used for the present research work are given in Table II.1. Those steels are all CMn steels, microalloyed. The tensile strength predicted by means of the empirical equation (I.12) is also indicated. The steel composition 6, microalloyed with Cr, Mo and B was first cast in laboratory. That composition was chosen for industrial development and a new casting was made with the composition 7. The industrial steel was cast at SIDMAR N.V., Ghent, Belgium. After cutting, the industrial material was further processed at the laboratory (LISm) in the same manner as the laboratory-cast material.

Table II.1: High strength microalloyed steels used for rolling simulation and investigation of the tensile properties, compositions in wt.%.

Casting	C	Mn	Mo	Si	Cr	Nb	P	Ti	B(ppm)	N(ppm)	TS, MPa
1. low C	**0.039**	1.36	-	0.150	-	0.032	0.013	0.100	-	73	674
2. Nb	0.155	1.75	-	-	-	**0.106**	0.013	0.082	-	20	937
3. Mo	0.145	1.66	**0.21**	-	-	0.083	0.012	0.069	-	10	914
4. MoB low C	**0.066**	1.92	**0.24**	0.14	-	0.047	0.014	0.023	**16**	50	823
5. MoB	0.163	1.61	**0.19**	0.25	-	0.072	0.013	0.054	**18**	50	947
6. MoCrB	0.161	1.60	**0.20**	0.26	**0.43**	0.061	0.020	0.023	**21**	42	971
7. Industrial	0.160	1.60	0.18	0.28	0.50	0.050	0.030	0.030	20	90	954
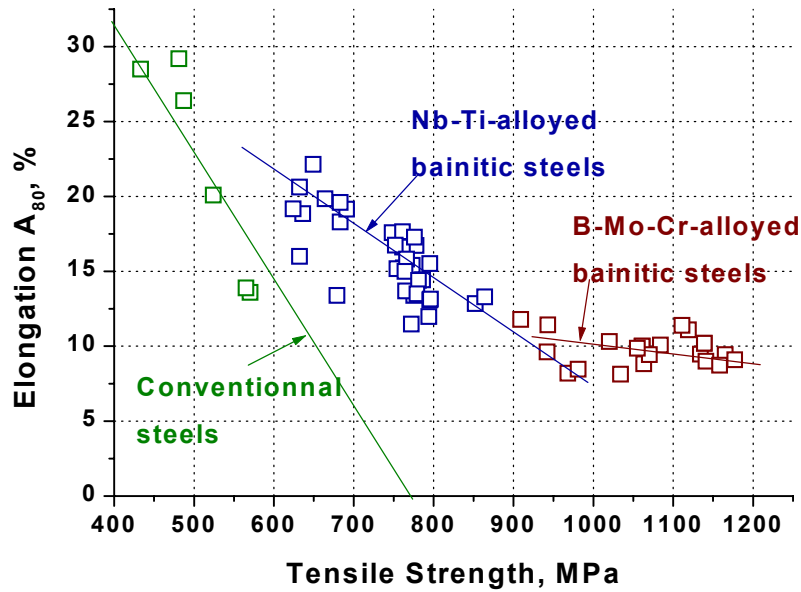
Figure II.1: Elongation *versus* Tensile Strength plot for some of the steels investigated.

It was found that B additions led to significant better tensile properties. Nb additions produced precipitation strengthening, leading to higher strength levels for the similar elongation. Finally, a combined effect between B and Nb was observed. A slower kinetics of phase transformations associated with a strengthening effect allowed the development of sheet steels having high strength levels with adequate elongation, as shown in Figure II.1. In this figure, a distinction is made between precipitation-strengthened steels containing Ti and Nb, and steels containing substitutional strengthening elements Cr and/or Mo in the presence of soluble B.

A more fundamental approach was made to study phase transformations in CMn steels and understand the effects of alloying elements B, Cr and Mo on the kinetics of phase transformations. New compositions were cast especially for this aim. The Interstitial Free (IF) steel was used as a reference for dilatometry because its slow cooling from the austenitic region to room temperature implies only one phase transformation. The CMn steel was used to validate a model for determining Continuous Cooling Transformation (CCT) diagrams by means of dilatometry. From this base steel, the effect of soluble B, protected from precipitation with N by Ti additions was investigated. Finally, the effects of Cr and Mo in combination with soluble B were investigated in CMn steels. The compositions of the steels used for the fundamental study of phase transformations are listed in Table II.2.

Table II.2: Compositions of the steels used for the study of phase transformations, in wt.%.

Steel	C	Mn	Mo	Si	Cr	Nb	P	Ti	B (ppm)	N (ppm)
8.IF	0.0034	0.97	-	0.007	-	0.025	0.073	0.010	10	27
9.CMn	0.190	1.64	-	-	-	-	0.015	-	-	50
10.CMnB	0.140	1.72	-	-	-	-	0.018	0.029	**35**	50
11.CMnBCr	0.174	1.66	-	-	**0.48**	-	0.017	0.019	**24**	36
12.CMnBMo	0.174	1.62	**0.21**	-	-	-	0.017	0.018	**25**	30
13.CMnBCrMo	0.166	1.63	**0.19**	-	**0.47**	-	0.017	0.018	**22**	40

II.3 Rolling and annealing simulations

Both hot rolling and cold rolling were performed using a 3000 kN Carl Wezel laboratory reversing mill.

The ingots were cut into blocks with 25 mm thickness and, after reheating at 1250 °C for 1 hour, were rolled in 6 passes to the final thickness of 2 mm. The final reduction of 30 % was in most cases carried out above 850 °C. This last temperature was chosen to be higher than Ar_3, the start temperature of the $\gamma \rightarrow \alpha$ transformation.

The fully computerised data acquisition during rolling allows for the determination of the mean flow stress (MFS), calculated by means of the formulas published by Maccagno *et al*:[1]

$$r = \frac{H-h}{H}, \; T_1 = \frac{\pi}{8}\left(\frac{h}{R}\right)^{1/2} \ln(1-r), \; T_2 = \frac{1}{2} Arc \tan\left(\frac{r}{r-1}\right)^{1/2}$$

$$\phi = \tan(T_1 + T_2)\left(\frac{h}{R}\right)^{1/2}, \; Y = 2R(1-\cos\phi) + h$$

$$T_3 = 2\pi T_2, \; T_4 = \left(\frac{R}{h}\right)^{1/2} \ln\left[\left(\frac{Y}{h}\right)^2 (1-r)\right]$$

$$Q = \frac{1}{2}\left(\frac{1-r}{r}\right)^{1/2} (T_3 - T_4) - \frac{\pi}{4}$$

$$MFS = P \Big/ \left(\frac{2}{\sqrt{3}} w (R(H-h))^{1/2} Q\right). \tag{II.1}$$

where P is the rolling force, w the plate width, R the roll radius, H the plate thickness before the pass and h the plate thickness after the pass.

The dimensions of a rolling mill are schematically shown in Figure II.2. The diameter of the rolls used at the laboratory is 320 mm, the rolling width is 125 mm.
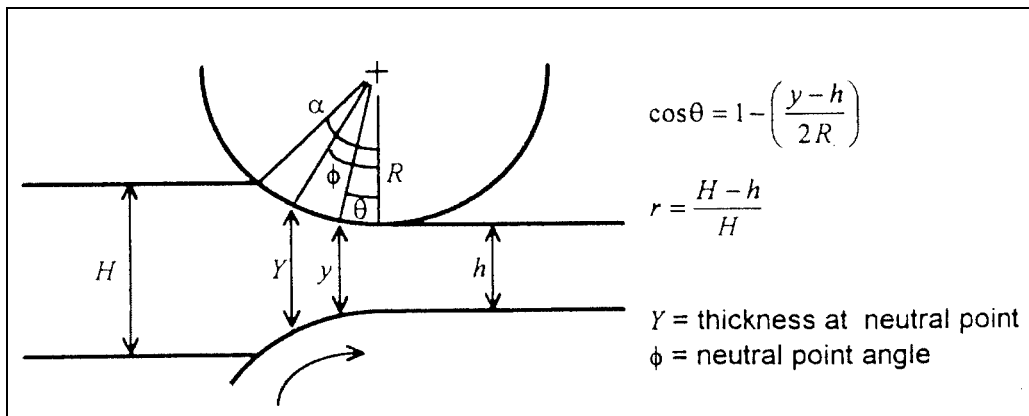
Figure II.2: Dimensions of a rolling mill.[1]

Table II.3 regroups hot rolling data for the industrial composition hot rolled in laboratory. The MFS values are plotted versus the temperature (before the rolling pass) in Figure II.3**.**

Table II.3: Typical measured rolling data and calculated MFS for the industrial composition rolled in laboratory.

pass	1	2	3	4	5	6
T before, °C	1133	1097	1042	985	918	837
rolling reduction	0.35	0.35	0.36	0.33	0.33	0.32
end thickness, mm	16.25	10.56	6.81	4.58	3.06	2.07
effective strain	0.50	0.50	0.51	0.46	0.47	0.45
strain rate, s^{-1}	7.78	9.66	12.11	14.21	17.50	21.02
rolling force, tons	103	125	145	168	187	212
MFS, Mpa	157	214	274	377	451	565

Hot rolling was followed by accelerated cooling at a rate of 30 °C/s to the coiling temperature, which was varied in the range 720 °C - 300 °C.

After a coiling simulation for 5 hours with an average cooling rate of 50 °C/h, the plates were air cooled to room temperature. The schematic of hot rolling route is shown in Figure II.4.

Some blocks were hot rolled to a final thickness of 2.5 mm. The hot rolled plates were then cold rolled with 60 % reduction to the final thickness of 1.5 mm.
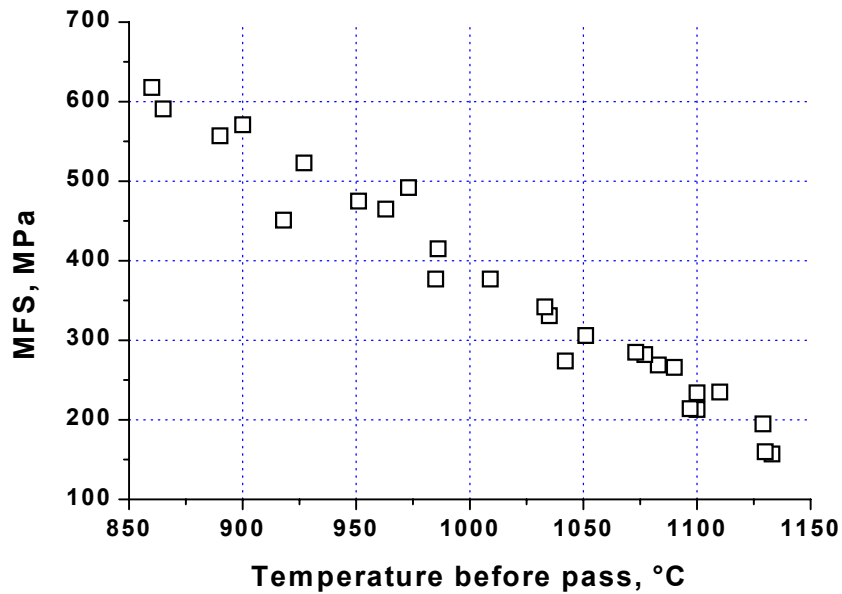
Figure II.3: MFS *vs.* T before rolling pass**.**
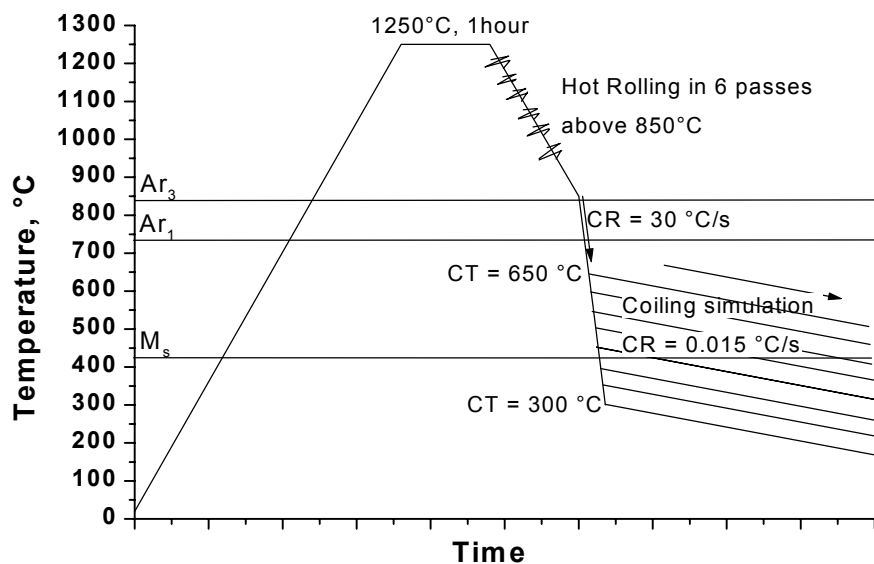
Figure II.4: Hot rolling cycles.

The non-recrystallisation temperature of austenite, T_{nr}, was calculated by means of the following equation for steels 1 to 7:[2]

$$T_{nr} = 887 + 464C + 890Ti + 363Al - 357Si + 6445Nb - 644\sqrt{Nb} + 732V - 230\sqrt{V} \qquad \text{(II.2)}$$

This parameter was to be considered in high strength steels as rolling below that temperature produced fine pancaked grains that did not further recrystallize during the cooling. In the industrial composition, T_{nr} was calculated using equation (II.2) to be 1066 °C. However, the equation (II.2) does not take into account the possible effects of the elements B, Cr, Mo on the recrystallisation of γ.

Hot torsion tests were performed in order to simulate the hot rolling and determine the actual T_{nr}. Cylindrical samples with 6 mm diameter were reheated to 1200 °C, twisted at a strain rate 1 s^{-1} with 0.3 strain each 20 °C during cooling at 1 °C/s, with an interpass time of 10 s. Figure II.5 shows the effective stress-effective strain curves obtained with the industrial composition.
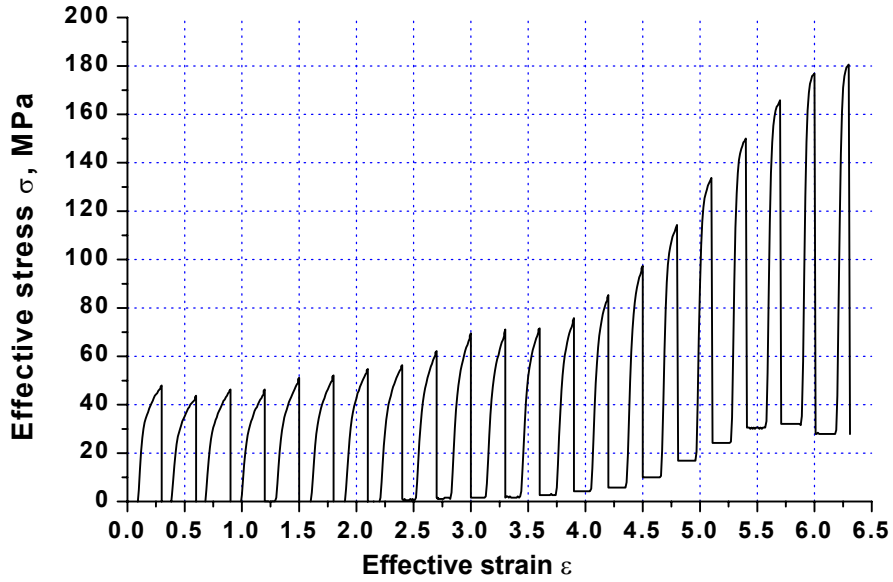
Figure II.5: Stress *vs.* strain for a torsion test of industrial composition.

The MFS is the area under each σ–ε curve divided by the total deformation. It was calculated by:

$$MFS = \frac{1}{\varepsilon_b - \varepsilon_a} \int_a^b \sigma \, d\varepsilon \qquad\qquad (II.3)$$
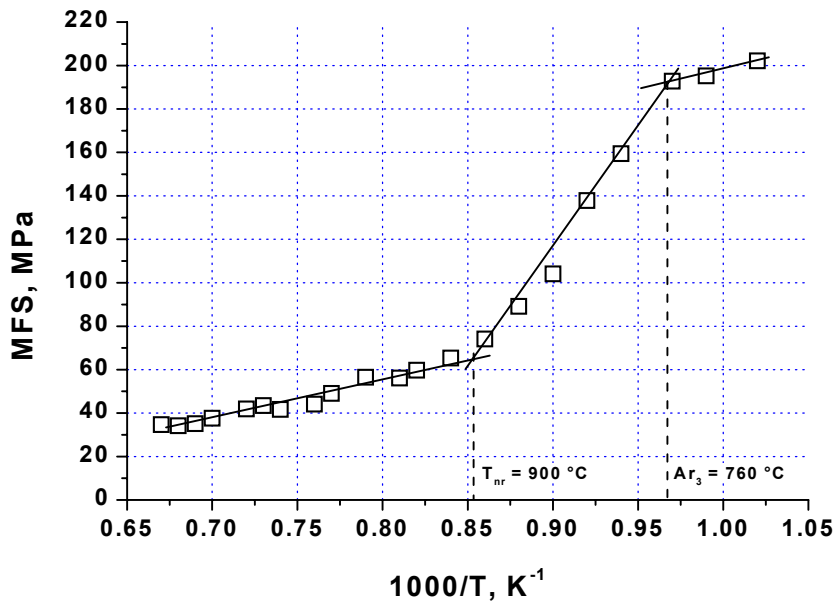
Figure II.6: MFS vs. 1000/T plot for the industrial composition.

Figure II.6 is a MFS *vs.* 1000/T plot. The two breaks in the curve indicate T_{nr} and Ar_3, respectively.

Cold rolled sheets with dimensions 125-250 mm x 750-800 mm were reheated in a high power (46 kVA) continuous annealing simulator (CASIM). Typical annealing cycles are shown in chapter I, Figure I.23.

II.4 Dilatometry

II.4.1 Study of phase transformations

The phase transformations were experimentally studied by means of dilatometry. The technique is based on the monitoring of the change in length of a sample during heating, cooling or isothermal holding. The lattice parameter for both ferrite and austenite of a given composition varies linearly with temperature in the temperature range 300-1200 °C. The ferrite lattice (bcc) contains 2 atoms in a cubic unit cell with a lattice parameter of 0.28965 nm in pure iron at 727 °C[3]; the austenite lattice (fcc) contains 4 atoms in a cubic unit cell with a lattice parameter of 0.36309 nm in pure iron at 727 °C[3]. Hence the specific volume (nm/at) is therefore higher for ferrite than for austenite. At the transformation temperature Ar_3 at which the austenitic phase transforms to ferritic phases, the steel exhibits a dilatation, due to its volume expansion. The thermal expansion coefficients, typically 1.61×10^{-5} and 2.25×10^{-5} $°C^{-1}$ for ferrite and austenite respectively, were measured for the IF steel with composition given in Table II.2.[4]

Cylindrical samples with 5 mm length and 3.5 mm diameter were used in a Tetha Dilatronic IIIS quench dilatometer, shown in Figure II.7.
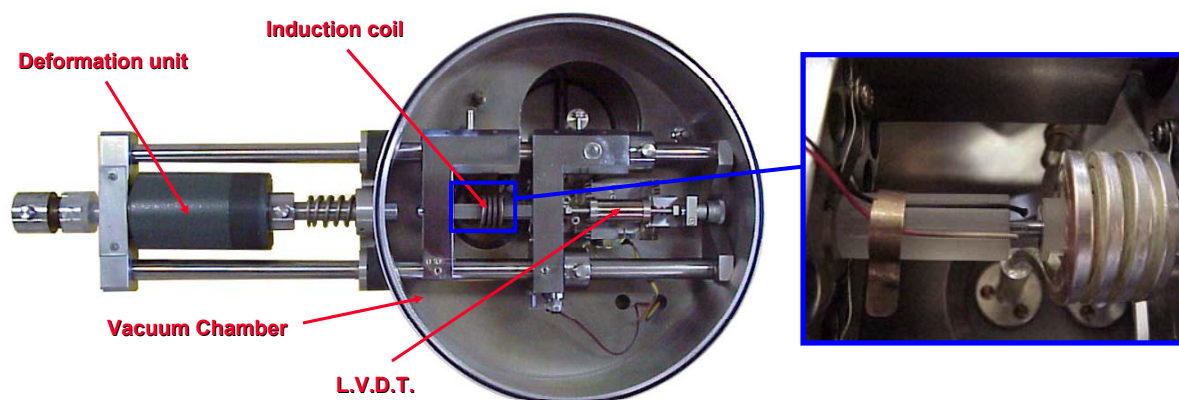
Figure II.7: Theta Dilatronic IIS quench dilatometer.

The linear variable displacement transducer (LVDT) transforms the displacement due to the length change of the sample to an electric signal, which is recorded by a computer.

Figure II.8 shows the continuous cooling cycles used in the dilatometer. Samples were reheated at the rate 600 °C/min to 1200 °C, maintained at that temperature for 2 minutes, cooled at the rate 300 °C/min to 950 °C for 1 minute and finally cooled at a constant rate. This procedure has two advantages: (1) Enough time is allowed for austenite grains to grow and thus the risk of heterogeneity of the austenite after several cycles are performed on the same sample is reduced; (2) A constant cooling rate in the austenitic range allows a comparison of its thermal expansion coefficient for all experiments, since this parameter may be affected by the cooling rate. To study isothermal transformations, samples were reheated using the same procedure, quenched from 950 °C to the transformation temperature by spraying He gas, kept at that temperature one hour, then quenched to room temperature.
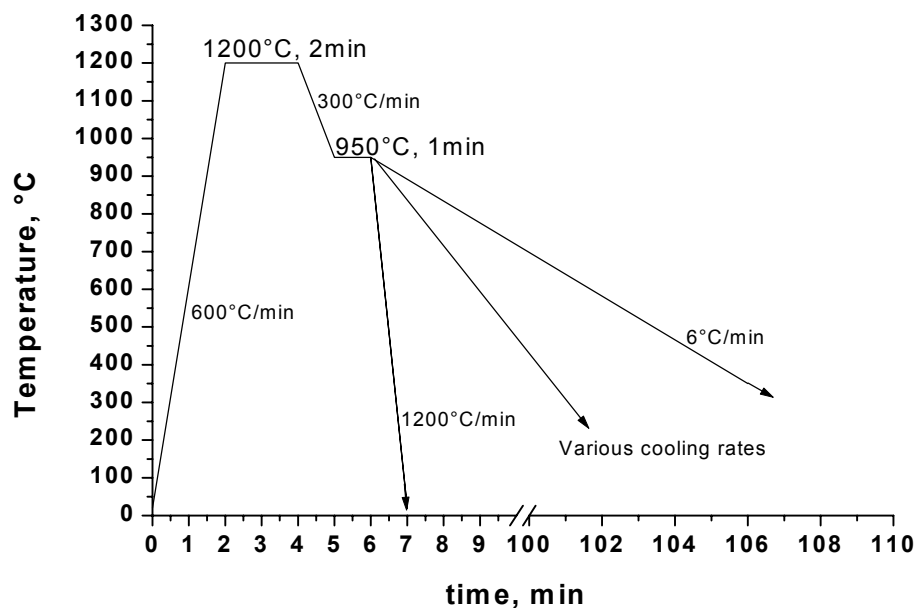
Figure II.8: Thermal cycles used during the dilatometric tests.

The graphical method or the "lever rule" is generally used to determine the transformation start and finish temperatures, as illustrated Figure II.9 for a single-phase transformation. The linear part of the thermal contraction curve is extrapolated before and after transformation. The $\gamma \rightarrow \alpha$ transformation start is defined as the temperature at which the thermal contraction first deviates from linearity.[5] In practice, that point is often subject to measurement errors due to some degree of curvature in the cooling curve since the thermal contraction before and after transformation is sometimes not linear. This deviation to linearity usually appears when carbides have formed during a pearlitic or a bainitic transformation. The thermal expansion coefficient for carbides is then a function of the temperature.[6] Changes in the cooling rate, especially at low temperatures where the cooling efficiency decreases, can also affect the dilatation curves. In order to avoid measurement errors due to these difficulties, the transformation temperatures were determined after respectively 2 % and 98 % of transformation. At any temperature, a vertical line may be drawn to intersect the dilatation *vs.* temperature curve as shown in Figure II.9.
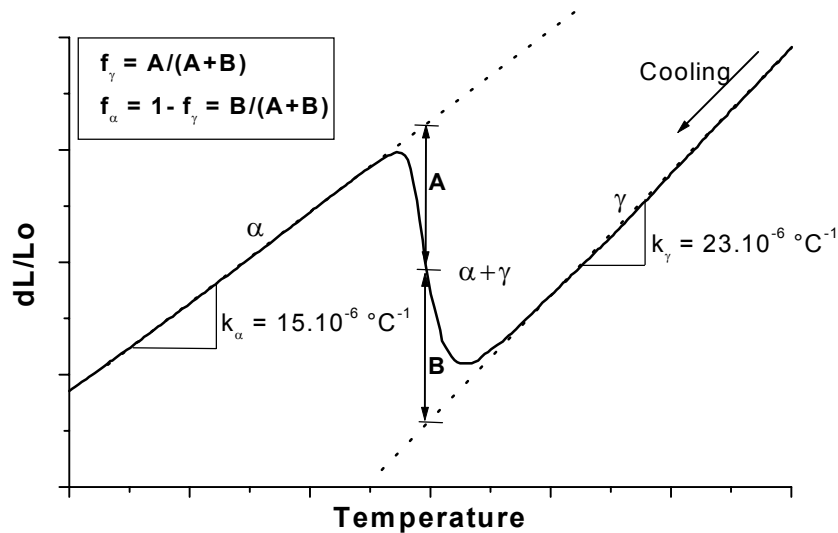
Figure II.9: Schematic dilatation-temperature curve during an austenite to ferrite phase transformation and the lever rule used to determine the volume fraction of phases. k_α and k_γ are the linear thermal expansion coefficients for α and γ, respectively.

From the lever rule, the volume fraction of austenite transformed to ferrite $(1-f_\gamma)$ at the temperature T is expressed by:

$$1 - f_\gamma(T) = f_\alpha(T) = \frac{B}{A+B} \qquad (II.4)$$

In the next chapter, an improved method to calculate the volume fraction of phases formed during either continuous cooling or isothermal transformations is introduced. Its practical application to CMn steels is made in chapters III to VI.

II.4.2 Magnetic transitions detected by Induction Power Monitoring (IPM)

Other types of transitions are related to the magnetic properties of Fe. Pure Fe is ferromagnetic below its Curie temperature T_c, of 1043 K. Above T_c Fe is paramagnetic. Using the feedback signal to the power supply of the induction heater of the dilatometer, any conventional dilatometer can be operated in the IPMT (Induction Power Monitoring Technique) mode, which is sensitive to second order transformations related to magnetic transitions in steels.

There are three types of magnetism states that are relevant for steels: paramagnetism, ferromagnetism and antiferromagnetism. Figure II.10 shows the different spin arrangements in a domain in pure Fe for paramagnetic, ferromagnetic and antiferromagnetic structures, respectively.
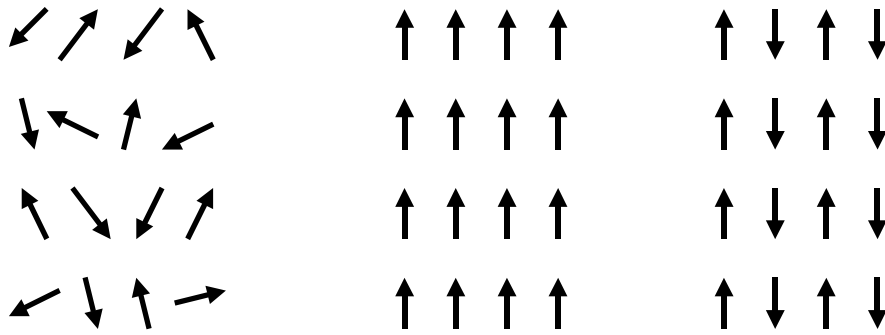
Figure II.10: Spin arrangement in a crystal or domain illustrating a) paramagnetism, b) ferromagnetism and c) antiferromagnetism.

Pure Fe at temperature above the Curie temperature T_c exhibits a magnetization that is proportional to the applied magnetic field in which the material is placed. The susceptibility χ of paramagnetic Fe obeys about a power law:

$$\frac{1}{\chi} = \frac{C}{(T - T_c)^{1.33}}$$
(II.5)

where C is Curie's constant.

In Fe, the atoms have inherent sources of magnetism because electron spin contributes a magnetic moment and electron orbits act as current loops that produce a magnetic field. In Fe at $T > T_c$ the magnetic moments of the electrons do not completely cancel each other.

Fe below T_c exhibits a long-range magnetic ordering phenomenon, which causes the unpaired electron spins to line up parallel with each other in regions called domains, within which the magnetic field is intense. The many domains are randomly oriented with respect to one another and ferromagnetism manifests itself when an external magnetic field causes the magnetic domains to line up with each other and magnetize the material. The driving magnetic field will then be increased by a large factor, which is expressed as a relative permeability for the material, μ_r. The magnetically ordered state of Fe disappears abruptly at the Curie temperature, 1043 K.

γ-Fe is antiferromagnetic below the Néel temperature, T_N, which depends on the alloy content. In this state the unpaired electron spin spontaneously align in an antiparallel fashion. Antiferromagnetic materials are paramagnetic above T_N, that is, they obey there a linear T = f(1/χ) law, with χ the magnetic susceptibility of the material. Below T_N, however, the inverse of the susceptibility may rise with decreasing temperature.

In dilatometry the heating is often achieved by means of induction. Electromagnetic induction refers to the phenomenon by which electric current is generated in a closed circuit by the fluctuation of current in another circuit placed next to it. In induction heating three basic elements are of importance: the laws of electromagnetic induction, the skin effect, and heat transfer. Figure II.11illustrates induction-heating system, consisting of an inductive heating coil and a sample that is inductively heated.
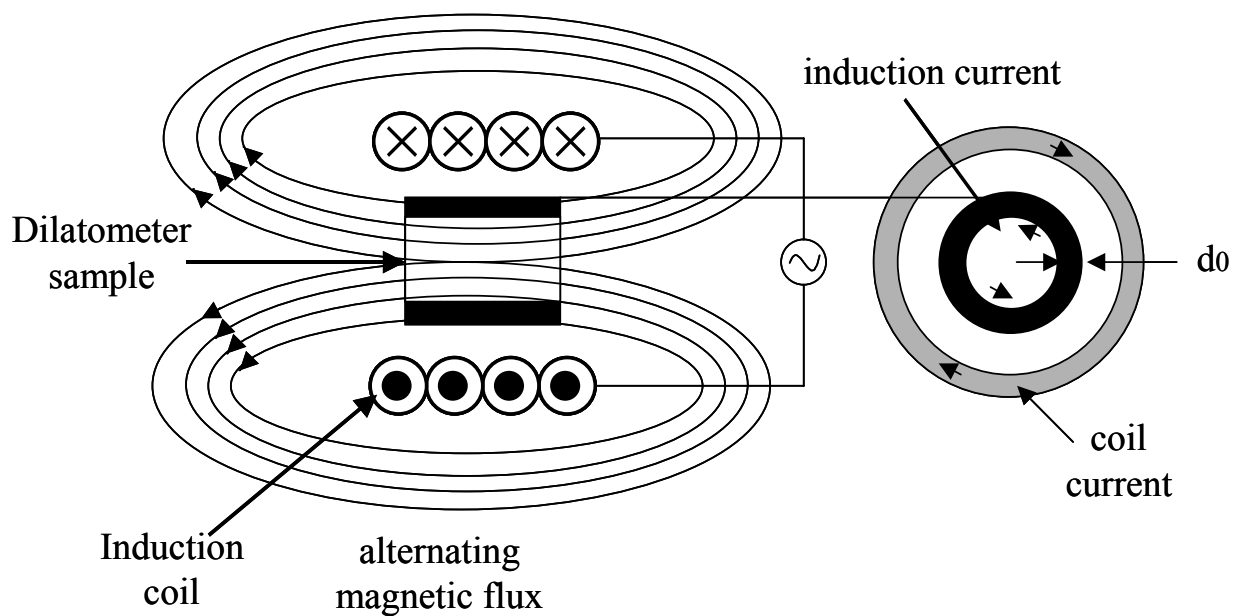
Figure II.11: basics of induction heating.

As shown in Figure II.11, when the AC current circulates in the coil, the magnetic field induced by the induction coil of the dilatometer is:

$$B = \mu_0 \mu_r ni \qquad \text{(II.6)}$$

where $\mu_0 = 4\pi.10^{-7}$ T/amp.m is the intrinsic permeability, μ_r is the relative permeability, about 200 T/amp.m in ferritic iron, and n is the number of turns divided by the core length, *i.e.* 5 mm for the dilatometer sample. The magnetic flux Φ is equal to the magnetic field multiplied by the sample section A:

$$\Phi = BA \qquad \text{(II.7)}$$

A small cylindrical steel sample put in the interior magnetic field causes a change in the velocity of the magnetic flux. According to Farraday's Law, an eddy current is generated on the surface of the conductive steel sample that has an inverse relationship with the current in the inducting circuit. The current on the surface of the object generates an eddy current E:

$$E = N \frac{d\Phi}{dt} \tag{II.8}$$

where N is the number of turns in the coil. As a result, the electric energy caused by the induced current is converted to heat energy according to:

$$P = \frac{E^2}{R} \tag{II.9}$$

The resistance R is determined by the resistivity (ρ) and permeability (μ) of the conductive object. The current i is determined by the intensity of the magnetic field. Heat energy is an inverse relationship with skin depth. The higher the frequency of the current administered to the coil, the more intensive is the induced current flowing around the surface of the load. The density of the induced current diminishes when flowing closer to the center. This is called the skin effect or Kelvin effect. From this effect, one can easily infer that the heat energy converted from electric energy is concentrated on the skin depth (surface of the object).

$$i_x = i_0 e^{-x/d_0} \tag{II.10}$$

where i_x is the current density at the distance x from the skin (surface) of the object, i_0 is the current density on skin depth ($x = 0$) and d_0 is a constant determined by the frequency (current penetration depth or skin depth) such as:

$$d_0 = \sqrt{\frac{2\rho}{\mu\omega}} \tag{II.11}$$

where ω is the frequency of the current flowing through the object. The equation (II.11) states that the skin thickness is determined by the resistivity, permeability, and frequency of the object.

The induced electro motive force (e.m.f.) is calculated by means of equation (II.8). The heat energy P is calculated by means of equation (II.9). For steels, the resistance R can be written:

$$R = \frac{\rho.l}{A} \tag{II.12}$$

where l is the sample length, A the section and ρ the resistivity. For ferritic iron, $\rho = 9.71.10^{-8}$ Ωm.

The relative magnetic permeability μ_r is about 200 T/amp.m in ferromagnetic iron, and it drops to about 1 T/amp.m in paramagnetic iron.

According to the equation (II.12), the electrical resistance of the dilatometer sample depends on the sample dimensions, its resistivity, and its magnetic permeability. As a consequence, if no phase transformation occurs, the ferromagnetic-paramagnetic transition can be followed in the α phase by plotting $R = f(T)$. In practice, R cannot be measured directly; neither can be the heat energy P. However, the signal of the device controlling the power necessary to reheat the sample can be measured. This electrical signal varies between 0 and +5 V (100 % of the power capability). It gives a very good indication on the heat energy, and is dependant on the resistivity and the magnetic permeability of the studied steel.
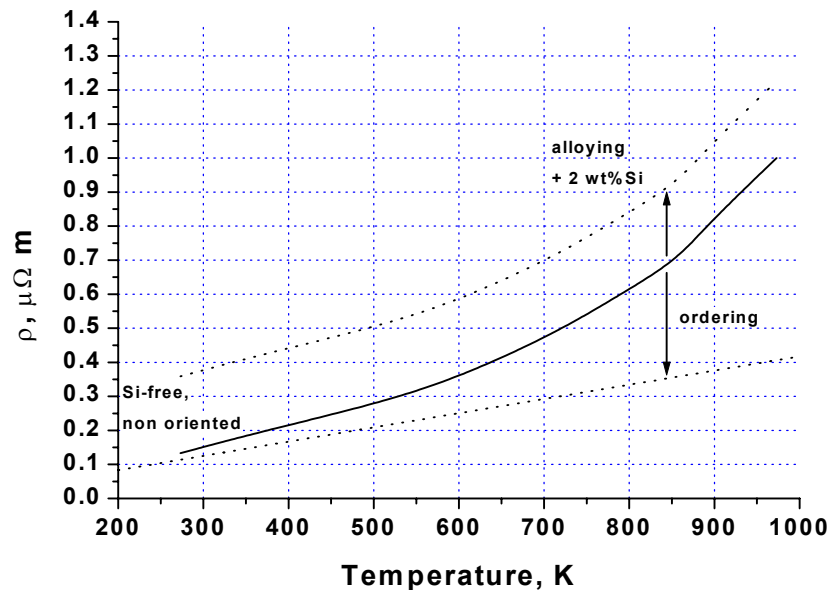
Figure II.12: Resistivity *vs.* temperature plot for steels, showing the effects of alloying and ordering.

II.5 Mechanical properties

Tensile specimens were tested with an Instron 5569 tensile testing machine. The mechanical properties were characterized by means of the yield stress (YS), the tensile strength (TS), the uniform elongation (UE) and the total elongation (TE). Two strain rates were used before and after a 3.4 % uniform elongation, $\dot{\varepsilon} = 2\,s^{-1}$ and $\dot{\varepsilon} = 20\,s^{-1}$, respectively. A_{80} traction specimens were 20 mm wide, and had an 80 mm strain gauge reference length. A_{50} traction specimens were also used. Those specimens were 12.5 mm wide and had a 50 mm strain gauge reference length. A comparison between several A_{80} and A_{50} specimen obtained from the industrial steel processed under different conditions was made. Figure II.13 shows that the yield and tensile strengths as well as the uniform and total elongations measured with both kinds of specimens are comparable.
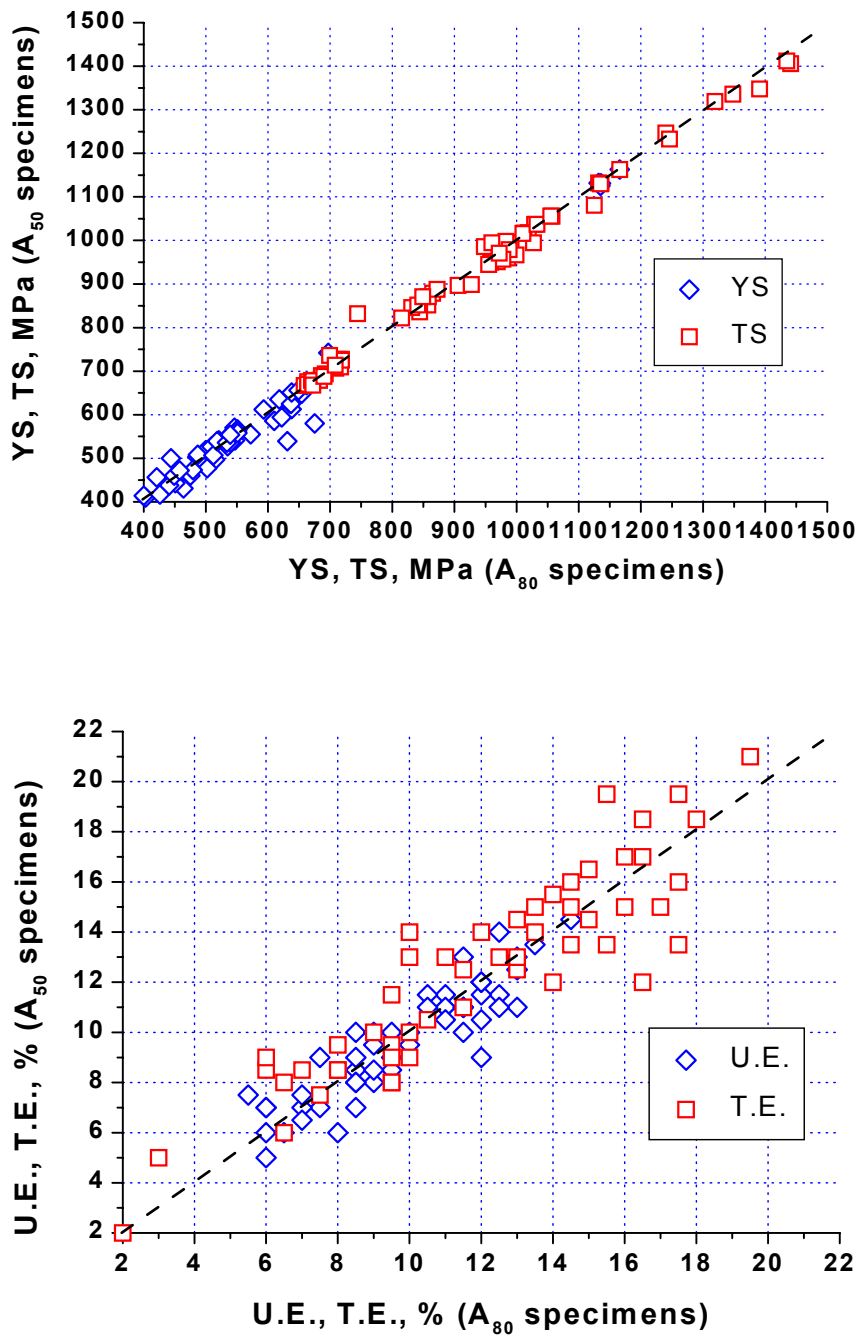
Figure II.13: Comparison between tensile results obtained with A_{80} and A_{50} specimens.

In order to evaluate the steel behaviour at high strain rates, an impact tension testing machine was developed in laboratory. Tensile specimens with 25 mm gauge length and 5 mm width were mounted on a specially adapted Charpy impact testing machine, equipped with a force measurement cell, and a type K (Ni-CrNi) thermocouple to measure the temperature increase due to impact energy. The maximum strain rate was 130 s^{-1}. Figure II.14 shows the equipment and an example of temperature measurement during the test.
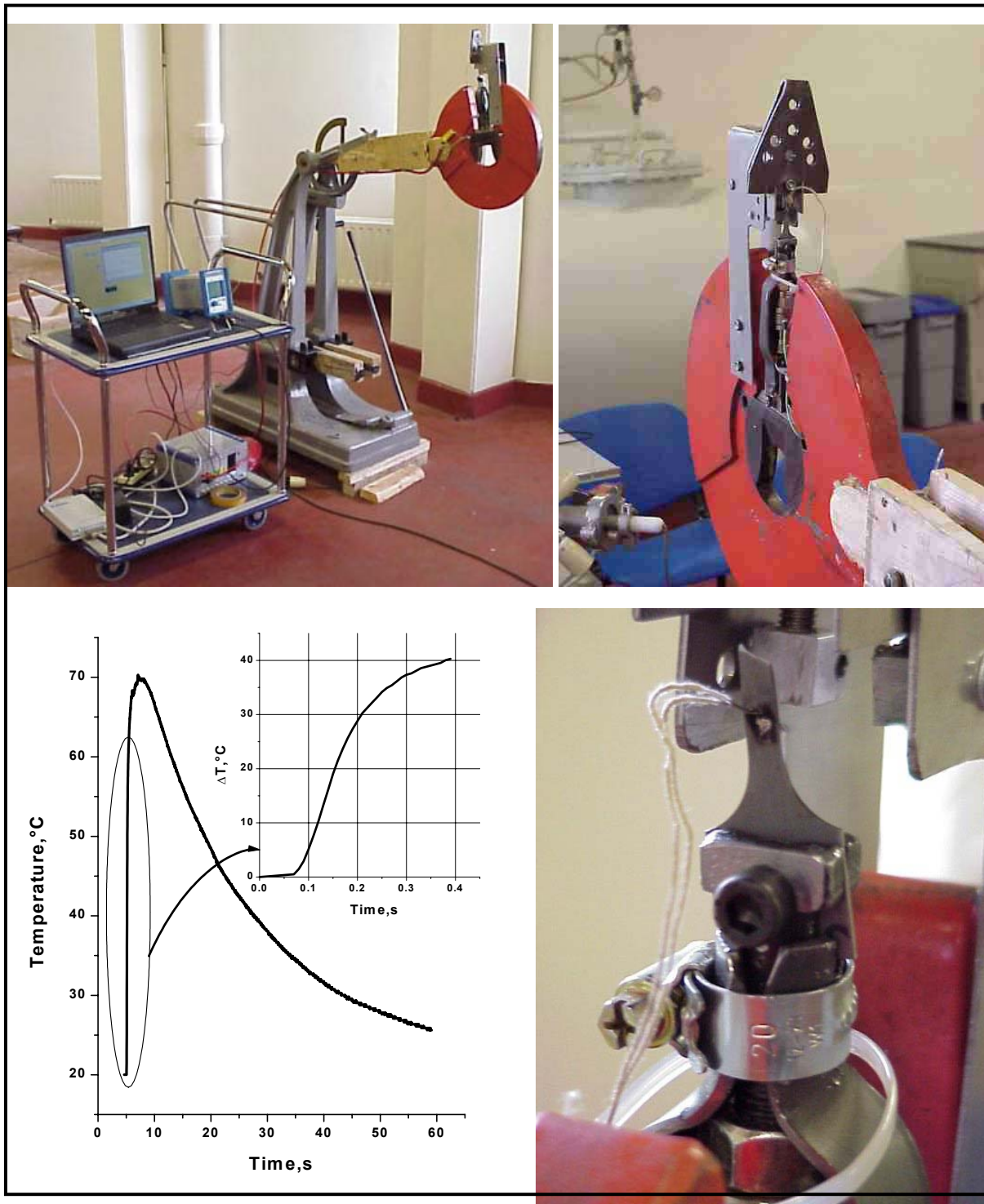
Figure II.14: Impact testing machine and example of temperature increase due to impact energy.

II.6 Microstructural investigation

The microstructure was investigated by light optical microscopy (LOM) on a ZEISS JENAVERT and scanning electron microscopy (SEM) on a ZEISS DSM 962. After mechanical polishing, the specimens used for LOM and SEM investigation were color etched using both the LePera method [7] or a 2 % nital solution. The LePera etchant is a mixture of two solutions whose compositions are given in Table II.4. The solutions are prepared separately and just before the etching is started, they are mixed in equal quantities.

Phase fractions were determined experimentally based on the LOM micrographs by means of a grid counting method and by means of a digital image analyzing software system (LUCIA Screen Measurement supplied by Laboratory Imaging Ltd.).

Table II.4: Composition of solutions for LePera etchant.

Reagent 1	Reagent 2
1 g $Na_2S_2O_5$	4 g dry picric acid
100 ml distilled H_2O	100 ml ethanol

The volume fraction of retained austenite, V_γ, was determined by X Ray Diffraction (XRD) on a Siemens D5000 Diffractometer with Mo K_α radiation using the Direct Comparison Method.[8] This method uses the integrated intensity of the $(200)_\alpha$ and $(211)_\alpha$ peaks and the $(220)_\gamma$ and $(311)_\gamma$ peaks, according to the equation:

$$V_\gamma = \frac{\dfrac{I_\gamma^{220}}{1.42I_\alpha^{200}+I_\gamma^{220}}+\dfrac{I_\gamma^{220}}{0.71I_\alpha^{211}+I_\gamma^{220}}+\dfrac{I_\gamma^{311}}{1.62I_\alpha^{200}+I_\gamma^{311}}+\dfrac{I_\gamma^{311}}{0.81I_\alpha^{211}+I_\gamma^{311}}}{4} \tag{II.13}$$

The positions of the peaks with Mo K_α radiation are given in Table II.5.

Table II.5: Calculated peak positions for Mo radiation.

Peak	α (200)	α (211)	γ (220)	γ (311)
2θ (°)	28.72	35.36	32.42	38.22

In addition, the lattice parameter of the austenite phase was used to calculate the carbon content of the retained austenite by means of:[9]

$$a_\gamma\,(nm) = (0.36309 + 0.00075C) \times (1 + (24.9 - 0.6C) \times 10^{-6}(T - 1000)) \tag{II.14}$$

II.7   TEM analysis

A JEOL 2010 Transmission Electron Microscope (TEM) with an acceleration voltage of 200 kV, equipped with an energy dispersive X-ray spectrometer (EDX) was used for the detection and analysis of precipitates after extraction replica.

Thin TEM foils were prepared to study the complex microstructure in cold rolled complex phase steels. The microstructural observations were made at the LISm using a Philips EM 420 TEM operating at 120 kV.

II.8   Texture measurements

Local texture measurements were made using the OIM-EBSD (Orientation Imaging Microscopy – Electron Back Scattering Diffraction) technique. The TSL OIM-EBSD attachment was mounted on a Philips XL30 environmental scanning electron microscope equipped with a LaB_6 filament and operating at 30 kV. The specimen tilt was 70° during OIM measurements. The samples were prepared for these measurements using mechanical polishing, electro polishing and a light etching with 2% Nital. The OIM-scans were carried out with a step-size of 0.5 μm. Further investigation of phases was done using the Image Quality (IQ) and the Confidence Index (CI) of the measurements provided by the commercial TSL OIM software. The IQ parameter describes the quality, *i.e.* the "sharpness" of an electron backscatter diffraction pattern. The factor affecting the quality of diffraction patterns is the perfection of the crystal lattice in the diffraction volume. Any distortions of the crystal lattice within the diffracting volume will produce more diffuse diffraction patterns. This enables the IQ parameter to be used to give a qualitative description of the strain distribution in a microstructure. However, the IQ parameter has some dependence on orientation. Thus, it cannot be used to distinguish small differences in strain from grain to grain. The CI parameter quantifies the reliability of the pattern indexing. For a given diffraction pattern, several possible orientations may be found when indexing the diffraction bands detected by the image analysis routines. The software ranks these orientations according to a voting scheme. The confidence index ranges from 0 to 1. In a multiphase situation, CI is calculated separately for each phase. Orientation Distribution Functions (ODFs) were calculated using a numerical software [10] and were transformed into ODFs of the product phase using orientation relationships as Kurdjumov-Sachs [11] (KS: $\{111\}_\gamma$ // $\{011\}_\alpha$ and $<011>_\gamma$ // $<111>_\alpha$), Bain [12] (B: $\{001\}_\gamma$ // $\{001\}_\alpha$ and $<001>_\gamma$ // $<110>_\alpha$) and Nishiyama-Wasserman [13, 14] (NW: $\{111\}_\gamma$ // $\{011\}_\alpha$ and $<211>_\gamma$ // $<011>_\alpha$).

References

[1]   T.M. Maccagno, J.J. Jonas, S. Yue, B.J. McCrady, R. Slobodian, D. Deeks: <u>ISIJ International</u>, Vol.34, No.11, 1994, p.917.

[2]   F. Boratto, R. Barbosa, S. Yue and J.J. Jonas: Proc. Int. Conf. Physical Metallurgy of Thermomechanical Processing of Steels and Other Metals (THERMEC '88), 1988, p.383; ed. I. Tamura, ISIJ, Tokyo.

[3]   M. Oninck, F.D. Tichelaar, C.M. Brackman, E.J. Mittemeijer, S. Van der Zwaag: <u>Z.metallkd</u>. 87, 1996, p.24.

[4]   J.Z. Zhao, C. Mesplont, B.C. De Cooman: <u>Z. Metallkd</u>. 92, 4, 2001, p.345.

[5]   G.K. Prior: <u>Materials Forum</u> 18, 1994, p. 265.

[6]   A. Jablonka, K. Harste, K. Schwerdtfeger: <u>Steel Research</u> 62, No1, 1991, p.24.

[7]   F.S. LePera: <u>Journal of Metals</u>, March 1980, p.38.

[8]   B.D. Cullity: Elements of X-Ray Diffraction, 2nd Ed., Addison-Wesley Publishing Co, Inc.,1978, p. 508.

[9]   M. Oninck, C.M. Brakman, F.D. Tichelaar, E.J. Mittemeijer, S. Van Der Zwaag, J.H. Root, N.B. Konyer: <u>Scripta Metallurgica et Materiala</u>, 29, 1993, p. 1011.

[10] P. Van Houtte: The MTM-FHM Software System Version 2, Users Manual, 1995.

[11] G. Kurdjumov, G. Sachs: Z. <u>Phys.</u>, 1930, Vol. 64, p. 225.

[12] E.C. Bain : <u>Trans. AIME</u>, 1924, Vol. 70, p. 25.

[13] Z. Nishiyama: <u>Sci. Rep. Res. Inst. Tohoku Univ.</u>, 1934-35, Vol. 23, p. 638.

[14] G. Wassermann: <u>Arch. Eisenhüttenwes.</u>, 1933, Vol. 16, p. 647.

CHAPTER III

Improved method to study multistep phase transformations kinetics from dilatometric data

III.1 Introduction

Steels exhibit a significant volume variation during a heating or cooling or an isothermal holding due to thermal expansion and phase transformation. This phenomenon can in principle be used to investigate phase transformation kinetics if the relation between the fraction of phases, the composition of phases, the temperature and the dilatation is known. Efforts have been made to analyze the dilatation during an isothermal transformation[1,2] or to calculate the dilatation during the heating of plain carbon steels using the thermodynamic function.[3] The existing models are, however, not applicable to the calculation of the phase transformation kinetics indicated by a dilatation curve.[4] In the literature, the relation between the amount of the product phase at a certain stage of a transformation and the associated volume change is often assumed to be linear and the volume fraction of the parent phase is determined from a curve of relative length change as a function of temperature by using the lever rule demonstrated in chapter II for the γ→α transformation in low C-steels.

The lever rule is, however, only applicable in the case of a process which involves only one phase transformation. In addition, it does not give any information about the composition of phases. This has set a limitation for the application of the dilatometric technique for the investigation of the phase transformation kinetics. A model was, therefore, developed based on thermal expansion coefficient to calculate the phase transformation kinetics from a dilatation curve. The model was first validated by comparing its results with the experimental results for a interstitial-free steel which involved only one phase transformation during a cooling from the austenite phase region. The model was then applied to investigate the bainite phase transformation process using the dilatation curves obtained from a bainitic grade steel.

III.2 Physical and mathematical analyses

Considering that it is relatively easy to determine the thermal expansion coefficient of a phase, the model is based on this parameter. The density ρ of a phase can be related to its thermal expansion coefficient by:

$$k_i^T(T,C) = -\frac{1}{3} \cdot \frac{1}{\rho_i(T,C)} \cdot \frac{d\rho_i(T,C)}{dT} \tag{III.1}$$

where k_i^T is the linear thermal expansion coefficient of a phase i, T is the temperature and C is the carbon concentration of phases.

Many experiments with pure iron were carried out to investigate the effect of temperature on the lattice parameter of ferrite and austenite.[5-13] The results demonstrate that the lattice parameter of austenite increases linearly with temperature up to 1200 °C, although small differences exist between the thermal expansion coefficients given by different authors.[6] The results also indicate that above 300 °C the lattice parameter of ferrite increases approximately linearly with temperature, as can be seen in Table III.1.

Table III.1: Thermal expansion coefficient of α-iron.

T (°C)	300	400	500	600	700	800	Ref.
$k_\alpha^T \times 10^{-6}\ {}^o C^{-1}$	14.87	14.85	14.83	14.81	14.78	14.76	Straumanis[7]
$k_\alpha^T \times 10^{-6}\ {}^o C^{-1}$	15.50	16.20	16.25	15.80	15.80	15.40	Sounders[8]
$k_\alpha^T \times 10^{-6}\ {}^o C^{-1}$			17.55 (527-927 °C)				Onink[6]

Generally, the addition of alloying elements does not affect the linear temperature dependence of the lattice parameter.[6,9] It is a common observation that a low carbon steel contracts with temperature approximately linearly during cooling in a temperature range above 300 °C if no phase transformations occur. If the lattice parameter for both ferrite and austenite of a given composition varies linearly with temperature in the temperature range 300 - 1200 °C, the density of the two phases may be obtained by integrating the equation (III.1):

$$\rho_i(T,C) = \rho_i(T_a,C)e^{-3k_i^T(T-T_a)} \tag{III.2}$$

where T_a is an arbitrarily selected temperature higher than 300 °C. In the case of steels, the subscript i refers to the possible phases: austenite, ferrite, carbide and martensite. The ferrite includes the primary ferrite, the ferrite formed during the pearlite decomposition and the bainitic ferrite.

Previous work on the effect of carbon content on the lattice parameter of austenite[14,15] and ferrite[16] showed that the density of austenite and ferrite varied linearly with carbon content for a constant temperature. The linear relation was given as:[17]

$$\rho_i(T_a,C) = \rho_i(T_a,C=0)g_i(C) \tag{III.3}$$

where $g_\gamma(C) = 1 - 0.0146$ wt.% C for austenite and $g_\alpha(C) = 1 - 0.0262$ wt.% C for ferrite.

One can find by substituting the equations (III.2) and (III.3) into the equation (III.1) that the carbon content of a phase does not affect the thermal expansion of the phase. This means that the equilibrium ferrite and the bainitic ferrite should have a same thermal expansion

coefficient. This has also been observed for experiments with a bainitic grade steel, as shown in Figure III.1 where, in the temperature range below 440 °C, the dilatation-temperature curve for the continuously cooled sample which consists mainly of equilibrium ferrite has the same slope as that for the isothermally transformed sample which consists mainly of bainitic ferrite.
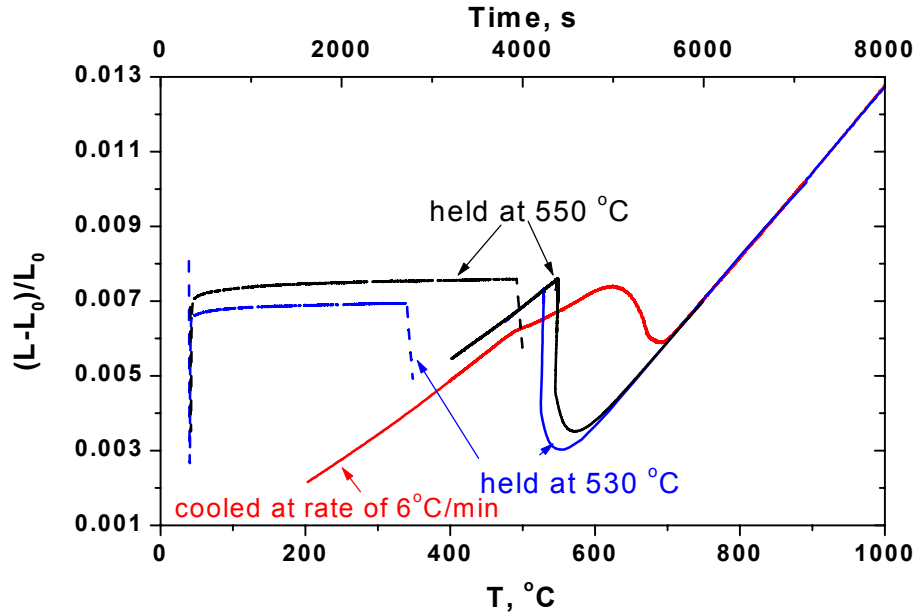
Figure III.1: Relative length change of the samples as a function of temperature for the sample cooled at a rate of 6 °C/min and samples isothermally transformed at 550 and 530 °C. Note that the slopes below 440 °C are parallel.

Figure III.2 shows the thermal expansion coefficients calculated from the dilatation curves.

The dilatation can be divided into three parts: the dilatation of phases due to the change in temperature, ΔL_i^T, the dilatation due to the changes of the composition of phases, ΔL_i^C, and the dilatation due to the phase transformation $\Delta L_{\gamma \to i(+j)}$. The thermal dilatation in a time interval is given by:

$$\Delta L_i^T = f_i(t)k_i^T(t)L_0\Delta T \tag{III.4}$$

where $f_i(t)$ is the volume fraction of phase i at time t, L_0 is the length of the sample at the reference temperature, and ΔT is the temperature change during the time interval Δt.

Considering the fact that generally the diffusion coefficient for substitutional alloying elements is small compared to that for carbon, their redistribution between phases during a bainitic phase transformation is negligible. Further, considering the kinetic characteristics of each kind of transformations, it is generally assumed that the austenite and the primary ferrite experience only changes in their carbon contents during the bainitic transformation (*i.e.* para-equilibrium conditions). The dilatation due to the change in the carbon content of a phase can be calculated by:

$$\Delta L_i^C = f_i(t)k_i^C L_0 \Delta C_i \qquad\qquad\qquad\qquad (III.5)$$

$$k_i^C = -\frac{1}{3}\frac{1}{\rho_i}\frac{d\,\rho_i}{d\,c^C} = -\frac{1}{3}\frac{1}{g_i(C)}\frac{dg_i\,(C)}{dc^C} \qquad\qquad\qquad\qquad\text{(III.6)}$$

where k_i^C is the solute expansion coefficient, ΔC_i is the change of the carbon content of phase i in a time interval Δt.

The dilatation due to the phase transformation in a time interval Δt can be calculated by:

$$\Delta L_{\gamma \to i(+j)}(t) = k_{\gamma \to i(+j)}^{Trans}(t)\Big[f_\gamma(t) - f_\gamma(t+\Delta t)\Big]L_0 \qquad\qquad\text{(III.7)}$$

where $k_{\gamma \to i(+j)}^{Trans}(t)$ is the expansion coefficient of the phase transformation $\gamma \to i(+j)$.
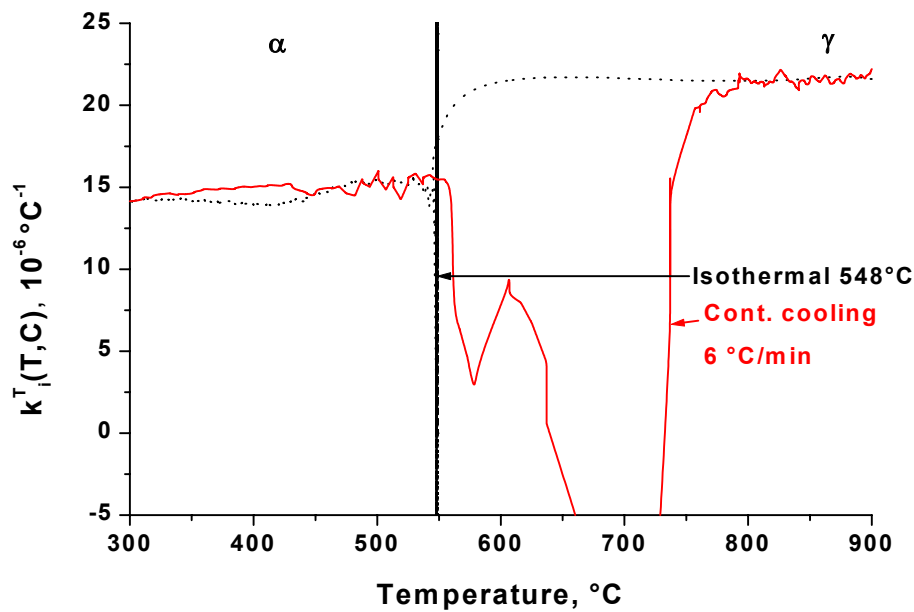
Figure III.2: Thermal expansion coefficient calculated using the derivative of the dilatation from dilatation curve for a continuous cooling (solid line) and a isothermal transformation (dotted line).

The phase transformations during a cooling of a hypo-eutectoid austenite can be divided into three groups: (1) The nucleation and growth type transformations which include the formation of primary ferrite and the formation of bainitic ferrite during the first period of a upper bainitic transformation; (2) The pearlite type transformations which include the pearlite decomposition and the last period of upper bainitic phase transformation when the carbon content of the residual austenite reaches the B_s line, B_s being the temperature for the start of the bainitic transformation, which is a function of the carbon content in austenite and, when the carbon-enriched residual austenite transforms into a mixture of bainitic ferrite and cementite (the expansion may be calculated just as if the austenite decomposed into a mixture of ferrite and cementite, although in reality the cementite precipitates from the austenite); (3) The martensitic transformation which does not involve any redistribution of alloying elements, including carbon. The martensitic transformation is not discussed in this doctoral dissertation because it takes place very often below 300 °C, where the ferrite does not expand

linearly with temperature. The lower bainitic transformation is not mentioned because more experimental data are needed to estimate accurately the carbon content in the bainitic ferrite.

For a nucleation and growth type transformation, it is proposed that the transformation is completed in two stages: First a small region of austenite adjusts its carbon content to $C_{x\alpha}$, which equals the equilibrium carbon content of ferrite, $C_{E\alpha}$, for the precipitation of primary ferrite and/or the carbon content of bainitic ferrite, $C_{B\alpha}$, for the precipitation of bainitic ferrite, through the rejection of the excess carbon, $C_\gamma - C_{x\alpha}$; this region then transforms to primary ferrite or bainitic ferrite. Therefore, $k_{\gamma \to x\alpha}^{Trans}$ and ΔC_γ are given by:

$$k_{\gamma \to x\alpha}^{Trans} = k_{\gamma \to x\alpha}^{Trans'} + k_\gamma^C (C_{x\alpha} - C_\gamma) \tag{III.8}$$

$$k_{\gamma \to \alpha}^{Trans'} = \sqrt[3]{\frac{\rho_\gamma (T_a, C = 0)}{\rho_{x\alpha} (T_a, C = 0)}} \sqrt[3]{\frac{e^{3k_\gamma^T (T_a - T)} g_\gamma (C_{x\alpha})}{e^{3k_\alpha^T (T_a - T)} g_\alpha (C_{x\alpha})}} - 1 \tag{III.9}$$

$$\Delta C_\gamma = \frac{(C_\gamma - C_{x\alpha}) \left[f_\gamma (t) - f_\gamma (t + \Delta t) \right] - \Delta C_{E\alpha} f_{P\alpha} \rho_{E\alpha} / \rho_\gamma}{f_\gamma (t + \Delta t)} \tag{III.10}$$

where the subscript P_α indicates the primary ferrite, the subscript E_α the equilibrium ferrite which includes the primary ferrite and/or the ferrite formed during a pearlite decomposition, the subscript B_α the bainitic ferrite.

The two-step transformation model can be applied to a phase transformation of the pearlite type, too. In this case it is assumed that the carbon content of the residual austenite always follows the phase diagram for the austenite decomposition to pearlite and/or the B_s line for the late stage of the bainitic transformation. That is, a small region of austenite adjusts first its carbon content to C^{Mix} to allow the residual austenite to vary its concentration according to the phase diagram. This region then decomposes into ferrite and cementite at a mass ratio of a_1 which depends on the composition of the small region and the temperature. a_1 can be determined by using the phase diagram based on carbon conservation relation. The density of the mixture of the ferrite and cementite is given by:[17]

$$\rho_{Mix} = \frac{\rho_{x\alpha} \rho_{Fe_3C}}{a_1 \rho_{Fe_3c} + (1 - a_1) \rho_{x\alpha}} \tag{III.11}$$

where the subscript x is E for the austenite decomposition to pearlite and B for the bainitic transformation and ρ_{Fe_3C} is the density of cementite.

The dilatation coefficient of the phase transformation can be calculated by using the following equation:

$$k_{\gamma \to Mix}^{Trans} = k_{\gamma \to Mix}^{Trans'} + k_\gamma^C (C^{Mix} - C_\gamma) \tag{III.12}$$

$$k_{\gamma \to Mix}^{Trans'} = \sqrt[3]{\frac{\rho_\gamma(T_a, C=0)}{\rho_{x\alpha}(T_a, C=0)}} \sqrt[3]{\frac{a_1 \rho_{Fe_3C} + (1-a_1)\rho_{x\alpha}}{\rho_{Fe_3C}}} \sqrt[3]{\frac{e^{3k_\gamma^T(T_a-T)} g_\gamma(C^{Mix})}{e^{3k_\alpha^T(T_a-T)} g_\alpha(C_{x\alpha})}} - 1 \qquad (III.13)$$

where C^{Mix} is the carbon content of the mixture of ferrite and cementite.

Taking into account the change of the carbon content of the primary ferrite and austenite during the transformation, C^{Mix} is given by:

$$C^{Mix} = C_r + \frac{\Delta C_\gamma f_\gamma(t+\Delta t) + \Delta C_{E\alpha} f_{P\alpha} \rho_{E\alpha} / \rho_\gamma}{f_\gamma(t+\Delta t) - f_\gamma(t)} \qquad (III.14)$$

where C_r is the carbon content in residual austenite.

It should be mentioned that the enrichment of the residual austenite with carbon starts at the transformation interface. This may lead to a carbon concentration profile across the austenite grain. However, as a two-stage transformation assumption is made for the detail of the phase transformation, this does not affect the calculated value of the expansion coefficient of phase transformation. As $g_\gamma(C)$ is close to unity, the inhomogeneity in carbon distribution in the grains has only a negligible effect on k_i^C. Therefore, instead of calculating the carbon concentration profile across the grain, the average concentration of carbon in austenite is used.

Taking all three terms of dilatation into account, the total relative length change in a time interval Δt is:

$$\Delta\varepsilon = \sum_i f_i(t) k_i^T dT + k_{\gamma \to i(+j)}^{Trans} \left[f_\gamma(t) - f_\gamma(t+\Delta t) \right] + k_\gamma^C f_\gamma(t+\Delta t) \Delta C_\gamma + k_\alpha^C f_\alpha(t) \Delta C_\alpha \qquad (III.15)$$

where $\Delta\varepsilon = (L - L_0)/L_0$ is the relative length change measured experimentally by dilatometry.

Note that the theoretical derivation is only correct for very small volume fraction of carbides and in the absence of difference in the elastic modulus between the phases present during the transformation. These conditions are met in the present case.

This relation holds no matter whether the phase transformation takes place during an isothermal hold or during a continuous cooling. It also holds for both equilibrium and non-equilibrium transformations.

III.3 Experimental verification of the model

Experiments were first carried out using an interstitial-free steel. The chemical composition of the steel is given in Table III.2.

Table III.2: Chemical composition of the interstitial-free steel and the bainitic grade steel (ppm).

Grade	C	Si	Mn	P	S	N	Al	Ti	Nb	B	Cr	Ni
9.IF	34	70	9700	730	38	27	430	100	250	10		
2.BG	1550	240	17500	128	15	20	410	821	1060		230	230

The steel was heated to 1200 °C, held at this temperature for 2 min and then cooled at the rate of 12 °C /min. Figure III.3 shows the dilatation as a function of temperature during the cooling. It demonstrates clearly a dilatation in three stages. The first stage corresponds to the period of cooling in the austenite phase field without a phase transformation taking place. It shows a perfect linear dilatation with temperature. In the second stage the austenite transforms to ferrite. The specific shape of the dilatation curve results from the thermal contraction of phases and the volume expansion due to the $\gamma \rightarrow \alpha$ phase transformation. The third stage begins when the phase transformation is finished. The composition of the steel and the cooling rate determine that this cooling process involves with only one phase transformation, as demonstrated in Figure III.3. The whole austenite transforms to ferrite during the cooling. In addition, the analysis of the dilatation curve indicates that the phase transformation begins at 878 °C where the solubility of carbon in ferrite is close to the carbon content of the steel. This means that the carbon redistribution during the formation of ferrite is negligible. The volume fraction of phases can, therefore, be accurately predicted with the lever rule shown schematically in chapter II, Figure II.9. The calculated results using both the lever rule and the proposed analysis model are shown in Figure III.3.
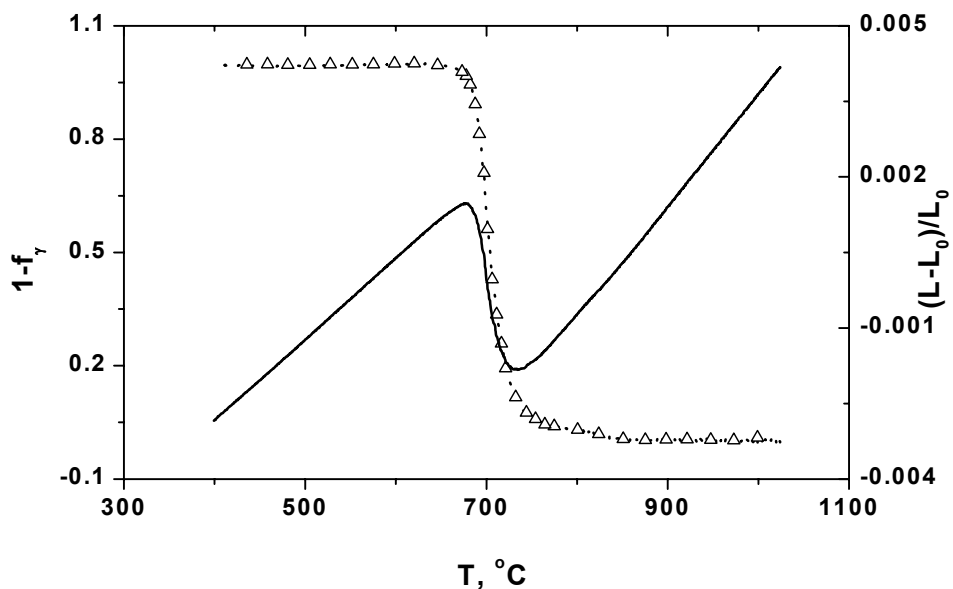

Figure III.3: The dilatation (solid line) and the volume fraction of the transformed austenite calculated from the dilatation with the model developed (doted line) and with the lever rule (triangles) as a function of temperature during the cooling of the interstitial free steel.

The thermal expansion coefficients were taken from the dilatation curve to be 1.61×10^{-5} and 2.25×10^{-5} °C^{-1} for the ferrite and the austenite, respectively. The temperature T_a was taken as 727 °C. At this temperature the lattice parameters of ferrite and austenite for pure iron are 0.28965 and 0.36309 nm, respectively.[6] The minor effect of the main alloying element Mn on the lattice parameter was taken into account by using the equation (III.16a) for the austenite[18] and the equation (III.16b) for the ferrite.[19]

$$a_\gamma (\text{Å}) = 3.6309(1 + 2.7 \times 10^{-4} \, at\%Mn) \tag{III.16a}$$

$$a_\alpha (\text{Å}) = 2.8965 + 0.00067 at\%Mn \tag{III.16b}$$

The densities $\rho_\gamma(T_a, C = 0)$ and $\rho_{E\alpha}(T_a, C = 0)$ calculated from the lattice parameters are 7735 and 7625 kg/m^3, respectively. The volume fraction of the transformed austenite calculated with the present model is also shown in Figure III.3. It can be seen that the results have a perfect coincidence with the results of the lever rule analysis.

The above calculations demonstrate that the thermal expansion coefficient k_i^T and the density $\rho_i(T_a, C = 0)$ for the phases present in the microstructure are the kinetic parameters needed for the calculation. It should be mentioned that $\rho_i(T_a, C = 0)$ should essentially be the true density of the phases. Its calculation is difficult especially because generally there are defects, *i.e.* dislocations, in steels. In fact, the density functions constructed are used only for the calculation of the dilatation due to the phase transformations. The equations (III.9) and (III.13) indicate that this dilatation depends mainly on the ratio $\rho_\gamma(T_a, C = 0) / \rho_{x\alpha}(T_a, C = 0)$. It may, therefore, be practical to substitute the austenite density calculated from its lattice parameter for $\rho_\gamma(T_a, C = 0)$ and take the density $\rho_{x\alpha}(T_a, C = 0)$ as the value that allows the best match between the model and the experiments. Also, although the thermal expansion coefficient of austenite can be determined from the dilatation versus temperature curve in the austenite phase field, the calculation of the thermal expansion coefficient of ferrite may not be straightforward due to the fact that a steel is generally a mixture of several phases at a temperature around 300 °C. But if only there is on the dilatation curve a temperature range above 300 °C where there is no phase transformation and where the ferrite is one of the main components of the microstructure, the thermal expansion coefficient of ferrite can be determined by calculating the phase transformation kinetics with this as a restriction. Therefore, to investigate the phase transformation kinetics of a steel of a given composition by using the dilatometric technique with the help of this model, one or two specially designed experiments have to been carried out first to determined the kinetic parameters needed by fitting the calculation results with the experimental ones. The whole procedure is demonstrated in paragraph III.4.
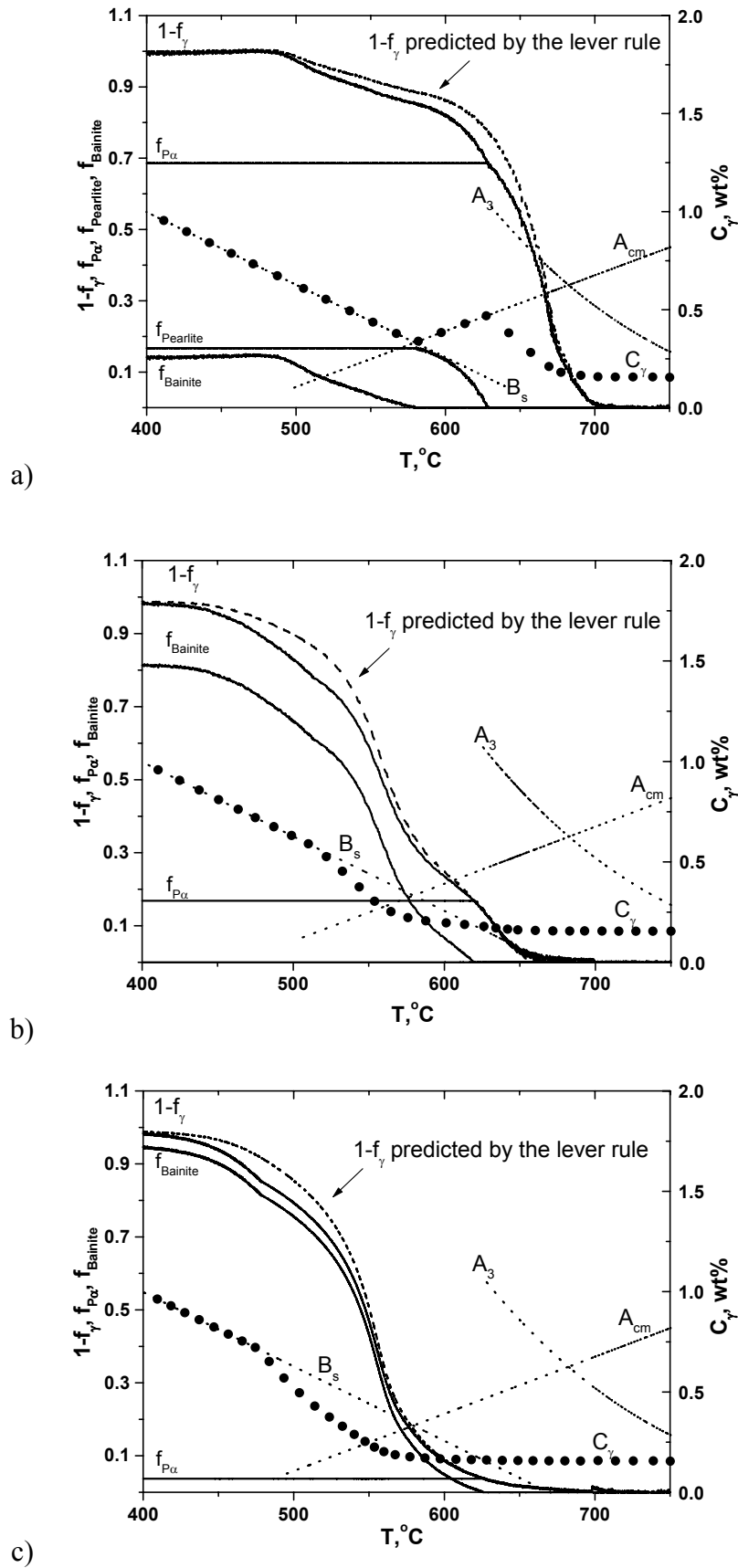
Figure III.4: Volume fraction of phases and C concentration of the residual austenite as a function of temperature for the sample cooled at the rate of a) 6 $^\circ$C/min, b) 100 $^\circ$C/min and c) 300 $^\circ$C/min.

III.4 Practical application of the model to the bainitic transformation

Experiments were done with the experimental bainitic grade steel with the chemical composition given in Table III.2. The equilibrium phase diagram of this steel was calculated using the Thermo-Calc^{TM} software. Part of the phase diagram (A_{cm} and A_3) is shown in Figure III.4.

The bainitic transformation start temperature, B_s, was estimated with the equation (III.17):[20]

$$B_s(°C) = 830 - 270C - 90Mn - 37Ni - 70Cr - 83Mo \tag{III.17}$$

The steel was heated to 1200 °C, held at this temperature for 2 min and then either cooled down at a rate of 6, 100 or 300 °C/min. The relative length change of the samples is shown in Figure III.5 as a function of temperature. The microstructure examination indicated that the sample continuously cooled at 6 °C/min consisted of primary ferrite, pearlite and bainite. It was free of residual austenite.
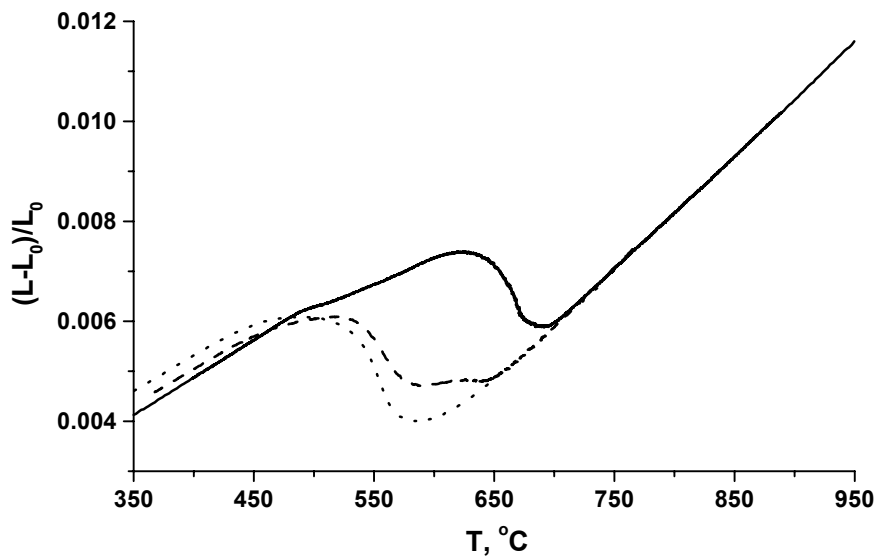
Figure III.5: Relative length change of the samples as a function of temperature for the sample cooled at a rate of 6 °C/min (solid line), 100 °C/min (dashed line) and 300 °C/min (dotted line).

According to the dilatation *versus* temperature curve in the austenite phase field the thermal expansion coefficient for the austenite is 2.25×10^{-5} °C^{-1}. The temperature T_a was taken as 727 °C. The lattice parameter of the austenite at T_a was calculated using:[18]

$$a_\gamma(\text{Å}) = 3.6309(1 + 2.7 \times 10^{-4} at\%Mn + 7.8 \times 10^{-4} at\%Al + 2.21 \times 10^{-3} at\%Nb + 1.7 \times 10^{-4} at\%Cr$$
$$- 5.6 \times 10^{-5} at\%Ni + 8.9 \times 10^{-4} at\%Ti) \tag{III.18}$$

The density $\rho_\gamma(T_a, C = 0)$, as calculated from the lattice parameters, was taken to be 7725 kg/m^3. The density of cementite was calculated using:[17]

$$\rho_{Fe_3C}(T \; in \; {}^\circ\text{C}) = 7686.45 - 6.63 \times 10^{-2} T - 3.12 \times 10^{-4} T^2 \tag{III.19}$$

The experimental data of the sample cooled continuously at 6 and 300 °C/min were used to determine the kinetic parameters needed for the calculation. Considering that the bainite was formed at a relatively high temperature, it was assumed that the carbon content of the bainitic ferrite follows the A_3 line, as the primary ferrite does. The calculations yielded the thermal expansion coefficient of the ferrite, the density $\rho_{E\alpha}(T_a, C = 0)$ and $\rho_{B\alpha}(T_a, C = 0)$. They are 1.50x10^{-5} °C^{-1}, 7640 and 7632 kg/m^3, respectively.

Figure III.4 shows the calculated volume fraction of phases and the carbon content of the austenite as a function of temperature using the model. Figure III.4a clearly demonstrates that the precipitation of primary ferrite beginning at 705 °C was companied by the enrichment of carbon in the residual austenite. The calculated volume fraction of the primary ferrite, f_P, is 68 vol.%, which is very close to the measured volume fraction of 67 ± 2 vol.%. Austenite decomposition to pearlite took place at 628 °C when the carbon content of the residual austenite reached the A_{cm} line and the bainitic transformation started at 558 °C when the carbon content of the residual austenite reached the B_s line. The volume fraction of the transformed austenite calculated using the lever rule is also shown in Figure III.4a. The large difference between the results of the model and the lever rule indicates that the lever rule is not applicable to the interpretation of a dilatation curve that involves more than one phase transformation. For the sample continuously cooled at 300 °C/min, Figure III.4c shows that less than 4 vol.% primary ferrite precipitated before the carbon content of the residual austenite reached the value limited by the B_s line at 626 °C. At that point the bainitic transformation started. The volume fraction of bainite found in the microstructure was 95 vol.%.

Using the thermal expansion coefficients and the densities of phases determined above, the transformation kinetics indicated by the dilatation curve of the sample continuously cooled at 100 °C/min could then be calculated. The volume fraction of phases and the carbon content of the residual austenite are shown in Figure III.4b. The primary ferrite started to precipitate at 662 °C. Compared with the sample continuously cooled at 6 °C/min, the temperature for the start of the primary ferrite formation was lowered by the fast cooling. 17 vol.% primary ferrite formed before the carbon content of the residual austenite reached the value limited by the B_s line at 619 °C. At that point the bainitic transformation started. The volume fraction of bainite in the microstructure was 82 vol.%. The results are in agreement with the metallographic observations, shown in Figure III.6.

Primary Ferrite

Bainite

Pearlite

100 µm

Primary Ferrite

Bainite

20 µm
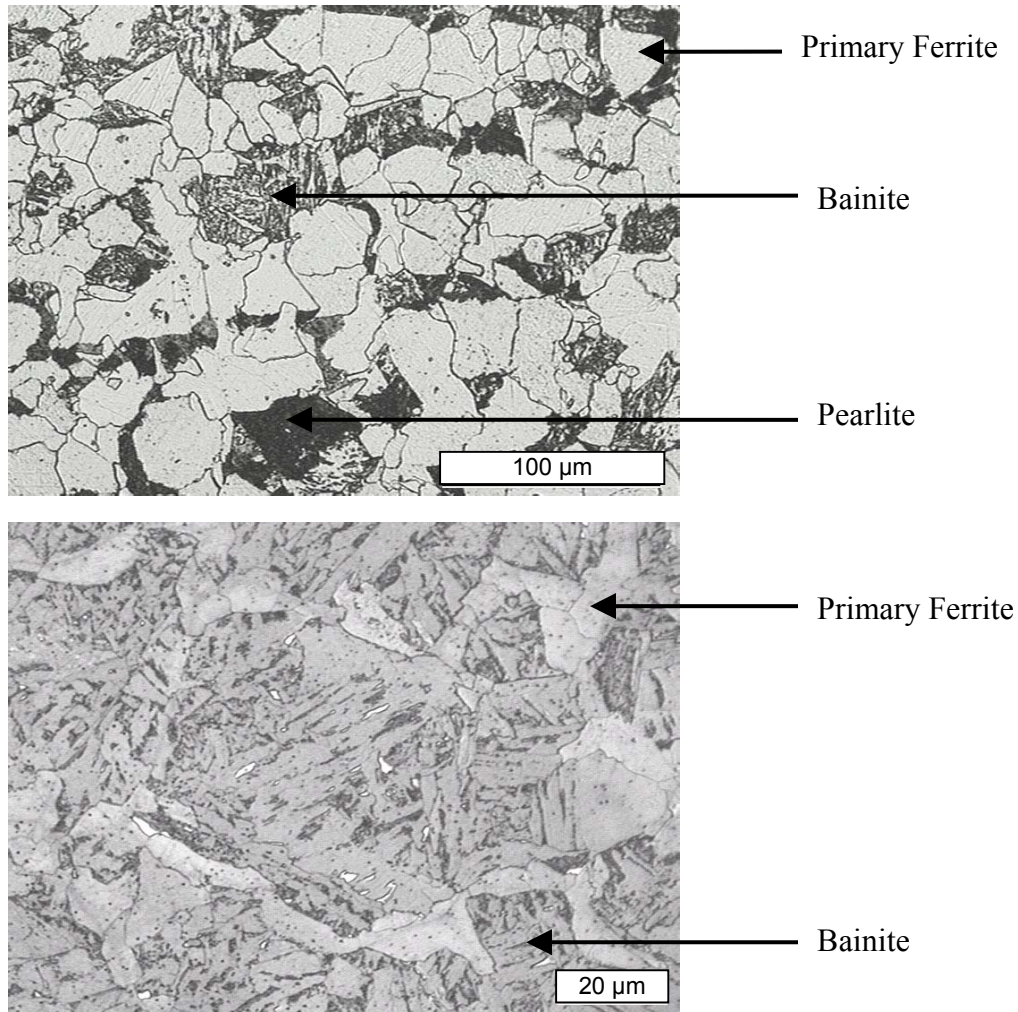
Figure III.6: Optical micrograph showing the microstructure for the samples cooled at a rate of 6 °C/min (upper) and 100 °C/min (lower). The specimens were etched with the LePera etchant.[21]

III.5 Conclusions

The dilatation of a steel during a phase transformation has been analyzed by using the density function of the phases. The model that has been developed to calculate the transformation kinetics from a dilatation curve of a hypo-eutectoid steel may be used for a multistep transformation process. After validation of the model by comparing its results with experiments obtained for an interstitial free steel which involves with only one phase transformation during a cooling through the austenite phase region, the model was applied to the calculation of the transformation kinetics indicated by the dilatation curves of a bainitic grade steel. Excellent agreement between the model and the experiments was found.

References

[1] M. Takahashi, H.K.D.H. Bhadeshia: <u>J. Mat. Sci. Letters</u>, 8, 1989, p.477.

[2] M. Onink, F.D. Tichelaar, C.M. Brakman, E.J. Mittemeijer, S. Zwaag: <u>Z. Metallkd.</u>87, 1996, p.24.

[3] C. Qiu, S. Zwaag: <u>Steel Res.</u> 68, 1997, p.1.

[4] T.A. Kop, J. Sietsma, S. Zwaag: Proc. Int. Conf. on Materials Solutions '97 on Accelerated Cooling/Direct Quenching Steels, Indianapolis, ASM International, 1997, p.159.

[5] A.T. Gorton, G. Bitsianes, T.L. Joseph: <u>Trans. Met. Soc. AIME</u> 233, 1965, p.1519.

[6] M. Onink, C.M. Brakman, F.D. Tichelaar, E.J. Mittemeijer, S. Zwaag*:* <u>Scripta Metallurgica et Materialia</u> 29, 1993, p.1011.

[7] M.E. Straumanis, D.C. Kim: <u>Z. Metallkd.</u> 62, 1997, p.272.

[8] W. Sounders, P. Hidnert: <u>U.S.B.S. Sci. Pap.</u> 21, 1926/1927, p.524.

[9] G.H. Cockett, C.D. Davis: <u>J. Iron Steel Inst.</u> 201, 1963, p.110.

[10] R. Kohlhaas, Ph. Dünner, N. Schmitz-Pranghe: <u>Z.angew. Phys.</u> 23, 1967, p.245.

[11] N. Ridley, H. Stuart: <u>Brit. J. Appl. Phys.</u> 1, 1968, p.1291.

[12] T.I. Babyuk, G.P. Kushta, V.P. Mikhal'chenko: <u>Phys. Met. & Metallogr.</u> 38, 1974, p.56.

[13] T.I. Babyuk: <u>Phys. Met. & Metallogr.</u> 49, 1980, p.82.

[14] N. Ridley, H. Stuart: <u>J. Met. Sci.</u> 4, 1970, p.219.

[15] H. Esser, G. Müller: <u>Arch. Eisenhüttenwes</u>. 7, 1933, p.265.

[16] E.J. Fasiska, H. Wagenblast: <u>Trans. Met. Soc. AIME</u> 239, 1967, p.1818.

[17] A. Jablonka, K. Harste, K. Schwerdfeger: <u>Steel Res.</u> 62, 1991, p.24.

[18] D.J. Dyson, B. Holmes: <u>JISI</u> 208, 1970, p.469.

[19] W.C. Leslie: <u>Metall. Trans.</u> 3, 1972, p.5.

[20] W. Steven and A.G. Haynes: <u>J. of the Iron and Steel Institute</u> 183, 1956, p.349.

[21] F.S. LePera: <u>J. Metals</u> 32, No3, 1980, p.38.

CHAPTER IV

Experimental study of multistep phase transformations kinetics during continuous cooling C-Mn steels

IV.1 Introduction

The kinetics of the decomposition of austenite and the volume fractions of product phases formed are fundamental in understanding the microstructures and mechanical properties of steels. Dilatometry is an efficient technique to obtain information about the transformation behaviour of steels.[1] The technique is based on the monitoring of the change in length of a sample during heating, cooling or isothermal holding. Although dilatometry can be used to determine the beginning and the end temperatures of transformations, the standard data analysis based on the lever rule is usually not appropriate to determine accurately the different volume fractions of phases when several phases are formed. In that case only the start temperature of the first transformation and the end of the last transformation are relevant, as the transformations usually overlap and thus, it is not possible to detect at which temperature they actually begin and end. Up to now, a complete Continuous Cooling Transformation (CCT) diagram could therefore only be determined after several experiments, supplemented with microstructural observation and hardness measurements. Even then, an uncertainty remained for the starting temperature for the formation of the secondary phases pearlite and bainite. In the previous chapter, an improved method for determining phase transformation kinetics for a multistep solid-state transformation from a dilatation curve has been proposed.[2,3,4] In addition to the well-known lever rule method, this new method is applied to transformations in a 0.2C-1.6Mn steel. Calculated volume fractions of phases are compared with microstructural observations and supplemented with hardness measurements. It is shown that a detailed CCT diagram can be obtained for C-Mn steels.

IV.2 Experimental procedure

Dilatometer samples were prepared from a steel with 0.19 wt.% C and 1.6 wt.% Mn (steel composition 9 in table II.2). A first set of cycles with increasing cooling rates from 6 to 840 °C/min was used on the same dilatometer sample. Separate samples were prepared for each thermal cycle for microstructural evaluation. An additional sample was heated separately in a furnace 30 min at 950 °C and water quenched to form martensite. The cooling curve was measured with a thermocouple placed inside the sample. The cooling rate obtained was 7300 °C/min. The different phases were observed by light optical microscopy (LOM) and scanning electron microscopy (SEM) after etching with nital. Vickers hardness measurements were done using a 5 kg load. Two methods, respectively the lever rule and the method proposed in chapter III, were used to analyse the dilatometer curves and obtain the CCT diagram.

IV.3   Construction of the CCT diagram

IV.3.1 Lever rule

The method described in chapter II as the lever rule was applied to the cooling curves obtained from dilatometry. Except for the high cooling rates, where the bainite and the martensite start temperatures could clearly be detected, only one beginning and one ending temperatures could clearly be detected from the dilatometric curves. Iso-transformation lines were represented on the CCT diagram to have an idea of the transformation kinetics. Hardness values give also an indication on the phases formed. The final CCT diagram based on lever rule results is shown in Figure IV.1. The diagram, based only on the lever rule, is not sufficient to predict the microstructure because of the unknown microstructural phase fractions and carbon content. Microstructure observations were performed to quantify the volume fractions of the different phases, but it was impossible to determine at what temperature the second and third phases appeared. It is necessary to cool different samples at the same rate and to interrupt the cooling by a severe quench in order to freeze the microstructure at different stages of the transformation to obtain this information. The drawback of this method is that it requires a large number of experiments on different samples. Additional equipments can be used to reduce the number of experiments. For instance, Kop *et al.* have stressed the potential of a combined dilatometric-calorimetric analysis, showing especially that Differential Thermal Analysis (DTA) is very effective in indicating the pearlite formation.[5]
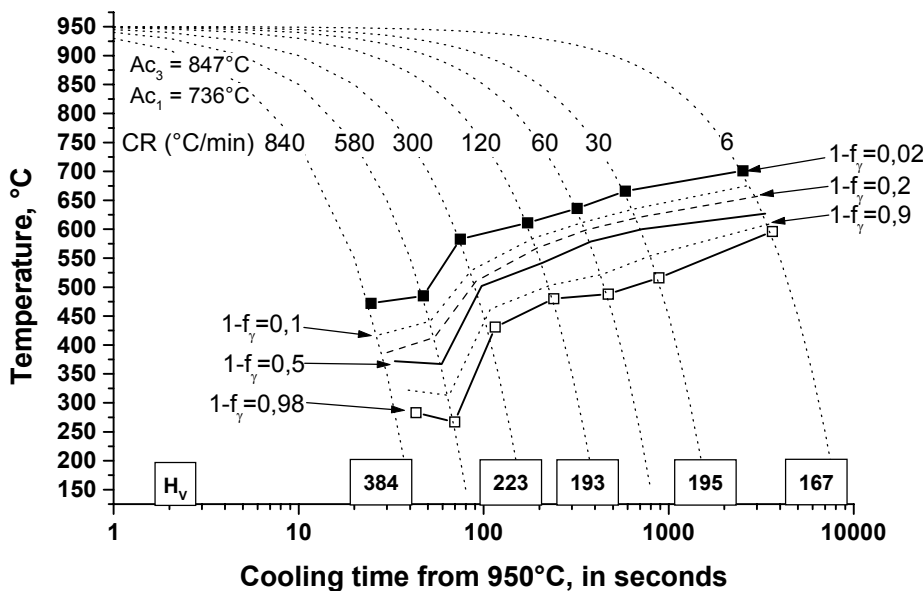

Figure IV.1: Experimental CCT diagram for the 0.19C 1.64Mn steel composition. The volume fractions of transformed austenite indicated were determined using the lever rule.

IV.3.2 Improved model

It was shown in the previous chapter, that the total dilatation could be divided into three parts:
The dilatation of the phases due to the change in temperature, ΔL_i^T, the dilatation due to the
changes of the composition of phases, ΔL_i^C, and the dilatation due to the phase transformation
$\Delta L_{\gamma \to i(+j)}$.

Taking all three terms of dilatation into account, the total relative length change in a time
interval is:

$$\Delta \varepsilon = \sum_i f_i(t) k_i^T dT + k_{\gamma \to i(+j)}^{Trans} \left[f_\gamma(t) - f_\gamma(t + \Delta t) \right] + k_\gamma^C f_\gamma(t + \Delta t) \Delta C_\gamma + k_\alpha^C f_\alpha(t) \Delta C_\alpha \qquad \text{(IV.1)}$$

where $\Delta \varepsilon = (L - L_0) / L_0$ is the relative length change measured experimentally by
dilatometry and $f_i(t)$ are the different phases volume fractions.

This relation holds no matter whether the phase transformation takes place during an
isothermal hold[2,3], during a continuous cooling[2-4] or whether it includes equilibrium phases or
non-equilibrium constituents.

A computer program was developed to relate the total relative length change measured at
each time interval into these three possible contributions to the sample dilatation. The
dilatation of phases due to the change in temperatures is determined using the linear regions
of the dilatometer curves. The dilatation due to the changes of the composition of phases is
calculated assuming the lower diffusion coefficient for substitutional alloying elements in
comparison with those for interstitial atoms. During a continuous cooling from the austenite
region with increasing cooling rate, the possible phases that can be encountered are ferrite,
pearlite, bainite and martensite. During a phase transformation, the carbon content of the
residual austenite is modified. If the first phase formed is ferrite, then the carbon
concentration in ferrite cannot be higher than the solubility limit given by the equilibrium Fe-
C diagram. The carbon concentration in austenite thus increases until it reaches the A_{cm} line
predicting the precipitation of cementite. The equilibrium A_3 and A_{cm} lines used in the
program were calculated using the ThermoCalc^{TM} software. In the case of the bainitic
transformation, it was assumed that the transformation starts when the carbon concentration in
residual austenite reaches the B_s line. Empirical formulae exist to predict the beginning of the
bainitic transformation as a function of the mass contents of alloying elements. The bainitic
transformation start temperature, B_s, was first estimated with the equation from Stevens and
Haynes:[6]

$$B_s(°C) = 830 - 270C - 90Mn - 37Ni - 70Cr - 83Mo \qquad \text{(IV.2)}$$

This formula is very often used to determine B_s for isothermal transformations, but it was not applicable to the studied steel during continuous cooling. During continuous cooling experiments, the kinetics of transformation is different. In particular, a certain amount of under-cooling is often needed before transformations start. It was observed that the equation (IV.2) overestimated the B_s temperature.

Li *et al.* recently proposed a new empirical formula:[7]

$$B_s(°C) = 637 - 58C - 35Mn - 15Ni - 34Cr - 41Mo \tag{IV.3}$$

The values obtained with the equation (IV.3) for the beginning of the bainitic transformation corresponded well with measured transformation temperatures.

In order to test the model, several samples were analysed by optical microscopy after each thermal treatment. The initial as-cast microstructure consisted in 60 % in volume of equiaxed ferrite and 40 % of pearlite, as shown Figure IV.2.
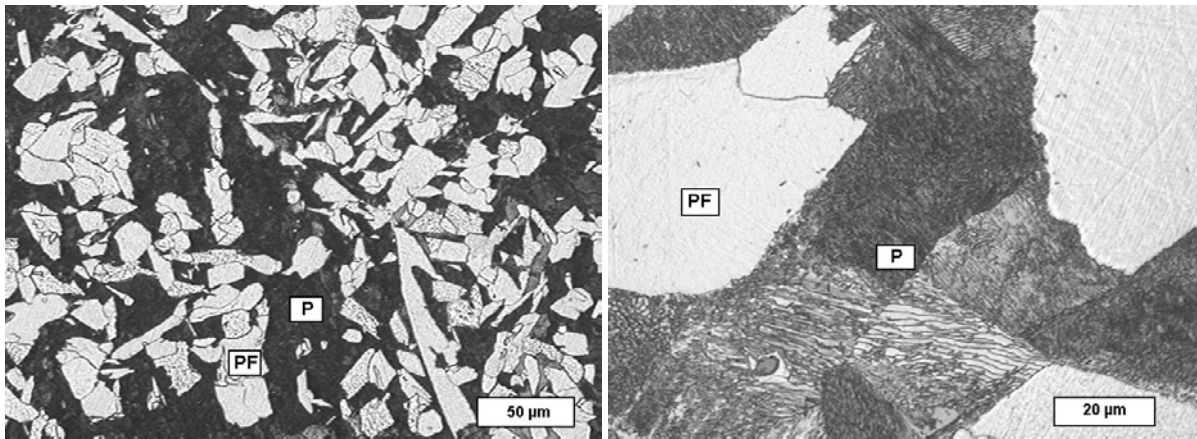

Figure IV.2: The as-cast microstructure of the studied C-Mn steel. PF = Primary Ferrite, P = Pearlite.

Part of the calculated equilibrium diagram (A_3 and A_{cm}) is plotted on Figure IV.3 to IV.6. The respective volume fractions of ferrite and pearlite expected at each equilibrium temperature are also indicated in Figure IV.3 in dashed lines. It can be seen that under equilibrium conditions, the ferrite precipitation is expected to start at 790 °C, and the pearlite would form at 715 °C with the eutectoid composition. In the dilatometer, despite the lowest cooling rate used (6 °C/min), the phase transformations occurred far from equilibrium.

According to the calculations, at the rate 6 °C/min, the ferrite formed at 710 °C. It can be seen on the micrographs shown in Figure IV.3, that it first formed at the grain boundaries, and, because of the low temperature, part of the ferrite also grew into the austenite as Widmanstätten side-plates and acicular ferrite. The carbon concentration in residual austenite reached the extrapolated A_{cm} line at 615 °C, where the pearlite transformation occurred. The austenite was fully transformed into ferrite and pearlite before reaching the B_s line. The calculation gave the respective volume fractions of ferrite and pearlite equal to 62 % and 37 %. These results are in good agreement with the image analysis measurements of the observed microstructures, which gave a ferrite fraction of 60 % ± 5 %.

Figure IV.3: Volume fraction of phases, carbon concentration of the residual austenite as a function of temperature and final microstructure for the sample cooled at the rate of 6 °C/min. PF = Primary Ferrite, W = Widmanstätten, AC = Acicular Ferrite, P = Pearlite.
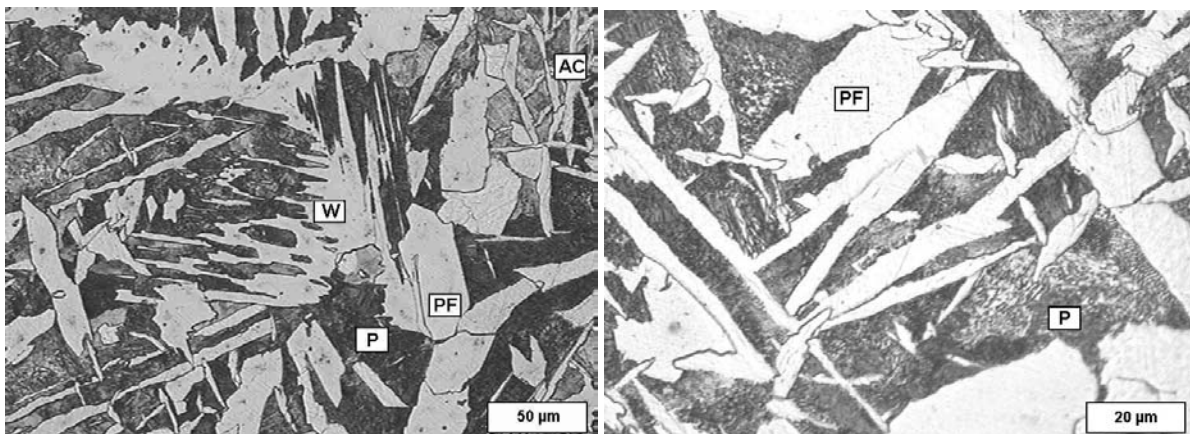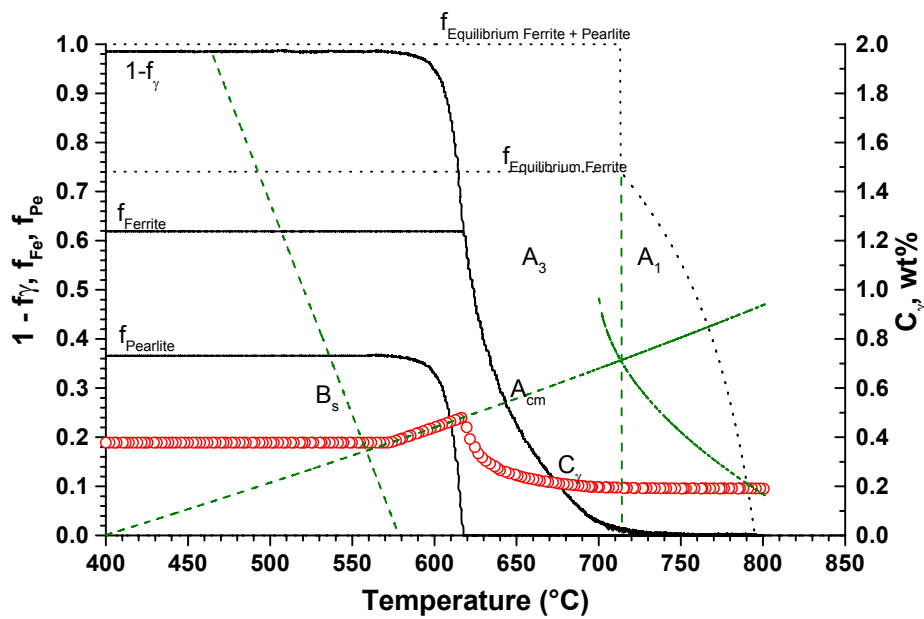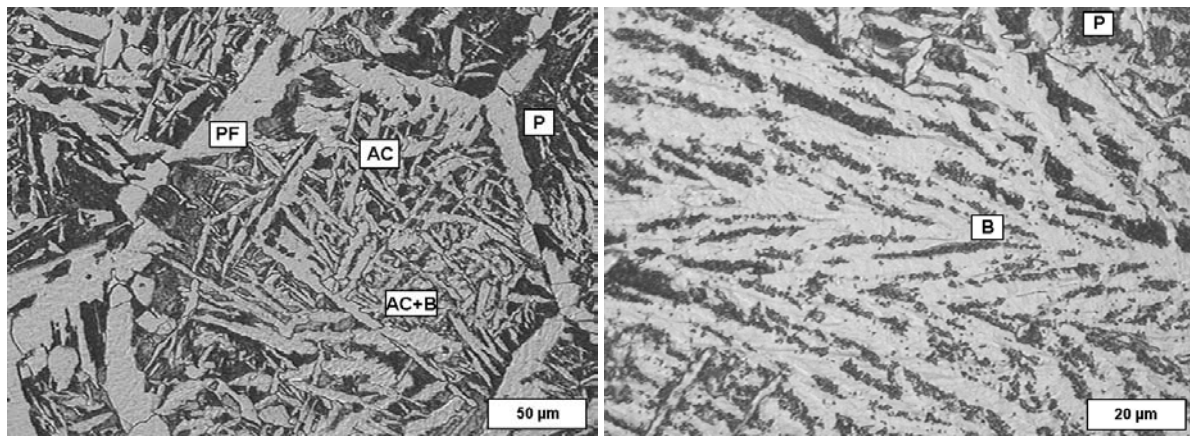
Figure IV.4: Volume fraction of phases, carbon concentration of the residual austenite as a function of temperature and final microstructure for the sample cooled at the rate of 30 °C/min. PF = Primary Ferrite, AC = Acicular Ferrite, P = Pearlite, B = Bainite.

At the cooling rate of 30 °C/min (Figure IV.4), the ferrite transformation started at 660 °C and 55 % of ferrite was formed. The pearlite transformation started at 585 °C, but not enough time was available for the austenite to decompose entirely into pearlite, due to the faster cooling rate. At 560 °C, the bainitic transformation occurred. The curve shows that the volume fraction of transformed austenite increases at 415 °C, due to the formation of martensite. Microstructure observation using the LePèra[8] etching method revealed the presence of martensite in the sample. The temperature at which martensite appeared corresponds with the martensite start temperature predicted by the equation for M_s of Steven and Haynes:[6]

$$M_s({}^oC) = 561 - 474C - 33Mn - 17Ni - 17Cr - 21Mo \qquad (IV.4)$$

This implies that the carbon content in the austenite at 415 °C was the original carbon content, *i.e.* there was no carbon enrichment of the residual austenite. Hence, the bainite formed must have had the original carbon content. It was concluded that, at the cooling rate 30 °C/min, the carbon in the bainite, *i.e.* present as interstitial C in the ferritic bainite and as carbides, was close to the initial carbon content of the steel, *i.e.* 0.19 wt.%.
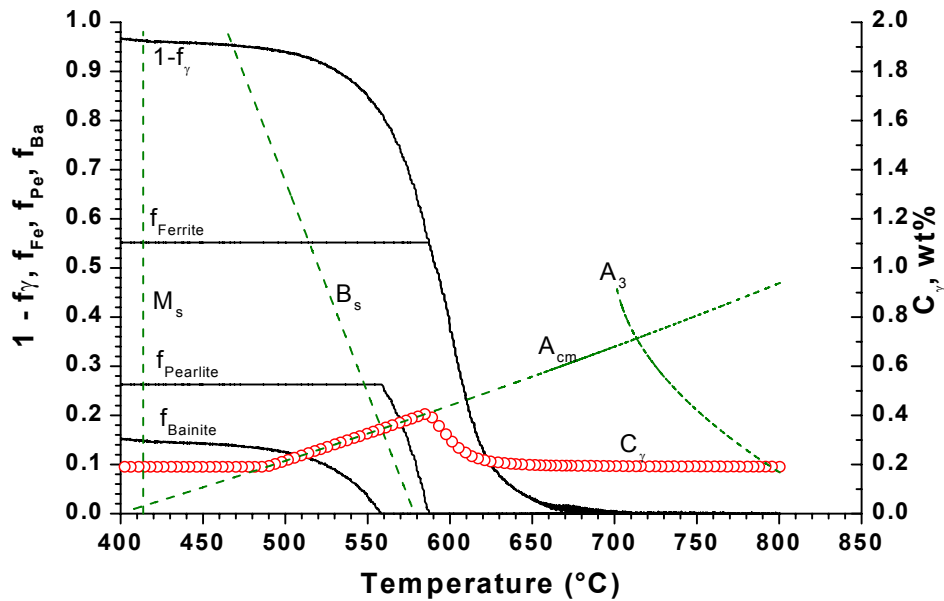

Figure IV.5: Volume fraction of phases, carbon concentration of the residual austenite as a function of temperature and final microstructure for the sample cooled at the rate of 120 °C/min. PF = Primary Ferrite, AC = Acicular Ferrite, P = Pearlite, B = Bainite.

Increasing the cooling rate to 120 °C/min (Figure IV.5) lead to a microstructure consisting in 50 % of ferrite, 12 % of pearlite, 35 % of bainite and 3 % of martensite. The measured M_s temperature was equal to 340 °C. This decrease in M_s means that the residual austenite was enriched in carbon prior to its transformation to martensite. Using the equation (IV.4), one finds that, at the temperature M_s, the carbon content in residual austenite was 0.37 wt.%.

Using the balance mass equation:

$$C_0 = C_{fe}V_{fe} + C_{pe}V_{pe} + C_{ba}V_{ba} + C_\gamma V_\gamma \qquad \text{(IV.5)}$$

where C_0 is the initial carbon content, C_i and V_i the carbon content and volume fraction of the phase i (ferrite, pearlite, bainite or austenite), the carbon contained in upper bainite, *i.e.* in the ferrite and between the bainite laths, was estimated to be 0.187 wt.%.
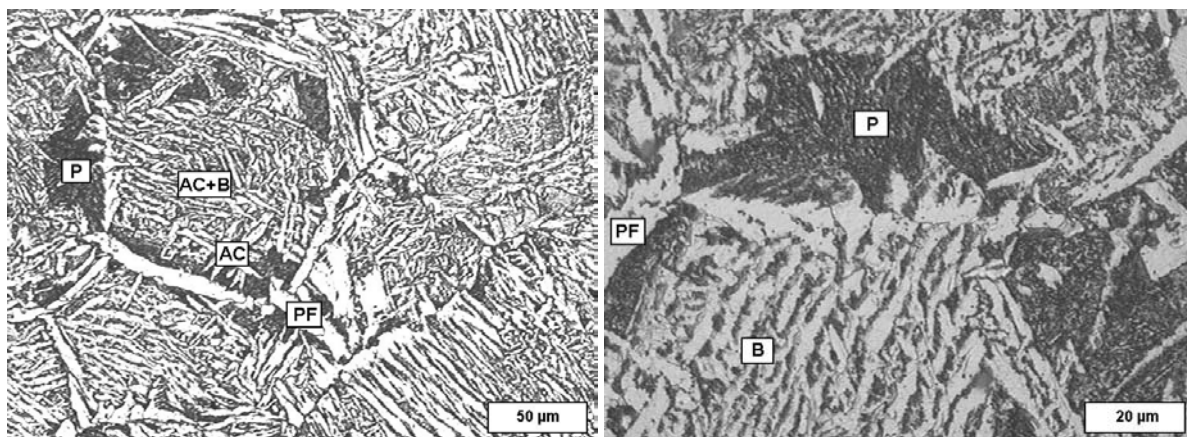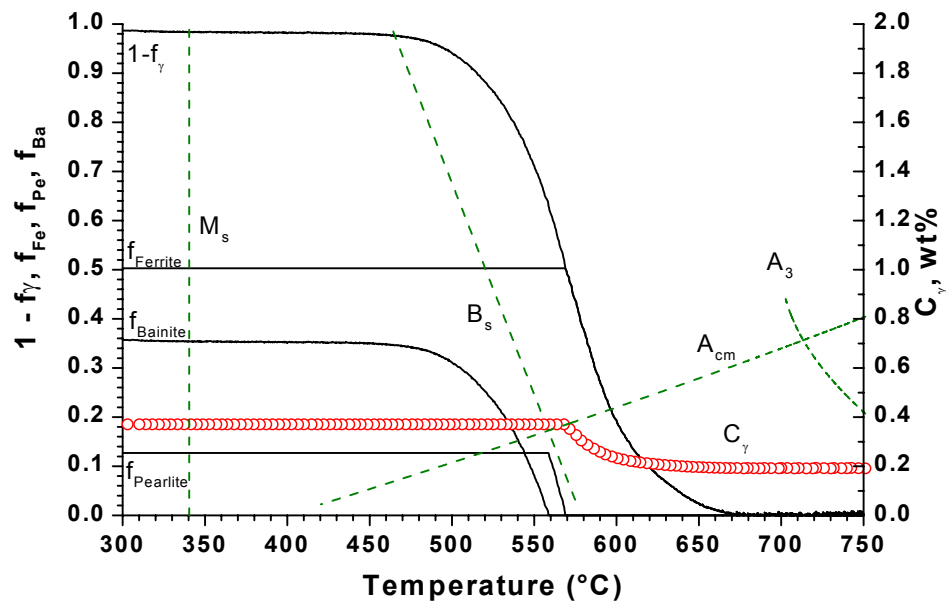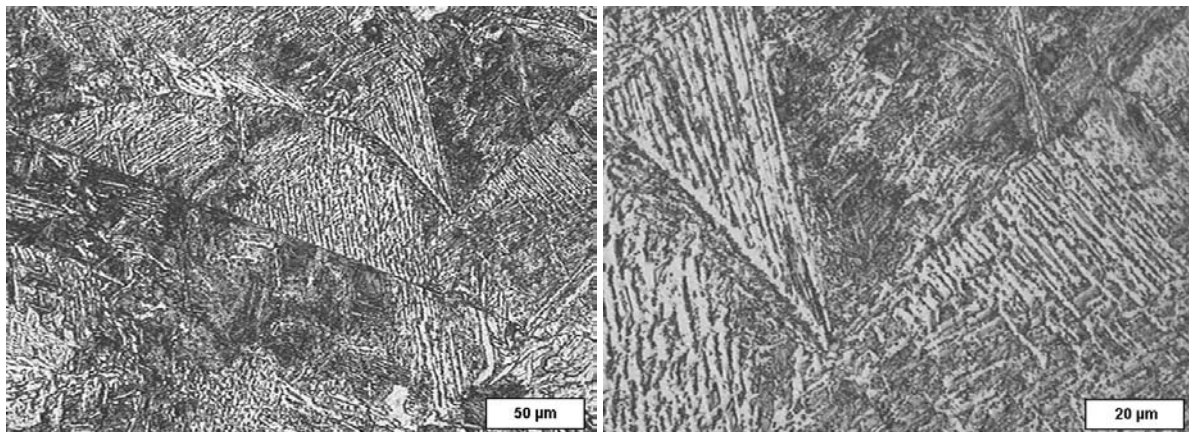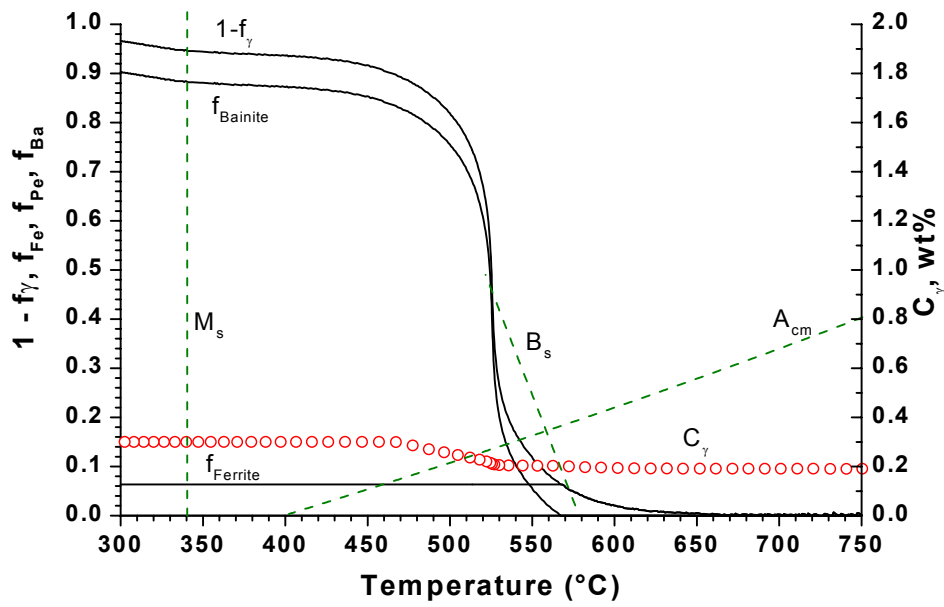

Figure IV.6: Volume fraction of phases, carbon concentration of the residual austenite as a function of temperature and final microstructure for the sample cooled at CR = 300 °C/min.

At the rate 300 °C/min (Figure IV.6), only 6 % of ferrite was formed, the formation of pearlite was entirely suppressed. The bainite was the main constituent (88 %). The martensitic transformation started at 340 °C, due to a carbon content in the residual austenite, calculated by means of equation (IV.4) to be 0.3 wt.%. The carbon in bainite was again found to be 0.19 wt.%.

A new sample was submitted to increasing cooling rates from 6 °C/min to 840 °C/min. For cooling rates of 580 °C/min and 840 °C/min, a mixture of bainite and martensite was formed. The volume fractions of phases formed are shown as a function of temperature in Figure IV.7 for the cooling rate of 580 °C/min. The Koistinen exponential equation was used to determine accurately the M_s temperature:[9]

$$f_m = 1 - \exp(-k(Ms - T)) \tag{IV.6}$$

where f_m is the fraction of martensite formed. The k coefficient was estimated to 0.025 from the experimental curves.

At the cooling rates 580 °C/min and 840 °C/min, the M_s temperatures were 385 and 390 °C, respectively. The volume fractions of bainite formed were 36 % and 24 %, respectively. Calculations led to carbon content in bainite of 0.05 wt.%. This implies that no interlath carbide precipitation took place during the bainitic transformation.
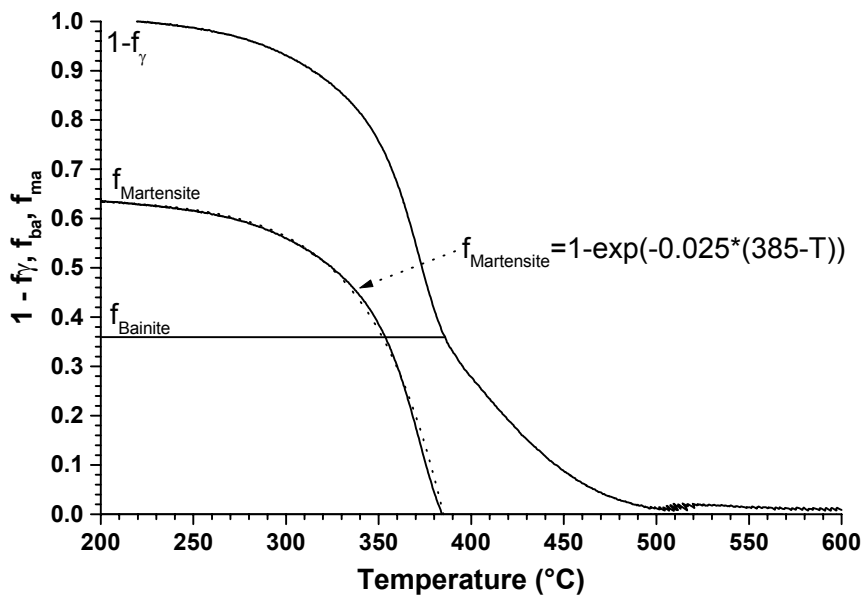
Figure IV.7: Volume fraction of phases bainite and martensite as a function of temperature determined for the sample cooled at the rate of 580 °C/min.

Indeed, it was reported[10] that during the formation of bainitic ferrite at high temperatures, the amount of carbide formed is proportional to the amount of bainitic ferrite at any stage of the reaction. On the other hand, for lower transformation temperatures, the carbide precipitation is found to lag significantly behind the formation of bainitic ferrite. It is very likely that a critical cooling rate exists, at which the carbide precipitation in austenite is suppressed during or after the bainite formation. The final CCT diagram is presented in Figure IV.8, with the phase domains and iso-transformation lines.
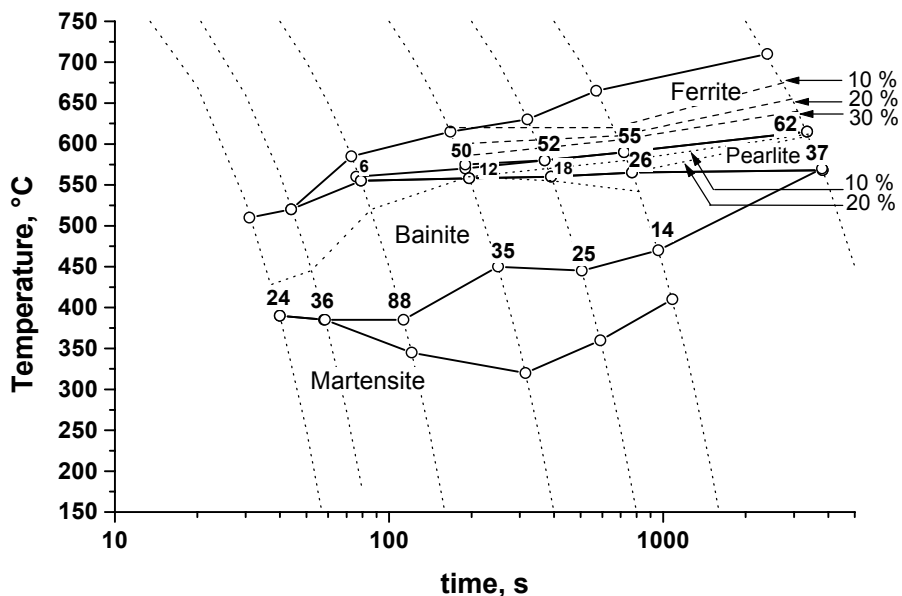
Figure IV.8: Improved CCT diagram for the studied steel showing the phase formation domains. Numbers indicate the volume fractions of the phases formed during the decomposition of the austenite.

IV.4 Discussion

The CCT diagram of Figure IV.8 was obtained after several thermal cycles were performed on one single dilatometric sample. The transformation temperatures Ac_1 and Ac_3 measured during the reheating of that sample were the same after each cycle. This implies that the austenite composition did not vary. In contrast, when new samples were used for each cycle, the reheating transformation temperatures Ac_1 and Ac_3 were slightly affected, meaning that small differences in the initial carbon content may exist between different samples, due to the heterogeneity of the carbon distribution in the original casting.

With the sample submitted to different cycles, the thermal expansion coefficient measured for the austenite increased slightly after the first cycle, and remained constant at 23.10^{-6} $°C^{-1}$. Before the first cycle, the sample contained undesirable point defects and dislocations due to its machining. After one cycle, most of these defects were removed due to the creep effect at high temperature. It is thus advantageous to perform many cycles on the same sample, to avoid any difference in chemical composition and reduce the defects due to machining.

The use of the improved model also allowed for the determination of the density of ferritic bainite in the studied steel. For the samples cooled at 30 °C/min to 300 °C/min, the density of the bainitic ferrite was determined from the dilatometric curves to be 7632 kg/m³ and 7635 kg/m³, respectively, which was consistent with the value of 7635 kg/m³ found for the bainitic grade steel of chapter III.[2-4]

The density of ferrite was lower than that of bainitic ferrite: 7625 kg/m³ for the sample fully transformed at 6 °C/min. It was shown that the carbon content in bainitic ferrite was higher than the maximum solubility of carbon in ferrite, which is 0.019 wt.% at 727 °C. Hence, for the same volume, the density of bainitic ferrite must be higher than that of ferrite. The higher density of the bainitic ferrite is mainly due to the presence of the interstitial carbon at the core of the dislocations.

According to the microstructural observations, the predictions of ferrite and pearlite volume fractions obtained using the extended equilibrium lines A_3 and A_{cm} were correct. The microstructure analysis showed that the model predicts the volume fractions of the phases. The estimations of microstructure were used to predict the hardness of the steel after transformation. The hardness can be calculated, based on the hardness of different phases, by means of the rule of mixture:

$$Hv = X_m Hv_m + X_b Hv_b + (X_f + X_p)Hv_{f+p} \qquad (IV.7)$$

where Hv is the hardness in Vickers; X_m, X_b, X_f and X_p are the volume fraction of martensite, bainite, ferrite and pearlite, respectively; and Hv_m, Hv_b, Hv_{f+p} are the hardness of martensite, bainite, and the mixture of ferrite and pearlite, respectively.

Empirically based formulas developed by Maynier *et al.*[11] and presented in chapter I, equations (I.29) to (I.31), were used for the calculation of Hv_m, Hv_b, and Hv_{f+p} as functions of steel composition and cooling rate.
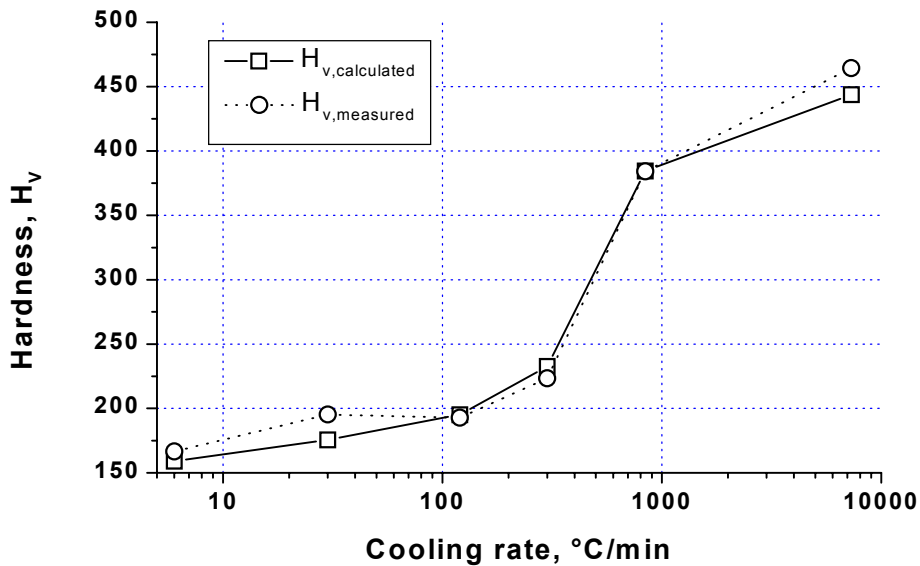

Figure IV.9: Comparison between measured and calculated hardness in samples cooled at different cooling rates.

The total hardness was measured at each cooling rate. The hardness of phases was estimated at each cooling rate using equations (I.29) to (I.31). The fractions determined using the model on dilatometric curves were introduced in the equation (IV.7). The sample cooled at 7300 °C/min was fully martensitic. The measured hardness and the calculated hardness are compared in Figure IV.9. The results show, albeit indirectly, that the estimated volume fractions of phases are in good agreement with the volume fractions obtained experimentally.

The model developed to extract quantitative information on phase transformations from dilatometric data was applicable to the C-Mn steel. The densities of ferrite and bainitic ferrite were determined in different samples and for different cooling rates. The results obtained showed that a single sample can be used to cover a large range of cooling rates. An accurate CCT diagram was produced with this single sample without a need for microstructure observations. The advantages of the model developed above are the accuracy of the analysis of the phase transformations. Indeed, scattering due to sampling is suppressed. Once the equilibrium diagram of the steel under consideration is calculated, the present method allows a detailed study of the austenite decomposition using a wide range of cooling rates.

IV.5   Conclusions

The transformation behaviour of a 0.2C-1.6Mn steel during cooling from the austenite region was studied by means of dilatometry. Two methods were used to analyse the cooling curves. In contrast to the lever rule, which can only predict the volume fraction of transformed austenite if more than one phase is formed, the improved method yields the transformation temperatures and the volume fractions of every formed phase. This model is in principle applicable to other steels, provided that the equilibrium diagram is known. Detailed CCT diagrams can be produced using a single dilatometric sample, reducing considerably the number of experiments. The method is believed to be well suited to study the effects of alloying elements on the austenite decomposition. The bainitic transformation can be analysed in detail as the model takes into account the carbon partitioning and its considerable enrichment in the bainite. The existence of a critical cooling rate, at which the carbide precipitation is suppressed after the bainite formation, was emphasized.

References

[1] G.K. Prior: <u>Materials Forum</u> 18, 1994, p.265.

[2] J.Z. Zhao, C. Mesplont, B.C. De Cooman: <u>Z. Metallkd.</u> 92, 2001, 4, p.345.

[3] J.Z. Zhao, C. Mesplont, B.C. De Cooman: <u>Materials Science and Engineering</u> A332, 2002, p.110.

[4] J.Z. Zhao, C. Mesplont, B.C. De Cooman: <u>ISIJ International</u>, vol.41, 2001, No.5, p.492.

[5] T.A. Kop, J. Sietsma, S. Van der Zwaag: Proc. Int. Conf. on Materials Solutions '97 on Accelerated Cooling / Direct Quenching Steels, Indianapolis, ASM International, 1997, p.159.

[6] W. Steven, A.G. Haynes: <u>J. of the Iron and Steel Institute</u>, 183, 1956, p.349.

[7] M.V. Li, D.V. Niebuhr, L.L. Meekisho, D.G. Atteridge: <u>Metallurg. Mater. Trans. B</u>, 29B, June 1998, p.661.

[8] F.S. LePera: <u>J. Metals</u> 32, No.3, 1980, p.38.

[9] D.P. Koistinen, R.E. Marburger: <u>Acta Metallurgica</u>, vol. 7, 1959, p.59.

[10] H.K.D.H. Bhadeshia: Bainite in Steels, Ed: The Institute of Materials, 1992, p.72.

[11] P. Maynier, J. Dollet, P. Bastien: Hardenability Concepts with Applications to Steels, D.V. Doane and J.S. Kirkaldy, eds., AIME, New York, NY, 1978, p.518.

CHAPTER V

Dilatometric study of the effect of soluble boron on the continuous and isothermal austenite decomposition in 0.15C-1.6Mn Steel

V.1 Introduction

The control of properties and microstructure is fundamental for the development of flat-rolled high strength sheet steel. Very high levels of strength and adequate elongations can be obtained in steels with a bainitic microstructure. Small additions of alloying elements having a strong effect on the hardenability are often used to control the microstructure with respect to industrial and economical constraints. Boron has a very strong effect on steel hardenability. Many studies have been carried out in boron-bearing steel to explain the hardenability mechanism.[1-5,7-9,13] Boron has a significant influence on the hardenability of low alloy engineering steels, with 0.003 wt.% soluble boron producing an increase of hardenability equivalent to about 0.5 wt.% of elements such as manganese, chromium, and molybdenum. However, the use of boron as a hardenability agent is generally confined to steels containing less than 0.4 wt.% C and the effect decreases markedly as the carbon content is increased. At carbon contents beyond the eutectoid composition of the base steel, boron additions reduce the hardenability and this has implications for *e.g.* the case hardened regions of carburised components.[1] The presence of boron clearly increases the incubation time for the formation of ferrite and substantially lowers the nucleation rate after the onset of ferrite formation. The presence of grain-boundary borocarbides precipitates during cooling has been reported as clear evidence of grain boundary boron enrichment.[2] It is likely that the boron enrichment was due to grain boundary segregation and precipitation of borocarbides. Observations made on austenitic stainless steels containing boron confirmed the tendency of boron atoms to migrate to austenite grain boundaries, and this behaviour has been linked to boron-vacancies interactions.[3] No high temperature boron segregation exists and segregation and precipitation occur during the cooling from the solution temperatures.[4] It has been shown using particle tracking autoradiography, that boron segregation took place mainly during cooling. Two segregation mechanisms during the $\gamma \rightarrow \alpha$ transformation have been identified:

- non equilibrium segregation occurring during cooling after soaking at high temperature (1260 °C);

- equilibrium segregation during holding at low temperature (870 °C).[5]

Since the nucleation of ferrite occurs at γ grain boundaries, particular attention must be devoted to the possible role of the grain-boundary $M_{23}(B,C)_6$ borocarbides. These precipitates formed during cooling with a face centered cubic (FCC) lattice, nucleate in austenite with a parallel cube // cube orientation relationship with the parent γ grain on one side of the boundary. This result was found assuming that austenite and martensite are related by the Kurdjumov-Sachs relationship.[6] Selected area diffraction patterns have revealed the following orientation relationship between martensite and $Fe_{23}(B,C)_6$:[7]

$$(111)_{Fe_{23}(B,C)_6} // (110)_{martensite}$$
$$[1\,\overline{1}\,0]_{Fe_{23}(B,C)_6} // [1\,\overline{1}\,1]_{martensite}$$

The interface between the precipitates and the parent γ grain has a substantially reduced energy compared to the energy of the γ grain boundary. It is expected that the nucleation of ferrite should be inhibited on that side of the γ grain boundary. The other interface of the precipitate bordering to the neighboring γ grain is fully incoherent and can be considered as having energy of the order of the γ grain boundary energy, *i.e.* about 0.5 J/m². Therefore, if the precipitates are small enough so that they do not provide large extra areas of incoherent boundaries, the net result is the inhibition of the ferrite nucleation rate. As discussed by Morral[8], a similar reasoning can be made concerning the possible influence of atomic boron segregation at the γ grain boundaries. It appears quite possible that both boron segregation and the early stages of $M_{23}(B,C)_6$ precipitation should be taken into account to explain the effect of boron. It is clear that for low austenitizing temperatures, many undissolved borocarbides are distributed in the microstructure. Since they may form during the thermal history of the steel, they are usually not in any specific crystallographic relationship with the austenite lattice. Hence, they can provide nucleation sites for ferrite formation during the subsequent cooling. This results in an increase in nucleation rate when boron content goes beyond the optimum 10 to 30 ppm.

The consensus is that soluble boron segregates to the austenite grain boundaries, where it reduces the strain energy in these regions, retarding the nucleation of ferrite and increasing the hardenabiliy of the steel.[1]

Boron must be in solid solution and therefore be protected against precipitation by reaction with nitrogen to BN to obtain the maximal effect. It is well known that nitrogen can poison the boron hardenability. In the absence of nitride forming, boron combines with nitrogen to form BN. Titanium is a potent nitride-forming element. It is frequently used to protect boron from nitrogen. TiN forms in the liquid state prior to solidification and it is a very stable compound in the solid state. Hence, it does not dissociate during heat treatments. When added in proper quantity, Ti efficiently stabilizes all nitrogen.[4]

Complete protection of the boron hardenability effect in a 0.18C-1.2Mn-0.002B steel was reported for Ti/N ratios ≥ 2.9; this ratio is slightly below the stoichiometric Ti/N ratio of 3.4.[9]

Boron is added to strip steels at the stoichiometric ratio B/N (wt.%) of 0.8 to remove nitrogen from solid solution and avoid the need for a high temperature coiling in low carbon steels destined for cold reduction and continuous annealing at a later stage. This practice leads to high values of r$_m$, the mean normal plastic strain ratio, and increases the formability, the creep ductility and the hot workability of strips.[1]

Little information is reported on the effects of boron on the bainitic transformation. Boron retards the heterogeneous nucleation of allotriomorphic ferrite at the austenite grain surfaces, to a greater degree than that of bainite.[10] It was found that the combination of 0.5 wt.% Mo with soluble boron in low carbon steels led to fully bainitic microstructures with improved properties.[11] However, the use of soluble boron to produce hot rolled bainitic sheet steels is relatively recent, and is linked to the emergence of high strength complex phase steels.[12]

Soluble boron affects differently the ferrite and the bainite formation. Hence, the mechanism of transformation, diffusive or displacive, determines how the nucleation rate is affected by soluble boron.

The growth process of ferrite may be slowed down by a solute drag like effect (SDLE) due to the partitioning of alloying elements. It has been shown, by means of calculations using the DICTRA software, that the rapid reaction is controlled by rapid interstitial diffusion allowing no partitioning of the substitutional elements during the early stages of ferrite growth. The growth rate is then controlled by very sluggish substitutional diffusion, after the activity gradients of the interstitial elements are leveled out. The growth then continues with the much slower rate until the full metastable ferrite + austenite equilibrium, where cementite is not allowed to form, is finally approached.[13]

This chapter studies the effects of small additions of soluble boron on the austenite decomposition in a 0.15C-1.6Mn wt.% steel. Continuous cooling from the austenitic region with different cooling rates and isothermal transformation cycles were performed in a dilatometer in order to produce controlled microstructures. The kinetics of austenite decomposition was studied in detail for the different decomposition reactions, with an emphasis on the bainitic transformation.

V.2   Experimental procedure

The compositions of the two CMn steels used for the study are given in Table V.1. In both steels, less than 50 ppm N was present. In the boron bearing steel, the Ti/N ratio higher than 5 prevents the BN precipitation completely and ensures the observation of the hardenability effect due to soluble boron only.

Table V.1: Chemical compositions of the studied steels, in ppm.

Steel grade	C	Mn	Ti	B	N
9. CMn	1900	16400	-	-	40
10.CMnB	1400	17200	285	35	50

The decomposition of austenite was studied by means of dilatometry during both continuous cooling and isothermal holding, using the reheating procedure described in chapter II. The samples were cooled to a temperature in the range of 950 °C-20 °C at a constant cooling rate. The cooling rates were varied between 6 and 840 °C/min during the continuous cooling experiments. Some samples were quenched to a isothermal transformation temperature between 450 °C and 660 °C, kept at this temperature one hour and quenched to room temperature. Samples were prepared for microstructure evaluation after each thermal cycle. The different phases were observed by light optical microscopy (LOM) and scanning electron microscopy (SEM) after etching with nital.

V.3   Results and Discussion

The kinetics of austenite decomposition was studied by means of dilatometry during isothermal holding and continuous cooling. A model accounting for the carbon partitioning effects was developed in chapter III to estimate the volume fractions of the phases formed during either the isothermal holding or the continuous cooling of a hypo-eutectoid steel from the austenitic region.[14,15,16] This model was shown to be applicable to low carbon CMn steels in chapter IV.[17]

The equilibrium phase diagrams were calculated using the ThermoCalc[TM] software. Figure V.1 shows the calculated equilibrium fractions of ferrite and pearlite for both steels. Due to the lower initial carbon content in the CMnB steel, more ferrite was formed in equilibrium conditions, and the $\gamma \rightarrow \alpha$ transformation started at a temperature slightly higher than in the CMn steel.
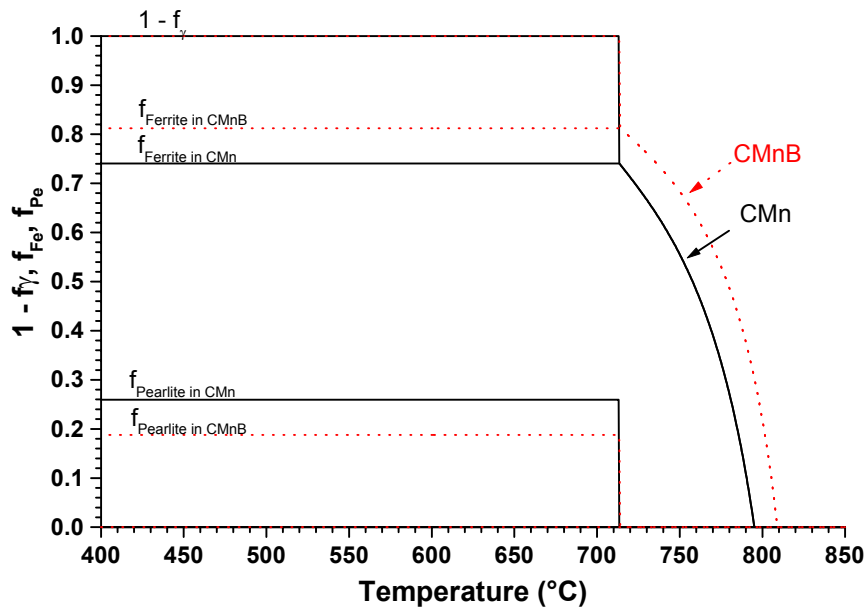

Figure V.1: Calculated equilibrium phases volume fractions as a function of the temperature.

The bainitic phase transformation start temperature (B$_s$) was calculated using the equation from Li *et al.*:[18]

$$B_s(°C) = 637 - 58C - 35Mn - 15Ni - 34Cr - 41Mo \qquad\qquad (V.1)$$

Note that equation (V.1) does not account for the element B. This is due to the fact that B does not influence the B$_s$ temperature. The calculated B$_s$ temperature depends only on the C and Mn contents and is equal to 569 °C in both CMn and CMnB steels.

The as-cast microstructures are shown in Figure V.2. In both steels it consisted in ferrite and pearlite with the equilibrium volume fractions calculated and shown Figure V.1. The remarkable effect of boron on the ferrite nucleation is clearly observed. Indeed, while in the CMn steel (Figure V.2a) grain boundary nucleation of ferrite was observed, no trace of grain boundary ferrite was found in the CMnB steel (Figure V.2b). In contrast to the usual mode of ferrite nucleation in proeutectoid steels, the ferrite nucleated in the interior of the austenite grains in the CMnB steel. The enrichment of the austenite in carbon during ferrite formation occurred at the edge of the austenite grains, and the pearlite has formed when the austenite reached the eutectoid composition.
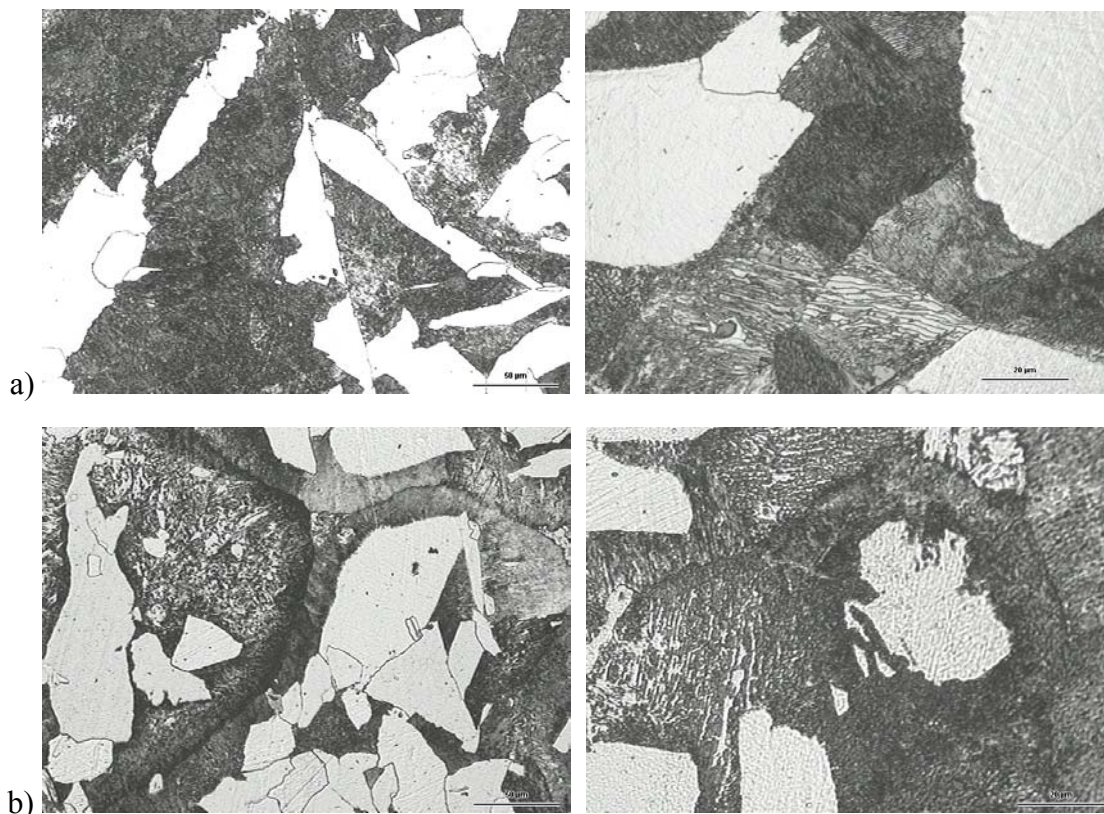

Figure V.2: Microstructure of the as-cast steel a) CMn, b) CMnB.

V.3.1   Isothermal transformation

Seven isothermal transformation temperatures were chosen (660 °C, 615 °C, 565 °C, 530 °C, 500 °C, 475 °C and 450 °C) to trace the decomposition of austenite into ferrite, pearlite and bainite.

The volume fraction of transformed austenite *y(t)* was calculated from the dilatation curves at each time *t* using the relation:

$$y(t) = 1 - f_\gamma = \frac{l(t) - l_0}{l_f - l_0} \tag{V.2}$$

where *l(t)*, l_0 and l_f correspond to the sample length at time *t*, at the beginning of the transformation and at the end of the transformation, respectively. In the temperature range 600 - 475 °C, the austenite decomposition was complete, *i.e.* there was no evidence for the presence of retained austenite.

At each transformation temperature, the Johnson-Mehl-Avrami (JMA) analysis was carried out by fitting the experimental data to the JMA equation:[19]

$$y(t) = 1 - \exp\left[-k(t - t_0)^n\right] \tag{V.3}$$

where

$$k(T) = A \exp\left(\frac{-Q}{RT}\right) \tag{V.4}$$

and *y(t)* is the fraction of austenite transformed, *t*, the time, *T*, the temperature, *A*, the frequency factor, *Q*, the activation energy, *k(T)*, the temperature-dependent rate constant and *n*, the Avrami exponent. *R* is the gas constant, 8.314 $JK^{-1}mol^{-1}$. *n* and *k* were determined experimentally by modifying equation (V.3) to:

$$\ln\left(\ln\left(\frac{1}{1 - y(t)}\right)\right) = \ln k + n \ln(t - t_0) \tag{V.5}$$

The time for the start of the austenite decomposition, t_0, was determined from the best linear correlation between *ln(ln(1/(1-y(t)))* and *ln(t-t_0)* in the range $0.05 \leq y(t) \leq 0.95$. The *n* and *k* values obtained experimentally at each transformation temperature are plotted in Figure V.3a and 3b, respectively.

The Avrami exponent *n* is temperature dependant as it is a function of (a) the nucleation mode, which is temperature dependant, and (b) the growth mode, *i.e.* the shape of the growing nuclei. Considering the case of spherical bodies growing with a constant rate *v* and a random nucleation in space with a constant nucleation rate $\dot{N}$, the Avrami law is:

$$y(t) = 1 - \exp(-\frac{\pi}{3} \dot{N} v^3 t^4) \qquad\qquad\qquad (V.6)$$
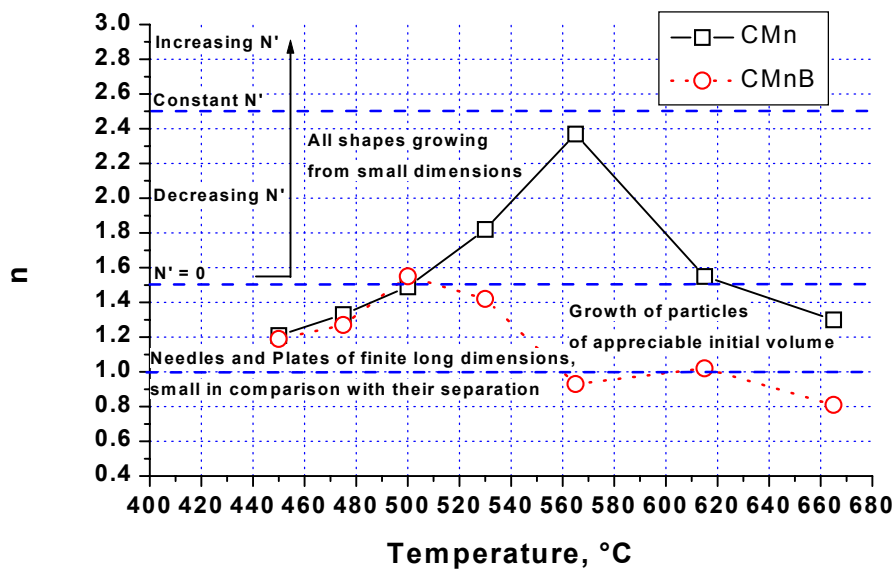
a)
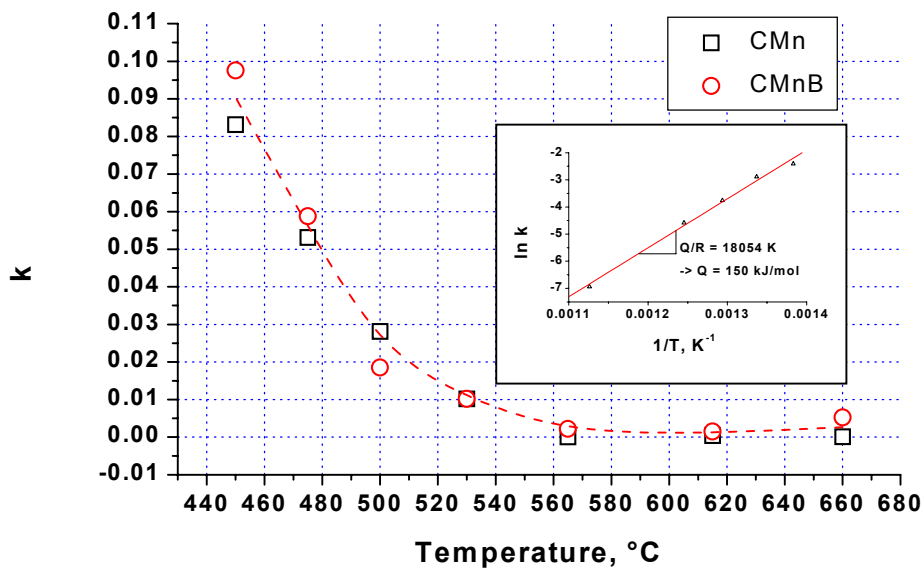
b)

Figure V.3: n and k values obtained experimentally after fitting the data with the JMA equation.

The Avrami exponent *n* varies between 1 and 4, with the following distribution:

- n = 1 for the constant growth rate: the number of new nuclei is proportional to *t*;

- n = 3 for the three-dimensional growth with constant rate: the transformed volume is proportional to t^3.

For a constant growth rate, *n* depends on the shape of the growing phase. For a two-dimensional growth (plates), *n* is equal to 3, and for the growth in one direction (needles), *n* is 2. The case *n* = 2 is generally observed for the growth of bainite laths.

The exponential growth law summarized in Avrami equation (V.3) is valid for linear growth under most circumstances, and approximately valid for the early stages of diffusion-controlled growth. Different values of the Avrami exponent *n* have been linked to the conditions of diffusion-controlled growth by Christian[20] and are reported in Figure V.3a.

In the CMn steel, the exponent *n* increases from 1.3 - 1.5 in the ferrite-pearlite transformation temperature range to a maximum of 2.4 at the B_s temperature, corresponding to the maximum nucleation rate in that steel. At this temperature, the nucleation rate is maximal, but the growth rate is low, as it is the early beginning of the bainite transformation. The exponent *n* decreases then with temperature, because the rate of transformation is controlled by the growth of bainite laths. It is very clear on Figure V.3a, that the soluble boron has a strong effect on the nucleation rate of ferrite. In the ferrite-pearlite temperature range, the Avrami exponent *n* lower than 1 means that no new nuclei are formed and the growth is limited. It increases at temperatures below 550 °C to reach a maximum for 1.5 between 500 °C and 530 °C. It finally decreases at temperatures below 500 °C following the same curve than that for the CMn steel. In the CMnB steel, two peaks are observed for the *n* value, corresponding to the respective noses of the C curves for ferrite and bainite in the TTT diagram.

The classical theory of nucleation explains why those peaks are observed. The number of nuclei can be estimated with the law of Arrhenius, as it is a thermally activated phenomenon:

$$n^* = n_o \exp\left(-\frac{\Delta G^*}{kT}\right)$$
(V.7)

where n_o is the total number of particles of new phase, ΔG^* the activation energy for nucleation, *T* the temperature and $k = 1.3806 \cdot 10^{-23}$ JK^{-1} the Boltzmann constant.

The nuclei grow by addition of atoms, the final step in nucleation. The rate of addition is proportional to the frequency of motion υ into the nucleus for a single atom, multiplied by the number of atoms m^* which actually do so, *i.e.* the immediate neighbors to the nucleus.

Consequently:

$$\dot{N} = n^* \upsilon m^*$$
(V.8)

where $\dot{N}$ is the rate of nucleation measured in units of nuclei per second. The motion of atoms into the nucleus is diffusive and therefore:

$$\upsilon \propto \exp\left(-\frac{\Delta G_D}{kT}\right) \tag{V.9}$$

where ΔG_D is the activation energy for diffusion. m^* is geometrical and depends on the shape and size of the nucleus.

The nucleation rate is a function of the form:

$$\dot{N} \propto m^* \exp-\left(\frac{\Delta G^* + \Delta G_D}{kT}\right) \tag{V.10}$$

As temperature drops, ΔG^* falls violently and the nucleation rate increases. Soon, however, ΔG^* becomes negligible compared to ΔG_D. ΔG_D thus dominates equation (V.10), and $\dot{N}$ then decreases with temperature. Consequently, there is a maximum in the homogeneous nucleation rate.

The k coefficient is temperature dependant and increases with decreasing temperature, in particular below B_s. The activation energy can be calculated by making the following derivative:

$$-\frac{\partial \ln k}{\partial\left(\frac{1}{T}\right)} = \frac{Q}{R} \tag{V.11}$$

In the temperature range 450 °C - 660 °C, the activation energy was calculated to be 150 kJ/mol for both steels. The rate controlling process of upper bainite formation is the diffusion of carbon in the austenite.[21] Using the equation proposed by Kaufman et al. for the activation energy of diffusion of carbon in the austenite:[22]

$$Q_C^\gamma(cal/mol) = 38300 - 1.9.10^5 x_C + 5.5.10^5 x_C^2 \tag{V.12}$$

with x_C the C concentration in at.%, one finds 153.5 kJ/mol for the CMn steel and 155.3 kJ/mol for the CMnB steel. These values for the activation energy for the nucleation of upper bainite are comparable to the present experimental value.

Iso-transformation lines are plotted in Figure V.4 for the CMn steel (solid lines) and the CMnB steel (dotted lines). In contrast to the CMn steel, the CMnB steel exhibits two separate C curves, corresponding to the ferrite and the bainite transformations, respectively. The ferrite transformation was found to start at a slightly higher Ar_3 temperature in the CMnB steel as expected considering its lower carbon content. The temperature for the beginning of ferrite formation, Ar_3, was measured during cooling at the rate 6 °C/min to be 710 °C for the CMn steel and 725 °C for the CMnB steel.
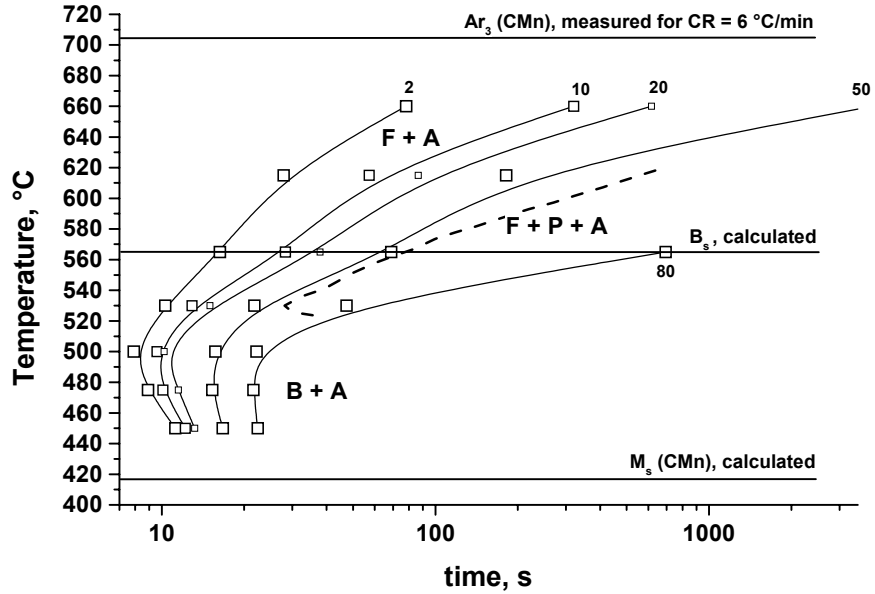
a)
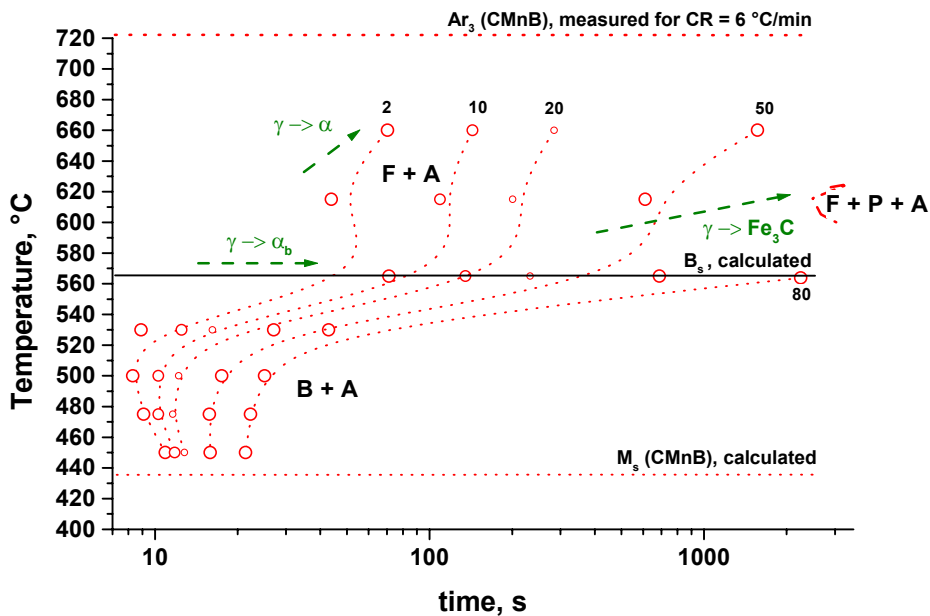
b)

Figure V.4: Time Temperature Transformation (TTT) diagram for a) the CMn steel (solid lines) and b) the CMnB steel (dotted lines). The arrows indicate the effects of boron on the phase transformations.

At temperatures between 615 °C and 550 °C, the incubation times for 2 % transformation were up to 60 s longer in the CMnB steel, showing clearly that soluble boron is responsible for the retardation of the ferrite formation. The pearlite formation was also strongly suppressed in the CMnB steel. The start of pearlite precipitation was clearly observed on the dilatometric curves measured for the CMn steel in the transformation temperatures range 615 °C - 530 °C.

In the CMnB steel, pearlite was formed only in the sample transformed isothermally at 615 °C. Below 530 °C, the incubation time for the bainite transformation was similar in both steels.

Microstructures obtained after isothermal holding for one hour at a temperature between 660 °C and 500 °C are shown in Figure V.5. The phase volume fractions were calculated from dilatometric data and compared with microstructures.

It can be seen Figure V.5a, that after holding the CMn steel one hour at 660 °C, only 50 % of the austenite was transformed to polygonal ferrite. A microstructure containing 50 % ferrite and 50 % martensite was obtained after cooling. Indeed, as the solubility limit of carbon in ferrite was 0.005 wt.% in the CMn steel at 659 °C, according to ThermoCalc calculations, the austenite was enriched in carbon to 0.375 wt.%. According to the Steven and Haynes equation for M_s:[23]

$$M_s(^oC) = 561 - 474C - 33Mn - 17Ni - 17Cr - 21Mo \tag{V.13}$$

the martensite start (M_s) temperature was 329 °C. This temperature was close to the temperature of 335 °C measured by means of dilatometry. The decomposition of austenite to martensite was therefore possible during the cooling.

It can be seen in Figure V.5b, that more ferrite was formed in the CMnB steel than in the CMn steel during holding at 660 °C. This was due to the lower initial carbon content in the steel. The solubility of C was calculated to be 0.012 wt.% at 657 °C in the CMnB steel. 60 % ferrite was formed and the carbon content in the austenite was calculated to be 0.33 wt.% before cooling. Using the equation (V.13), the M_s temperature was 348 °C. However, M_s was measured at 320 °C, indicating that the actual carbon content in the austenite was higher. A microstructure consisting of 60 % ferrite and 40 % martensite was produced.

Isothermal holding at 615 °C produced a microstructure containing 73 % ferrite and 5 % pearlite in the CMn steel (Figure V.5c). The 23 % remaining austenite decomposed into martensite during the subsequent cooling at the measured M_s temperature of 305 °C. At the transformation temperature 615 °C, the kinetics of austenite decomposition was much lower in the CMnB steel than in the CMn steel. At first, a large incubation time was needed before the nucleation of ferrite. It can be clearly seen Figure V.5d, that at the difference with the CMn steel, the ferrite nucleated inside the austenite grains instead of the grain boundaries in the CMnB steel. The pearlite concentration at the grain boundaries shows that the carbon was rejected from the ferrite grains to the exterior of parent austenite grains. 77 % ferrite was formed and 2 % pearlite precipitated during the isothermal holding. More pearlite was formed during the cooling.

Holding the CMn steel at 565 °C led to the formation of 80 % upper bainite (Figure V.5e). The dilatometric results showed that pearlite precipitation occurred after the bainite formation. The remaining austenite decomposed into lower bainite and martensite during cooling.
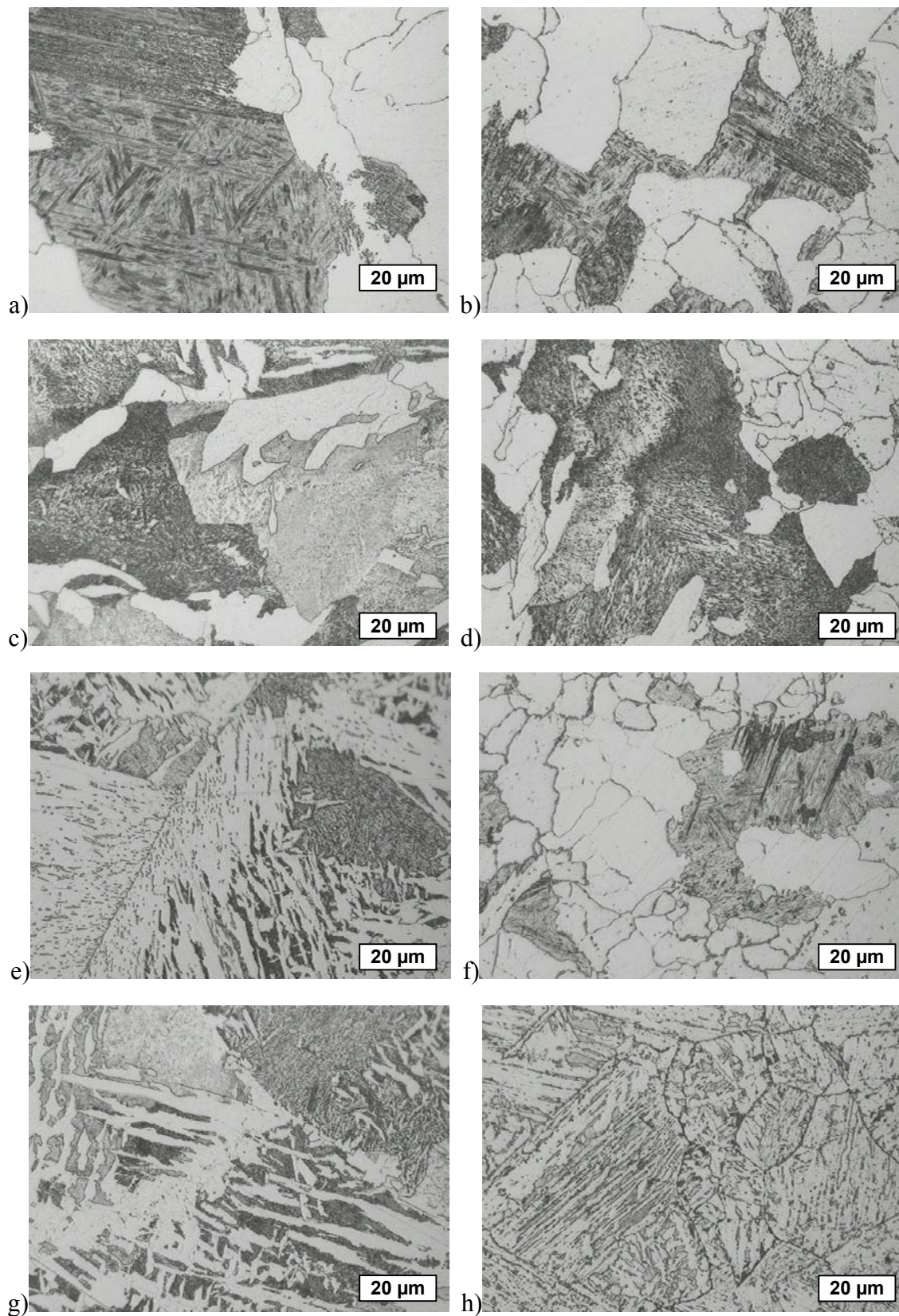
Figure V.5: Final microstructures for the CMn steel (left) and CMnB steel (right). From top to bottom: IT = 660 °C, 615 °C, 565 °C and 500 °C.

No bainite was formed during holding the CMnB steel at 565 °C (Figure V.5f). The microstructure consisted in ferrite and martensite formed during cooling. As no pearlite was formed, carbide precipitation was fully suppressed.

Finally, the holding at 500 °C led to the formation of 90 % bainite in the CMn steel (Figure V.5g). It can be seen on the micrograph Figure V.5e that, at 565 °C, bainite consists in ferrite laths with carbides formed simultaneously between the laths. Figure V.5g shows that, at 500 °C, carbon supersaturated ferrite laths formed first.

The bainitic transformation was very fast at 500 °C in the CMnB steel, and led to a microstructure with a particular morphology (Figure V.5h). The prior austenite grain boundaries were still clearly visible. The bainitic ferrite formed from nuclei inside the initial austenite grains, and can be compared to acicular ferrite. However, clear orientation of the ferrite laths is seen in some grains. Residual austenite was observed in the microstructure between bainitic ferrite laths, using the LePera etching method.[24] It is very likely that austenite was enriched in C and Mn during the bainitic transformation. As a result, the residual austenite was more stable, and the carbide precipitation was suppressed.

V.3.2 Continuous cooling

In most industrial processing lines, isothermal treatments at high temperatures are never used as such. If isothermal or semi isothermal (coiling) processes are used, they are obligatory preceded by a cooling from the austenite region. Continuous Cooling Transformation (CCT) diagrams are used to predict the microstructure after cooling a steel from the austenite region, but their characteristics are strongly dependent on the size and state (recrystallized or deformed) of the prior austenite grains. For the present study, the conditions were quite different from those used in industrial processes. Indeed, large recrystallized austenite grains were produced to make the observations of phase transformations during cooling easier. The austenite grains formed in the CMn steel were larger than those formed in the B bearing steel in the same conditions. The mean grain size was 150 μm in the CMn steel and 80 μm in the CMnB steel.

The dilatometer curves obtained during cooling the CMn steel and the CMnB steel are shown in Figure V.6a and 6b, respectively. It can be seen that although the austenite decomposition started at slightly higher temperatures in the CMnB steel, due to its lower C content, the austenite decomposition was slower, especially for cooling rates 6 °C/min and 30 °C/min. At these cooling rates, the pearlite formation was clearly delayed. At higher cooling rates, however, the kinetics of austenite decomposition was similar. The analyses of the dilatometric curves yielded the different phases fractions. The volume fractions of ferrite and pearlite obtained after cooling at 6 °C/min were close to the equilibrium volume fractions (Figure V.1). In the CMnB steel the pearlite formation was clearly retarded. Cooling at 30 °C/min led to the formation of less pearlite and more bainite in the boron bearing steel. At the cooling rate 120 °C/min the pearlite formation was suppressed in the CMnB steel and the final microstructure was a mixture of ferrite (44 %), bainite (52 %) plus martensite (4 %). During cooling at the rate 300 °C/min, both steels transformed mainly to bainite, with the same kinetics, independently on their initial carbon content.
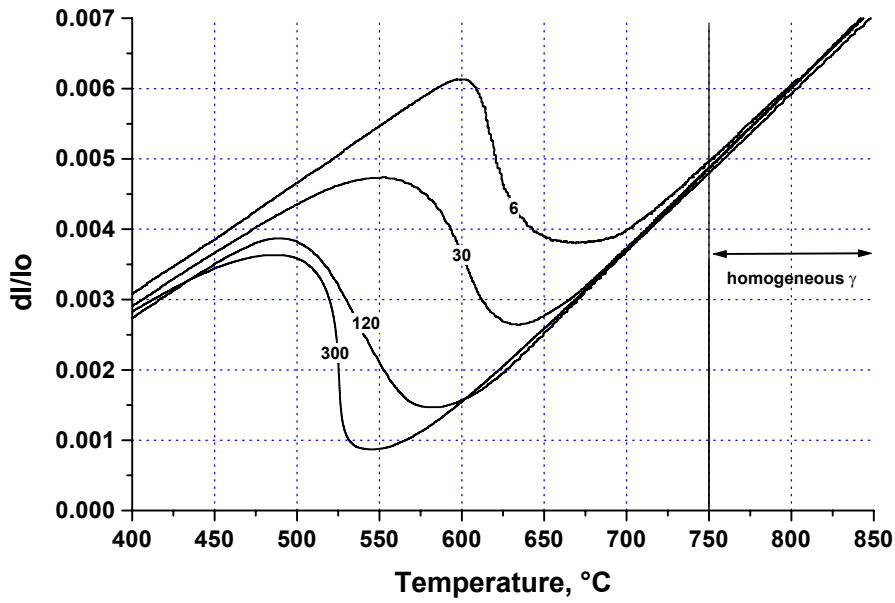
a)
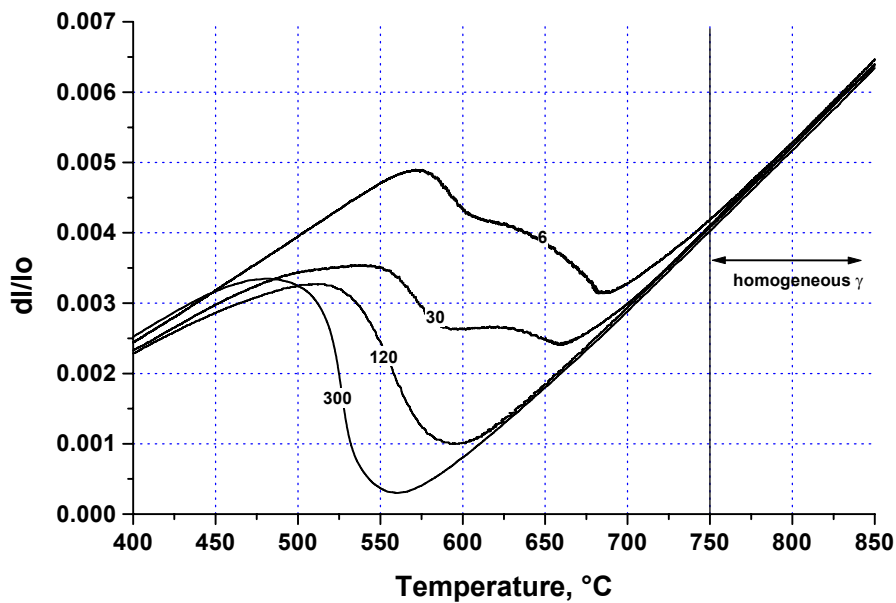
b)

Figure V.6: Dilatometric cooling curves for a) the CMn steel and b) the CMnB steel. The numbers are the cooling rates in °C/min.

Figure V.7 shows the volume fraction of transformed austenite as a function of the cooling time from 800 °C for different cooling rates. Figure V.7b is a plot of the rate of transformation as a function of the cooling time for 4 different cooling rates. The rate of transformation is similar in both CMn and CMnB steels at cooling rates 300 °C/min and 120 °C/min. At lower cooling rates, the CMnB steel shows two distinct peaks of maximal transformation rate corresponding to the formations of polygonal ferrite and acicular ferrite, respectively. It is clearly seen, that the formation of primary ferrite retards the formation of acicular ferrite.

At the fixed fractions of austenite transformed, *f'*, corresponding to the maximal rate of transformation, the temperature $T_{f'}$, was determined.

It has been shown, that the non-isothermal transformations kinetics could be analyzed by means of the equation:[25]

$$\ln \frac{T_{f'}^2}{\phi} = \frac{E}{RT_{f'}} + \ln \frac{E}{Rk_0} + \ln \beta_{f'}$$

(V.14)

where $T_{f'}$ is the temperature at which the formation of the fixed fraction *f'* of ferrite was achieved, and Φ is the cooling rate. $\beta_{f'}$ is a state variable.
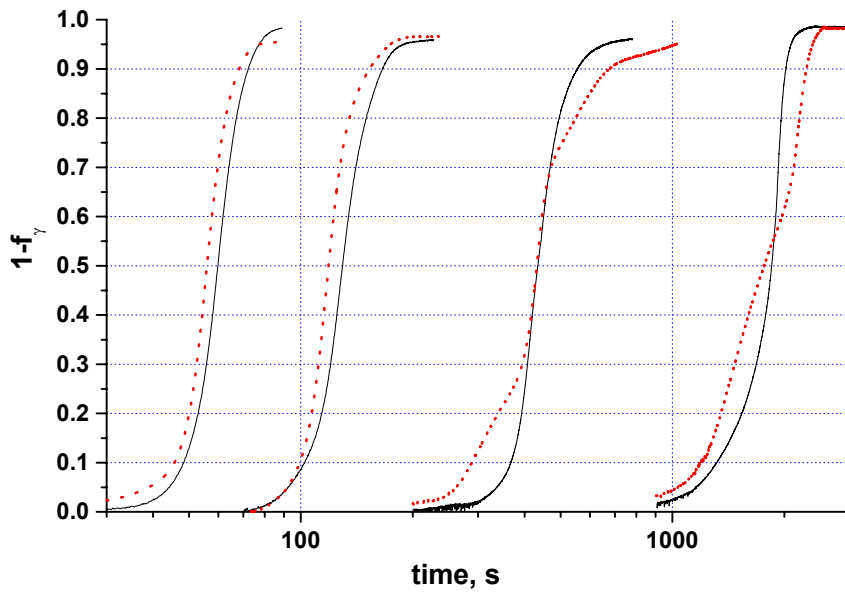
a)
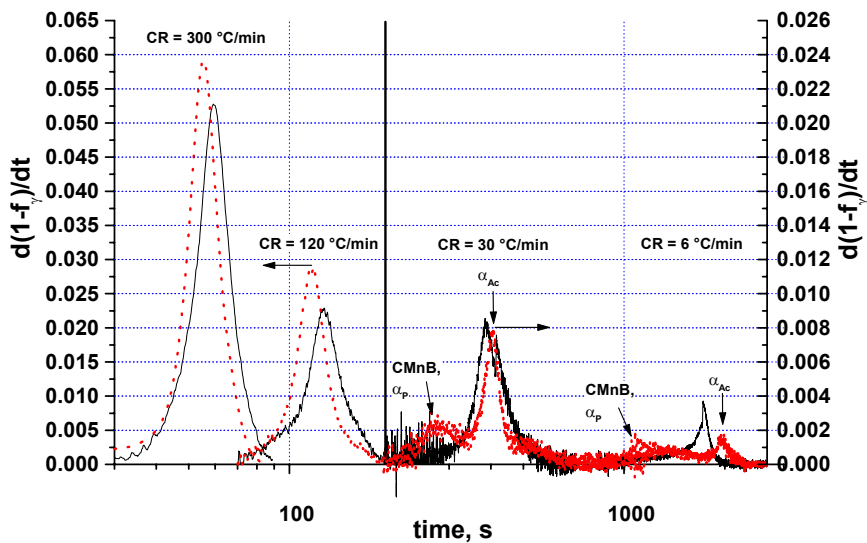
b)

Figure V.7: a) Volume fraction of transformed austenite and b) rate of transformation as a function of the cooling time from 800 °C, for the CMn steel (solid lines) and the CMnB steel (dotted lines).

The activation energy for the formation of ferrite could be determined from the slope of the straight line obtained by plotting $ln(T^2_{f'}/\Phi)$ *vs. $1/T_{f'}$*. From the plot of Figure V.8 the activation energies were determined from the linear region corresponding to the cooling rates 120 °C/min and 300 °C/min in both steels. The activation energies were 130 kJ/mol in the CMn steel and 142 kJ/mol in the CMnB steel. These values are close to the value of 150 kJ measured in isothermal conditions. Note that for low cooling rates, the plot of Figure V.8 is not linear anymore. The activation energy increases strongly with decreasing cooling rate, *i.e.* increasing transformation temperature. That effect is particularly important in the CMnB steel, meaning that the ferrite formation is strongly suppressed.
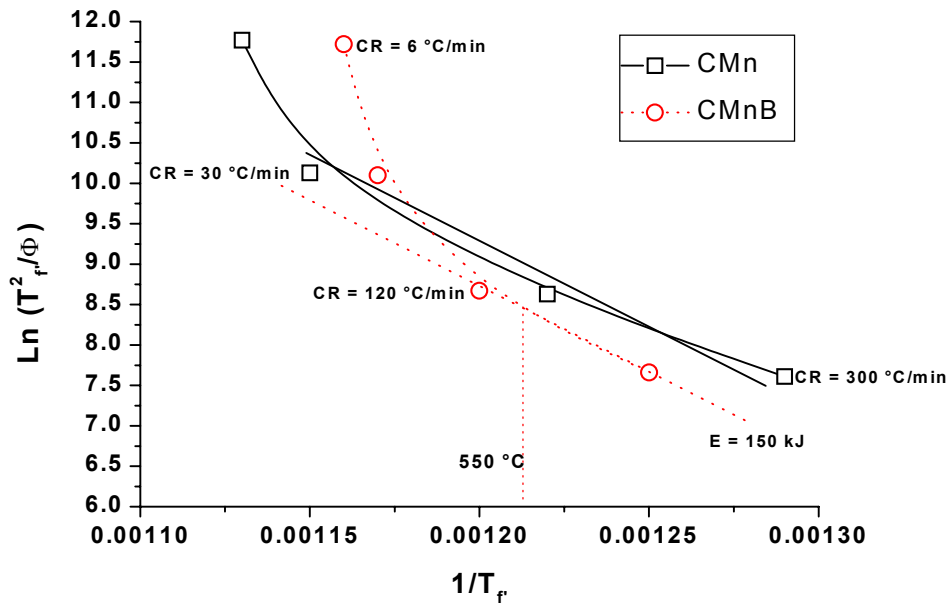
Figure V.8: Determination of the activation energy during cooling using the *Ln (T²/Φ) vs. 1/T* plot.

The final microstructures of the two different steels differed strongly in morphology after cooling in all cases. Microstructures corresponding to increasing cooling rates are shown in Figure V.9. The major difference between the CMn steel (Figure V.9a,c,e,g) and the CMnB steel (Figure V.9b,d,f,h) is the phase morphology. In equilibrium conditions or very low cooling rates, like during continuous casting, time is let for nucleation to occur at small under cooling on grain corners edges and boundaries (Figure V.2a). As these nuclei grow the carbon rejected in the austenite has time to diffuse over large distances and the austenite grain should maintain a uniform composition given by the equilibrium phase diagram. Finally the austenite reaches the eutectoid composition and transforms to pearlite.

The microstructure that results from more rapid cooling depends on the γ grain size and the cooling rate. If the rate is moderately high the specimen will not remain long enough at high temperature for nucleation to occur. Thus nuclei will not be formed until higher supersaturation is reached. The nucleation rate will then be rapid and large areas of grain boundary will become covered by nuclei.

If the temperature is below T$_w$, the start temperature of Widmanstätten ferrite formation, the ferrite will grow into the austenite as Widmanstätten side plates with a spacing that becomes finer with decreasing temperature.[26] Such morphology of ferrite is seen in Figure V.9a.
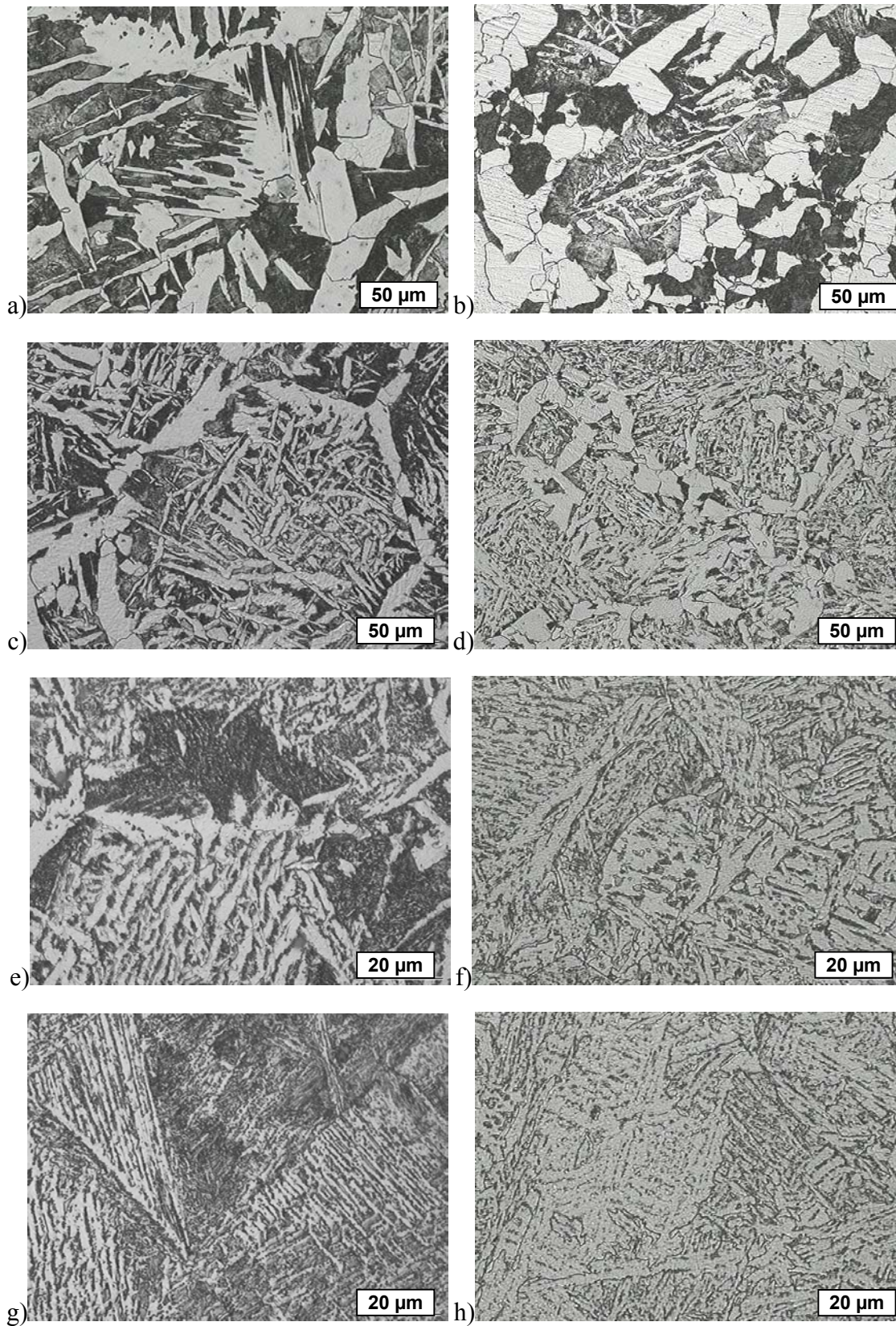

Figure V.9: Final microstructures after cooling at CR = 6°C/min, 30°C/min, 120°C/min and 300°C/min (from top to bottom) the CMn steel (left) and the CMnB steel (right).

In the boron bearing steel, ferrite nucleated from the interior of prior austenite grains, leading to the enrichment of austenite in carbon at the edge of austenite grains. Moreover, less carbide was formed during the cooling at cooling rates superior to 30 °C/min. At low cooling rates, no Widmanstätten ferrite was formed. It is very likely that boron effectively segregated to grains boundaries during the cooling from the austenite region, suppressing heterogeneous grain boundary nucleation sites. In the CMn steel, increasing the cooling rate led to microstructures containing primary ferrite at prior austenite grain boundaries and acicular ferrite inside the initial grains (Figure V.9c, e).

It has been observed, especially in chromium- and molybdenum-containing steels, that allotriomorphic ferrite influenced the development of acicular ferrite in mixed microstructure.[27] In the CMn steel, this effect is observed until the cooling rate is high enough to avoid the primary ferrite formation. Upper bainite nucleated at austenite grain boundaries is then formed (Figure V.9g).

In the CMnB steel, the primary ferrite formation is delayed. Acicular ferrite is the main constituent at cooling rates above 30 °C/min (Figure V.9d,f,h). It is very likely that the presence of Ti, added to protect boron from nitrogen by forming TiN provides thus heterogeneous nucleation sites for the ferrite nucleation. At high cooling rates, acicular ferrite is formed in the CMnB steel whereas upper bainite, *i.e.* ferrite subunits with carbides between the subunits, is formed in the CMn steel, with however a very similar kinetics.

The final CCT diagrams are plotted in Figure V.10 for both steels. Boron was found to delay the pearlite formation. The ferrite growth rate was slightly reduced as less ferrite was formed at cooling rates 1 °C/s and 2 °C/s and an extended ferritic domain was formed in a larger temperature range. The lower carbon content in the CMnB steel was responsible for the higher Ar_3 transformation temperature in that steel. The kinetics of bainite formation was slightly decreased as less bainite (acicular ferrite) was formed in the CMnB steel at cooling rates higher than 5 °C/s.
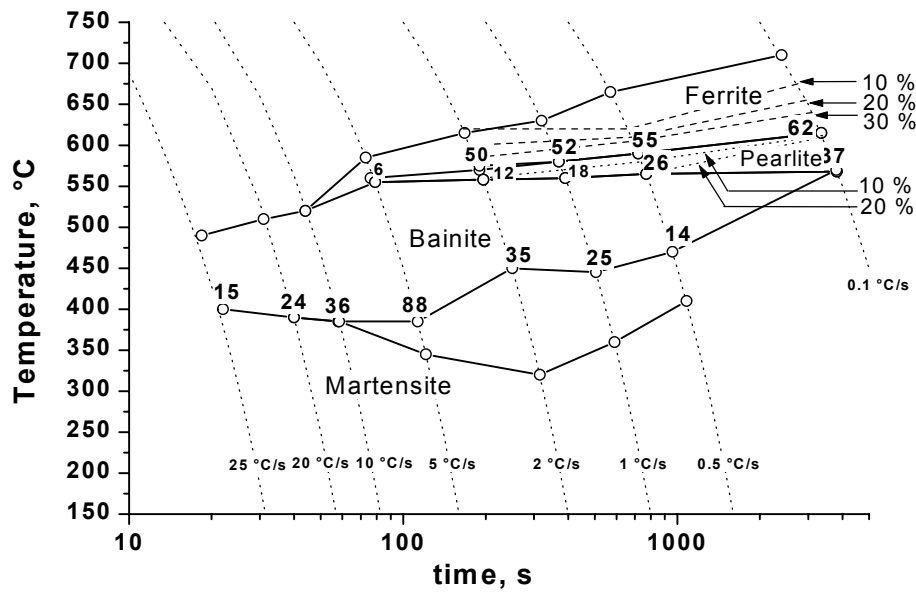
a)
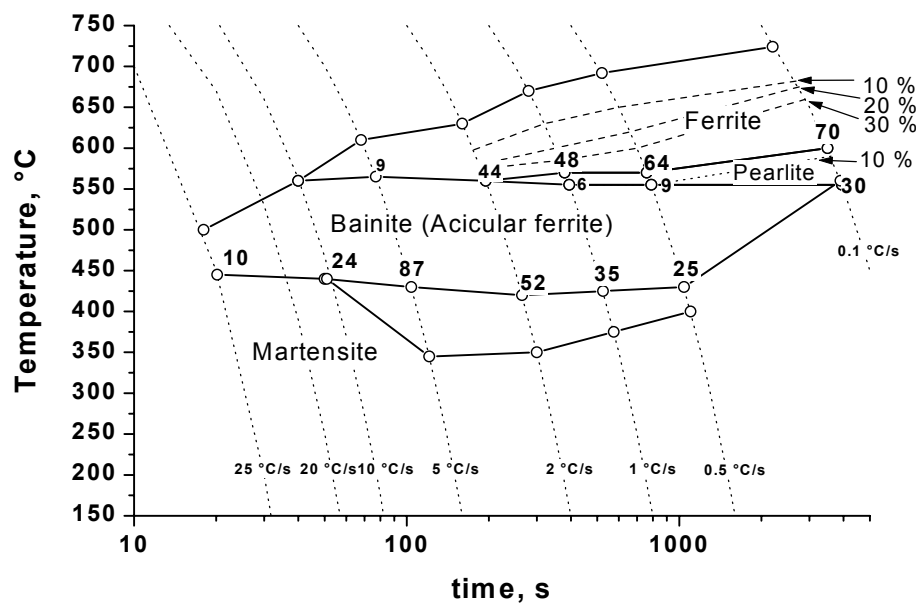
b)

Figure V.10: Continuous Cooling Transformation (CCT) diagrams for a) CMn steel and b) CMnB steel.

V.3.3 Continuous heating

As boron segregates to grain boundaries, it is likely that the partitioning of Mn during the austenite decomposition is affected in the CMnB steel. Samples of CMn and CMnB steels were continuously cooled in the dilatometer at different rates to produce different microstructures, *i.e.* ferrite, bainite and martensite, to check this assumption. The samples were then reheated at the rate 60 °C/min to 1200 °C, and the transformation temperatures Ac_1 and Ac_3 were measured. It can be seen in Figure V.11a, that the microstructure had very little

influence on Ac_1 and Ac_3 in the CMn steel. In the CMnB steel, the initial microstructure had a strong effect on Ac_1. Indeed, increasing the cooling rate produced microstructures that were reaustenitized at lower temperatures when reheated. In particular, the Ac_1 temperature for the bainitic sample was 70 °C lower than the Ac_1 temperature for the ferritic sample. However, martensite transformed to austenite at the same Ac_1 temperature of 720 °C than the as-cast microstructure.
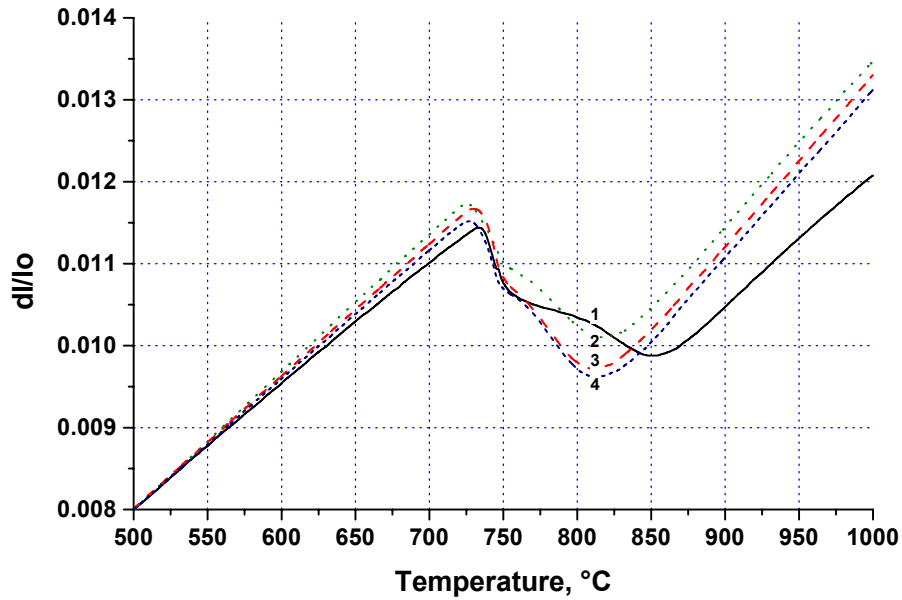
a)
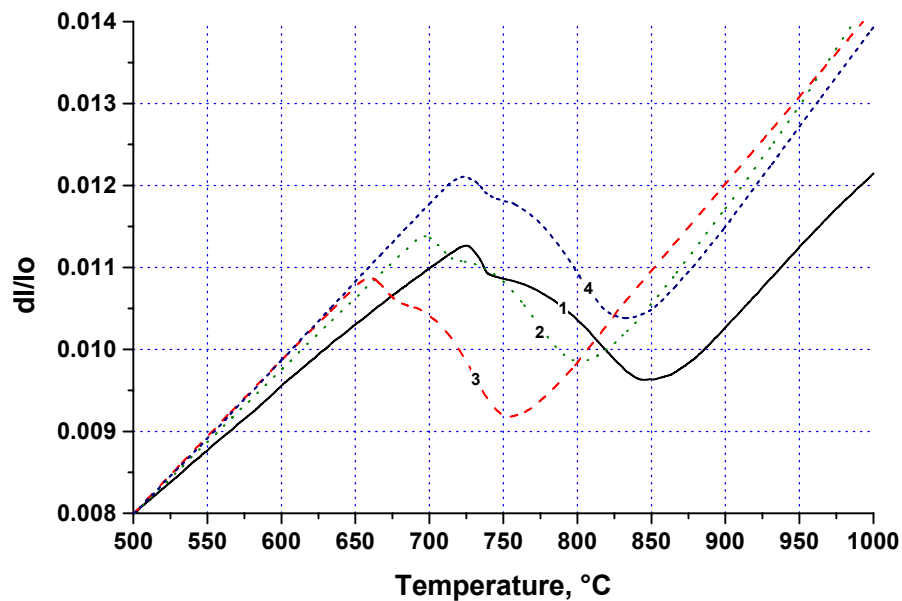
b)

Figure V.11: Heating curves for a) CMn steel and b) CMnB steel with different starting microstructures. 1: As-cast (Fe-P); 2: After cooling 6 °C/min (Fe-P); 3: Bainite; 4: Martensite.

In the Fe-C system, C has no effect on Ae_1. In Fe-Mn-C alloys, Mn decreases the Ae_1 temperature.

According to Andrews:[28]

$$Ae_1(°C) = 727 - 10.7Mn - 16.9Ni + 29.1Si + 16.9Cr + 6.38W + 290As \qquad (V.15)$$

Plot with x-axis "Mn, wt%" ranging 0.4 to 1.7 and y-axis "Ac_1, °C" ranging 720 to 750. Data points at (0.45, 745), (0.75, 740), (1.0, 736), (1.65, 725). Annotation: $Ac_1 = 752.4 - 16.6\ Mn$.
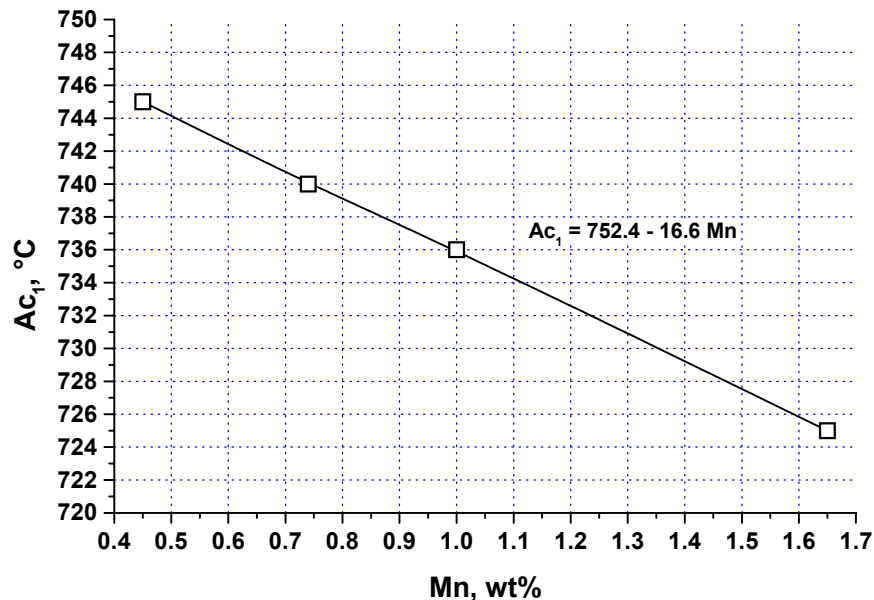
Figure V.12: Linear relation between Ac_1 and Mn content in CMn steels containing 0.1-0.2 wt.% C.

Using the value Ac_1 = 725 °C measured in the CMn steel and other values for Ac_1 measured in similar steels with lower Mn content[29], the following linear relation between the Mn content and Ac_1 plotted Figure V.12 was obtained:

$$Ac_1(°C) = 752.4 - 16.6Mn \qquad (V.16)$$

If Mn is assumed responsible for the decrease of Ac_1 in the CMnB sample containing bainite, some regions of the microstructure should contain more than 6 wt.% Mn according to the extrapolation of the equation (V.16). SEM observation of the microstructure in the sample cooled at 300 °C/min showed the presence of the Martensite/Austenite (M/A) constituent. At the interface between these M/A constituents and bainite, up to 5 wt.% Mn was measured by Energy Dispersive X Ray Spectrometry (EDS) as shown Figure V.13. The Mn-rich M/A constituents acted as nucleation sites for the austenite formation and transformed first to austenite during the reheating of the sample. Ac_1 was thus decreased. In the martensitic sample, the martensite had the original austenite content. Hence, Ac_1 was not lowered in that case. Finally, it is known that Mn partitions preferentially to cementite in the pro-eutectoïd ferrite-pearlite mixture.[30] In the CMn steel, this partitioning certainly occured but the Ac_1 temperature was not lower. It is very likely that in the CMnB sample cooled slowly to room temperature, small amounts of martensite or austenite with a high Mn content were present.

These can act as nucleation sites for the austenite formation during heating, thereby decreasing Ac_1.
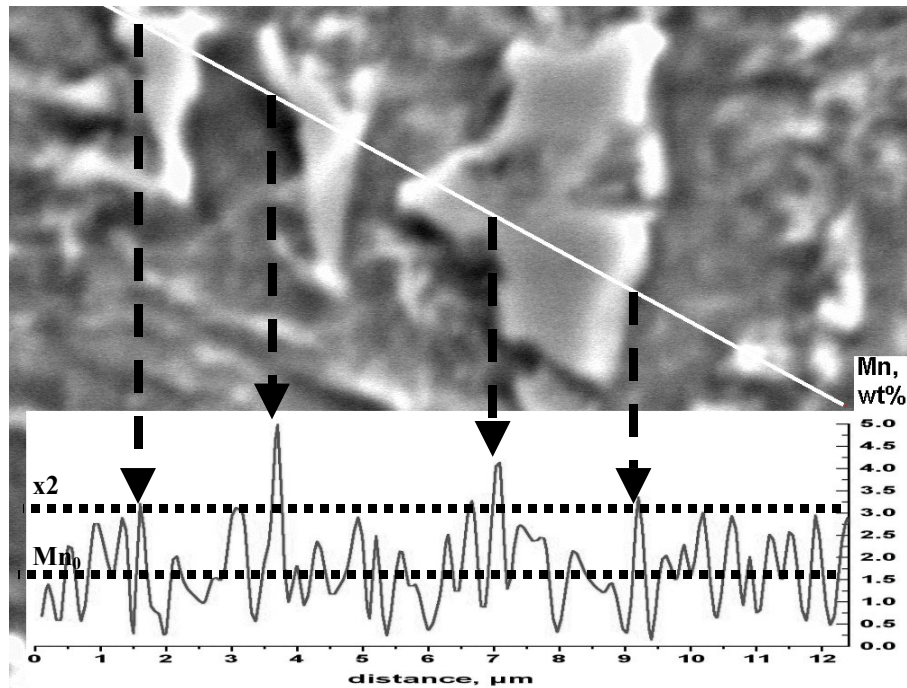
Figure V.13: SEM image and EDS scan showing the Mn partitioning in the CMnB steel cooled at 300 °C/min.

V.4 Conclusions

The effects of soluble boron on the austenite decomposition during isothermal holding and during continuous cooling have been investigated by means of dilatometry. The kinetics of ferrite formation during an isothermal holding and a continuous cooling was clearly slowed down by the boron addition. It was observed that no grain boundary nucleation of ferrite occurred in the boron bearing steel. The carbide precipitation was also found to be retarded in the steel containing boron. The kinetics of bainite formation was not influenced by boron additions. The segregation of boron to γ-grain boundaries effectively suppressed the grain boundary nucleation of the ferrite. Ferrite and bainite likely nucleated from TiN precipitates inside the austenite grains. As a result, the microstructures obtained after any heat treatment were morphologically different than the microstructure of the boron free reference steel. Indeed, in the CMnB steel, the formation of the primary ferrite was suppressed, and the upper bainite was acicular ferrite. The interaction between Mn and boron resulted in the enrichment of the austenite in Mn. As a result, after cooling at cooling rates between 6 °C/min and 840 °C/min, the Mn-rich residual austenite zones acted as nucleation sites for the reverse α→γ transformation and resulted in the decrease of the Ac_1 temperature in the CMnB steel. The present study showed that, the combination of soluble boron with small amounts of substitutional alloying elements may lead to mixed microstructures with large compositional differences, in particular due to the solute drag effect and the stabilization of the austenite. This may imply new potentials in terms of mechanical properties.

[1] D.T.Llewellyn: <u>Ironmaking and Steelmaking</u> Vol 20, No.5, 1993, p.338.

[2] Y.Ohmori and K.Yamana: <u>Boron in Steel</u> ,18 september 1979, p.44.

[3] B.J.Thomas, G.Henry: <u>Boron in Steel</u> ,18 september 1979, p.80.

[4] Ph.Maitrepierre, J.Rofes-Vernis and D.Thivellier: <u>Boron in Steel</u> ,18 september 1979, p.1.

[5] Y. Shen and K.A. Taylor: <u>40th MWSP Conf. Proc., ISS</u>, 1998, p.837.

[6] G. Kurdjumov and G. Sachs: <u>Z. Phys.</u>, 64, 1930, p.325.

[7] Ph. Maitrepierre, D. Thivellier and R. Tricot: <u>Metallurgical Transactions A</u>, Vol. 6A, February 1975, p.287.

[8] J.E.Morral and T.B.Cameron: <u>Boron in Steel</u> ,18 september 1979, p.19.

[9] Y. Shen and S.S. Hansen: <u>Metallurgical and Materials Transactions A</u>, Volume 28A, October 1997, p.2027.

[10] H.K.D.H. Badeshia: Bainite in Steels, second edition, IOM communications Ltd, 2001, p.176.

[11] F.B. Pickering, Transformation and Hardenability in Steels Symposium, February 1967, Michigan, Climax Molybdenum, p.109.

[12] C.Mesplont, T.Waterschoot, S.Vandeputte, D.Vanderschueren, B.C. De Cooman: Thermomechanical Processing of Steels Conference, London, May 2000, p.495.

[13] S. Yoshida and J. Ågren: Proceedings of the Thermomechanical Processing of Steels conf. London, May 2000, p.275.

[14] J.Z. Zhao, C. Mesplont, B.C. De Cooman: <u>Z. Metallkd</u>. 92, 2001, 4, p.345.

[15] J.Z. Zhao, C. Mesplont, B.C. De Cooman: <u>ISIJ </u>vol.41, 2001, N°5, p.492.

[16] J.Z. Zhao, C. Mesplont, B.C. De Cooman: <u>Materials Science and Engineering</u> A332, 2002, p.110.

[17] C.Mesplont, J.Z. Zhao, S. Vandeputte, B.C. De Cooman: <u>Steel Research</u> 72, 2001, 7, p.263.

[18] M.V. Li, D.V. Niebuhr, L.L. Meekisho, D.G. Atteridge: <u>Metallurgical and Materials Transactions B</u>, Vol. 29B, June 1998, p.661.

[19] J. Burke: The Kinetics of Phase Transformation in Metals, Pergamon Press, Elmsford, NY, 1965.

[20] J.W. Christian: The Theory of Transformations in Metals and Alloys, Second Edition, Pergamon Press, 1975, p.542.

[21] D. Quidort: Ph.D. report, december 1999, p.129.

[22] L. Kaufman, S.V. Radcliffe and M. Cohen: Decomposition of Austenite by Diffusional Processes, Interscience, NY, 1962, p.313.

[23] W. Steven, A.G. Haynes: <u>J. of the Iron and Steel Institute</u>, 1956, vol. 183, p.349.

[24] F.S. LePera: <u>J. Metals</u> 32, N°3, 1980, p.38.

[25] E.J. Mittemeijer, L. Cheng, P.J. Van der Schaaf, C.M. Brakman, B.M. Korevaar: <u>Metal. Trans.</u> 19A, 1988, p.925.

[26] D.A. Porter, K.E. Easterling: Phase Transformations in Metals and Alloys, Second Edition, Stanley Thornes (Publishers), 2000, p.322.

[27] H.K.D.H. Bhadeshia: Bainite in Steels, Second Edition, IOM Communications (Eds), 2001, p.237.

[28] K.W. Andrews: <u>JISI</u>, Vol. 203, 1965, p.721.

[29] M. Thompson, M. Ferry, P.A. Manohar: <u>ISIJ International</u>, Vol. 41, 2001, No.8, p.891.

[30] N.A. Razik, G.W. Lorimer, N. Ridley: <u>Acta Metallurgica</u>, Vol.22, October 1974, pp.1249.

CHAPTER VI

Effects of combinations of Mo, Cr and B on phase transformations during continuous cooling

VI.1 Introduction

Alloying elements are added to steels in order to achieve high levels of strength and elongation. It was shown in chapter I, that alloying elements added in proper quantity influenced the phase transformations kinetics. It was thus possible to control the microstructure. Mo and Cr are often used to increase the steel hardenability. The effects of Cr and Mo on phase transformations have been studied in Fe-C alloys. Cr and Mo are α-stabilizers. They raise the $\gamma \rightarrow \alpha$ transformation temperature and are soluble in cementite. Their diffusivity in γ limits the growth of pearlite. After the pearlite formation, Cr and Mo can partition between the α and the cementite. The type and composition of the carbides obtained is therefore affected, as Cr may replace up to 20 % and Mo up to 4 % of the Fe atoms in Fe_3C. During the decomposition of the austenite in CMn steels, both the alloying elements and the carbon must be redistributed or "partition" between the different phases. Cr and Mo usually form alloy carbides while Mn is soluble in cementite.

The growth of ferrite is in general slower in Fe-C-X alloys than in binary Fe-C alloys. This is partly because alloying elements affect the thermodynamic stability of the γ relative to the α.

When partitioning of the alloying element between α and γ is required for the growth of ferrite, the ferrite growth rate is determined by the diffusion of the alloying element in γ. Mn has a tendency to partition to the γ phase while Mo and Cr do not partition. The known effects of Mo and Cr on the phase transformations in Fe-C alloys are summarized below.

VI.1.1 Effects of Mo

In steels, Mo is found both in solid solution and in carbides. The molybdenum content in proeutectoid ferrite is the same than in prior austenite. In carbide, Mo can be dissolved in orthorhombic iron carbide (Fe_3C-cementite), or it can enter into a iron-molybdenum carbide, fcc (($Fe,Mo)_{23}C_6$-kappa).[1]

It has been reported that in a 0.4 wt.% C steel, after transformation between 510 and 675 °C, the ferrite constituent appeared almost totally at grain boundaries. While adding as low as 0.2 wt.% Mo, the pearlite formation was highly retarded, so that the volume fraction of ferrite formed increased considerably. Ferrite formed both at prior austenite grain boundaries and inside these grains. This effect increased with the molybdenum content up to 0.75 wt.% at least. Molybdenum was also found to increase the acicular character of ferrite.[1]

The ferrite lattice parameter was reported to be affected by the Mo content as follows:

$$1000 Mo = 0.03624((a_\alpha - 2.86) \times 10^5)^2 - 2.691(a_\alpha - 2.86) \times 10^5 + 26.11 \qquad \text{(VI.1)}$$

where the Mo content is in wt.% and a_α is the ferrite lattice parameter in Angstrom units.[2]

A detailed study of the effects of Mo on the kinetics of phase transformations above the B_s temperature showed that the ferrite phase morphology was predominantly grain boundary allotriomorph. Mo_2C carbides were found in ferrite in both a fibrous and an interphase boundary form. Their growth kinetics was found to be controlled by volume diffusion of carbon in austenite. A strong Solute Drag Like Effect (SDLE) was produced by the segregation of Mo to austenite-ferrite boundaries. Despite the fact that no transformation stasis (incomplete transformation) was observed in any of the 19 studied alloys, growth stasis (slow down of the ferrite growth rate) occurred just above B_s in alloys with higher C and Mo concentrations.[3]

While Mo accelerates ferrite nucleation in Fe-C binary alloys at high transformation temperatures, it was shown to reduce the nucleation rate as the transformation temperature decreased toward B_s, due to its segregation to austenite grain boundaries.[4]

The study of the bainitic phase transformation in Fe-C-Mo alloys showed that the SDLE due to Mo segregation to the austenite-ferrite boundaries varied in magnitude with the C and Mo contents. Transformation stasis occurred when the sympathetic nucleation of carbide-free ferrite ceased due to carbon enrichment of the remaining austenite.[5]

VI.1.2 Effects of Cr

It was reported that during the transformation of austenite to pearlite in a eutectoid steel containing 1.29 wt.% Cr, the Cr partitioned preferentially to the cementite phase at the interface above the no-partition temperature, T_p, which was measured as 703 °C. Cr continued to segregate to cementite behind the austenite-pearlite interface, at all transformation temperatures, while pearlite formation was still occurring, and after it was complete. Cr additions to eutectoid steel decreased the growth rate of pearlite. Calculations assuming C volume diffusion control suggested that interfacial C diffusion may also be involved in pearlite growth.[6]

Transformation stasis was observed during the study of the austenite decomposition kinetics in a hypo eutectoid Fe-C-Cr alloy containing 3 wt.% Cr. As in Fe-C-Mo alloys, this effect was due to the SDLE, based upon the gradual sweeping up of a non-equilibrium concentration of Cr which markedly decreased the activity of C in austenite at the mobile areas of advancing α-γ boundaries. However, the smaller size difference between Cr and Fe than between Mo and Fe was very likely the reason for the less pronounced SDLE in the Fe-C-Cr system.[7]

VI.1.3 Effects of Mo and Cr in presence of soluble B

From Reynolds *et al.*[8], individual alloying elements may selectively alter ferrite growth or carbide precipitation and lead to synergetic effects when added in the proper combinations. However, combinations of two carbide formers such as Cr and Mo can discourage transformation stasis if carbides form too quickly.

In chapter V, it was shown that soluble B was very effective in suppressing ferrite formation and carbide precipitation by segregating to austenite grain boundaries. It is thus very likely that the strong effect of soluble B in combination with Cr and Mo enhances the SDLE, which would lead to transformation stasis in low C steels with low Mo and Cr contents.

It has been reported that B could affect the growth rate of pro-eutectoid ferrite essentially through synergetic effects with Mo and Nb.[9]

Moreover, a very effective mean of isolating the bainite reaction in low carbon steels has been found by adding about 0.002 wt.% solute boron to a 0.5 wt.% Mo steel.[10] While the molybdenum steel encouraged the bainite reaction, the boron markedly retarded the ferrite reaction, by preferential segregation to the prior austenite boundaries. This permitted the bainite reaction to occur at shorter times. At the same time, the bainite C-shaped curve was hardly affected by the boron addition, so that martensite formation was not enhanced. Consequently, by the use of a range of cooling rates, fully bainitic steels could be obtained.[11]

This chapter studies the influence of Cr and Mo in the presence of soluble B on the austenite decomposition during continuous cooling. Experimental CCT diagrams were obtained using the method described in chapter III. Extraction replica obtained from dilatometer samples allowed the identification of the carbides formed during the cooling at different rates. Dictra simulations were performed in order to clarify the different nucleation and growth mechanisms and predict the local partitioning of alloying elements during the austenite decomposition.

VI.2   Experimental procedure

The compositions of the steels used for the present study are given in Table VI.1. In all steels, less than 50 ppm N was present. In the boron bearing steels, the Ti/N ratio higher than 5 prevents the BN precipitation completely.

**Table VI.1:** Chemical compositions of the studied steels, in ppm.

	C (%)	Mn (%)	Cr (%)	Mo (%)	B (ppm)	Ti (ppm)	N (ppm)
9. CMn	0.19	1.64	0.023	-	-	-	40
10.CMnB	0.14	1.72	0.026	-	35	285	50
11.CrB	0.17	1.66	0.48	-	24	190	36
12.MoB	0.17	1.62	0.06	0.21	25	177	30
13.CrMoB	0.17	1.63	0.47	0.19	22	179	40

The decomposition of austenite was studied by means of dilatometry during continuous cooling, using the reheating procedure described in chapter II. The cooling rates were varied between 6 and 840 °C/min during the continuous cooling experiments. Samples were prepared for microstructure evaluation after each thermal cycle. The different phases were observed by light optical microscopy (LOM) and scanning electron microscopy (SEM) after etching with nital. A JEOL 2010 Transmission Electron Microscope (TEM) with an acceleration voltage of 200 kV, equipped with an energy dispersive X-ray spectrometer (EDX) was used for the detection and analysis of precipitates using extraction replicas.

VI.3   Experimental results

VI.3.1 CCT diagrams

The kinetics of austenite decomposition was studied by means of dilatometry during continuous cooling. A model accounting for the carbon partitioning effects was developed in chapter III to estimate the volume fractions of the phases formed during either the isothermal holding or the continuous cooling of a hypo-eutectoid steel from the austenitic region.[12,13,14] This model was shown to be applicable to low carbon CMn steels in chapter IV.[15] Detailed CCT diagrams were obtained by combining dilatometry and microstructure observations by optical microscopy. The CCT diagrams for the CMn steels containing Cr + B, Mo + B, and Cr + Mo + B respectively are plotted in Figure VI.1. The temperatures Ar_3 and Ar_1, measured at CR = 6 °C/min, as well as B_s measured at CR = 120 °C/min and M_s measured at the highest CR, *i.e.* 1200 °C/min, are reported in Table VI.2.
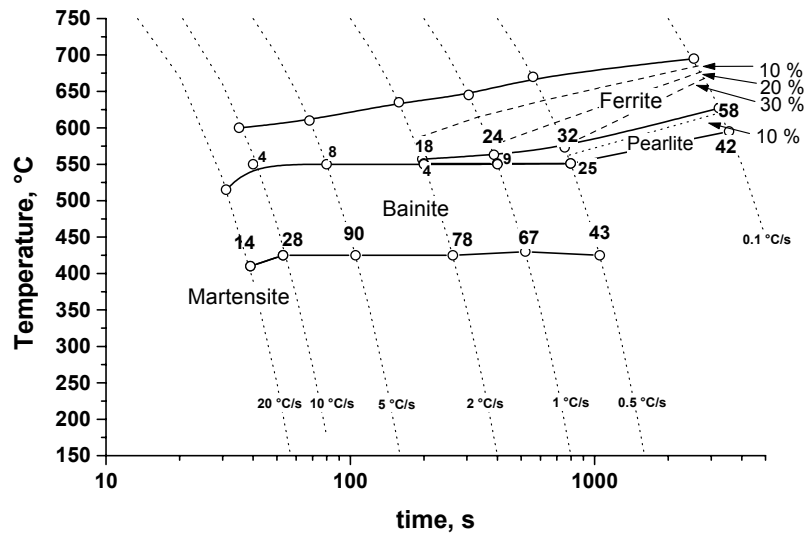
a)
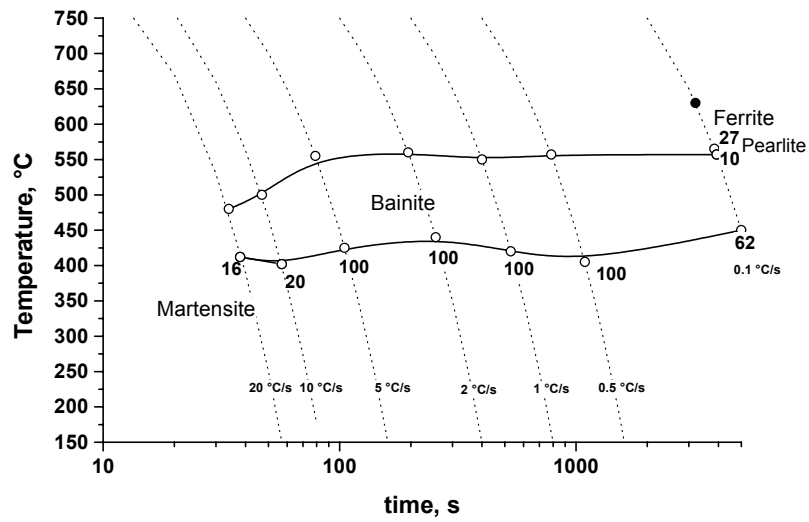
b)
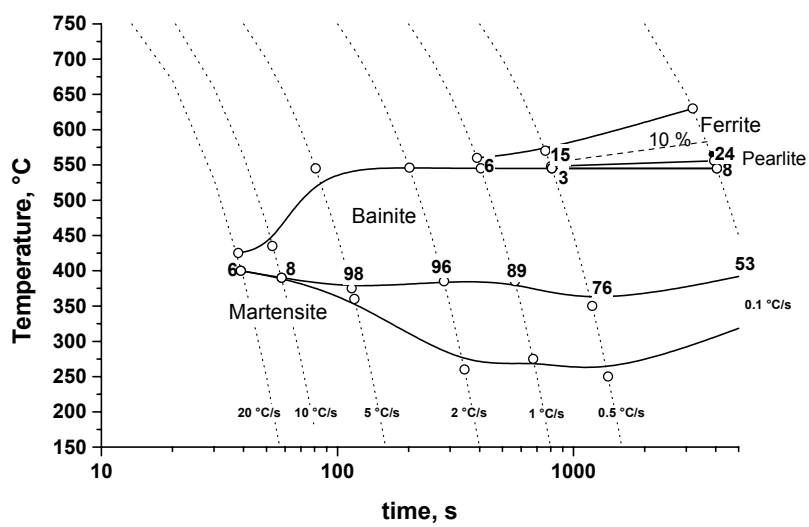
c)

Figure VI.1: Experimental CCT diagrams obtained for the a) CMnCrB, b) CMnMoB and c) CMnCrMoB steel compositions, respectively.

Table VI.2: Measured transformation temperatures in °C. The CR are indicated into brackets.

Steel	Ar$_3$ (6 °C/min)	Ar$_1$ (6 °C/min)	B$_s$ (120 °C/min)	M$_s$ (> 1200 °C/min)
CMn	710	615	560	400
CMnB	724	600	560	440
CrB	695	627	550	410
MoB	630	565	560	412
CrMoB	630	556	545	400

In the steel alloyed with Cr and B, the ferrite formation was retarded, while the pearlite formation was enhanced, compared to the CCT diagram of the CMnB steel shown in chapter V, Figure V.10. In the same cooling conditions, less ferrite was formed in the CrB alloyed steel, as Cr caused carbides to precipitate earlier. At the cooling rate 6 °C/min, Ar$_3$ was decreased from 724 °C in the CMnB steel to 695 °C in the CrB steel. However, the pearlite started earlier, at 627 °C, in the CrB steel than in the CMnB steel where it formed at 600 °C. The bainite start temperature, B$_s$, was 550 °C in the CrB steel, which was 10 °C lower than in the steels without Cr.

The effect of 0.2 wt.% Mo combined with soluble B was more pronounced, as both the ferrite and pearlite formation were suppressed for cooling rates > 6 °C/min. The present steel was fully bainitic after cooling in a wide range of cooling rates. The B$_s$ temperature was 560 °C, *i.e.* it was not affected by the presence of Mo.

In the steel containing Cr, Mo and B, Ar$_3$ and Ar$_1$ were strongly decreased to 630 °C and 556 °C, respectively, at the cooling rate 6 °C/min. However, while in the MoB steel no proeutectoid ferrite was found before the bainite transformation at cooling rates < 6 °C/min, some ferrite was formed at cooling rates up to 60 °C/min in the steel alloyed with Cr and Mo. The B$_s$ temperature was measured to be 545 °C. Finally, it was observed that the bainitic transformation was not complete during continuous cooling, *i.e.* transformation stasis did occur. From these results it was clear that transformation stasis could be observed in steel containing low Cr and low Mo contents, probably because their synergistic effect was enhanced by the presence of soluble B.

The non-isothermal transformation kinetics were studied by means of the method discussed in chapter V. For each steel composition, the activation energies for the formation of ferrite and bainite were determined from the slopes of the straight lines obtained by plotting *ln(T^2$_f$/Φ) vs. 1/T$_f$*.[16] In the Cr containing steels, the ferritic and bainitic transformations were distinct enough to determine the activation energies for ferrite and bainite formation. New analyses were done on the cooling curves of the CMn and CMnB steels. The results of calculations are reported in the Table VI.3.

Table VI.3: Activation energies calculated for ferrite and bainite formation during continuous cooling.

Steel	Microconstituent	Activation energy, kJ/mol
CMn	Ferrite	533
CMn	Bainite	172
CMnB	Ferrite	533
CMnB	Bainite	163
CrB	Ferrite	517
CrB	Bainite	186
MoB	Bainite	187
CrMoB	Ferrite	576
CrMoB	Bainite	162

It can be seen that the activation energies for bainite increased in the steels alloyed with Cr + B and Mo + B, due to the possible accumulation of substitutional solute at the interphase boundary. However, the lower activation energy calculated for the CrMoB steel was close to 150 kJ/mol. This implies that the carbon diffusion was the rate controlling process. According to the Table VI.3, the presence of Cr decreased the activation energy of ferrite formation, while the addition of Cr and Mo resulted in an increased activation energy.

VI.3.2 Microstructures

Figure VI.2 to VI.4 show the microstructures of the steels alloyed with Cr + B, Mo + B and Cr + Mo + B, respectively, obtained for various cooling rates. As in the case of the CMnB steel, the microstructures of which were presented in chapter V Figure V.9, it appears that ferrite nucleated from the interior of prior austenite grains rather than from austenite grain boundaries, meaning that the prior segregation of soluble B to γ grain boundaries was still effective.

At low cooling rates (< 30 °C/min), the primary ferrite grew under the form of polygonal ferrite in the CrB steel, while in steels alloyed with Mo, it grew with a more pronounced acicular morphology. Moreover, carbides precipitated clearly between ferrite grains in the CrB steel, while in Mo containing steels, carbide precipitation clearly occurred also inside ferrite grains.

At higher cooling rates (> 30 °C/min), acicular ferrite was formed in all studied steels. It nucleated on precipitates, very likely TiN, inside prior austenite grains rather than from grain boundaries. Prior austenite grains can even be observed on microstructures of Figure VI.2 to VI.4, d) to f).

Figure VI.3d shows that the MoB steel cooled at 120 °C/min was fully bainitic. In the CrMoB steel cooled at the same CR, the microstructure was a mixture of bainite and martensite, both phases being well separated, as can be seen in Figure VI.4d. This shows clearly that transformation stasis occurred in that steel. At the cooling rate 840 °C/min, all steels were mainly martensitic. Some large precipitates, likely TiN, could be clearly seen by optical microscopy at the prior austenite grain boundaries and inside those grains.

Figure VI.2: Microstructure of the CrB steel a) as-cast and after cooling at b) 6 °C/min, c) 30 °C/min, d) 120 °C/min, e) 300 °C/min and f) 840 °C/min.
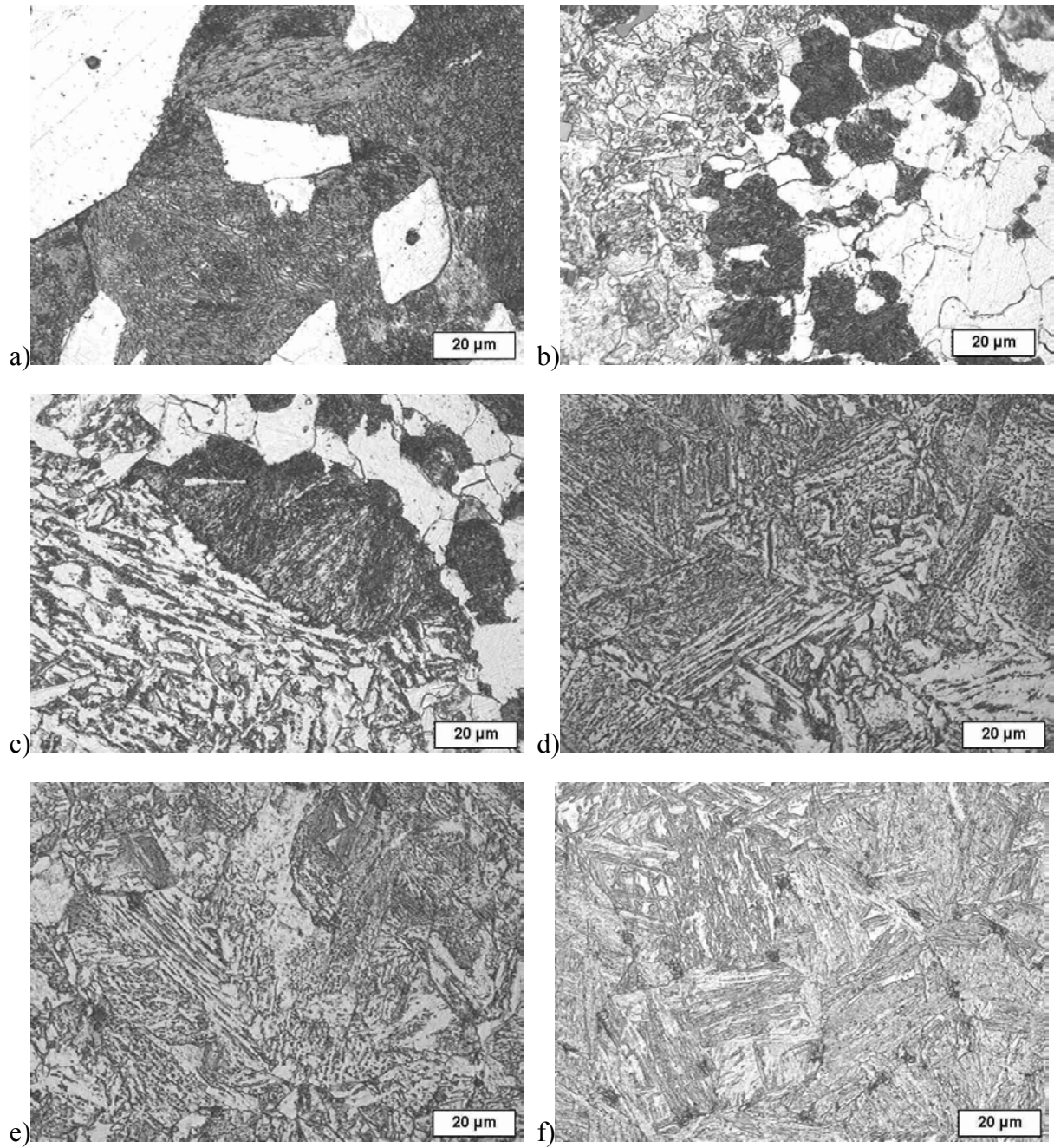
Figure VI.3: Microstructure of the MoB steel a) as-cast and after cooling at b) 6 °C/min, c) 30 °C/min, d) 120 °C/min, e) 300 °C/min and f) 840 °C/min.

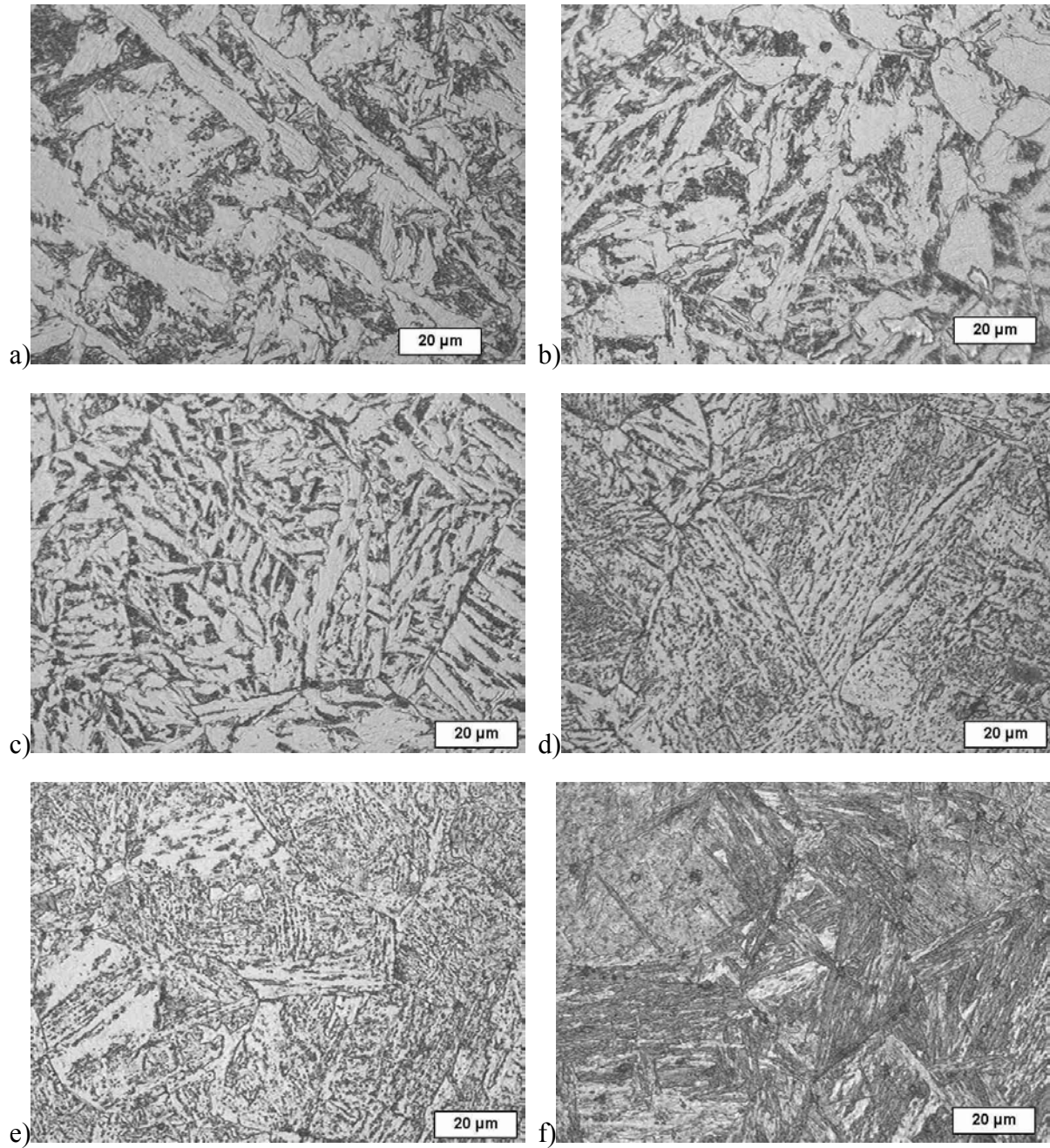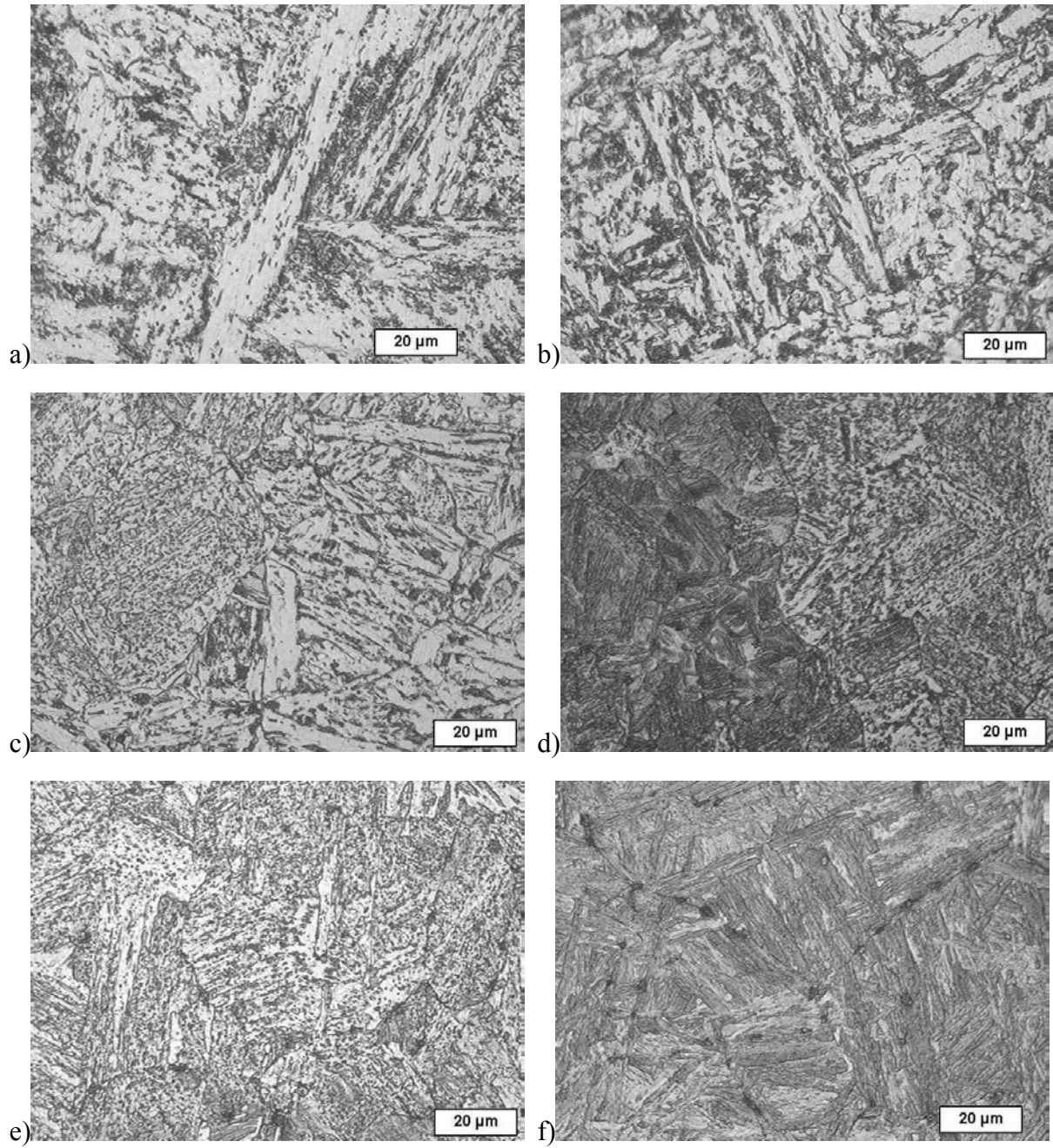**Figure VI.4:** Microstructure of the CrMoB steel a) as-cast and after cooling at b) 6 °C/min, c) 30 °C/min, d) 120 °C/min, e) 300 °C/min and f) 840 °C/min.

VI.3.3 Extraction replica

Extraction replica were prepared from dilatometer samples of the steels containing Cr and/or Mo, cooled at CR = 6 °C/min and 300 °C/min. The detection and analysis of precipitates was done by means of EDX.

The CrB steel, cooled at CR = 6 °C/min contained many Fe-C-Cr-Mn rich precipitates, which had a needle-like structure in Figure VI.5a. They were similar to the ribbon-type carbides found previously in a Fe-0.13C-2.99Cr steel.[7] TiCN, TiN and TiC were also found. In some parts of TiCN Cr was also detected. CuMnS precipitates were present sporadically.

The MoB steel cooled at CR = 6 °C/min contained many Fe, C, O, Cu, Si, Mn rich precipitates, varying strongly in dimensions (Figure VI.5c). TiCN and TiN were also found. Mo was detected in some of those precipitates. CuS was found sporadically.

TiCN and TiN precipitates formed the main precipitates in the CrMoB steel cooled at CR = 6 °C/min. As can be seen in Figure VI.5e, their diameter was between 20 and 100 nm. Small TiC precipitates were detected. In TiCN, TiN and TiC, Mo was incorporated. Mo-C rich areas were also observed. These were very likely Mo_2C. CuMnS was present sporadically.

It can be seen in Figure VI.5b, that in the CrB steel cooled at CR = 300 °C/min, precipitates rich in Fe, C, O, Cr and Mn were found, varying in size and having different shapes. TiC precipitates were detected, rounded and oval shapes, with diameter < 20 nm. TiN precipitates were also clearly found with diameter between 50 and 200 nm.

In the MoB steel cooled at CR = 300 °C/min, many TiCN, TiC and TiN precipitates were found. In most precipitates Mo was present. CuMnS precipitates were also detected.

Finally, in the CrMoB steel cooled at CR = 300 °C/min, TiCN and TiN represented the main fraction of the precipitates. Their size-order varied between 20 and 150 nm. Small TiC precipitates were found. In TiCN, TiN and TiC precipitates Mo was present, however in low concentrations. Cu, O, Si, Cl, Cr and Mo rich areas were detected. MnS and CuMnS were sporadically remarked.

From these results it was clear that Cr influenced the shape of precipitates but not their composition, while Mo was soluble in the precipitates. The presence of large amounts of titanium nitrides and carbides in all samples confirmed that the precipitation of BN was effectively suppressed.
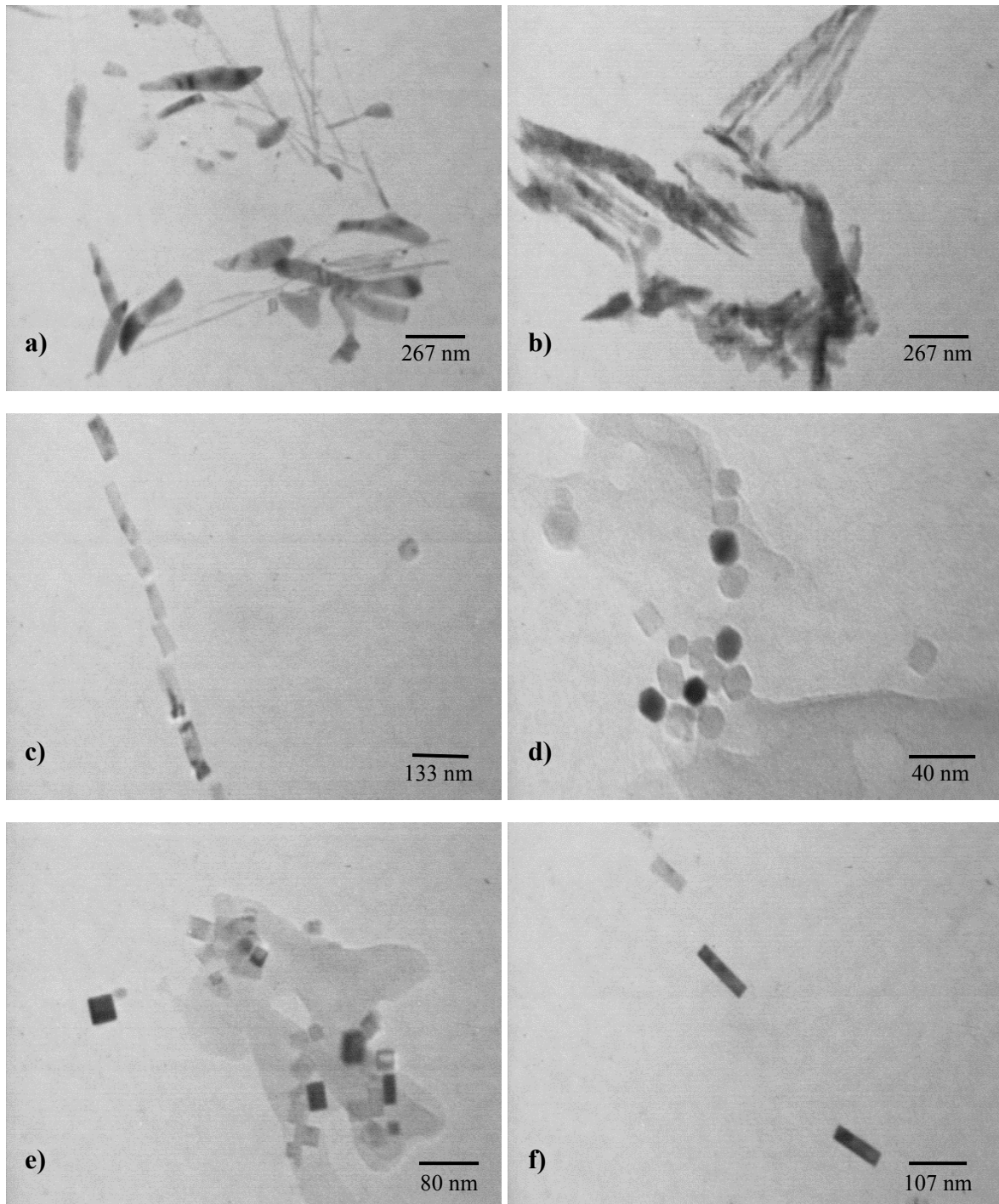
Figure VI.5: Extraction replica of CMn steels alloyed with Cr + B, Mo + B, Cr + Mo + B (from top to bottom), cooled at CR = 6 °C/min (left) and 300 °C/min (right).

VI.3.4 Effects of Cr, Mo and B on Ac₁

Samples of CrB, MoB and CrMoB steels were continuously cooled in the dilatometer at different rates and different microstructures were produced. The samples were then reheated at the rate 60 °C/min to 1200 °C, and the transformation temperatures Ac_1 and Ac_3 were measured. Ac_3 was not affected by the initial microstructure. It was shown in chapter V, that in the CMnB steel the Ac_1 temperature for the bainitic sample was 70 °C lower than the Ac_1 temperature for the ferritic sample. However, martensite transformed to austenite at the same Ac_1 temperature of 720 °C than the as-cast microstructure. The measured Ac_1 temperatures for the CrB, MoB and CrMoB steels are reported in Figure VI.6 as functions of the preceding cooling rate.
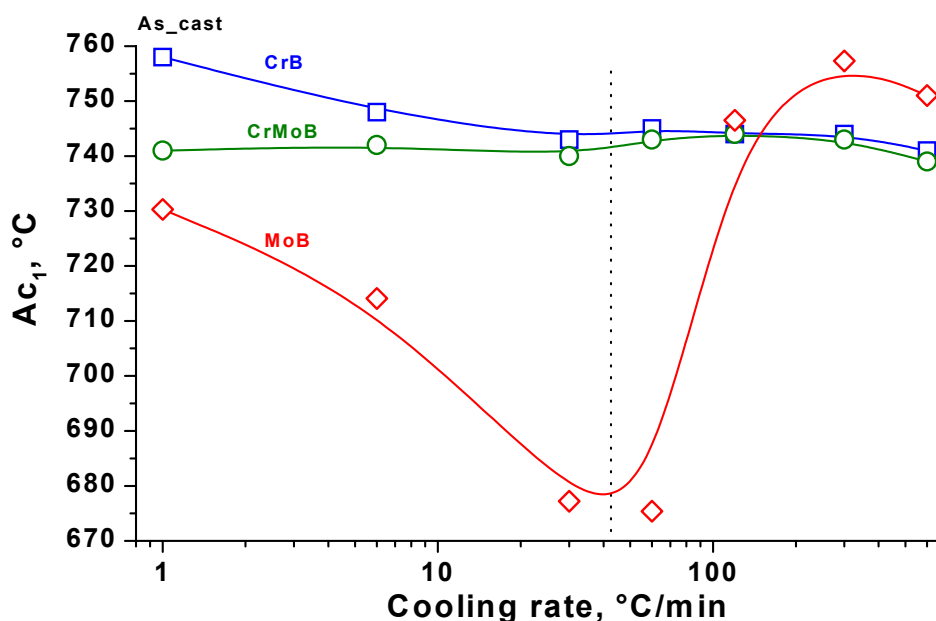

Figure VI.6: Ac_1 temperatures measured after reheating Cr and Mo alloyed steels previously cooled at different CR.

It can be clearly seen that the presence of Cr suppressed the effect observed in the CMnB steel. Cr however increased the mean value of Ac_1, to about 10 °C more than in the CMn steel, which is in accordance with the coefficient affected to Cr in the Ae_1 equation of Andrews:[17]

$$Ae_1(°C) = 727 - 10.7Mn - 16.9Ni + 29.1Si + 16.9Cr + 6.38W + 290As \qquad (VI.2)$$

It is very likely that in the MoB sample cooled at 30 °C/min and 60 °C/min, small amounts of martensite or austenite with a high Mn content were present, due to the retardation of carbides formation thanks to Mo and B segregation to grain boundaries. These can act as nucleation sites for the austenite formation during heating, thereby decreasing Ac_1.

It is likely that the Mn partitioning to austenite is affected by the presence of Cr as Cr provokes carbides precipitation.

VI.3.5 Isothermal bainitic transformation

Though continuous cooling experiments showed the evidence of transformation stasis in the CrMoB steel, extra dilatometer cycles were performed to check whether this phenomenon occurred during isothermal holding. Cycles with isothermal bainitic transformation at 500 °C were performed on the steels alloyed with Cr and/or Mo. The relative length change *vs.* time plot of Figure VI.7 shows clearly that the kinetics of the bainitic transformation was very similar in the MoB and CrB steels, while in the CrMoB steel the reaction was clearly retarded and incomplete. Transformation stasis clearly occurred in the steel alloyed with Cr and Mo, due to a synergism between Cr, Mo and B.
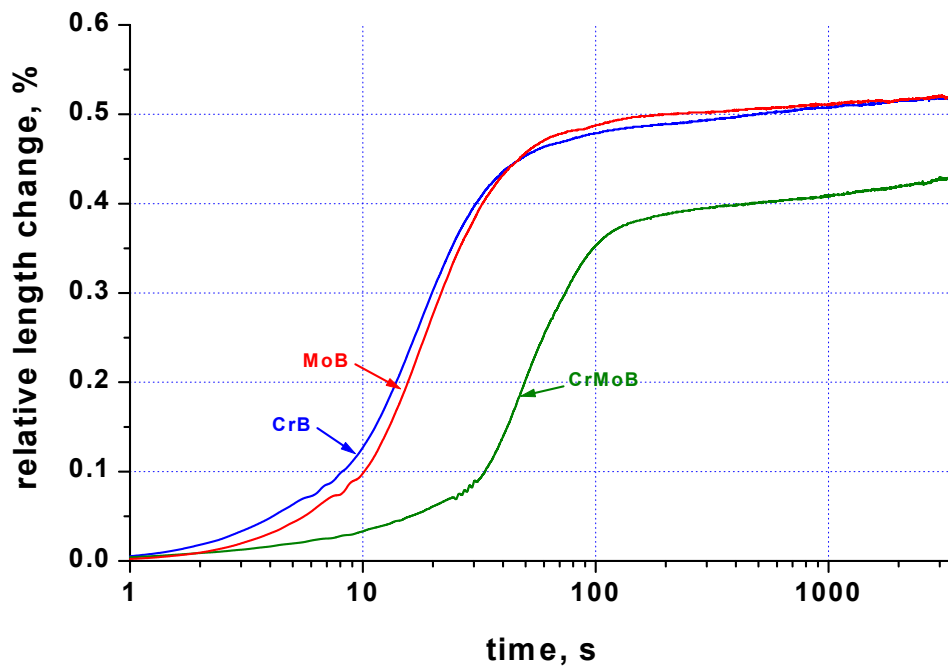

Figure VI.7: Isothermal bainitic transformation at 500 °C of the Cr and/or Mo alloyed steels.

VI.4 Dictra simulations

From the results of continuous cooling experiments, 2 types of nucleation mode have been identified:

- from grain edges in the CMn steel without soluble B;

- from TiN, TiC precipitates or impurities inside the grains in B-bearing steels.

From these nuclei, 2 types of growth mode were possible:

- spherical growth at low cooling rates, for *e.g.* primary ferrite;

- planar growth at high cooling rates for acicular ferrite and bainite.

Those mechanisms are represented schematically in Figure VI.8.
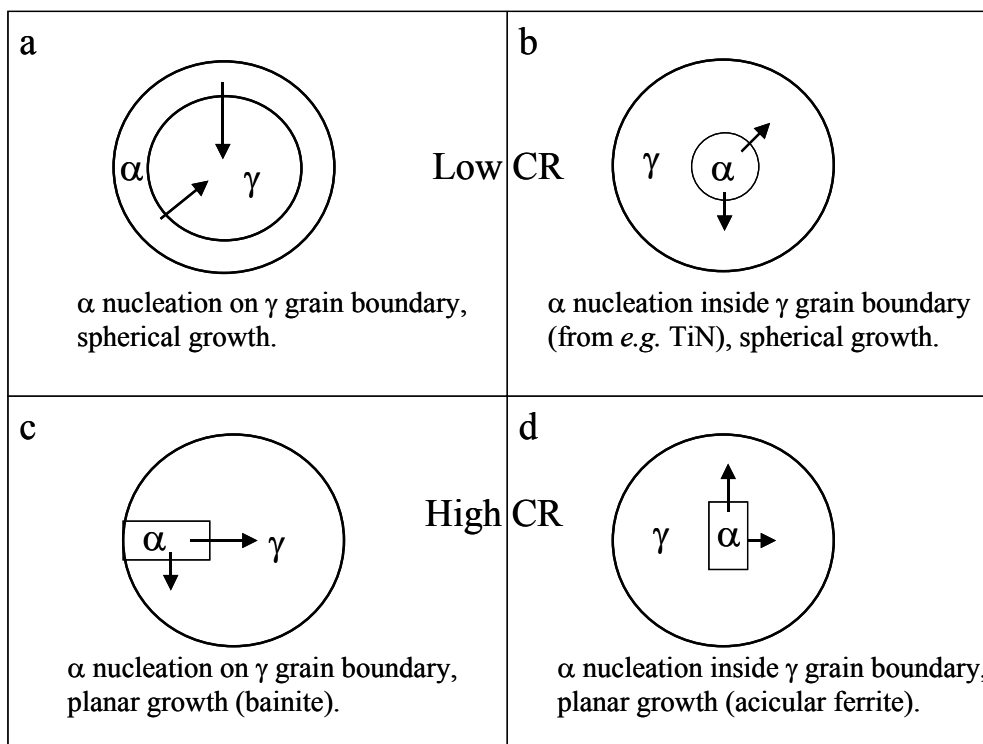
Figure VI.8: Schematic representation of ferrite nucleation and growth from spherical austenite grains.

Dictra simulations were first carried out using the CMn steel composition and a fixed cooling rate 6 °C/min. The ferrite formation in the CMn steel was simulated assuming the nucleation of ferrite on austenite grain boundaries in spherical cells, *i.e.* the case schematically represented in Figure VI.8a. By comparing the results with experimental data the cell size was evaluated to be approximately 40 μm. Simulations were then performed using the same parameters, but with the nucleation and growth modes represented in Figure VI.8b and VI.8d. Evidently, the kinetics of ferrite planar growth was the same independently on the nucleation mode. The results of calculations are shown in Figure VI.9.

Figure VI.9: Dictra simulation of different nucleation and growth modes.

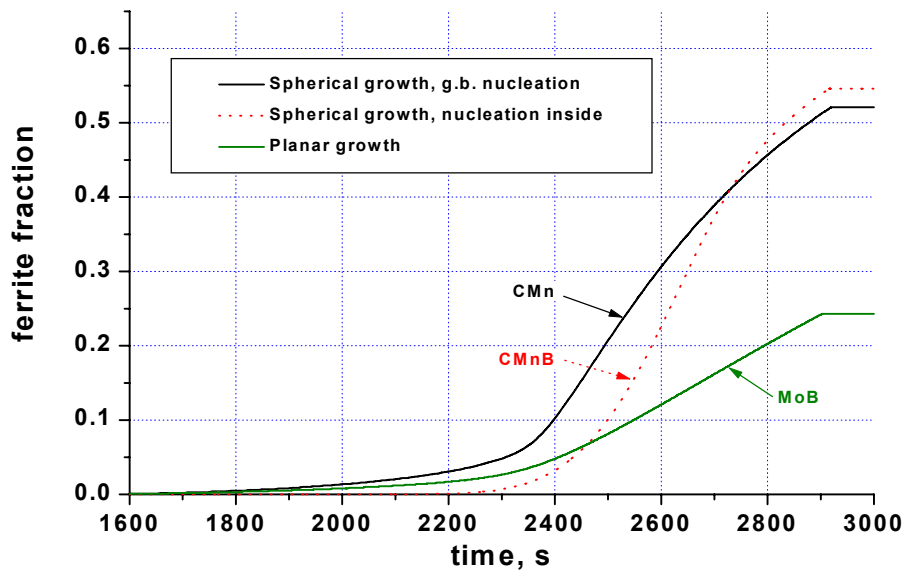Comparing those predictions with experimental results obtained from dilatometry showed that the assumption of nucleation inside the grains to simulate the effect of B was consistent. The planar growth mode described well the acicular ferrite formation in the MoB steel. Moreover, the calculated ferrite fractions corresponded quite well to the fractions of ferrite measured by means of dilatometry, considering that either the initial cell size and the initial C concentration were kept constant for the different calculations and that the model is very simple. More in depth Dictra simulations of the effect of B on the ferrite nucleation were done previously and showed that B lowered the number of active grain corners for nucleation.[18]

The mobilities for C, Mn, Cr and Mo were taken from the mobility database in Dictra. The effect of B was simulated considering nucleation from precipitates inside the grains rather than from grain boundaries.

Depending on the partitioning mode of substitutional elements, different thermodynamic situations, *e.g.* orthoequilibrium and paraequilibrium, may be established at the α−γ interface. In orthoequilibrium, both C and substitutional elements redistribute between ferrite and austenite whereas in paraequilibrium carbon redistributes without any partitioning of substitutional elements. Between those two situations, local equilibrium non-partitioning involves the carbon redistribution between ferrite and austenite and a local concentration of substitutional at the interphase boundary. This last situation has been suggested to reasonably reflect experimental growth rates.[19] Recently, a mixed-mode approach has been adopted to incorporate solute drag explicitly and was successfully applied to the study of continuous cooling transformations of a TRIP steel.[20]

To simulate the effect of soluble B on the nucleation of ferrite during low cooling rate (CR = 6 °C/min), spherical cells represented the prior austenite grain. Ferrite growth was simulated starting from grain boundaries and from the centre of the grain. Using both approaches, the Mn concentration was calculated at different cooling times (t = 0 s at 950 °C).
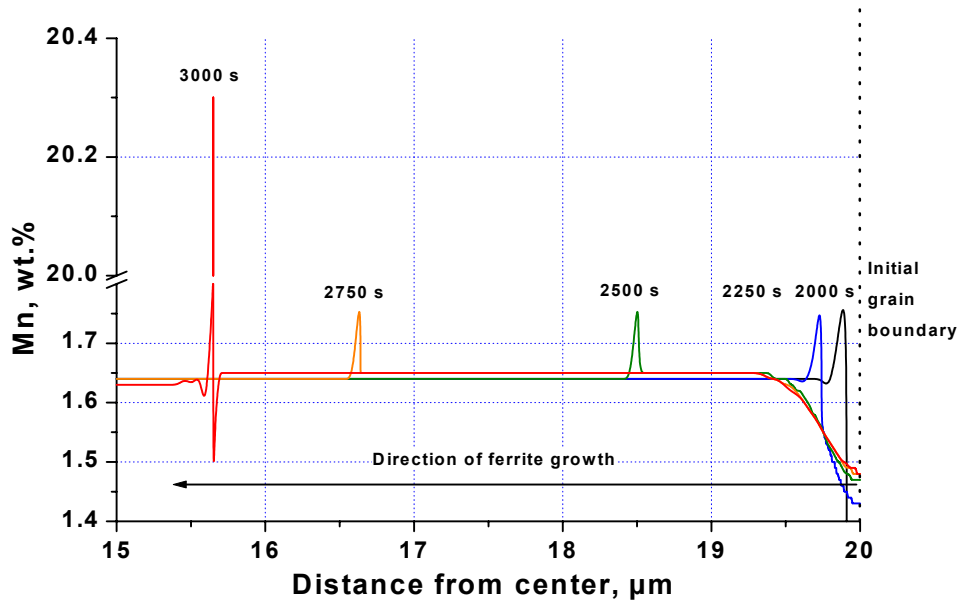
a)
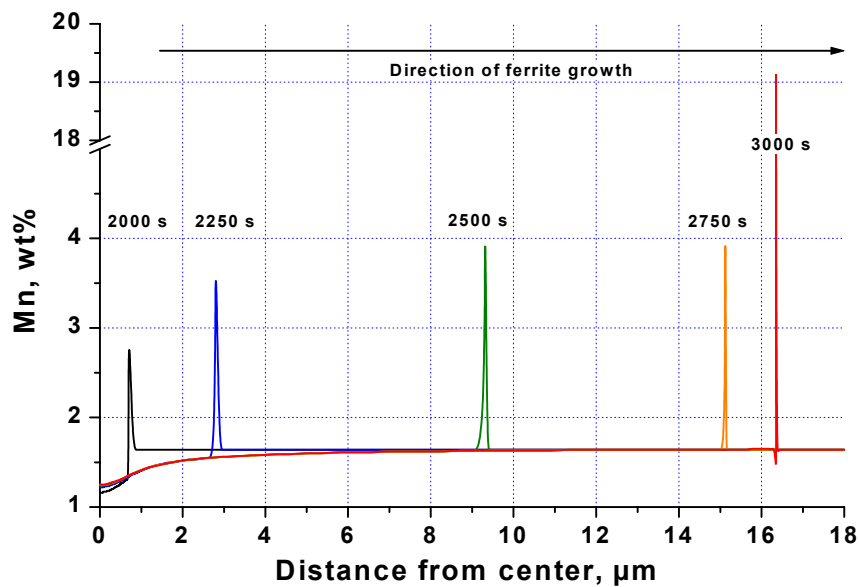
b)

Figure VI.10: Mn profile at the $\alpha-\gamma$ interphase boundary after different cooling times for a) sphere boundary nucleation and b) nucleation from the center of a sphere. CR = 6 °C/min.

Figure VI.10 shows the calculated Mn concentration at the moving α−γ interphase boundary during cooling (a) the CMn and (b) the CMnB steel with CR = 6 °C/min. It can be clearly seen that the nucleation mode, from grain boundaries or from inside the initial austenite grain has a strong effect on the local Mn concentration. While in the CMn steel, the Mn concentration locally increased from 1.6 to 1.8 wt.% at the moving interphase, in the CMnB steel, the local concentration of Mn was 4 wt.%. Mn followed the local equilibrium non partitioning in both case, but in the case of CMnB steel, the nucleation mode implied a much higher Mn content at the moving interphase, very likely responsible for a SDLE. The local Mn equilibrium calculated with Dictra was consistent with the EDX measurements, performed on the CMnB steel cooled in dilatometer at CR = 6 °C/min, and reported in the chapter V.

The spherical growth mode and nucleation inside the grains conditions were used to simulate the γ−α transformation during slow cooling (6 °C/min) in B-bearing steels. The influence of the alloying elements Mo and Cr on the C partitioning was then studied. Figure VI.11 shows the evolution of the C content at the moving interphase during the γ−α transformation in the CMnB, CrB and MoB steels, respectively. From Figure VI.11a and VI.11b, the start of the phase transformation is controlled by substitutional diffusion, *i.e.* partitioning, and later by interstitial carbon diffusion (Figure VI.11c and VI.11d), with para equilibrium or local equilibrium-non partitioning, depending on the substitutional solute concentration at the boundary.
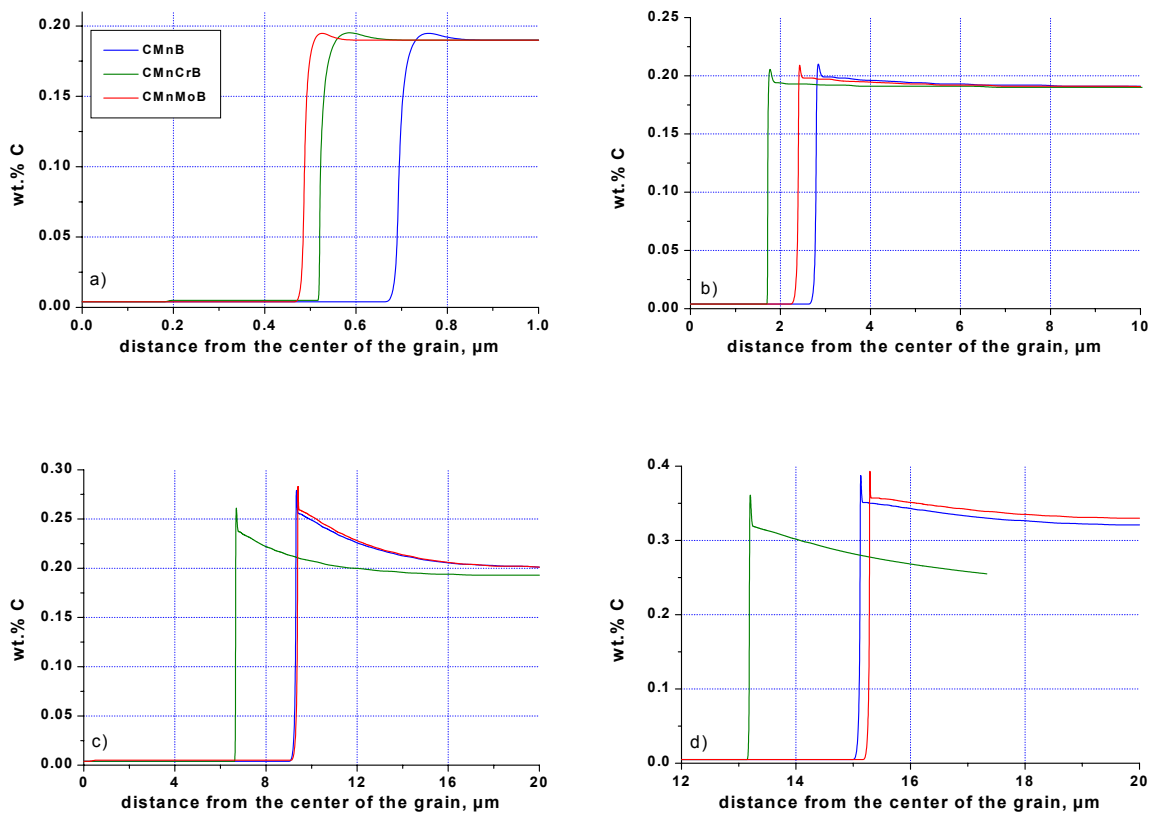

Figure VI.11: Carbon concentration at the α−γ interphase boundary during cooling from 950 °C at CR = 6 °C/min after a) 2000 s (750 °C), b) 2250 s (725 °C), c) 2500 s (700 °C), d) 2750 s (675 °C).

The Cr and Mo partitioning during the $\gamma-\alpha$ transformation was simulated with Dictra in the CrB and the MoB steels, respectively. In the CrB steel, local equilibrium was observed for Cr without partitioning. In the MoB steel, no local equilibrium of Mo was observed. In that steel, the transformation occurred likely under the paraequilibrium condition. However, it can be seen in Figure VI.12 that, at the end of the transformation a clear SDLE was predicted. It must be noted that if Mo and Cr do not partition, the Mn responsible for a SDLE in the CMnB steel very likely interacts with Mo and Cr, increasing the intensity of the SDLE. As a consequence, transformations stasis was possible in the CrMoB steel.
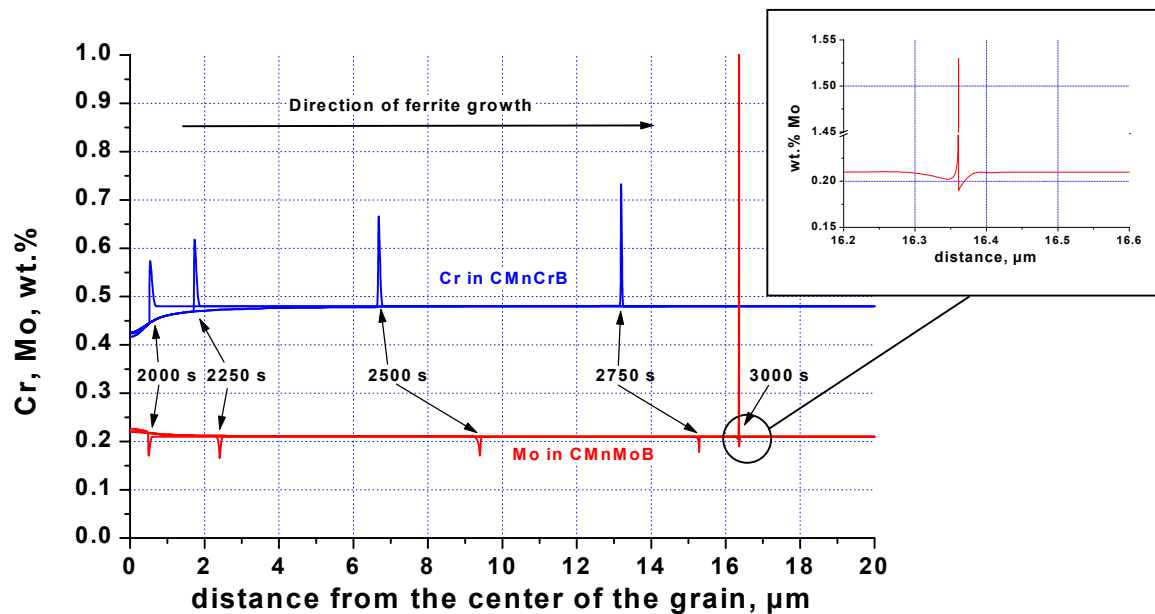
Figure VI.12: Cr and Mo concentrations at the $\alpha-\gamma$ interphase boundary during cooling from 950 °C at CR = 6 °C/min after a) 2000 s (750 °C), b) 2250 s (725 °C), c) 2500 s (700 °C), d) 2750 s (675 °C).

VI.5 Conclusions

The effects of Cr and Mo on the austenite decomposition during continuous cooling have been studied in CMn steels containing soluble B by means of dilatometry.

It was found that 0.5 wt.% Cr in a CMn steel containing soluble B decreased Ar$_3$ and decreased B$_s$ of 10 °C. The carbides formation was enhanced.

In the CMn steel alloyed with soluble B and 0.2 wt.% Mo, the ferrite and pearlite transformation were suppressed, and no effect on B$_s$ was observed. Mo increased the acicular character of ferrite.

The combination of Cr, Mo and soluble B produced a dual phase bainite-martensite microstructure in a wide range of cooling rates, due to transformation stasis during cooling. In that steel, the isothermal bainite transformation at 500 °C was also incomplete. This effect was attributed to a strong SDLE due to local concentration of Cr, Mo and Mn decreasing the mobility of the $\gamma-\alpha$ interphase boundary.

In the MoB steel, Ac_1 was strongly lowered when reheating a bainitic microstructure, likely due to the presence of residual austenite with high substitutional (Mn + Mo) content. That effect was not observed in the Cr containing steels due to the carbide forming property of Cr.

The analysis of extraction replicas revealed the presence of numerous TiN and TiC precipitates, showing that the precipitation of BN was prevented and soluble B was thus effective. Mo was found to be soluble in TiN and TiC precipitates and Cr influenced the shape of carbides. More carbides were found in the CrB steel than in the MoB steel.

Finally, Dictra simulations were performed to estimate the partitioning of Cr, Mo and Mn during the austenite decomposition to ferrite. The effect of soluble B was found to be well represented by considering spherical growth from the center of grains, *i.e.* the grain boundary nucleation was suppressed. Using those conditions, Mn was found responsible for the SDLE in the CMnB steel due to its high concentration at the moving interphase boundary.

Local equilibrium without partitioning of substitutional elements was predicted in the CrB steel, while in the MoB steel, the transformation occurred under paraequilibrium. Mo was clearly responsible for SDLE.

In CMn steels, the combination of Cr and Mo with soluble B produced transformation stasis due to a strong SDLE. As a result, with small amounts of alloying elements, complex bainite + martensite microstructures were produced in a wide range of cooling rates.

[1] R.S.Archer, J.Z.Briggs, C.M.Loeb, Jr. Molybdene Aciers, Fontes, Alliages. Climax Molybdenum Company, 1948.

[2] F.E.Bowman, R.M.Parke and A.J.Herzig: Transactions of the A.S.M., vol.31, 1943, p.487.

[3] G.J. Shiflet, H.I. Aaronson: Metallurgical Transactions A, vol. 21A, June 1990, p. 1413.

[4] M. Enomoto, H.I. Aaronson: Metallurgical Transactions A, vol. 17A, 1986, p. 1385.

[5] W.T. Reynolds, Jr., F.Z. Li, C.K. Shui, H.I. Aaronson: Metallurgical Transactions A, vol. 21A, June 1990, p.1433.

[6] N.A.Razik, G.W.Lorimer, andN.Ridley: Metallurgical Transactions A, vol.7A, February 1976, p.209.

[7] H. Goldenstein, H.I. Aaronson: Metallurgical Transactions A, vol. 21A, June 1990, p.1465.

[8] W.T. Reynolds, Jr., S.K. Liu, F.Z. Li, S. Hartfield, H.I. Aaronson: Metallurgical Transactions A, vol. 21A, June 1990, p. 1479.

[9] Ph. Maitrepierre, J. Rofes-Vernis, D. Thivellier : Boron in Steel, 18 september 1979, p.1.

[10] F.B. Pickering, Transformation and Hardenability in Steels Symposium, February 1967, Michigan, Climax Molybdenum, p.109.

[11] R W K Honeycombe and H K D H Badeshia : Steels, Microstructure and properties. Second edition, 1995. Edward Arnold. p.133.

[12] J.Z. Zhao, C. Mesplont, B.C. De Cooman: Z. Metallkd. 92, n°4, 2001, p.345.

[13] J.Z. Zhao, C. Mesplont, B.C. De Cooman: ISIJ vol.41, n°5, 2001, p.492.

[14] J.Z. Zhao, C. Mesplont, B.C. De Cooman: Materials Science and Engineering A332, 2002, p.110.

[15] C.Mesplont, J.Z. Zhao, S. Vandeputte, B.C. De Cooman: Steel Research vol.72, No.7, 2001, p.263.

[16] E.J. Mittemeijer, L. Cheng, P.J. Van der Schaaf, C.M. Brakman, B.M. Korevaar: Metal. Trans. 19A, 1988, p.925.

[17] K.W. Andrews: JISI, Vol. 203, 1965, p.721.

[18] S. Yoshida, J. Ågren : Proceedings of the Thermomechanical Processing of Steels conf. London, May 2000, p.275.

[19] G.R. Purdy, D.H. Weichert, J.S. Kirkaldy: Trans. TMS-AIME 230, 1964, p.1025.

[20] F. Fazeli, M. Militzer: Proc. of the Int. Conf. on TRIP-Aided High Strength Ferrous Alloys, Ghent, Belgium, B.C. DeCooman, ed., June 2002, p.271.

CHAPTER VII

Combined dilatometric-crystallographic texture study of the effect of austenite deformation on the phase transformations in a micro alloyed bainitic steel

VII.1 Introduction

It is well known that the crystallographic orientation of the parent austenite leads to specific crystallographic orientation of the ferrite, due to the crystallographic orientation relationships that exist between the two phases.[1] In hot rolled low carbon sheet steels, the final crystallographic texture results from the deformation and recrystallisation of the austenite, and the γ–to-α phase transformation. Deformation generates characteristic crystallographic deformation textures in the γ phase. Dynamic recrystallisation during rolling and static recrystallisation between the rolling passes alter these textures. The austenite decomposition kinetics is influenced by its deformation state. Unrecrystallised γ will transform to pro-eutectoïd ferrite at a faster rate than recrystallised γ due to two effects:

  (a) the higher internal energy of the deformed and thus less stable γ, and

  (b) the larger number of nucleation sites provided by defects.

Therefore different crystallographic orientations will be present in the resulting ferrite phase depending on whether the parent phase is recrystallised austenite or deformed austenite, even though the same crystallographic orientations exist between the α and the γ phases. Figure VII.1[2] gives a summary of crystallographic texture phenomena adapted from the work of Ray and Jonas.[3]

The major deformation texture components of austenite are the $\{110\}_\gamma < 1\overline{1}2 >_\gamma$ brass texture and the $\{112\}_\gamma < 11\overline{1} >_\gamma$ copper texture. The type of texture developed by fcc crystals depends on the stacking fault energy (SFE), which in turn depends on the alloy composition and the temperature. Low SFE materials have typically the brass texture, while copper is favoured in high SFE materials. In low carbon steels the austenite has usually a low SFE.
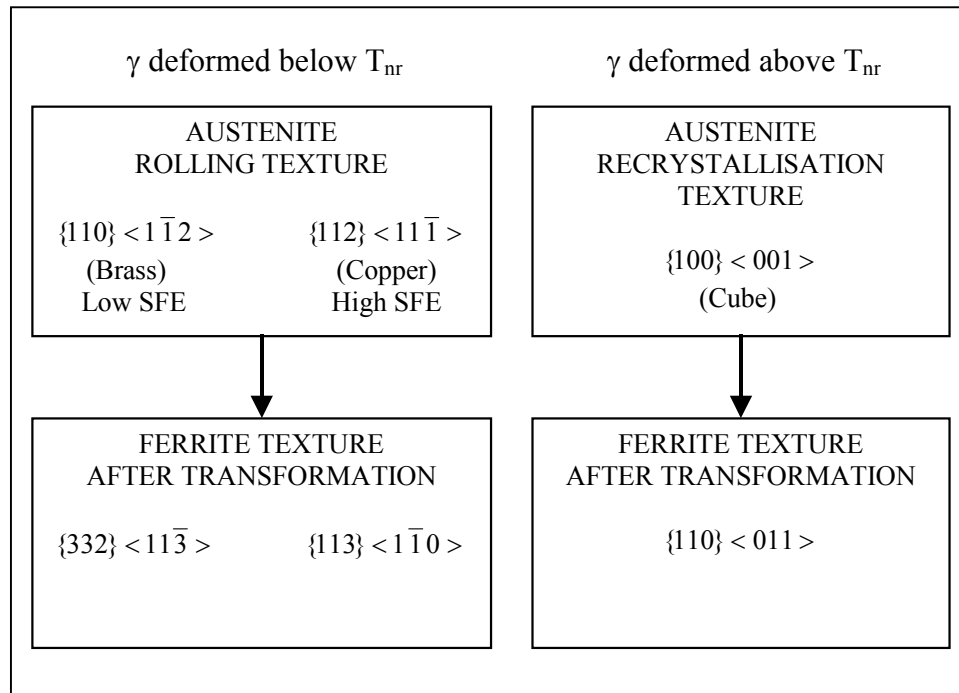
```
┌─────────────────────────────────────────────────────────────────────┐
│   γ deformed below Tₙᵣ              γ deformed above Tₙᵣ              │
│  ┌───────────────────────┐        ┌───────────────────────┐          │
│  │       AUSTENITE       │        │       AUSTENITE       │          │
│  │    ROLLING TEXTURE    │        │   RECRYSTALLISATION   │          │
│  │                       │        │        TEXTURE        │          │
│  │ {110}<1-12>  {112}<11-1>│      │                       │          │
│  │  (Brass)    (Copper)  │        │      {100}<001>       │          │
│  │  Low SFE    High SFE  │        │        (Cube)         │          │
│  └───────────────────────┘        └───────────────────────┘          │
│             │                                 │                       │
│             ▼                                 ▼                       │
│  ┌───────────────────────┐        ┌───────────────────────┐          │
│  │    FERRITE TEXTURE    │        │    FERRITE TEXTURE    │          │
│  │   AFTER TRANSFORMATION │       │   AFTER TRANSFORMATION │         │
│  │                       │        │                       │          │
│  │ {332}<11-3>  {113}<1-10>│      │      {110}<011>       │          │
│  └───────────────────────┘        └───────────────────────┘          │
└─────────────────────────────────────────────────────────────────────┘
```

Figure VII.1: Summary of crystallographic texture relations[2].

Clear crystallographic orientation relationships exist between the ferrite and the austenite lattices:
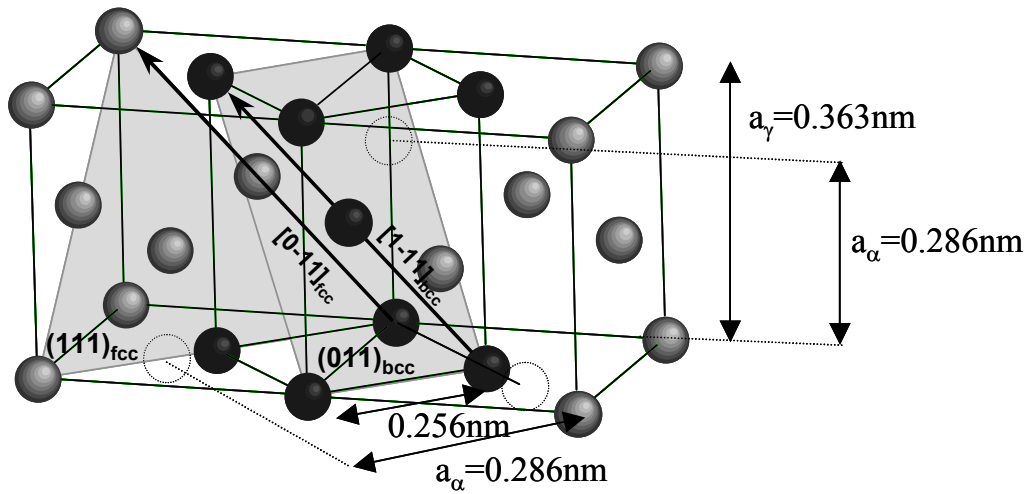
The Kurdjumov-Sachs (KS)[4] orientation relationship: $\{111\}_\gamma//\{011\}_\alpha$ and $<011>_\gamma//<111>_\alpha$.

The Bain (B)[5] orientation relationship: $\{001\}_\gamma//\{001\}_\alpha$ and $<001>_\gamma//<110>_\alpha$.

The Nishiyama-Wasserman (NW)[6] orientation relationship: $\{111\}_\gamma//\{011\}_\alpha$ and $<211>_\gamma//<011>_\alpha$.

A schematic of these orientation relationships is represented Figure VII.2.

a) Kurdjumov-Sachs orientation relations: {111}$_\gamma$ // {011}$_\alpha$ and <011>$_\gamma$ // <111>$_\alpha$

b) Bain orientation relations: {001}$_\gamma$ // {001}$_\alpha$ and <100>$_\gamma$ // <110>$_\alpha$
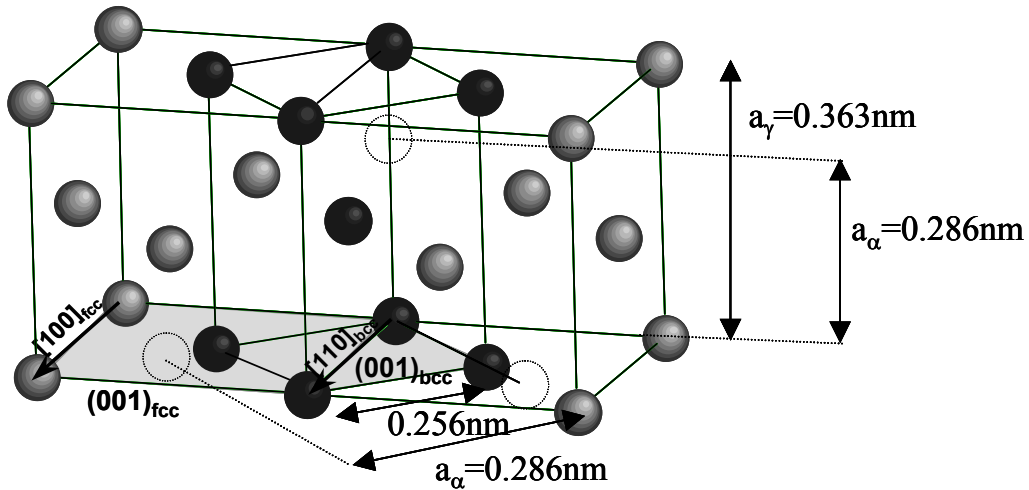
c) Nishiyama-Wasserman orientation relations: {111}$_\gamma$ // {011}$_\alpha$ and <211>$_\gamma$ // <011>$_\alpha$
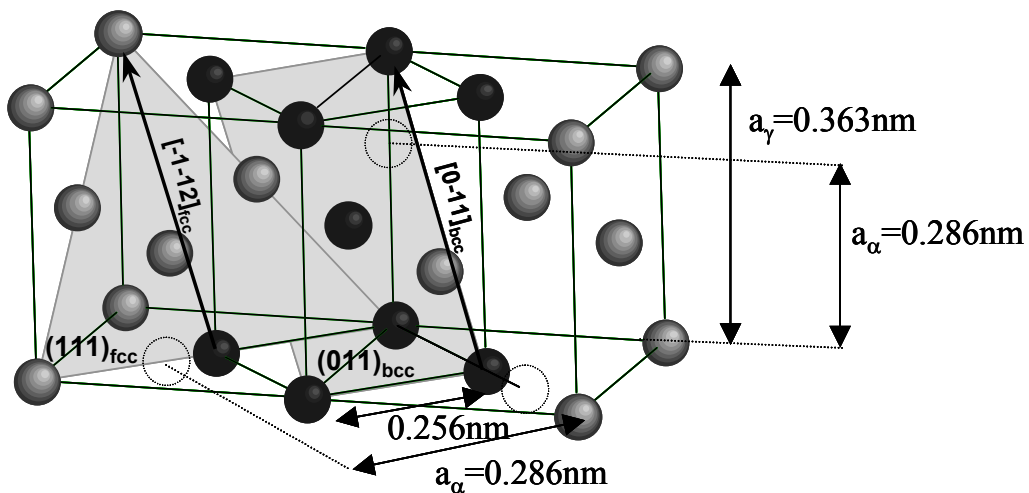

Figure VII.2: Schematic of orientation relationships between the γ (fcc) and the α (bcc) lattice.

These three sets differ from one another by only a few degrees and a spread of intermediate orientation relationships is often observed experimentally. Because ferrite has a crystallographic orientation relationship with the austenite, the brass austenite texture will result in the $\{332\}_\alpha < 11\bar{3} >_\alpha$ ferrite texture component, and the copper austenite texture will transform in the $\{113\}_\alpha < 1\bar{1}0 >_\alpha$ ferrite texture component. FigureVII.3 shows the calculated bcc texture components resulting from the $\gamma \rightarrow \alpha$ transformation starting from deformed austenite with the respective texture components copper $\{112\}_\gamma < 111 >_\gamma$, S $\{123\}_\gamma < 634 >_\gamma$, brass $\{110\}_\gamma < 112 >_\gamma$ and Goss $\{011\}_\gamma < 100 >_\gamma$, based on the KS orientation relationship between α and γ. The resulting texture components in ferrite shown in FigureVII.3 do not take into account the variant selection determined by:

- the morphology of austenite grains;

- the slip activity;

- the residual stresses: these may be stresses remaining in the material after rolling, or transformation-related internal stresses due to the difference of the specific volume between austenite and ferrite.

The aspect ratio of pancaked grains plays an important role in favouring selection of the transformed copper $\{311\}_\alpha<011>_\alpha$ and $\{211\}_\alpha<011>_\alpha$ components, and the extent of shear on active slip planes during prior rolling promotes the formation of the transformed brass $\{332\}_\alpha<113>_\alpha$ and $\{211\}_\alpha<113>_\alpha$ components.[7]

The recrystallised austenite contains mainly the $\{100\}_\gamma < 001 >_\gamma$ cube recrystallisation texture component. It results in the $\{100\}_\alpha < 011 >_\alpha$ rotated cube component after transformation. The $\{110\}_\alpha<001>_\alpha$ Goss and $\{110\}_\alpha<110>_\alpha$ rotated Goss components are usually not observed experimentally, due to the effect of residual stresses on variant selection.[7]

Texture analyses using the Electron Back Scattering Patterns (EBSP) method were recently reported for TRIP steels[8] and for DP steels[9]. In both types of high strength multiphase steels, the primary ferrite had a texture originating from both the brass and the copper texture components of deformed γ. The Cu texture component had a weaker intensity. The textures of the constituents formed at low temperature in the DP steel, *i.e.* bainite and martensite, had a maximum intensity on the $\{001\}_\alpha < 110 >_\alpha$ rotated cube component, suggesting that these phases originated from recrystallised austenite grains.[9] It was found that a clear variant selection occurred during the austenite decomposition in the TRIP steels. Indeed, in the retained austenite present in the TRIP steels, the cube component $\{001\}_\gamma < 100 >_\gamma$ was less sharp than predicted from the bainite texture using calculations of Orientation Distribution Function (ODF) transformations, based on the KS, Bain and NW orientation relations.[8]
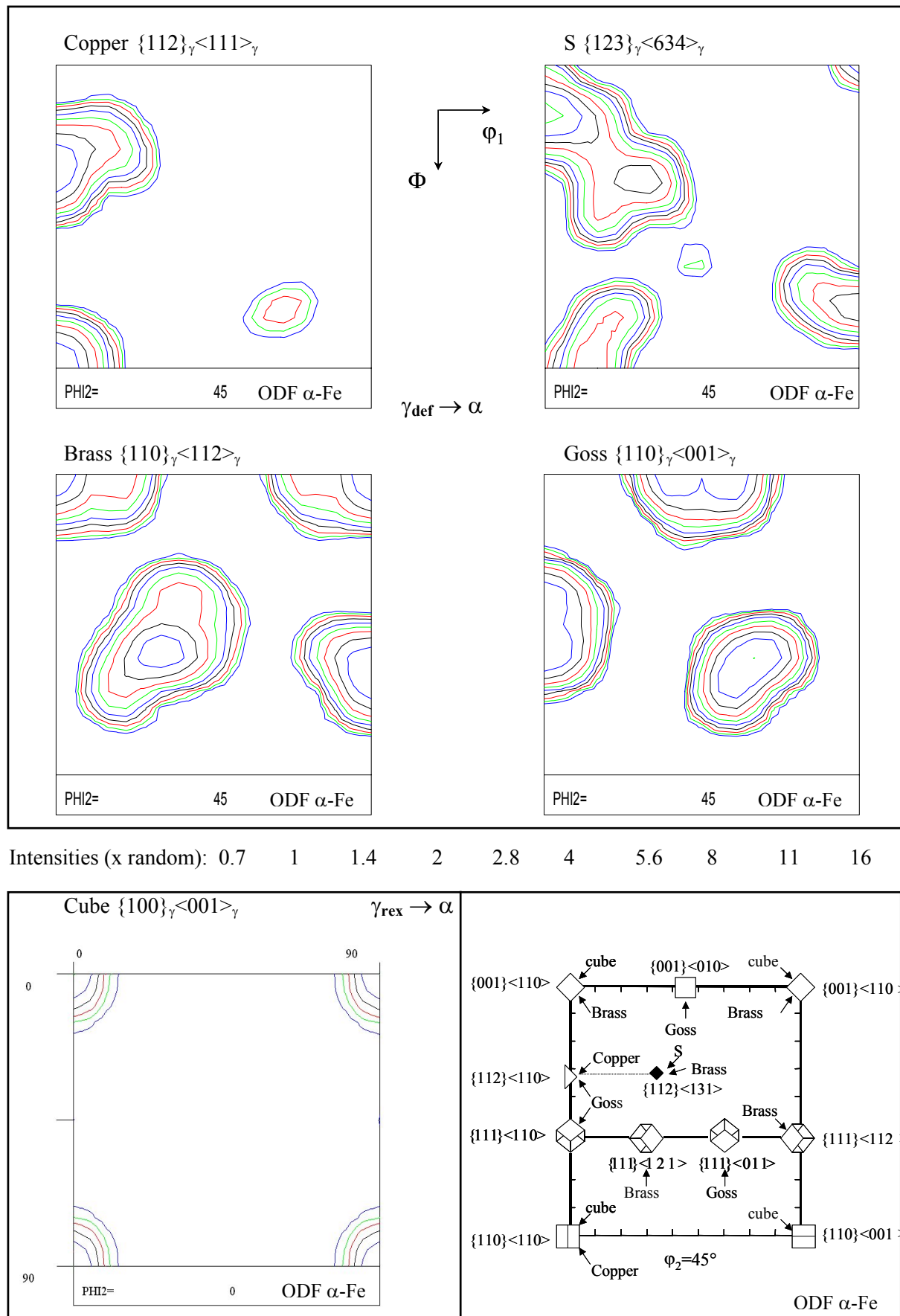
FigureVII.3: Resulting bcc transformation components of the copper, S, brass and Goss component in deformed fcc[9], and cube in recrystallised fcc, based on the KS orientation relations for transformation. The variant selections are not taken into account.

In the present chapter, the Nb-microalloyed CMnMoCrB bainitic steel 6 with the composition given in chapter II table II.1, was hot rolled and coiled at different coiling temperatures (CT) to produce controlled microstructures with different mechanical properties. The base CMn steel containing 0.16 wt.% C and 1.6 wt.% Mn was alloyed with Mo, Cr and B to retard the ferrite and pearlite formations and favour the bainitic transformation during the coiling stage of the hot rolling process. B in solid solution is particularly efficient in retarding the ferrite formation. Soluble boron segregates to the austenite grain boundaries, where it reduces the strain energy in these regions, retarding the nucleation of ferrite and increasing the hardenabiliy of the steel.[10] Ti was added to avoid loss of interstitial boron to nitrogen by forming TiN.[11] Nb was added to increase the strength level by precipitation strengthening. P was added to increase the strength by solid solution hardening. Nb is also known to raise the non-recrystallisation temperature, T_{nr}[12]. The calculated value of T_{nr} was 1084 °C, using the equation given by:[13]

$$T_{nr} = 887 + 464C + 890Ti + 363Al - 357Si + 6445Nb - 644\sqrt{Nb} + 732V - 230\sqrt{V} \qquad \text{(VII.1)}$$

Rolling in the austenitic region below T_{nr} therefore produces deformed "pancaked" austenite grains. Fine-grained ferrite nucleates on γ-grain boundaries and internal defects within the γ-grains.

The evolution of the texture in the ferrite as a function of the CT was studied by means of Electron Back Scattering Diffraction (EBSD) and X Ray Diffraction (XRD). The attention was focussed on the bainitic transformation. The study was supplemented with dilatometric simulation of the austenite to bainite transformation starting from different grain sizes and deformation states of the austenite in order to follow the kinetics of austenite decomposition during the coiling process. It was found that the austenite deformation state had a pronounced effect on both the kinetics of the bainitic transformation and the crystallographic orientation of the resulting bainite.

VII.2 Experimental

Blocks with 120 mm length, 60 mm width and 25 mm thickness of the CP steel containing 0.16 wt.% C, 1.6 wt.% Mn, 0.2 wt.% Mo, 0.5 wt.% Cr, 500 ppm Nb, 300 ppm P and 20 ppm B were reheated to 1270 °C for one hour and hot rolled to a final 2.5 mm thickness. Three coiling temperatures were used to produce different microstructures. Ferrite and pearlite were obtained after coiling at 720 °C, and a bainite-martensite microstructure was obtained after coiling at 550 °C. The different phases were observed by light optical microscopy (LOM) and scanning electron microscopy (SEM) after etching with Nital or with the LePèra etchant.[14] Local texture measurements were made using the OIM-EBSD (Orientation Imaging Microscopy – Electron Back Scattering Diffraction) technique. XRD was carried out using Mo K_α source radiation to detect the presence of retained austenite at room temperature.

The coiling simulations were also simulated in a Tetha Dilatronic III quench dilatometer equipped with a deformation unit. A coiling temperature CT of 600 °C was chosen because it is above the bainite start temperature, which was calculated to be 548 °C using the empirical formula of Li *et al.*[15] In addition, coiling at 600 °C results in a continuous yielding behaviour which is particularly interesting in terms of formability. Different states of deformation and initial grain sizes of the austenite were produced in the dilatometer; Coiling simulations were carried out in the dilatometer on the following types of samples:

a) undeformed samples;

b) samples deformed 30 % at 950 °C;

c) samples deformed at room temperature and reheated at 1050 °C;

d) samples deformed at room temperature and reheated at 950 °C.

The difference in the reheating temperature after cold deformation led to austenite with different grains sizes. Figure VII.4 shows the corresponding cycles.
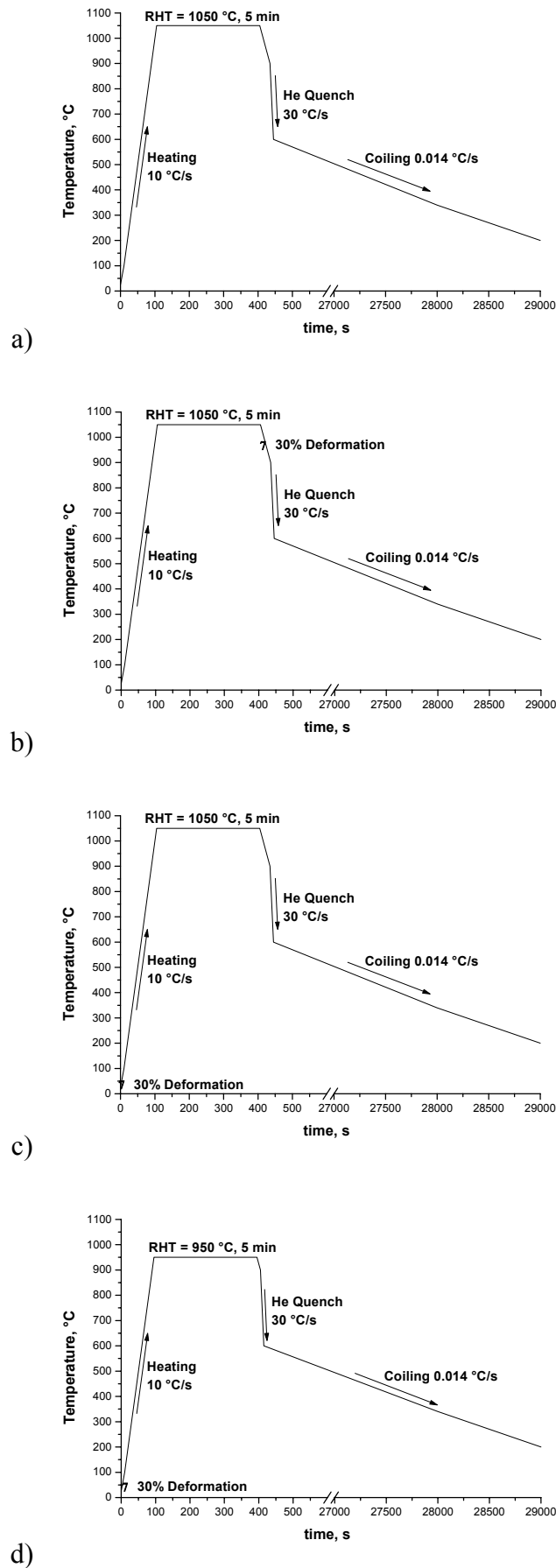
Figure VII.4: Dilatometer cycles used for simulating the coiling during the hot rolling process.

VII.3 Microstructures-mechanical properties

The CP steel composition selected in the present chapter had a bainite-martensite microstructure when coiled at 550 °C, and a ferrite-pearlite microstructure when coiled at 720 °C. Coiling at 680 °C produced a mixed microstructure consisting of ferrite, pearlite, bainite and martensite. The corresponding micrographs are shown FigureVII.5.
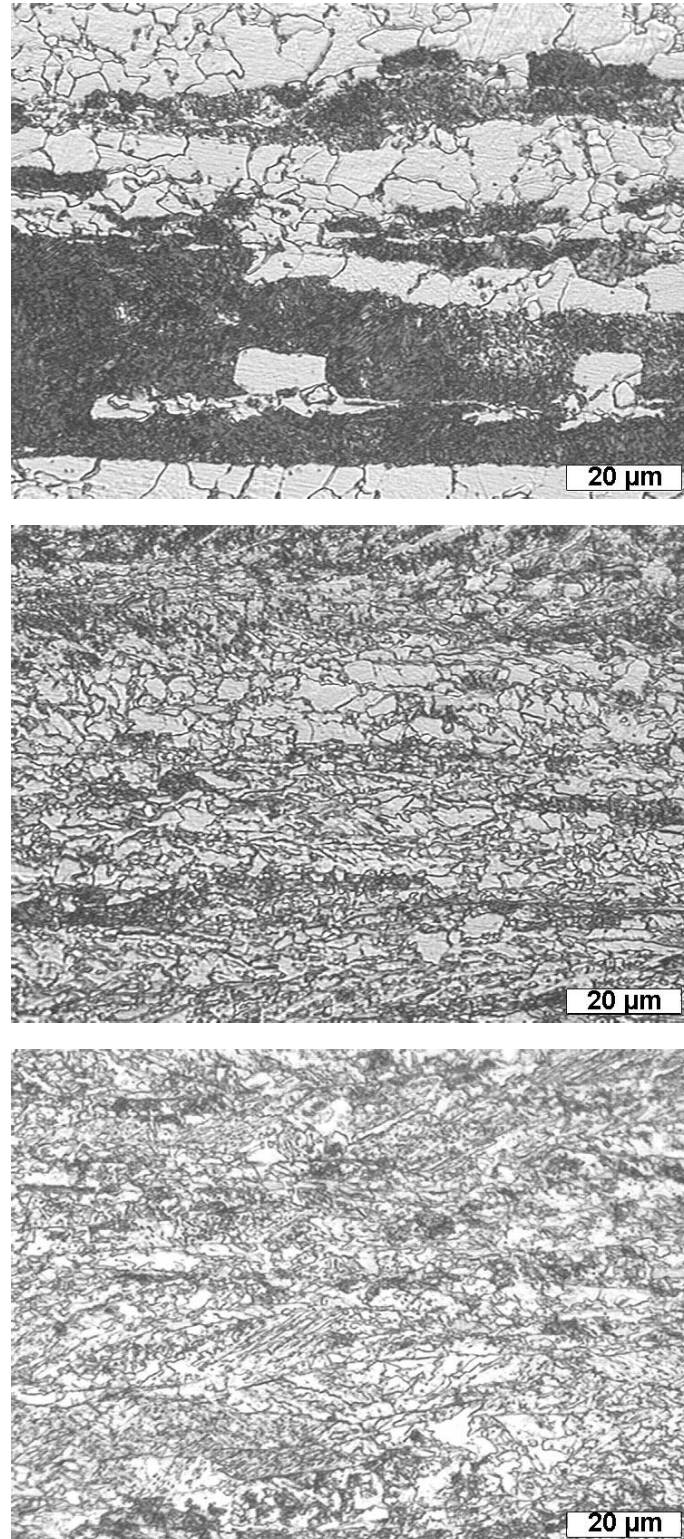
FigureVII.5: Light optical micrographs showing microstructures after hot rolling and coiling at 720 °C, 680 °C and 550 °C (from top to bottom). Etchant: nital.

FigureVII.6 shows the comparison between the hot rolling data of the complex phase steel and the hot torsion data for a low C HSLA steel with 520 ppm C, 0.3 wt% Mn and 170 ppm Nb. In the CP steel, there is no DRX because:

- the slope of the mean flow stress (MFS) versus 1000/T curve is higher than expected;

- there is no change in the temperature dependence of the flow stress, which has a linear 1/T dependence without a change in slope, which would indicate a T_{nr} above 1115 °C.
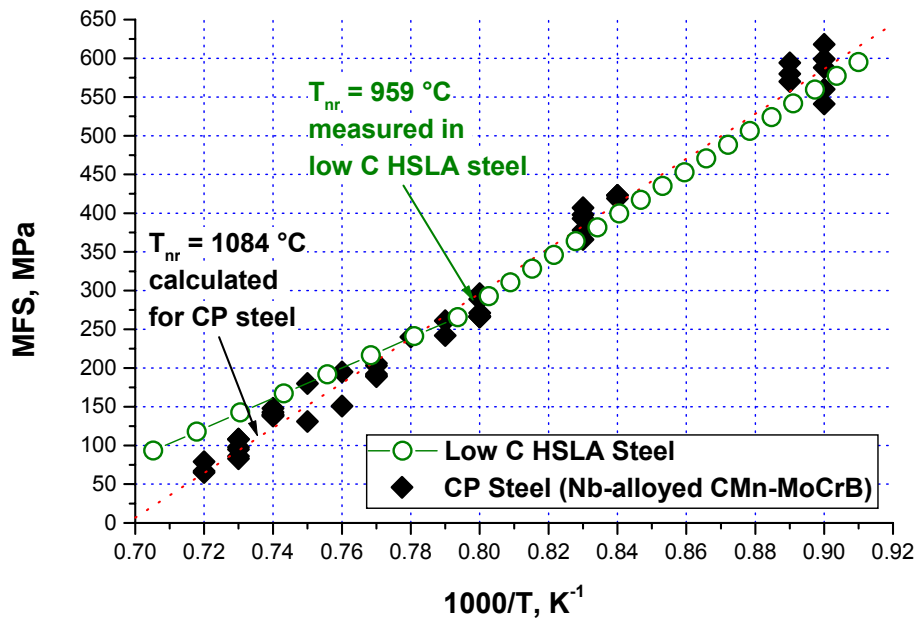

FigureVII.6: MFS vs 1000/T. Rolling data.

In this graph, the temperature T was measured before each rolling pass, and the MFS was calculated accordingly to the model of Maccagno *et al.*[12].

Additional hot torsion tests were performed on cylindrical samples in order to measure accurately T_{nr}. Figure VII.7 shows clearly that T_{nr} could be determined at 900 °C. However, during torsion tests, a constant strain rate of 1 s^{-1} was used, while during hot rolling the strain rate increased from 8 s^{-1} in the first pass to 20 s^{-1} in the last pass. It is thus very likely that in the present CP steel, dynamic recrystallisation was sensitive to the strain rate.

New hot rolling simulation were performed using different finishing rolling temperatures (FRT) in order to see whether that parameter had an influence on the initial austenite grains size. Rolling with FRT equal to 930, 840 and 785 °C respectively and coiling at 720 °C produced similar ferrite-pearlite microstructures. The measured tensile properties are reported in Table VII. 1. It can be seen clearly that decreasing FRT decreased TS and increased the elongation. Moreover larger Lüders plateaus were measured with decreasing FRT, due to higher dislocation densities. It is thus very likely that decreasing FRT produced more deformed initial austenite grains, meaning that the $\gamma-\alpha$ transformations likely occurred from a mixture of deformed and recrystallised austenite grains. A previous study showed that the FRT influenced the final product texture.[16]

Table VII. 1: Effect of FRT on the tensile properties of the industrial steel, CT = 720 °C.

FRT, °C	YS, MPa	TS, MPa	A_{80}, %	UE, %	Luders, %
930	495	623	18.75	13	2.25
840	511	614	19	13.5	3.04
785	500	596	21.75	14.75	3.51
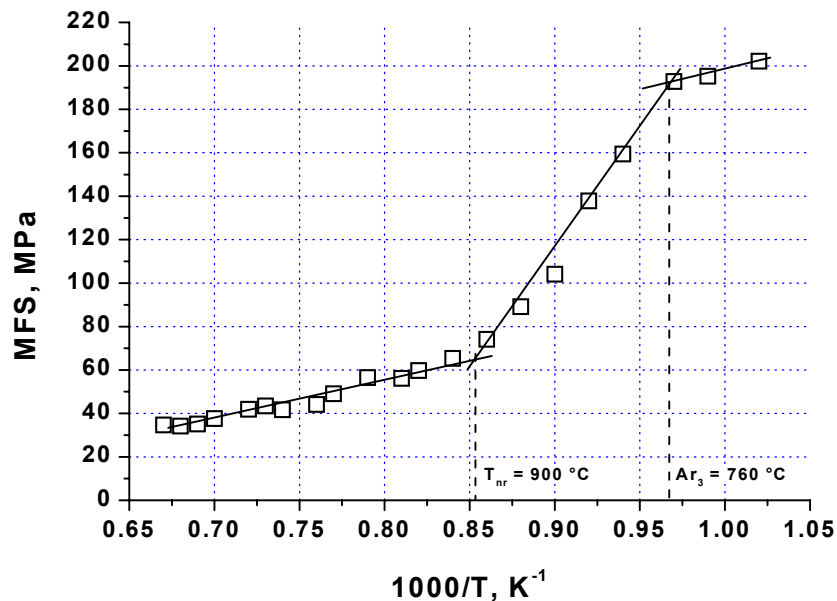
Figure VII.7: MFS vs 1000/T**.** Hot torsion.

Tensile testing after coiling simulation showed a marked difference in mechanical properties. In particular, continuous yielding was always observed after coiling at temperatures from which the bainite transformation occurred during cooling, *i.e.* just above the bainite start temperature, B_s = 548 °C. FigureVII.8 shows the stress-strain curves. It can be seen that the ferrite-pearlite microstructure produces a large yield point elongation. This tensile behaviour is typical for CMn steels with a ferrite-pearlite microstructure. The yield point occurs as a result of unlocking the dislocations by a high stress, or in the case of strong pinning, by creating new dislocations at the point of stress concentration.[17] Three conditions are necessary to obtain the yield point elongation:

1) a low density of mobile dislocations;

2) a large value of the strain rate sensitivity parameter, *i.e.* a large change in dislocation velocity in response to change of the shear strain, and;

3) a sudden generation of large amounts of mobile dislocations.

The microstructures obtained after cooling at 680 °C and 550 °C lead to a continuous yielding during tensile testing. This type of stress-strain curve is well known for C steels that have martensite in the microstructures.

This is *e.g.* the case for dual phase steels with martensite contents of more than about 4 %.[18] The presence of austenite was detected in the steel coiled at 550 °C by both XRD and EBSD. 11 % residual austenite in volume was present in that case. The residual austenite had a carbon content of 1.08 wt.%. Part of this austenite retained after a long holding time in the bainitic region is able to transform to martensite under stress and produce a transformation induced plasticity (TRIP) effect. Hence the continuous yielding observed is due to a combination of these two effects, which result in internal stresses at low temperatures.
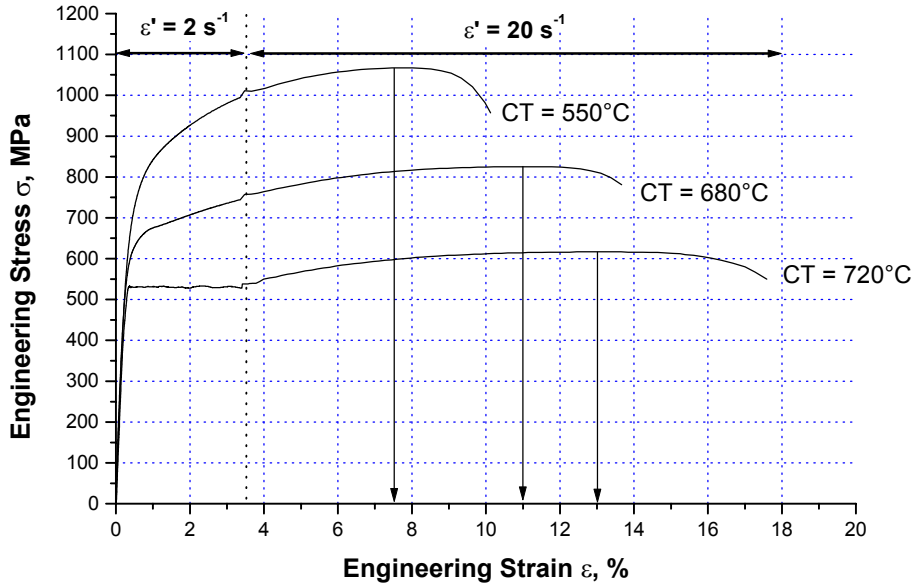

FigureVII.8: Tensile curves of hot rolled complex phase steel coiled at different CT. Vertical arrows indicate uniform elongations.
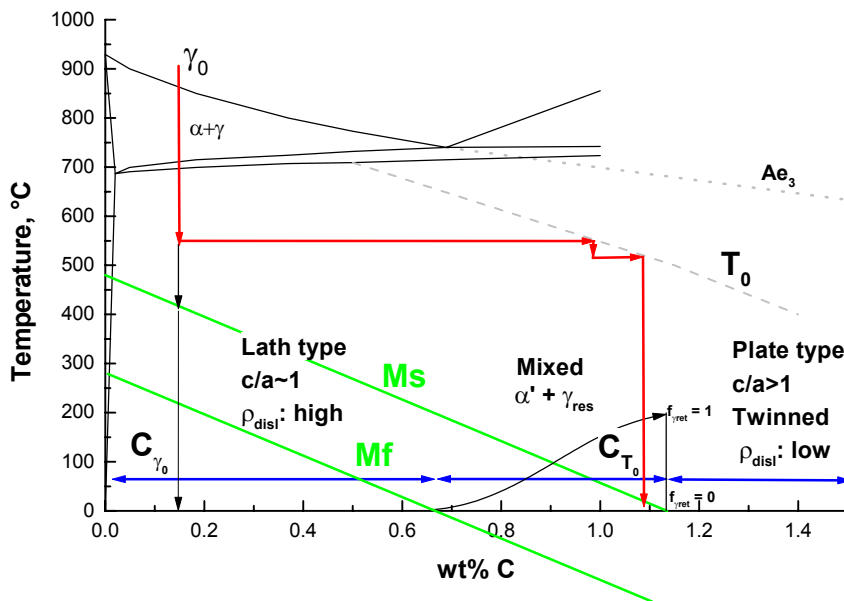

FigureVII.9: Pseudo-binary Fe-C diagram showing the C enrichment in γ_{res} during the bainite formation, and the type of martensite and/or austenite eventually formed during the cooling.

FigureVII.9 is a pseudo binary diagram showing the evolution of the carbon content in the austenite during the coiling process. It shows that the C content in γ_{res} enriched during the bainitic transformation determines the type of martensite that may form during the subsequent cooling. Coiling the present steel in the bainitic transformation temperature range leads to a microstructure containing a mixture of martensite and austenite. This constituent will be referred to as the M/A constituent in this chapter.

VII.4 Texture analysis

Local texture measurements were carried out on hot-rolled samples coiled at 720 °C, 680 °C, and 550 °C, respectively. The ODF sections at $\phi_2 = 45$ ° were calculated for the bcc phase and the results were analysed separately for the range of the CT parameter. In the samples coiled at 680 °C and 550 °C, retained austenite was present and the ODF could therefore also be calculated for the fcc phase.

VII.4.1 CT = 720 °C

FigureVII.10 shows the location of the EBSD measurements on the ferrite-pearlite microstructure. These two distinct regions were chosen to differentiate the texture of primary ferrite and ferrite formed within the ferrite-pearlite bands. Due to the segregation of alloying elements, in particular Mn, during the continuous casting and the subsequent hot rolling and controlled cooling, the final material had a banded microstructure due to an inhomogeneous distribution of alloying elements.[19] In the Mn-enriched bands the transformation start is delayed with respect to the neighbouring Mn depleted regions. Those regions enrich in carbon while the other regions transform to ferrite. The carbon-enriched areas will eventually transform to pearlite. The often-observed banded structure in CMn steels thus indicates a non-uniform transformation in time.[19,20] The ODF for the primary ferrite shows a ferrite fiber:

ND // $(001)_\alpha$ orientation. The main texture components are the $(001)_\alpha \left[\overline{2}\,\overline{3}0\right]_\alpha$ and $(001)_\alpha \left[2\overline{3}0\right]_\alpha$ components originated from the austenite brass $\{110\}_\gamma$<112>$_\gamma$ component, and the $\{001\}_\alpha$<130>$_\alpha$ originated from the austenite Goss $\{110\}_\gamma$<001>$_\gamma$ component. These texture components are usually not observed in transformation products from deformed austenite. It is thus very likely that these texture components originated from partially recrystallised austenite. A strong $\{112\}_\alpha < 131 >_\alpha$ texture component is also present in the ODF. It results from the S $\{123\}_\gamma < 634 >_\gamma$ texture component of the parent austenite. The S texture component is a deformed austenite texture component. Hence the primary ferrite formed from both deformed austenite and recrystallised austenite. Static recrystallisation of the initially deformed austenite grains occurred during the rather slow cooling from the finishing rolling temperature to the coiling temperature of 720 °C and during the subsequent $\gamma \rightarrow \alpha$ transformation.
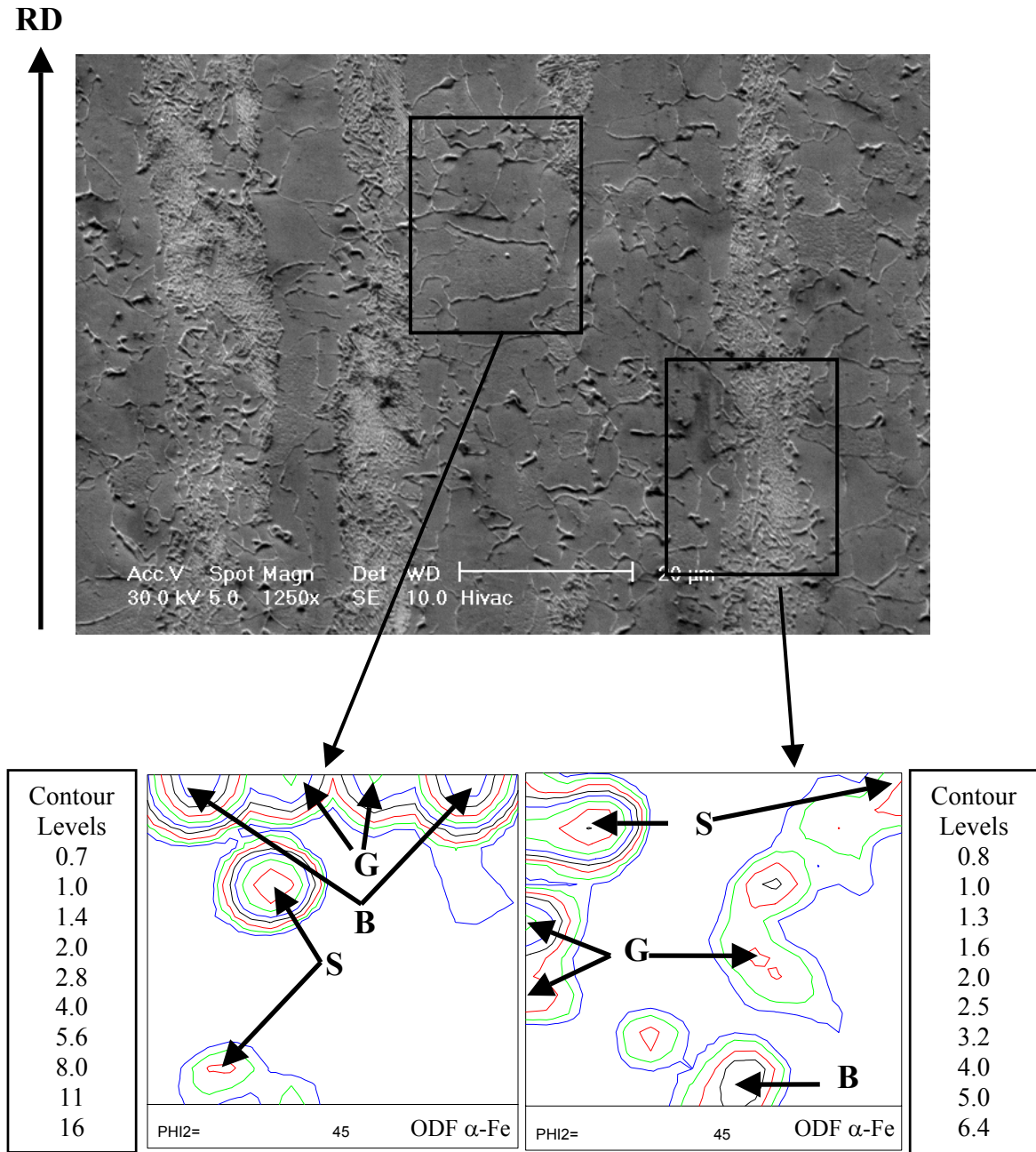
RD

FigureVII.10: Ferrite-Pearlite microstructure and bcc texture ODF sections ($\varphi_2 = 45°$) in selected areas. The letters indicate the austenite texture components from which the observed ferrite texture components originated. B = brass, G = Goss. CT = 720 °C. The contour levels are in times the untextured sample intensity.

The ODF for the ferrite in the ferrite-pearlite band has a clear ferrite α-fiber with the rolling direction RD // $[1\,\overline{1}\,0]_\alpha$. The maximum intensities were obtained for the $(112)_\alpha[1\,\overline{1}\,0]_\alpha$ and the $(111)_\alpha[1\,\overline{1}\,0]_\alpha$ texture components. Both components originate from the transformation of the deformed austenite Goss $\{110\}_\gamma<001>_\gamma$ texture component. An additional high intensity texture component was located close to the $(110)_\alpha[1\,\overline{1}\,2]_\alpha$ orientation. This texture component results from the transformation of the brass $\{110\}_\gamma<112>_\gamma$ texture component of deformed austenite. An other strong $(116)_\alpha[1\,\overline{2}\,0]_\alpha$ texture component originates from the transformation

of the S $\{123\}_\gamma$ <634>$_\gamma$ texture component of deformed austenite. Finally, a second weaker fiber appears that includes the texture component $(111)_\alpha \left[0\,\overline{1}\,1\right]_\alpha$. It lies on the ferrite $[111]_\alpha$ // ND γ-fibre. It results from the transformation of the Goss $\{110\}_\gamma$ < 001 >$_\gamma$ texture component in deformed austenite. In the ferrite-pearlite bands, the ferrite texture results mainly from the transformation of deformed austenite.

It is clear from these texture measurements that the austenite recrystallised statically during the time right after the rolling and during the $\gamma \rightarrow \alpha$ transformation. This explains why the primary ferrite formed from both deformed and recrystallised austenite during the coiling from 720 °C.

VII.4.2 CT = 680 °C

The EBSD scans for the steel coiled at 680 °C were analysed on the basis of the CI parameter. In all cases, the histogram of the CI of the EBSD pattern indexing for the bcc phase showed two clear peaks. High values of CI (0.6<CI<1) corresponded to the primary ferrite, whereas low values of CI (0.1<CI<0.5) corresponded to the secondary transformation products, *i.e.* the bainitic ferrite. FigureVII.11 shows the ODF sections at $\varphi_2 = 45$ ° for the low CI and high CI constituents, respectively. For both low and high CI phases, the ferrite has a strong γ-fibre (RD//<111>$_\alpha$). In high CI ferrite, the texture component $(332)_\alpha \left[\overline{1}\,\overline{1}\,3\right]_\alpha$ and a texture component between the $(112)_\alpha \left[1\,\overline{3}\,1\right]_\alpha$ and the $(111)_\alpha \left[1\overline{2}1\right]_\alpha$ texture components have a strong intensity. These texture components are both transformation products from the deformed austenite brass $\{110\}_\gamma$ < 112 >$_\gamma$ texture component. A texture component close to the $(116)_\alpha \left[1\overline{2}0\right]_\alpha$ found previously in the ferrite-pearlite band was also present in the ODF. It originates from the transformation of the deformed austenite S $\{123\}_\gamma$ <634>$_\gamma$ texture component. Finally, a ferrite rotated cube component $(001)_\alpha \left[\overline{1}\,\overline{1}\,0\right]_\alpha$ resulting from the transformation of partially recrystallised austenite with the cube orientation was observed.

The main components for the low CI EBSD data set corresponded to $(112)_\alpha \left[1\,\overline{1}\,0\right]_\alpha$ and $(111)_\alpha \left[0\,\overline{1}\,1\right]_\alpha$ along the α-fibre. Both result from the transformation of the Goss $\{110\}_\gamma$ < 001 >$_\gamma$ texture component in deformed austenite. The weak ferrite texture components $(115)_\alpha \left[1\,\overline{1}\,0\right]_\alpha$ (on the ferrite α-fibre) and $(112)_\alpha \left[1\,\overline{3}\,1\right]_\alpha$ were also present. Both are transformation products from the S $\{123\}_\gamma$ <634>$_\gamma$ texture component of deformed austenite. Finally, the ferrite texture components $(100)_\alpha \left[\overline{1}\,\overline{2}0\right]_\alpha$ and $(110)_\alpha \left[1\,\overline{1}\,1\right]_\alpha$ due to transformation from the brass texture component of deformed austenite were also observed.

Hence, the main ferrite orientation and the main bainite orientation are rotated by an angle of $\varphi_1 = 30$ ° with respect to each other. The ferrite has a texture similar to the texture of the C-free IF steel, and the bainite has a texture closer to that of ELC steel. It is likely that the enrichment of the austenite in C during the ferrite formation as well as its partial recrystallisation are responsible to this C-related variant selection during the phases transformation during the cooling. A similar variant selection has been observed in a C-free IF steel after 75 % cold rolling and after recrystallisation at 800 °C, 1 min.[21]
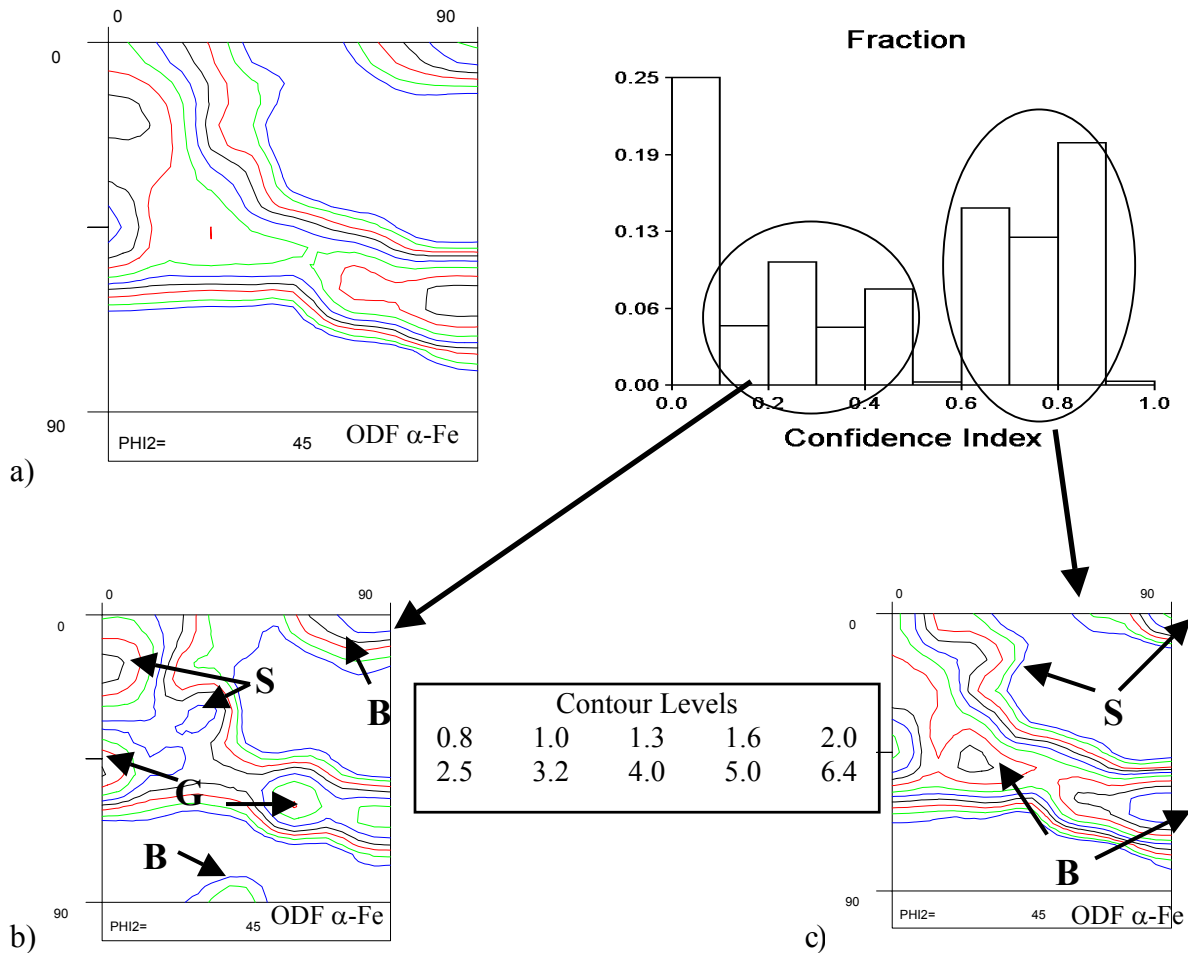
FigureVII.11: bcc texture ODF sections ($\varphi_2 = 45°$) for a) overall ferrite, b) bainite (low CI) and c) primary ferrite (high CI). CT = 680 °C.

Diffraction patterns indexing determined locally the presence of 15% of fcc phase in the area scanned. ODF sections with constant values of φ_2 are shown in FigureVII.12. For $\varphi_2 = 0$ and $\varphi_2 = 90$ ° the intensities at the corners of the ODF show that the main fcc texture components correspond to the cube orientation $\{001\}_\gamma<100>_\gamma$. For $\varphi_2 = 45$ ° the main texture components belong to the brass orientation. The retained austenite is thus deformed austenite with the brass orientation and partially recrystallised austenite. The KS orientation relation applied to the retained austenite leads to a typical ferrite texture and can be compared to the ferrite texture originating from the deformed austenite brass texture component as shown in FigureVII.3. From these results, it is clear that at the intermediate coiling temperature, CT = 680 °C, ferrite and bainite originate from different orientations of the austenite.
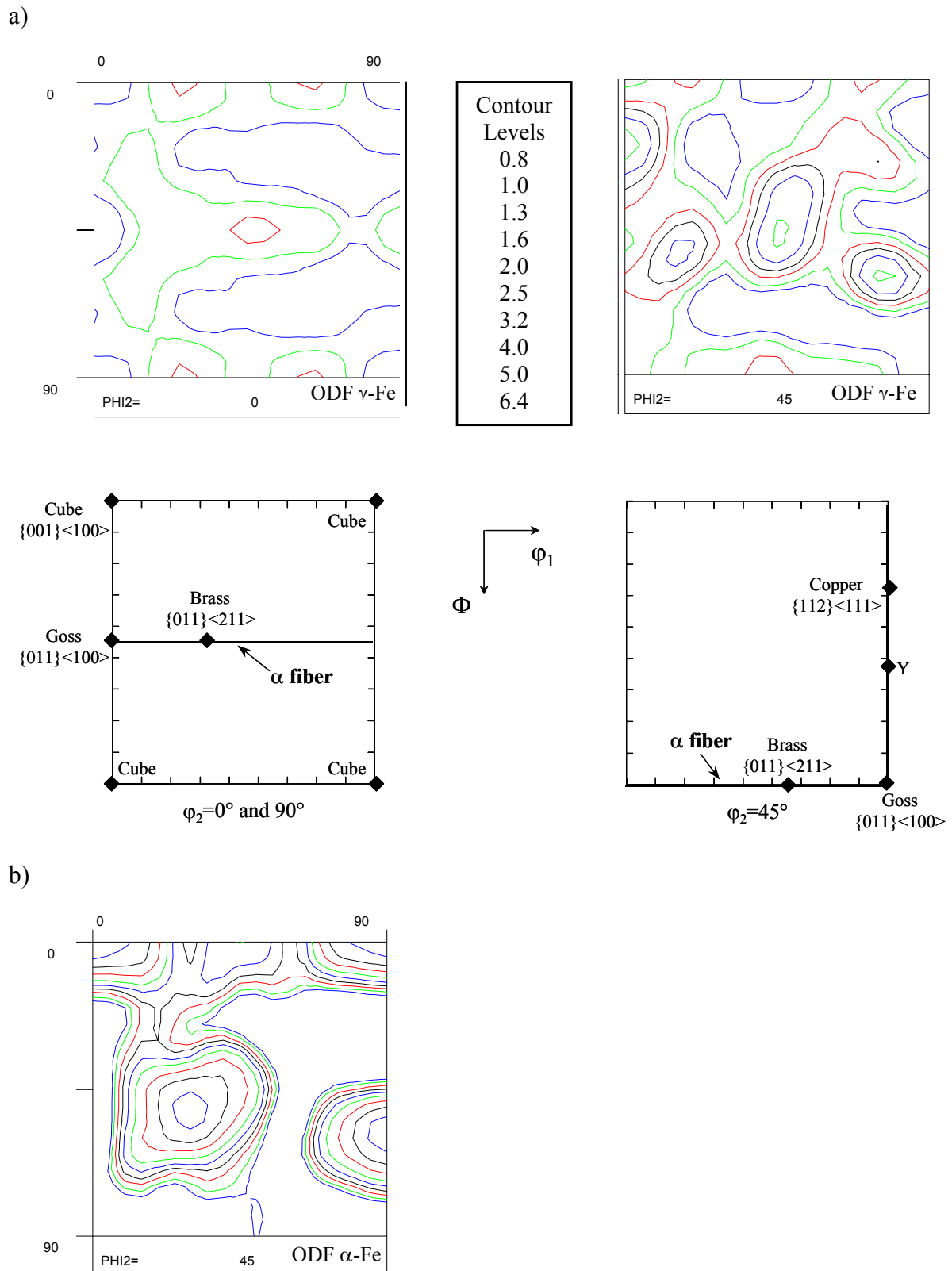
a)

b)

FigureVII.12: a) fcc texture ODF sections (φ_2 = cte) calculated from the EBSD pattern obtained on the residual austenite. b) calculated ODF for ferrite after KS transformation from the fcc texture. CT = 680 °C.
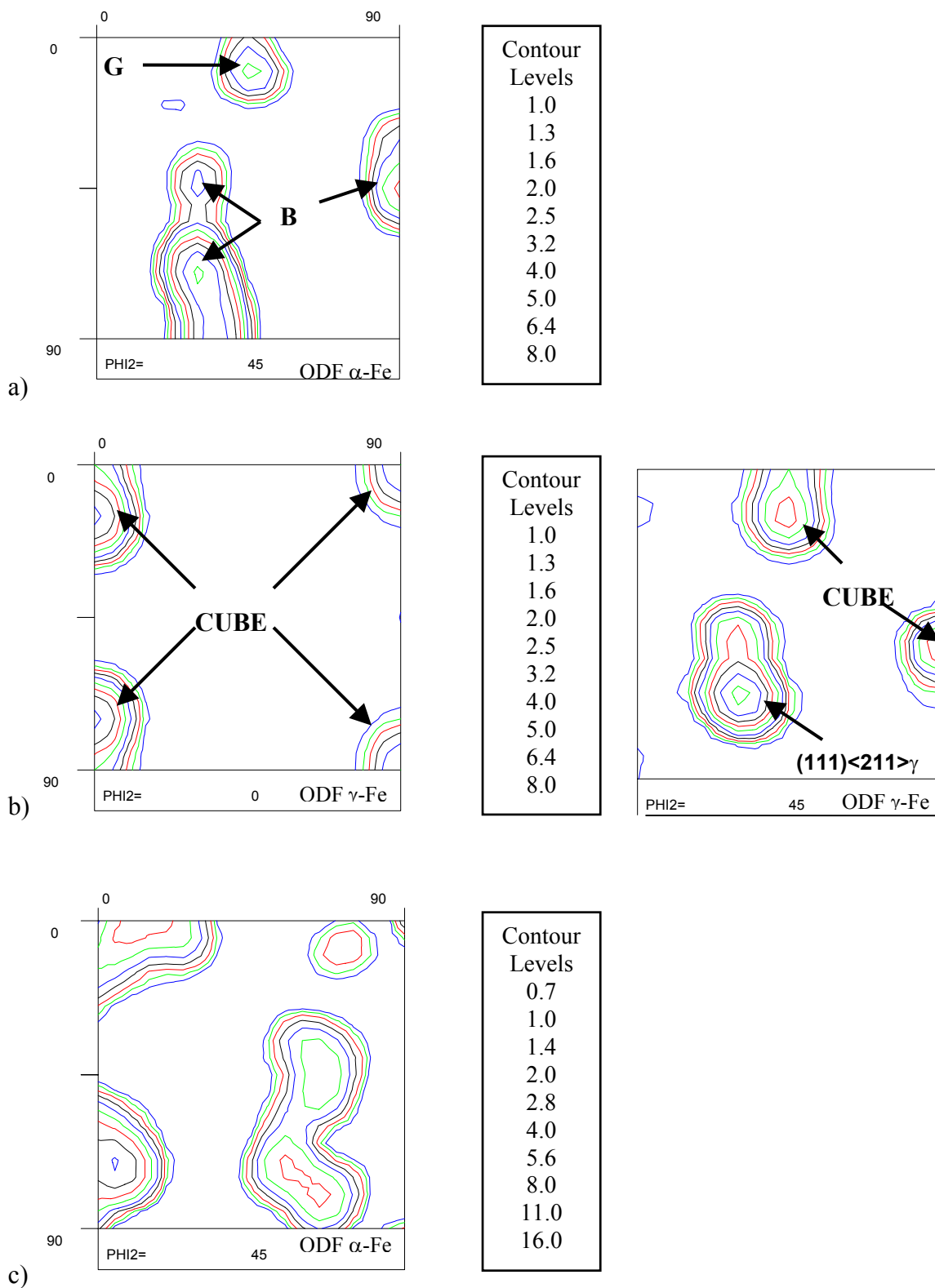
VII.4.3 CT = 550 °C

FigureVII.13: a) bcc bainite texture ODF section with $\varphi_2 = 45$ °. b) fcc residual austenite ODF sections with $\varphi_2 = 0$ ° and $\varphi_2 = 45$ °. c) calculated ODF for ferrite after KS transformation from the fcc texture. CT = 550 °C.

No primary ferrite was formed in samples coiled at 550 °C. The bcc phase detected by OIM was upper bainite of type B_3 accordingly to the Bramfitt-Speer classification:[22] acicular ferrite with a significant fraction of martensite/austenite (M/A) islands. FigureVII.13a shows the φ_2 = 45 ° ODF section. The ferrite cube texture component $(001)_\alpha \left[1\overline{3}0\right]_\alpha$ results from the transformation of the deformed austenite Goss $\{110\}_\gamma < 001 >_\gamma$ texture component. The other texture components found in bainitic ferrite have the orientations $(112)_\alpha \left[1\overline{3}1\right]_\alpha$, $(221)_\alpha \left[2\overline{3}2\right]_\alpha$ and $(223)_\alpha \left[1\overline{1}1\right]_\alpha$. They are ferrite texture components resulting from the decomposition of deformed austenite with the brass $\{110\}_\gamma < 112 >_\gamma$ orientation.

FigureVII.13b shows ODF sections with constant values of φ_2 calculated from the EBSP data for the retained austenite. The main component was the cube $\{001\}_\gamma<100>_\gamma$. In the $\varphi_2 = 45$ ° section of the ODF, a weak intensity texture component has an orientation close to the austenite Goss orientation. Indeed, the KS transformation of the residual austenite leads to a weak ferrite $(111)_\alpha \left[0\overline{1}1\right]_\alpha$ texture component. FigureVII.13c shows the result of the KS transformation applied to the residual austenite. It leads mainly to ferrite with the rotated cube orientation. It is clear from the comparison of FigureVII.13a and VII.13c, that the residual austenite and the austenite that transformed to bainite had a different orientation. The residual austenite could not transform to ferrite with the measured orientation, because it would mean that the bcc and fcc unit cell cubes would have to be parallel, whereas there must be a rotation angle of 45 ° between them according to the KS orientation relation.

VII.5 XRD results

XRD analyses of the samples also confirmed the presence of retained austenite in the samples coiled at 550 °C and corroborate the local texture measurements results. The diffractograms obtained for the samples coiled at 720 °C, 680 °C and 550 °C, respectively, are shown in FigureVII.14. Austenite diffraction peaks were observed in the sample coiled at 550 °C. In that sample, the volume fraction of retained austenite was estimated at 11 vol.%.[23] It must be noted that this value slightly overestimated the actual retained austenite content, as the presence of carbides is not taken into account. From the position of the austenite peaks, the lattice parameter of residual austenite was estimated to be $a_\gamma = 0.361$ nm, and the carbon content in the residual austenite was calculated to be $C_\gamma = 1.08$ wt.% at 20 °C using the equation from Onink:[24]

$$a_\gamma (nm) = (0.363067 + 0.0783/(1 + 0.2151(100/C - 1)))$$
$$\times (1 + (24.92 - 51/(1 + 0.2151(100/C - 1) \times 10^{-6}(T - 1000))$$

(VII.2)

where *T* is the temperature in K. In the sample coiled at 680 °C, the peaks were too small to allow a reliable determination of the austenite volume fraction. The intensities of diffraction peaks for both fcc and bcc phases are representative of the global texture in the material. Each diffraction peak corresponds to a fiber, *i.e.* a family of texture components with a common plan parallel to the sample surface. The highest intensity observed in FigureVII.14a was measured for the $(110)_\alpha$ diffraction plan in the bainite. It results from the transformation of

the brass and Goss texture components of deformed austenite. It must be noted that the peak intensity increased with the decreasing CT, which is in good agreement with the localization of the ferrite texture components observed previously. In FigureVII.14b no peak was measured for the $(220)_\gamma$ corresponding to the austenite α-fiber, containing the brass and Goss orientations. This confirms that the deformed austenite with the brass and Goss orientations fully transformed to ferrite or bainite. On the contrary, the intensity of the $(200)_\alpha$ peak was lower in bainite than in ferrite. This peak is related to the transformation products of austenite with the brass, Goss or cube orientations, *i.e.* partially or fully recrystallised austenite. Bainite formed preferentially from deformed austenite, and the retained austenite is essentially recrystallised austenite.
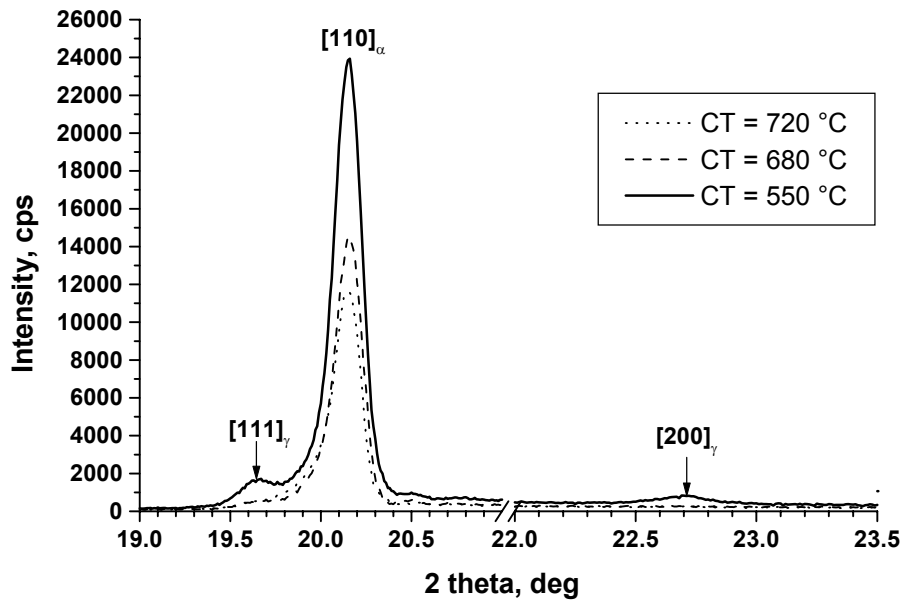
a)
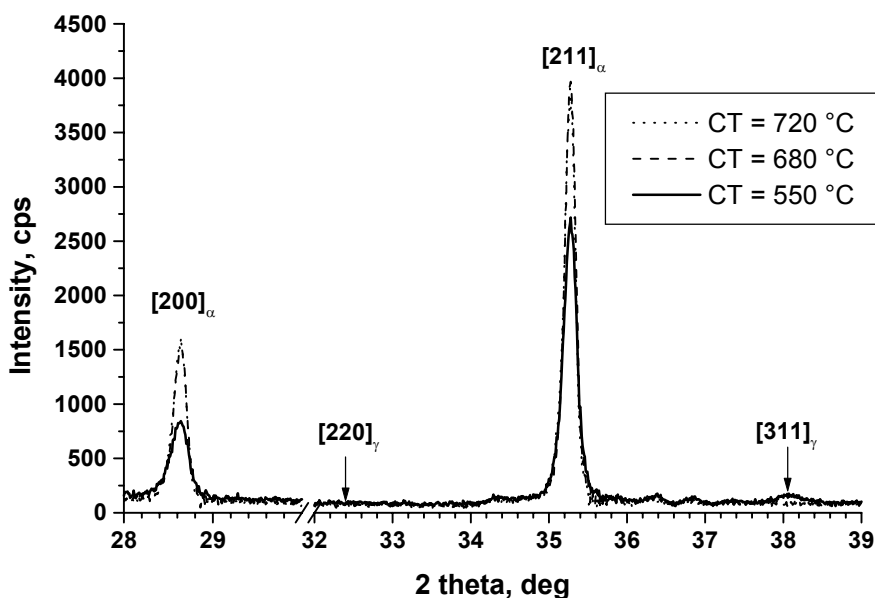
b)

FigureVII.14: X Ray diffractogram measured for hot rolled samples coiled at 720 °C, 680 °C and 550 °C, respectively.

VII.6 Discussion

From the results of texture measurements, it is clear that the deformed austenite transformed more easily to ferrite or bainite during cooling and/or coiling. Due to the high value of T_{nr}, only static recrystallisation is likely to occur in the austenite. It was found that the deformed austenite had mainly the brass orientation. This indicates that this austenite had a low SFE. Consequently, recovery is poor. The dislocations present in the non-recrystallised austenite thus provide numerous nucleation sites for ferrite. The retained austenite was found to be mainly recrystallised austenite. The austenite recrystallisation very likely occurred during the $\gamma \rightarrow \alpha_b$ transformation.

Table VII. 2: Main texture components of parent austenite and residual austenite for different CT.

| PHASES		CT = 720 °C	CT = 680 °C	CT = 550 °C
	Primary Ferrite	S, Brass, Goss	S, Brass	-
	Pearlite	S, Brass, Goss	-	-
	Bainite	-	S, Brass, Goss	Brass, Goss
	Residual Austenite	-	Brass, Cube	Goss, Cube

: from deformed γ
: from recrystallised γ

A summary of the parent austenite orientations that transform to ferrite as well as the orientation of the residual austenite is given in Table VII. 2. Note that the austenite texture components S, brass, Goss and cube correspond to a microstructural state that evolves continuously from deformed to fully recrystallised austenite. The cooling time between the last rolling pass, the type of transformation and its kinetics determine the time available for the recrystallisation of the deformed austenite. The distributions of soluble boron and alloying elements during the thermomechanical process have a strong effect on the kinetics of phase transformations. The presence of boron as alloying element in the studied steel is of particular importance. It is known that soluble boron segregates to grain boundaries and dislocations.[25,26] It was also found that segregation of boron occurred during cooling from the austenite region.[11,27] In samples containing deformed austenite, the soluble boron present in the austenite does not partition homogeneously. Due to sites competition and combined effects between the different alloying elements present in the steel, it is likely that the solute drag like effect (SDLE)[28,29] is favoured in samples with some deformed austenite. In hot rolled steel, this behaviour certainly appears and would be responsible for the alteration of the phase transformations kinetics at low temperature, during the very slow cooling during the coiling stage.

Coiling simulations were therefore carried out on dilatometer samples starting with different states of deformation in the austenite to test this assumption.

VII.7 Dilatometry

Coiling simulations at CT = 600 °C were done in a dilatometer. FigureVII.15a shows the dilatation curves for the different samples as a function of the temperature. FigureVII.15b shows the length change due to the austenite decomposition as a function of the time from the beginning of the coiling simulation.
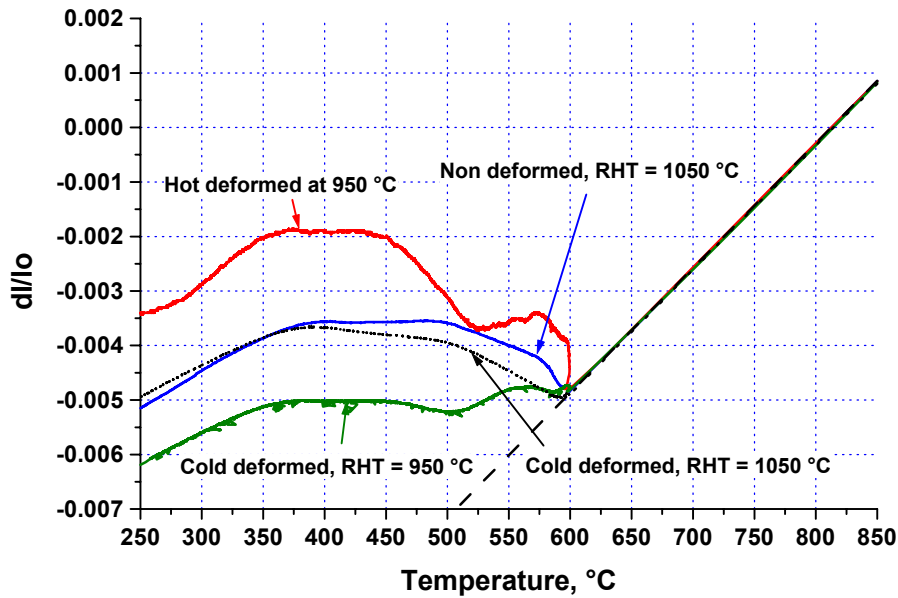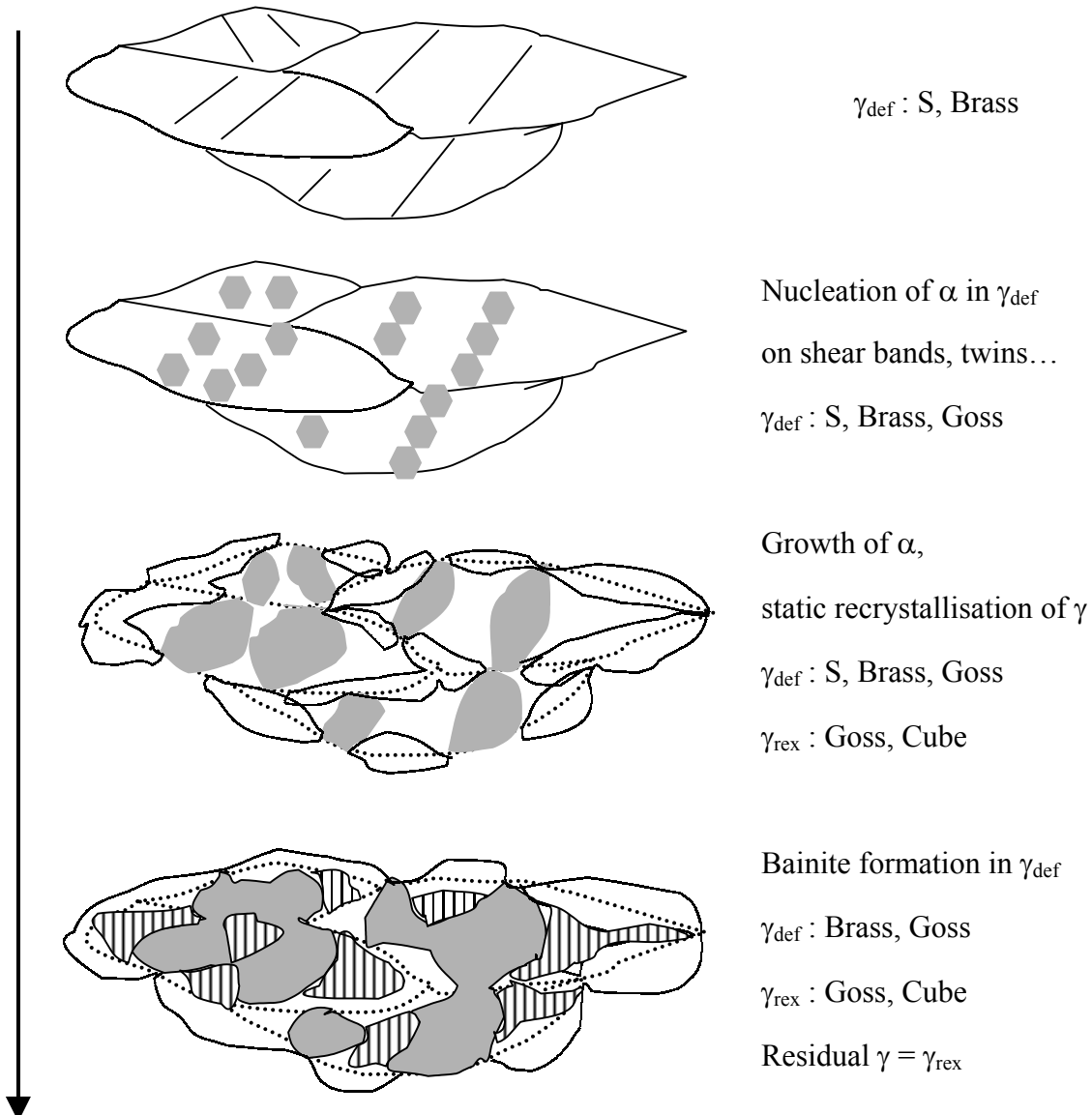

a)
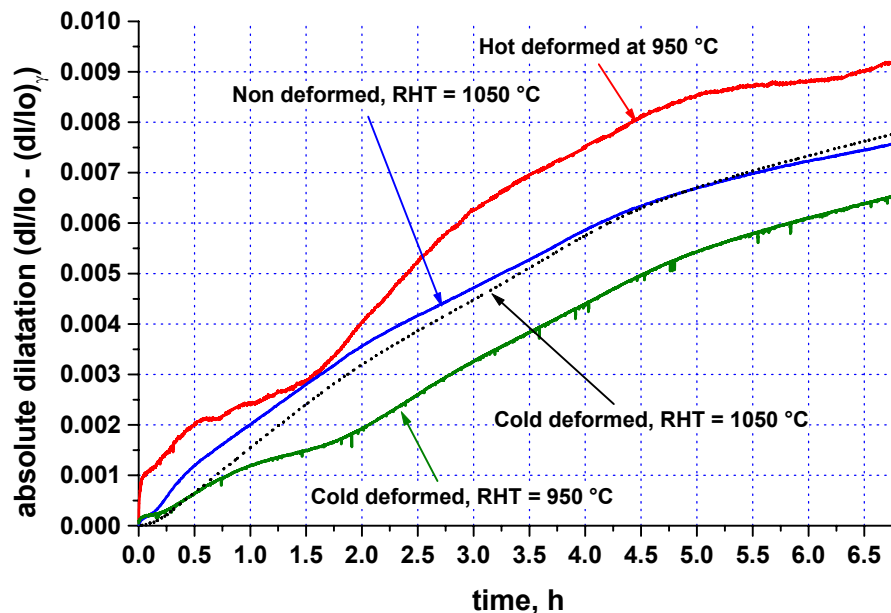
b)

FigureVII.15: Dilatometric curves showing the effects of austenite grain size and state of recrystallisation on the transformation behaviour during coiling from CT = 600 °C.

a) Hot deformed at 950 °C.

γ_{def} : S, Brass

Nucleation of α in γ_{def}

on shear bands, twins…

γ_{def} : S, Brass, Goss

Growth of α,

static recrystallisation of γ

γ_{def} : S, Brass, Goss

γ_{rex} : Goss, Cube

Bainite formation in γ_{def}

γ_{def} : Brass, Goss

γ_{rex} : Goss, Cube

Residual $\gamma = \gamma_{rex}$

b) Not deformed. RHT = 1050°C.

γ_{rex} : Brass, Goss, <u>Cube</u>

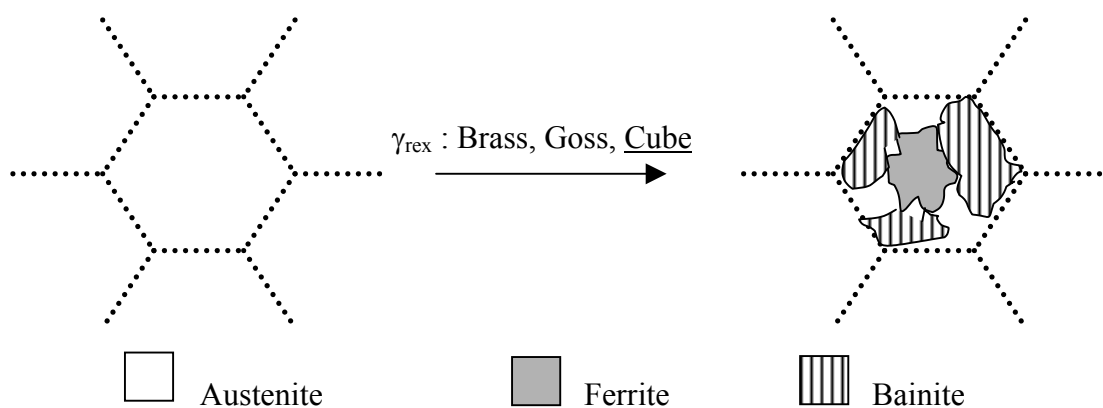☐ Austenite   ▨ Ferrite   ⫴ Bainite

FigureVII.16: Schematic representation of the effects of the initial austenite texture, grains size and deformation state on the transformations during coiling at 600 °C. a) sample hot deformed, b) non deformed sample with RHT = 1050 °C.

In all samples the decomposition of austenite led to a microstructure consisting of ferrite, bainite, martensite and retained austenite. The sample deformed at 950 °C had the fastest austenite decomposition. In that sample, it is very likely that no partitioning of B occurred after deformation. As a consequence, the deformed austenite contains many free dislocations and defects acting as nucleation sites for the ferrite formation.
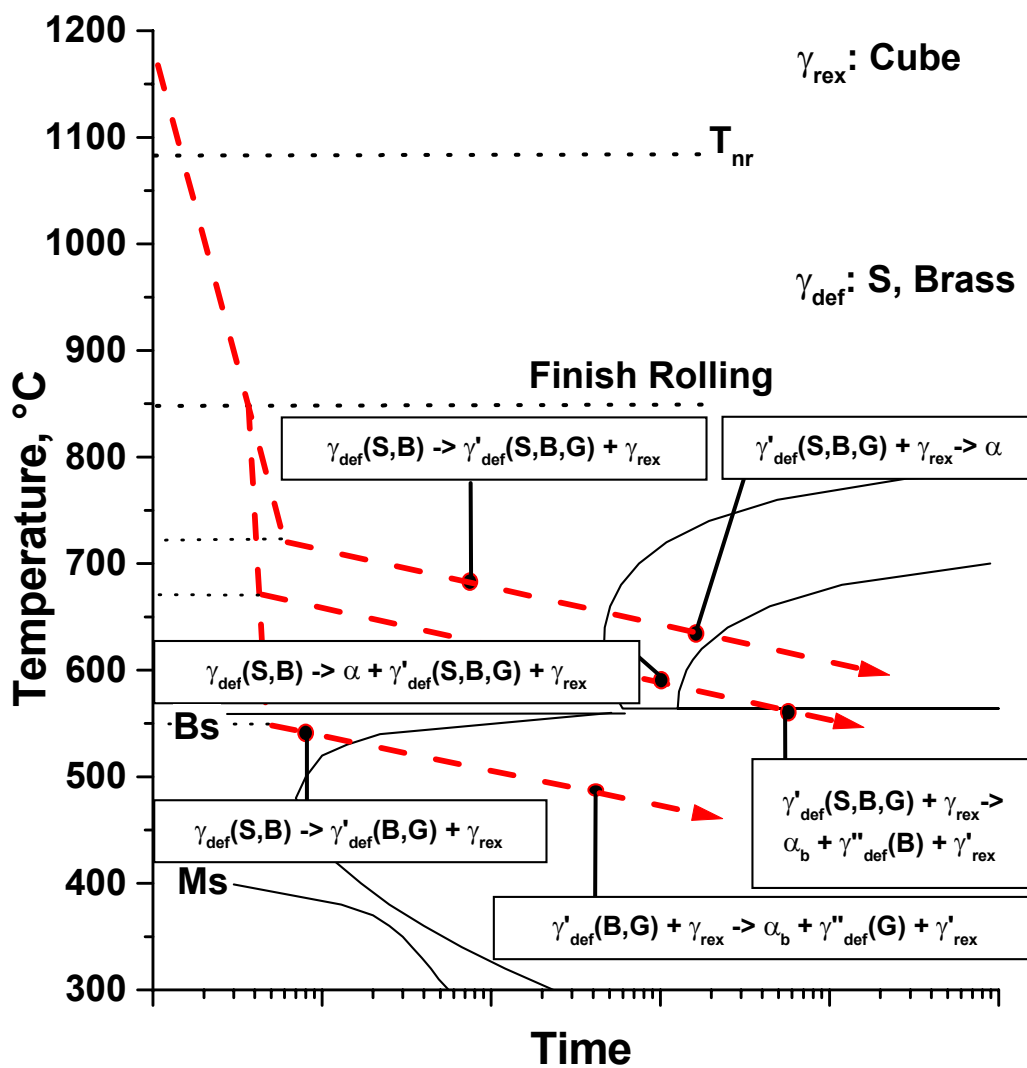
Partial recrystallisation of the austenite probably occurs during the $\gamma \rightarrow \alpha$ transformation, which would explain the higher dilatation observed in the hot-deformed sample. As the deformed γ grains are small, the initially fast growth of α is limited and a transformation stasis is observed. The bainitic transformation then starts when the undercooling is sufficient.

In both non-deformed and cold-deformed samples reheated at 1050 °C, the transformation behaviour of the austenite was very similar. The same annealing temperature and time resulted austenite with similar grains size in both samples. The austenite grains containing few defects had a low SFE and few nucleation sites for the ferrite formation, if it is considered that ferrite did not nucleate preferentially at γ grain boundaries due to the presence of B. When ferrite formed within the austenite grains, its growth was not limited by the austenite grains size. As a consequence no transformation stasis was observed between the ferrite and bainite formations. Finally, the sample cold-deformed and reheated at 950 °C had small recrystallised γ grains containing few defects, thus few nucleation sites, due to the lower temperature of austenitisation. As a consequence, the kinetics of austenite decomposition was the slowest in that sample and transformation stasis was observed. FigureVII.16 represents schematically the mechanisms of austenite decomposition and the evolution of its original texture in different kinds of samples.

VII.8 Conclusions

Local texture measurements were performed using the OIM-EBSD technique on a Nb-alloyed complex phase hot rolled CMnMoCrB steel coiled at CT = 720 °C, 680 °C and 550 °C. The analysis of hot-rolling data showed that no dynamic recrystallisation occurred during the rolling. EBSD Measurements supplemented with XRD showed that up to 11 vol.% austenite was retained in the sample coiled at 550 °C. The retained austenite was mainly recrystallised. Dilatometry was performed on samples with different states of deformation in the austenite to see whether the rolling conditions had real implications on the phase transformations. In samples containing deformed austenite, the bainite transformation was strongly retarded due to the combination of small grains size and the presence of microalloying elements such as B responsible for SDLE. As no dynamic recrystallisation of the austenite occurred during the rolling process, static recrystallisation occurred in the course of the phase transformation. As a result, the final microstructure contained metastable recrystallised austenite, and low temperature transformation products such as bainite and martensite, with high densities of immobile dislocations, which are probably responsible for the continuous yielding behaviour observed during tensile testing hot rolled steels coiled at CT below 650 °C.

FigureVII.17 summarizes the evolution of the austenite texture in the present steel during hot-rolling, cooling, and coiling. The rolling below T_{nr} produced essentially deformed austenite with the main texture components S and brass. Due to the slow cooling between the end of the rolling and the coiling at 720 °C, the deformed austenite recrystallised statically partially. This leads to austenite with the texture components S, brass, Goss and cube. During the $\gamma \rightarrow \alpha$ transformation, ferrite was formed from both recrystallised and deformed austenite. Due to the segregation of alloying elements, the state of deformation in the austenite was homogeneous and a clear variant selection occurred. Primary ferrite nucleation likely occurred in the deformed austenite with the S orientation. The presence of both the cube and rotated cube texture components in ferrite showed that the recrystallisation of the austenite occurred during the $\gamma \rightarrow \alpha$ transformation. In the ferrite-pearlite bands, the ferrite formed from the S, brass and Goss texture components of the austenite. It was remarkable that a clear α-fiber was present in the ODF, showing that the banding depends on the parent austenite orientation.

FigureVII.17: Schematic representation of the evolution of the austenite texture during the coiling at 720 °C, 680 °C and 550 °C, respectively.

In the sample coiled at 680 °C, the faster cooling between the end of rolling and CT did not allow a partial recrystallisation of the austenite, and the primary ferrite formed from deformed austenite with the S and brass texture components. Static recrystallisation of the austenite occurred during the $\gamma \rightarrow \alpha$ transformation, and bainite formed from both deformed austenite with the orientations S, brass and Goss, and recrystallised austenite with the cube orientation. The ODF for ferrite had the highest intensities for the texture components resulting from the transformation of the austenite with the brass orientation.

Bainite mainly resulted from the transformation of austenite with the Goss orientation. A clear rotation of $\varphi_1 = 30\,°$ occurred in the austenite between the ferrite and the bainite formations. The steel coiled at 550 °C consisted of B_3 bainite with M/A islands. In this microstructure the S orientation of deformed austenite did not lead to a clear ferrite texture component. This means that the texturing of the ferrite did not occur due to the recrystallisation of austenite before the bainitic transformation. The bainite was found to form from the brass and Goss orientations of deformed austenite. The residual austenite was mainly recrystallised, with the cube orientation.

In recent publication of the research group of Bhadeshia[30] a possible alternative explanation for the present observation, is made; Singh *et al.*[31] and Shipway *et al.*[32] propose that the slower bainitic transformation observed when the parent austenite phase is in a plastically deformed state is due to the mechanical stabilization of the austenite. In this model the bainitic transformation is impeded by the presence of dislocations, which limits the growth of the bainite laths.

References

[1] B. Hutchinson, L. Ryde, E. Lindh, K. Tagashira: <u>Mater. Sci. Eng. A.</u>, A257, 1998, p.9.

[2] H.K.D.H. Bhadeshia: 'Bainite in Steels', Second Edition, 2001, IOM communications, p.351.

[3] R.K. Ray, J.J. Jonas: <u>International Materials Reviews</u>, 35, 1990, p.1.

[4] G. Kurdjumov, G. Sachs: <u>Z. Phys.</u>, 64, 1930, p.325.

[5] E.C. Bain : <u>Trans. AIME</u>, 70, 1924, p.25.

[6] Z. Nishiyama: <u>Sci. Rep. Tohoku Imp. Univ.</u>, 1934/1935, 23, p.638.

[7] M.P. Butrón-Guillén, C.S. Da Costa Viana, J.J. Jonas: <u>Metallurgical and Materials Transaction A</u>, 28A, 1997, p.1755.

[8] M. De Meyer, L. Kestens, L. Tosal-Martinez, B.C. De Cooman: <u>Materials Science and Technology</u>, 17, 2001, p.1353.

[9] T. Waterschoot, L. Kestens, B.C. De Cooman: 'Hot Rolling Texture Development in CMnCrSi Dual Phase Steels', <u>Metallurgical and Materials Transaction A</u>, *in press*.

[10] D.T. Llewellyn: <u>Ironmaking and Steelmaking</u>, 20, (5), 1993, p.338.

[11] Ph. Maitrepierre, J. Rofes-Vernis, D. Thivellier: in 'Boron in Steel', (ed. S.K. Banerij and J.E. Morral), 18 september 1979, Milwaukee, Wisconsin, USA, p.1.

[12] T.M. Maccagno, J.J. Jonas, S. Yue, B.J. McCrady, R. Slobodian, D. Deeks: <u>ISIJ International</u>, 34, (11), 1994, p.917.

[13] F. Boratto, R. Barbosa, S. Yue, J.J. Jonas: Proc. Int. Conf. Physical Metallurgy of Thermomechanical Processing of Steels and Other Metals (THERMEC '88); ed. I. Tamura, ISIJ, Tokyo, 1988, p.383.

[14] F.S. LePéra: <u>J. Metals</u>, 32, (3), 1980, p.38

[15] M.V. LI, D.V. Niebuhr, L.Y. Meekisho, D.G. Atteridge: <u>Metallurgical and Materials Transaction B</u>, 29B, 1998, p.661

[16] I.F. Hughes: <u>Metallurgical Transactions</u>, vol.2, april 1971, p.929.

[17] G.E. Dieter: 'Mechanical Metallurgy', (SI Metric Editions), 1988, p.201.

[18] D.T. Llewellyn, D.J. Hillis: <u>Ironmaking and Steelmaking</u>, 23, (6), 1996, p.471.

[19] R. Grossterlinden, R. Kawalla, U. Lotter, H. Pircher: <u>Steel Research</u>, 63, (8), 1992, p.331.

[20] T.A. Kop, J. Sietsma, S. Van der Zwaag: <u>Materials Science and Technology</u>, 17, 2001, p.1569.

[21] H. Réglé, S. Lanteri : <u>Materials Science Forum</u>, 273-275, 1998, p.447.

[22] B.L. Bramfitt, J.G. Speer: Metallurgical and Materials Transaction A, 21A, 1990, p.817

[23] M. De Meyer, D. Vanderschueren, K. De Blauwe, B.C. De Cooman: Proc. 41st Conf. on 'Mechanical Working and Steel Processing', Baltimore, MD, USA, October 1999, ISS, p.483.

[24] M. Onink, C.M. Brakman, F.D. Tichelaar, E.J. Mittemeijer, S. van der Zwaag, J.H. Root, N.B. Konyer: Scripta Metallurgica at Materialia, 29, (8), 1993, p.1011.

[25] Y.Ohmori, K.Yamana: in 'Boron in Steel', (ed. S.K. Banerij and J.E. Morral), 18 september 1979, Milwaukee, Wisconsin, USA, p.44.

[26] B.J.Thomas, G.Henry: in 'Boron in Steel', (ed. S.K. Banerij and J.E. Morral), 18 september 1979, Milwaukee, Wisconsin, USA, p.80.

[27] Y. Shen and K.A. Taylor: Proc. 40th Conf. on 'Mechanical Working and Steel Processing', 1998, ISS, p.837.

[28] G.J. Shiflet, H.I. Aaronson: Metallurgical Transactions A, 21A, 1990, p.1413.

[29] W.T. Reynolds, Jr., S.K. Liu, F.Z. Li, S. Hartfield, H.I. Aaronson: Metallurgical Transactions A, 21A, 1990, p.1479.

[30] H.K.D.H. Bhadeshia: Materials Science and Engineering A, A273-275, 1999, p.58.

[31] S.B. Singh and H.K.D.H. Bhadeshia: Materials Science and Technology, Vol. 12, 1996, p. 610.

[32] P.H. Shipway, H.K.D.H. Bhadeshia: Materials Science and Technology, Vol. 11, 1995, p.1116.

CHAPTER VIII

Microstructure, mechanical properties and strain hardening behaviour of hot-rolled C-Mn steels

VIII.1   Introduction

Bainitic steels are complex, heterogeneous and multiphase in nature. The presence of other microconstituents in minor amounts is known to have a very pronounced effect on the final properties of the steels. The study of the microstructure-properties relations for bainitic steels is limited if it is not accompanied by a discussion of the morphology of the type of bainite, which influences their mechanical behaviour.

This chapter deals with the analysis of the transformation behaviour in hot rolled high strength low-carbon CMn steels containing 1.5 wt.% Mn and alloyed with low concentrations of elements which can stabilize the undercooled austenite. The mechanical properties of these multiphase steels with a predominantly bainitic matrix and various micro structural features resulting from the use of different coiling temperatures were especially analysed for further development of the composition to obtain a high tensile strength bainitic steel with an adequate elongation.

The chemical composition of the steels and their thermo-mechanical processing are traditionally used to control both their microstructure and mechanical properties. A large number of high strength bainitic steels based on a CMn steel with additions of Cr, Mo, Si, and micro-alloying additions of B, Ti and Nb have been developed recently.[1,2,3] The effects of the elements Cr, Mo and B on the microstructure formation were studied in detail in chapters V and VI. Ti and Nb cause precipitation strengthening. Ti prevents the formation of BN precipitates and Nb retards the recrystallization of γ and the grain growth by forming fine carbides. Therefore, Ti and Nb control the state of the hot rolled γ before transformation, to obtain small grain sizes and precipitation hardening.

The effect of these elements on the tensile strength of the steel strip continuously cooled after hot rolling is usually expressed by regression formulas that do not take into account the thermal cycle and the final microstructure.[1,3] The formation of the hot rolled microstructure of a bainitic steel results from both the thermomechanical processing in the γ phase region and the transformation temperature and time after rolling. The traditional representation of the transformation behaviour with continuous cooling transformation (CCT) or time-temperature transformation (TTT) diagrams does not reflect a real industrial cycle including the hot rolling, the run-out table cooling pattern and the slow cooling of the coiled sheet. The thermal cycle of hot-rolled sheet steels usually includes the first stage of accelerated cooling from the temperature of the final hot rolling pass to the second stage of slow cooling corresponding to

the coiling operation. Investigations of transformation in bainitic steels alloyed with Mo, Cr and B were reported in chapter VI. They revealed clearly delayed kinetics of the transformation reactions, in particular the ferrite formation was suppressed, leading to bainitic microstructures.[2,4,5,6] This implies that there is a possibility that much of the microstructural features are formed in a wide temperature interval during the very slow cooling of the coiled strip. The present contribution focuses on the features of microstructure and transformation behaviour for high-performance ferrous alloys during the specific thermal cycle undergone by the hot strips when coiled in the temperature range of 300 - 650 °C.

VIII.2   Experimental procedure

The compositions of steels used in the present work are given in Table VIII.1. The selection was based on two carbon content levels of about 0.05 and 0.15 wt.% and manganese content about 1.5 ± 0.1 wt.%. Additional alloying with Mo, Mo+B and Mo+Cr+B was used to influence the transformation behaviour in the diffusional and intermediate ranges. Ti was added mainly to avoid the loss of interstitial B due to the formation of boron nitride and $Fe_{23}(C,B)_6$ during the hot rolling. Nb and the excess Ti are active as austenite grain size refiners and increase the strength as a result of their precipitation-hardening effects. The Si content was lower than 0.24 wt.% and the P concentration was lower than 0.020 wt.%.

Table VIII.1: Chemical composition of laboratory cast 1.5%Mn steels, in wt.%.

Steel	C	Mo	Cr	Nb	Ti	B	T_{nr}[7], °C	Steel Type
1	0.039	-	-	0.032	0.100	-	1085	micro-alloyed CMn, low C steel
2	0.155	-	-	0.106	0.082	-	1323	micro-alloyed CMn steel
3	0.145	0.21	-	0.083	0.069	-	1304	Mo-added micro-alloyed CMn steel
4	0.066	0.24	-	0.047	0.023	0.0016	1189	MoB-added micro-alloyed CMn, low C steel
5	0.163	0.19	-	0.072	0.054	0.0018	1302	MoB-added micro-alloyed CMn steel
6	0.161	0.20	0.43	0.061	0.023	0.0021	1233	MoCrB-added micro-alloyed CMn steel

The ingots were cut into blocks with 25 mm thickness and, after reheating at 1250 °C for 1 hour, were hot rolled in 6 passes to the final thickness of 2 mm. The final reduction of 30 % was carried out above 850 °C.

This temperature is lower than the predicted non-recrystallisation temperature of austenite, T_{nr}[7]:

$$T_{nr} = 887 + 464C + 890Ti + 363Al - 357Si + 6445Nb - 644\sqrt{Nb} + 732V - 230\sqrt{V} \qquad \text{(VIII.1)}$$

Hot rolling was followed by accelerated cooling at a rate of 30 °C/s to the coiling temperature, which was varied in the range from 650 °C to 300 °C.

After a coiling simulation for 5 hours with an average cooling rate 50 °C/h, the samples were air cooled to ambient temperature.

Dilatometer samples from the steel composition 6 in Table VIII.1 were heated at 10 °C/s to the temperature of austenitization 1050 °C, soaked 5 minutes and then cooled at 5 °C/s to 850 °C. The rate of cooling to the start temperature of coiling was 30 °C/s. Coiling simulations were performed with the constant cooling rate of 50 °C/h. The samples were then tempered 6 hours at 550 °C to decompose the eventual residual austenite into carbides and ferrite.

LePèra[8] and Nital etched transversal (TD) and longitudinal (RD) cross-sections were used for microstructure characterization by both scanning electron microscopy (SEM) and light optical microscopy (LOM). The volume fraction of retained austenite was measured by means of X ray diffraction. Mechanical properties were determined on an Instron tensile testing machine using flat 80 mm gauge length samples.

VIII.3 Dilatometry simulations and microstructure

The study focused on features of transformation behaviour of the MoCrB added CMn steel 6, with the composition given in Table VIII.1, during coiling in the 550-650 °C temperatures range. Indeed, a high strength-plasticity value was obtained after rolling and coiling the steel 6 in this temperature range. A multiphase high performance state was found in that steel under the condition of a low cooling rate from a wide temperatures region. Coiling the steel from temperatures up to 100 °C above the bainitic transformation start temperature, B_s, produced similar mechanical behaviours. Sufficient volume fraction of bainite was found in the microstructure after coiling at 600-650 °C, implying delayed kinetics of diffusional transformation.
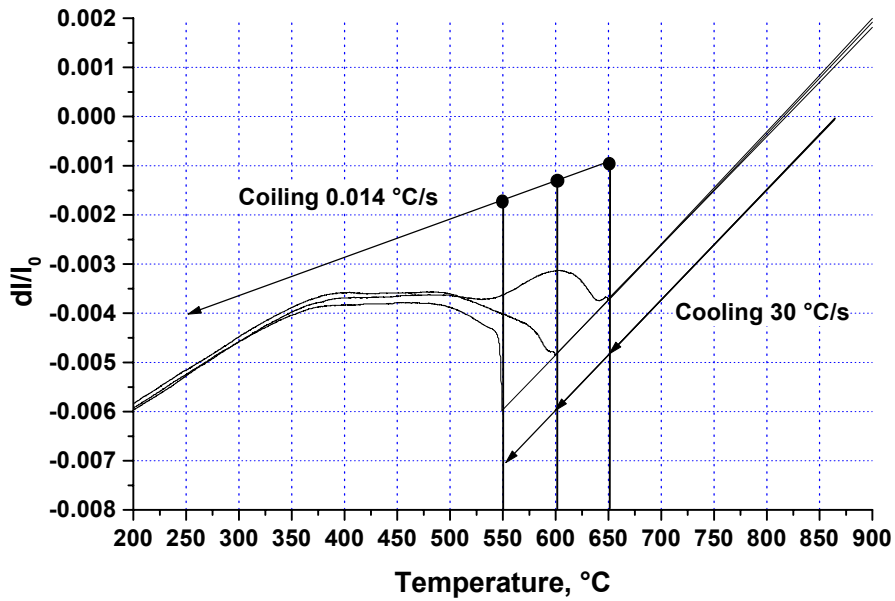
Figure VIII.1: Dilatometer curves after coiling simulations with CT = 550 °C, 600 °C and 650 °C.

The transformation behaviour of the steel reheated to 1050 °C for 5 minutes and coiled at different temperatures can be seen in Figure VIII.1. The temperature of coiling affected only the beginning of the process, while the transformation of most of the austenite was found to be almost independent of the variation of the coiling start temperature.
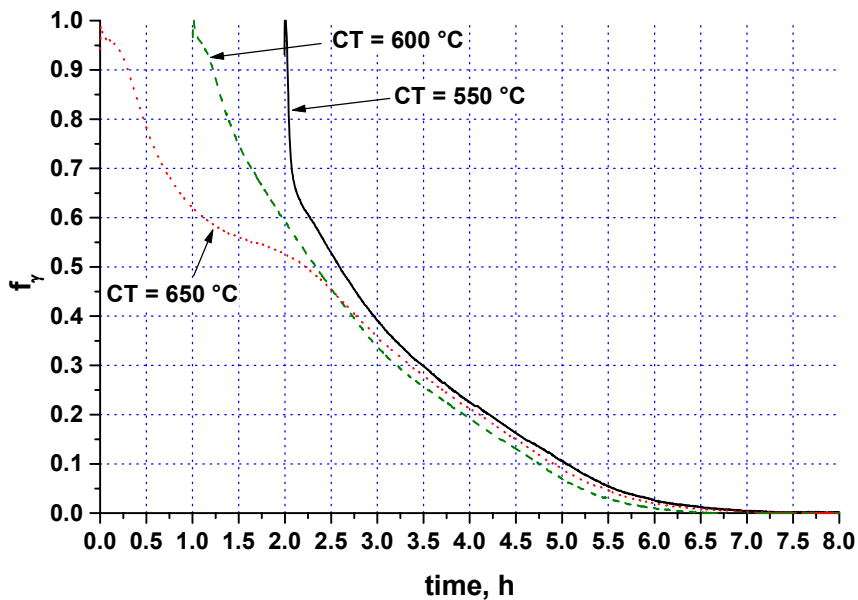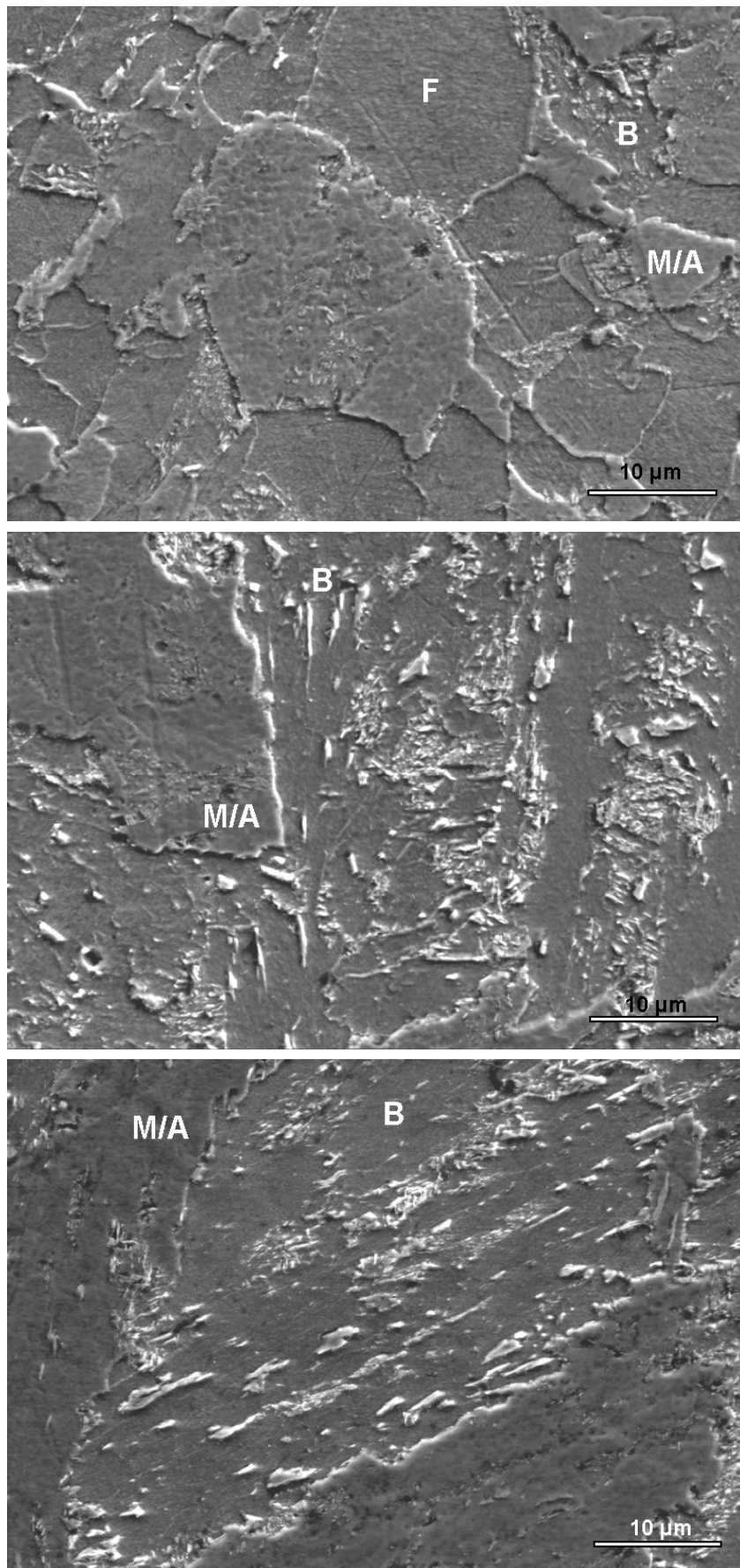

FigureVIII.2: Fraction of austenite decomposed as a function of the cooling time during coiling from CT = 650 °C, 600 °C and 550 °C, respectively.

It can be seen in FigureVIII.2 that about 40-50 vol.% of ferrite was formed in the steel coiled at 650 °C, when the remaining austenite started to transform to bainite.

FigureVIII.3: SEM Microstructures obtained after coiling simulations on steel 6 with from top to bottom CT = 650 °C, CT = 600 °C and CT = 550 °C. F = Ferrite, B = Bainite, M/A = Martensite/Austenite. Etchant: LePera.

Decreasing the coiling temperature to 550 °C increased the rate of ferrite or bainite formation, but below about 530 °C, the kinetics of the austenite decomposition was very similar and independent on the coiling temperature. Moreover, below 420 °C about 10-15 vol.% of the austenite transformed to low temperature decomposition products such as lower bainite and martensite. The presence of the latter phase is likely responsible for the continuous yielding behaviour observed in the hot rolled plates coiled below CT = 650 °C. SEM observation confirmed the morphological correspondence of these microstructural elements with typical microconstituents found in hot rolled steel coiled in similar temperature regions.

The microstructure of samples after dilatometer tests is presented in FigureVIII.3. In the sample coiled at 650 °C, polygonal ferrite was present with bainite and martensite. In the samples coiled below 600 °C, small islands containing both austenite and martensite (M/A islands) were observed between laths of granular and elongated shape. Carbides were also found between bainite laths and inside tempered martensite. The decomposition of M/A islands in ferrite and fine carbides was observed during the tempering at 550 °C for 6 hours. Fine carbide precipitations decorating cell boundaries were found in the tempered bainitic ferrite.
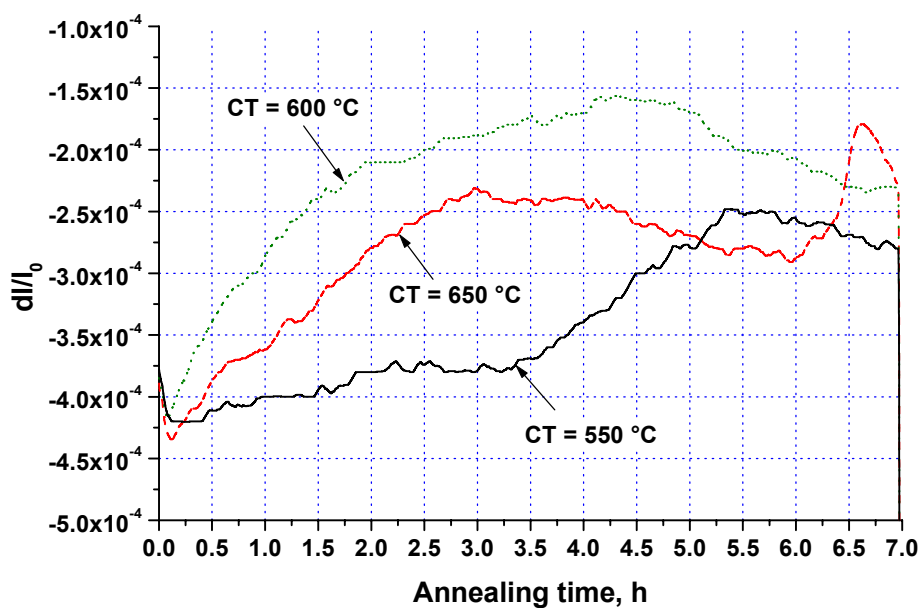
FigureVIII.4: Relative length changes measured during the isothermal annealing at 550 °C of steel 6 after the coiling simulation at 550 °C, 600 °C and 650 °C.

These microstructural changes were in good agreement with dilatometer data of isothermal tempering at 550 °C. It can be seen in FigureVIII.4 that both the volume expansion attributed to the austenite decomposition and the volume reduction corresponding to the carbide precipitations from the ferrite and the austenite phases [9] at a later stage induced respectively a dilatation and a contraction during holding at 550 °C. Note that during holding at 550 °C the volume expansion started at a later stage in the sample coiled at 550 °C than in samples coiled at higher temperatures. This is very likely due to the enhanced stability of the retained austenite formed at lower temperatures.

The maximum dilatation observed for the steel coiled at 600 °C corresponded to a volume increase of 0.075 % due to the austenite transformation to bainite.

VIII.4   Microstructure of hot rolled steels

Microstructural diagrams based on the SEM and LOM investigations of hot-rolled steels are presented in FigureVIII.5. It can be seen that the type of microstucture formed at the different coiling temperatures is strongly influenced by the steel composition. The 0.039 wt.% C alloyed CMn steel 1 (FigureVIII.5a) had a fully ferrite microstructure after coiling at 650 °C and 600 °C. A decrease of the coiling temperature led to a gradual substitution of the ferritic component by bainite. However, the volume fraction of the ferrite and bainite remained almost unchanged for coiling temperatures below 450 °C in spite of the higher martensite start temperature M_s, which was calculated to be 480 °C using the M_s formula due to Kung *et al.*:[10]

$$M_s(°C) = 539 - 423C - 30.4Mn - 17.7Ni - 12.1Cr - 7.5Mo + 10Co - 7.5Si \qquad (VIII.2)$$

This was likely due to the low austenite stability in both the bainitic and ferritic regions of transformation. This resulted in a partial suppression of the austenite to pro-eutectoid ferrite transformation even for a cooling rate of 30 °C/s. In this composition, it is believed that the bainitic microstructure was formed mainly during the cooling preceding the quasi-isothermal holding for lower temperatures of coiling simulation. The low carbon concentration and the limited alloying promote a fast decomposition of the undercooled austenite into pro-eutectoid ferrite and bainite. Microstructures formed in the sample coiled at 500 °C and at 400 °C were similar (FigureVIII.6a and 6b) and contained upper bainite of type B_3 according to the Bramfitt-Speer bainite classification introduced in chapter I:[11]

- B_1 = Acicular ferrite with intralath (plate) precipitation:

- cementite ($B_1{}^c$) ;

- epsilon carbide ($B_1{}^\varepsilon$);

- B_2 = Acicular ferrite with interlath (plate) particles or films:

- cementite ($B_2{}^c$) ;

- austenite ($B_2{}^a$);

- martensite ($B_2{}^m$);

- B_3 = Acicular ferrite with "discrete-island" constituent:

- austenite ($B_3{}^a$);

- martensite ($B_3{}^m$);

- pearlite ($B_3{}^p$).

It contained extremely low amounts of "discrete islands" constituents due to the low carbon concentration. Traces of fine polygonal ferrite were also found in some areas.
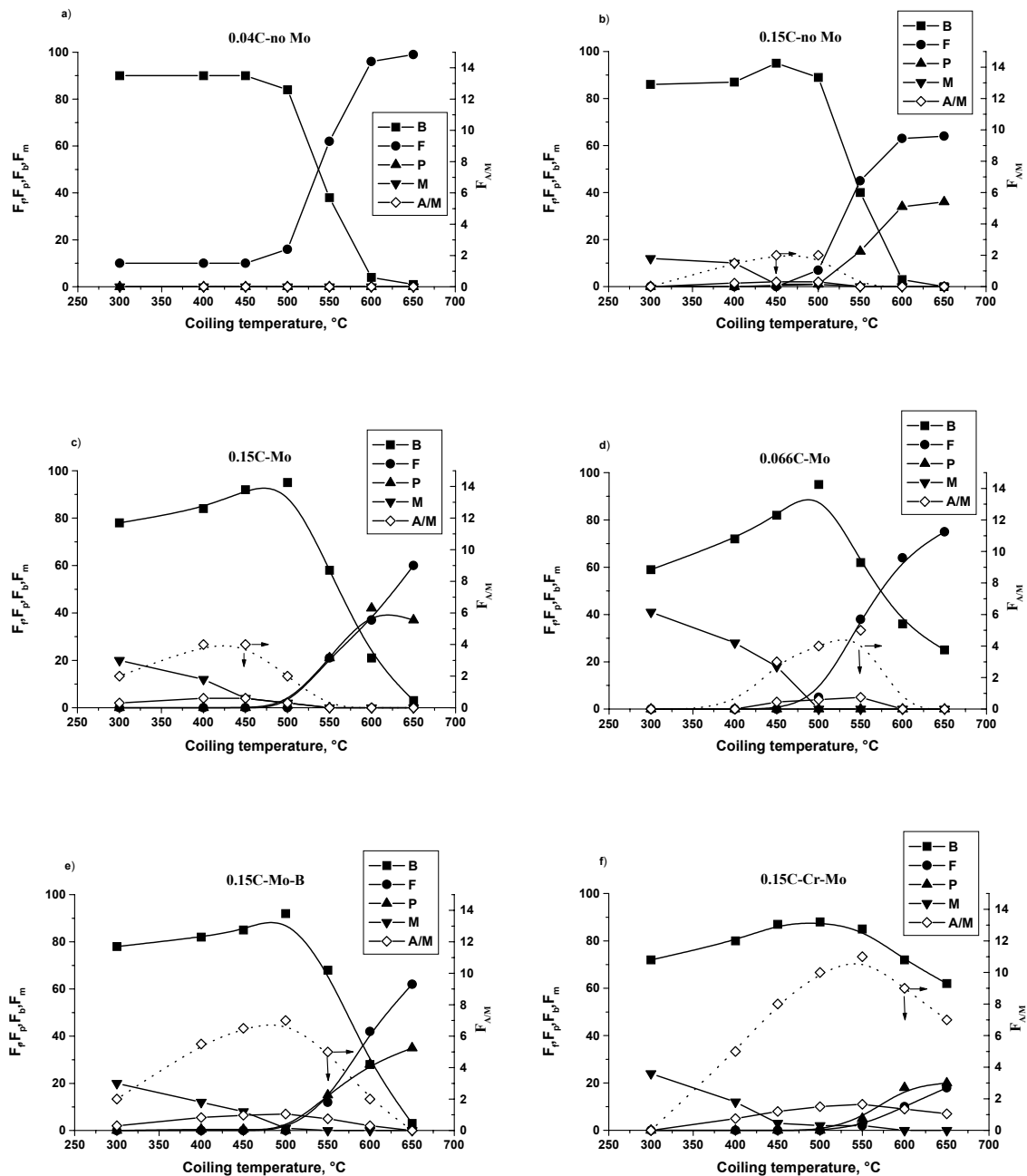
FigureVIII.5: Microstructural diagrams of investigated steels.

The microstructure of steels with higher carbon content was different (FigureVIII.5b). Coiling the 0.16 wt.% C CMn steel 2 at 650 °C and 600 °C led to the formation of a typical ferrite-pearlite microstructure. A decrease of the coiling temperature in this range did not result in notable changes of the volume fraction of the constituent but initiated a natural refinement of the ferrite grain size and a transition from the pearlite to troostite, degenerated pearlite, morphology of the second microstructure component. At a coiling temperature of 550 °C the start of the upper bainite formation was observed. A microstructure containing ferrite, bainite and troostite was found after coiling at this temperature. Decreasing the coiling temperature down to 500 °C or 450 °C provided a fully bainitic microstructure.
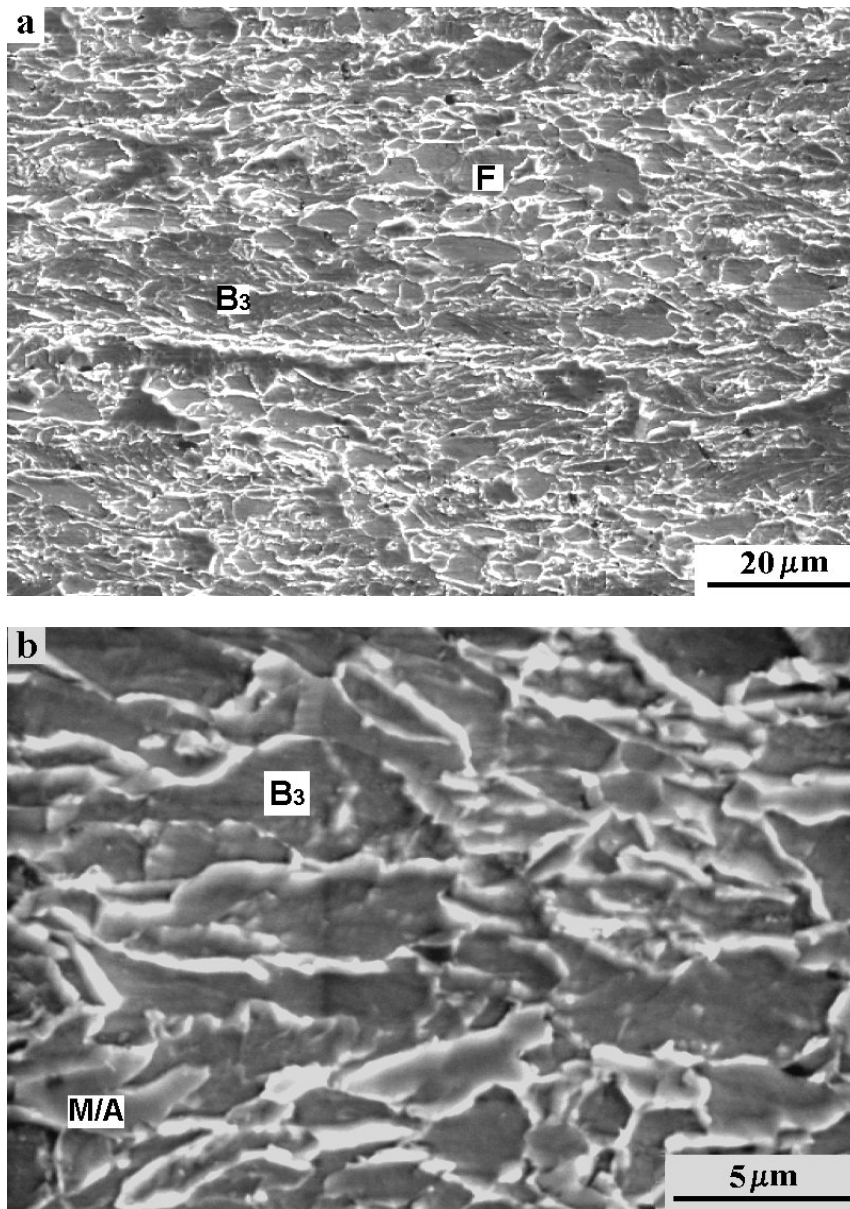
FigureVIII.6: Microstructure of steel 1 after coiling (a) at 500 °C, (b) at 400 °C.

Alloying a low C CMn steel with molybdenum (steel 3) resulted in a substantial change of the microstructure (FigureVIII.5c). The volume fraction of pearlite (troostite) after coiling at 650 °C and 600 °C increased slightly in comparison to the molybdenum-free CMn steel. Moreover the formation of ferrite at 550-600 °C was suppressed. The start of the bainite formation was found to occur during coiling below 650 °C in this steel. The microstructure formed by this treatment consisted of troostite, ferrite and B_3 type bainite with small islands of second phase (FigureVIII.7a). As the coiling temperature decreased, the ferrite-pearlite areas disappeared and a B_2 type bainite appeared with more pronounced interlath film-like precipitates (FigureVIII.7b). Some of the precipitates had a clear discrete interlath morphology.
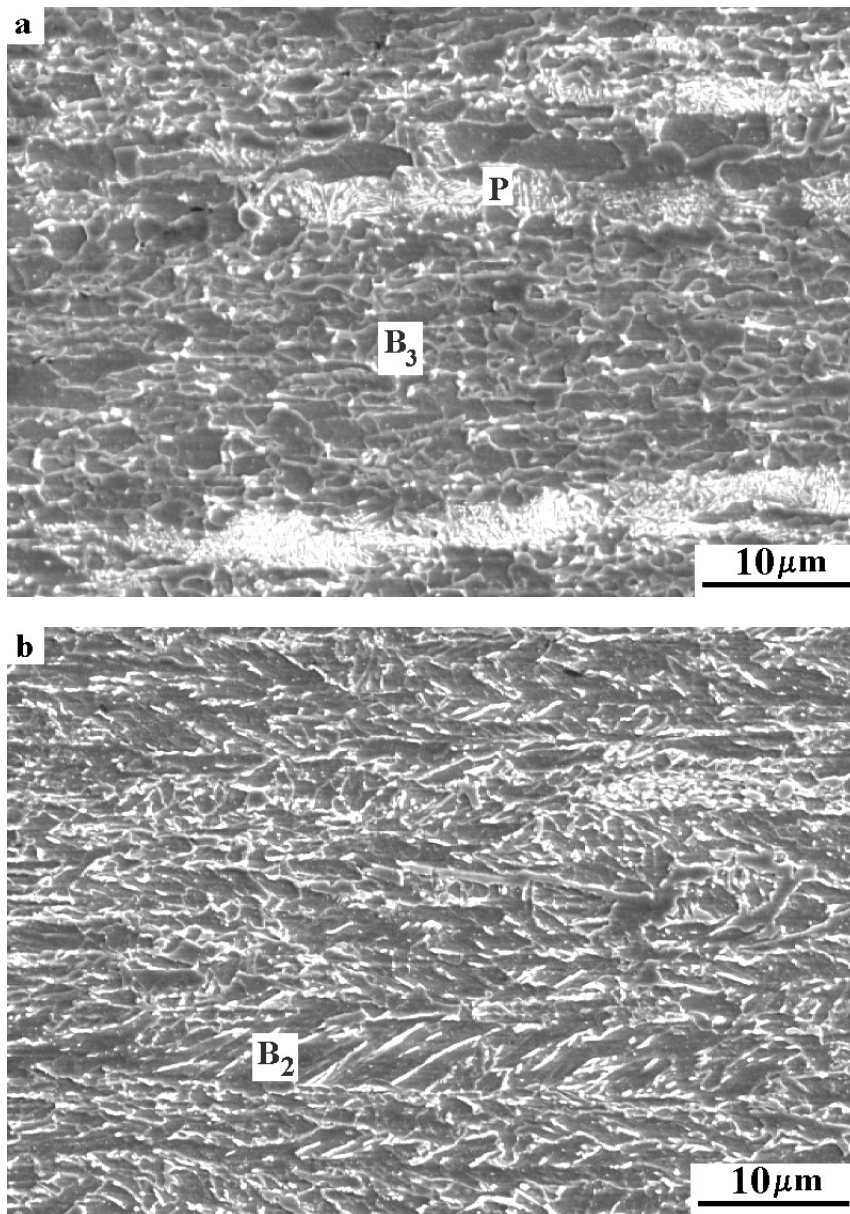
FigureVIII.7: Microstructure of steel 3 coiled (a) at 600 °C, (b) at 400 °C.

A remarkable influence of the undercooling on the microstructure was found in the MoB alloyed CMn steels. After coiling at the highest temperature the microstructure of the low carbon steel 4 contained a significant amount of pro-eutectoid ferrite and bainite (FigureVIII.5d). No pearlite was found. The steel coiled at 550 °C had a fully bainitic microstructure of the B_3 type (FigureVIII.8a) in which small amounts of M/A islands were easily recognizable. Coiling at temperatures below 500 °C led to changes of the bainite morphology, which developed pronounced lath morphology (FigureVIII.8b). The volume fraction of the interlath precipitations was evidently lower than in steels with higher carbon contents and they were in discrete form. At low coiling temperatures the stability of the austenite against bainite formation was low due to the low initial carbon content and as a result, microstructures containing bainite and martensite were found in the steel coiled at 300 °C.
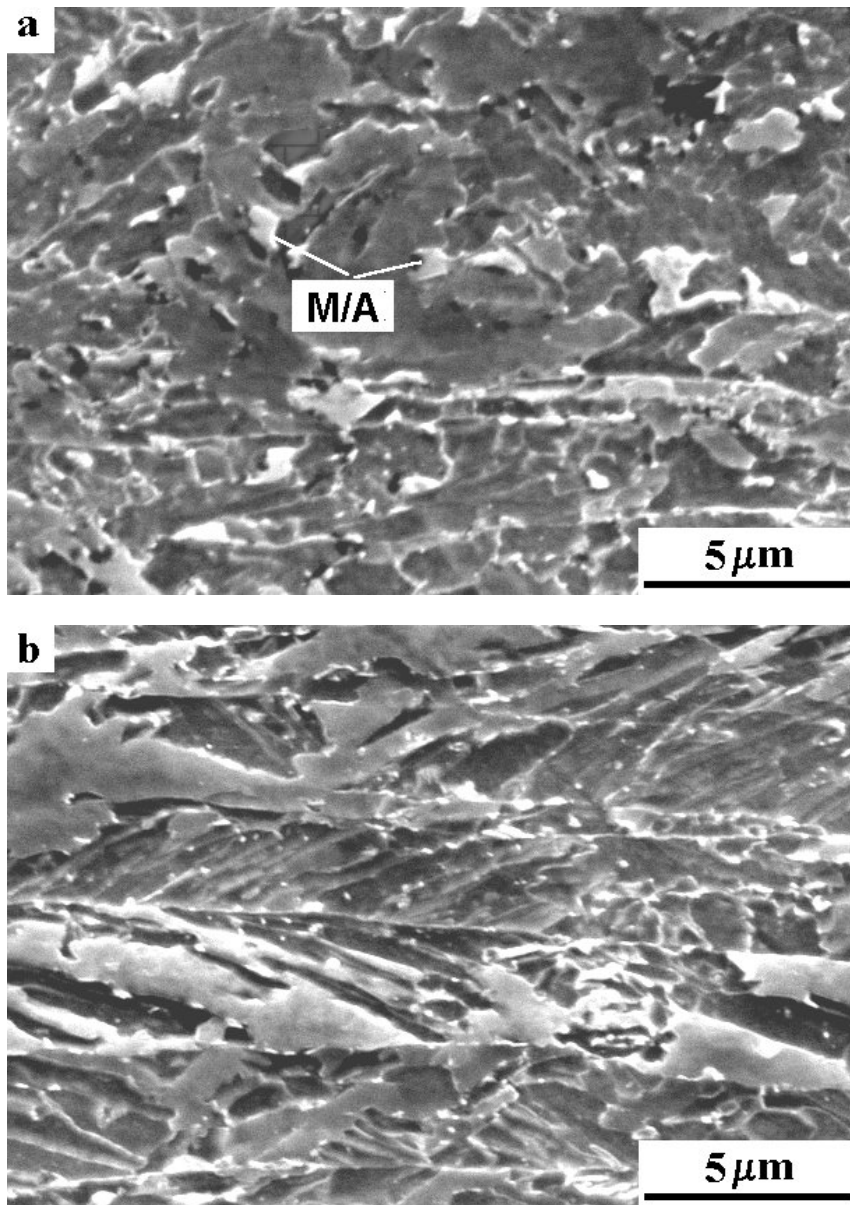
FigureVIII.8: Microstructure of steel 4 coiled (a) at 550 °C, (b) at 450 °C.

An increased amount of bainite and a more pronounced stabilization of the retained austenite were found in the MoB CMn microalloyed steels with 0.15 wt.% C (FigureVIII.5e and 5f).

This effect was even more pronounced in the MoCrB CMn steel 6. In this steel, the formation of the pearlite and the pro-eutectoid ferrite was strongly suppressed even at the higher coiling temperatures. As a result more than 50 vol.% of the microstructure was bainite in steel 6 after a coiling simulation at 650 °C (FigureVIII.9a). As the coiling temperature decreased, the B_3 bainitic microconstituents continuously replaced the pearlite (troostite). In addition, a clear increase of the M/A islands volume fraction was observed (FigureVIII.9b). It is remarkable that the steel 6 had a significant fraction of M/A islands in a wide range of coiling temperatures.
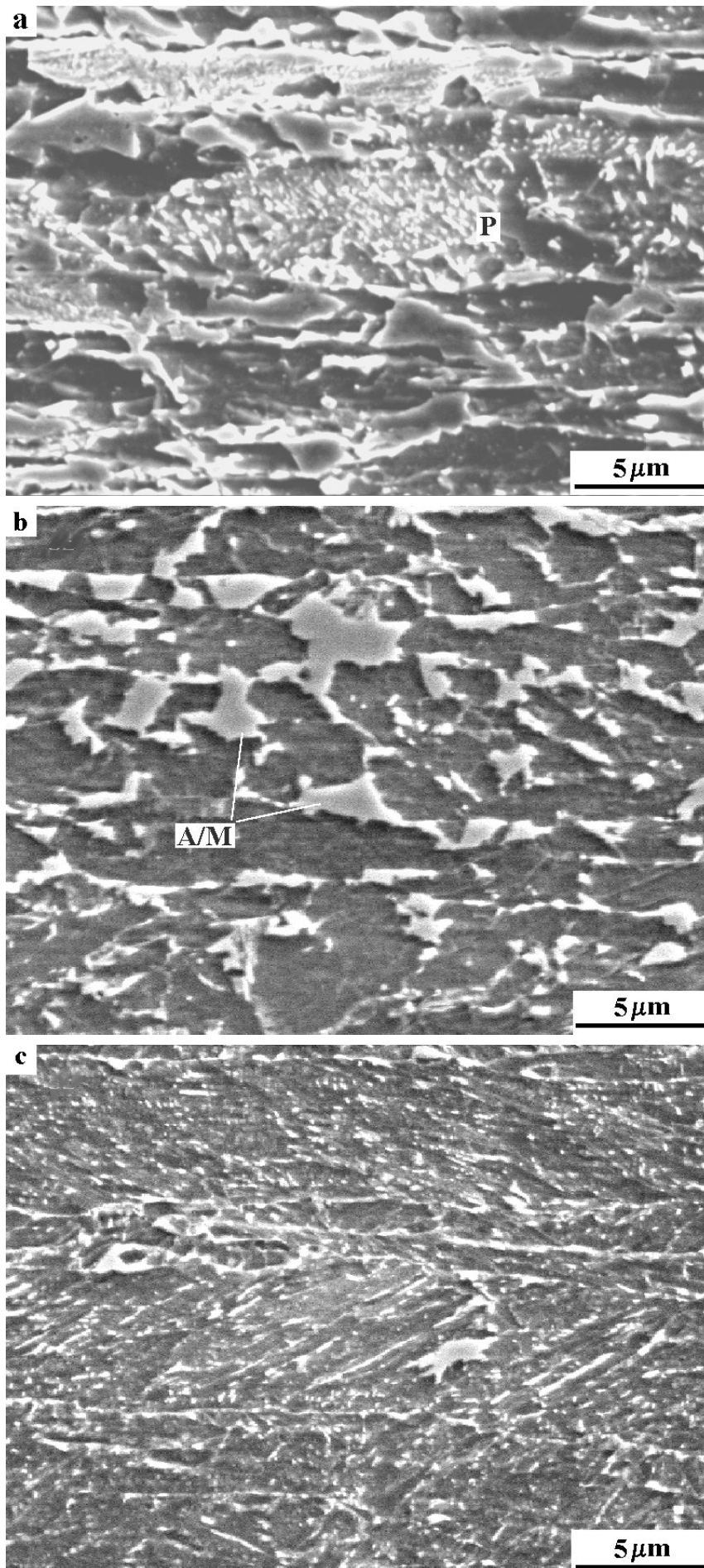
FigureVIII.9: Microstructure of steel 6 coiled (a) at 650 °C, (b) at 550 °C, (c) at 450 °C.

Stabilization of retained austenite was measured by XRD. About 10 vol.% retained austenite was present in steel 6 after coiling simulation at 550 °C. The transition to B_2 bainite with subsequent change of interlath precipitation morphology from discrete to film-like was detected in samples coiled in the temperature range of 450 - 400 °C. At lower temperatures significant fractions of martensite, formed during the rapid cooling stage, were found. The main microstructure constituents observed in each steel composition coiled at varied temperatures are summarized in Table VIII.2.

Table VIII.2: Summary of the microstructure observed after coiling at varied temperatures. The main constituents are indicated in bold. F = Ferrite, P = Pearlite, B = Bainite, M = Martensite, A = Austenite.

	Coiling temperature, °C						
Steel	**650**	**600**	**550**	**500**	**450**	**400**	**300**
1	**F**	**F**	**F**-B_3	**F**-B_3	**F**-B_3	**F**-B_3	**F**-B_3
2	**F-P**	**F-P**	**F-P**-B_3	**F**-B_3	B_3-(M+A)	B_3-(M+A)	B_3-(M+A)
3	**F-P**	**F-P**-B_3	**F-P**-B_3	B_3-(M+A)	(B_3+B_2)-(M+A)	B_2-(M+A)	B_2-M
4	**F**-B_3	**F**-B_3	**F**-B_3	B_3-F	B_2-M	B_2-M	B_2-M
5	**F-P**	**F-P**-B_3	**F-P**-(B_3+B_2)	B_2-(M+A)	B_2-(M+A)	B_2-(M+A)	B_2-(M+A)
6	**F-P**-B_3	**F-P**-B_3	B_3-**P**-(M+A)	B_3-(M+A)	(B_3+B_2)-(M+A)	B_2-(M+A)	B_2-M

VIII.5   Mechanical properties

The dependence of the yield stress, YS, on the coiling temperature is presented in FigureVIII.10a. It shows a maximum for YS at 550 - 600 °C for steels 1 through 4. It is noteworthy to mention that the maximum yield stress of steel 1 was found after coiling at 600 °C *i.e.* for the fully ferritic state. The transition to the mainly bainitic microstructures due to the decrease of coiling temperature resulted in a slightly lower yield stress. The constant level of YS for this steel coiled below 500 °C corresponds nicely to the absence of microstructural changes for lower values of the undercooling in this range. The yield stress peak at 600 °C is likely due to precipitation hardening of the ferrite during holding at temperatures susceptible to lead to the formation of fine (Nb,Ti)C particles. These carbides were initially dissolved at the reheating temperature. It was reported that soluble Nb lowers the Ar_3 transformation temperature and its precipitation during transformation can retard the progress of transformation by a solute drag effect at the α/γ interface.[6] Eventually, strain induced precipitation during the rolling process would have the same retarding effect, but it is likely that most of the (Nb,Ti)C particles precipitated during the $\alpha \rightarrow \gamma$ transformation. The stronger strengthening effect was observed in steel 3, which had the highest Nb content. Obviously, the precipitation hardening was less effective at 650 °C, which lead to natural formation of coarser particles. At temperatures lower than 550 °C the process of precipitation was clearly

suppressed and a decrease of yield stress was observed in the steels 1 through 4 with the coiling temperature decreasing from 600 °C to 500 °C.

A wide strengthening peak was present for the steels 2 and 3. The higher carbon content caused a less effective precipitation hardening at 550 °C combined with an increased strengthening due to the significantly increased fraction of "hard phase" M/A.

The similar maximum in the yield stress was found in the MoB alloyed low carbon CMn steel 4 with a mainly ferritic microstructure after coiling at temperatures 600 °C and 650 °C. This steel, with a B_3 type bainite microstructure formed after coiling at 500 °C or 550 °C, had a lower yield strength. A further decrease of the coiling temperature below M_s resulted in a mainly B_2 type bainitic microstructure with different fractions of martensite, accompanied by an increase of yield stress.

The MoCrB alloyed CMn steel 6 with 0.15 wt.% C, characterized by an improved austenite stability, had an exceptional behaviour with the continuous increase of yield stress as the undercooling decreased. The absence of recognizable strengthening peak in the precipitation temperature region is due to the combination of different factors: the lower Nb content, a more gradual growth of the "hard phase" fractions determining the level of yield stress and an increased fraction of M/A islands in the relatively soft matrix. The latter should result in a distinctive mechanical behaviour and a characteristic strain-hardening rate.
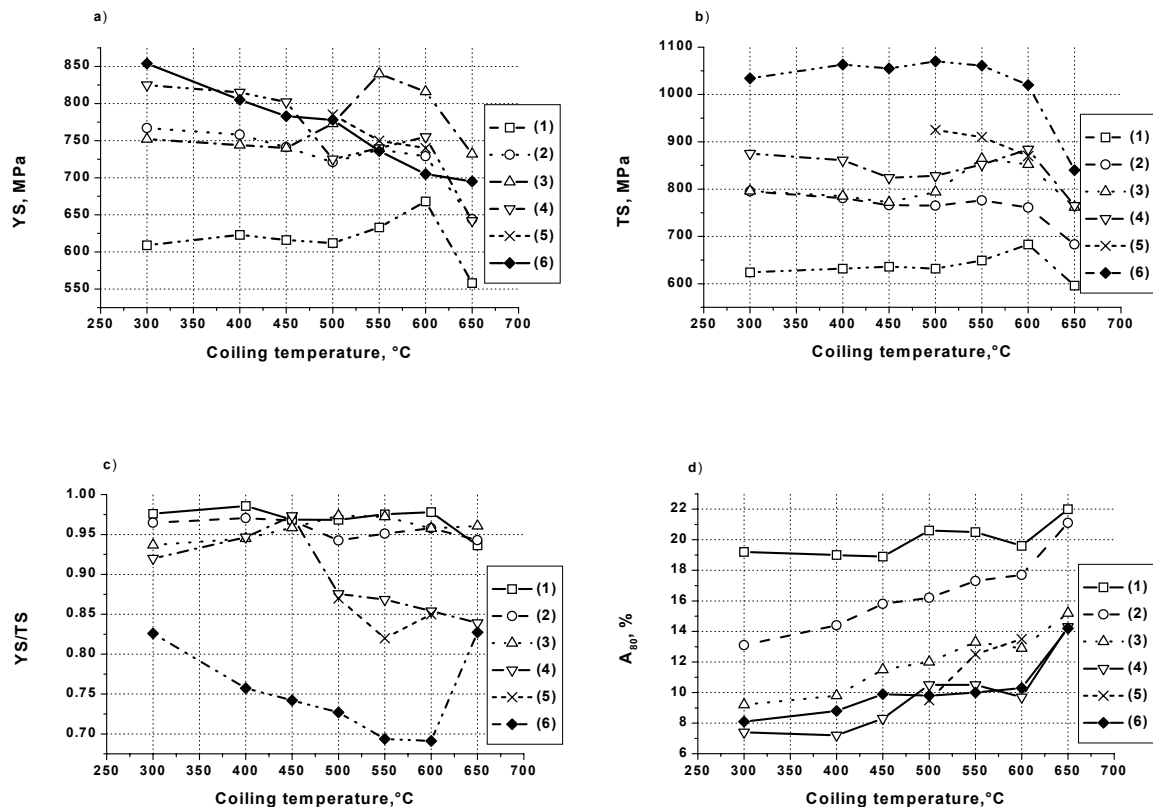

FigureVIII.10: Mechanical properties of investigated steels.

The tensile strength, TS, of the MoCrB added CMn micro-alloyed steel 6 was higher than in other steels in the whole range of coiling temperatures (FigureVIII.10b). The increase of TS coincided with the transition from a ferrite-pearlite-bainite microstructure to a bainite-martensite microstructure. This provided a high strength level independent of the coiling temperature. Tensile strength variations with a pronounced maximum in the temperature range of micro alloying carbide precipitation were found for all other steels.

The evaluation of mechanical behaviour by the consideration of the ratio of yield strength to tensile strength (YS/TS) revealed clear differences between the steels (FigureVIII.10c). Independently of the C content, the B-free CMn and Mo alloyed CMn steels 1 to 3 had the highest YS/TS ratio in the whole range of coiling temperatures. Note that the yield ratio for these steels had a weak coiling temperature dependence. The YS/TS ratio was more temperature dependant for the 0.15 C-CrMoB steel 6. In this steel the value of the yield ratio was reduced sharply when the coiling temperature was decreased from 650 to 600 °C. This induced the transition from a microstructure containing a sufficient fraction of ferrite-pearlite constituent to a mainly bainitic microstructure. A decrease of the coiling temperature below 550 °C led to a gradual increase of the yield ratio caused mainly by the increase of the yield stress YS at an almost constant TS value. It corresponded with the microstructural changes showing the gradual transition to lower temperature decomposition products such as the B_2 bainite and the martensite.

In the low-carbon MoB added CMn steel 4 a continuous increase of the YS/TS ratio with decreasing coiling temperature between 650 and 500 °C was found. This corresponds to the transition from a ferritic to a fully bainitic microstructure. As the coiling temperature decreased below the martensite start temperature M_s, the formation of low-carbon martensite and the formation of lath type B_2 bainitic microconstituent led to a small decrease of the yield ratio mainly due to an increase in yield stress.

The influence of the coiling temperature on the elongation is in good agreement with the microstructure changes (FigureVIII.10d). Ferritic or ferritic-low carbon bainitic microstructure of steel 1 had both the highest elongation and lowest strength in the whole range of coiling temperatures. Obviously, the plasticity of all the steels was sensitive to the precipitation hardening occurring during coiling at 600 °C. The formation of low temperature transformation products in steels 2-6, with a higher austenite stability due to decrease of coiling temperature, resulted in a lower elongation.

VIII.6   Microstructure and strain hardening

The analysis of the strain-hardening rate for the different microstructural states was done in order to explain the influence of the microstructure on the mechanical properties. Changes in the shapes of tensile curves with the coiling temperature, presented in FigureVIII.11, were pronounced in the MoCrB added CMn steel 6.
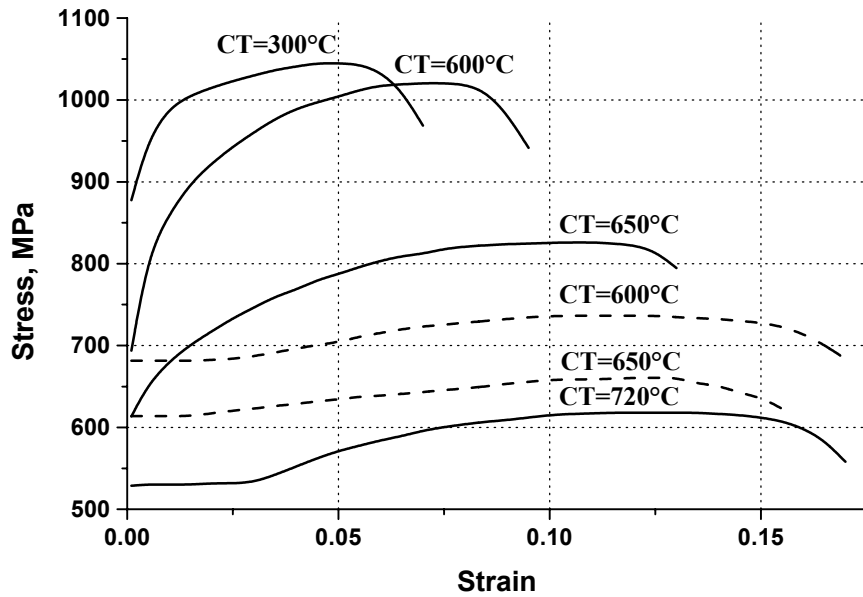
FigureVIII.11: Influence of the coiling temperature CT on tensile curves. Dashed lines: steel 2(0.155C-1.5Mn). Solid lines: steel 6(0.161C-1.5Mn-0.4Cr-0.2Mo-B).

It can be seen that after coiling at 720 °C the steel had a discontinuous yielding behaviour with large yield point elongation of about 3 %. This is typical for the coarse ferrite-pearlite microstructure. The decrease of the coiling temperature led mainly to changes in the work hardening rate. The tensile curve for steel 6 coiled at 650 °C is continuous at moderate strain hardening. It must be noted, that in this multiphase state the yield stress was lower than in the steel 2 coiled at the same temperature. According to the microstructural diagrams and the micrographs, the steel 2 had a fine ferrite-pearlite microstructure, which in combination with a more effective precipitation hardening resulted in a discontinuous yielding behaviour at higher stress level than in the coarser ferrite-pearlite microstructure formed at 720 °C in steel 6.
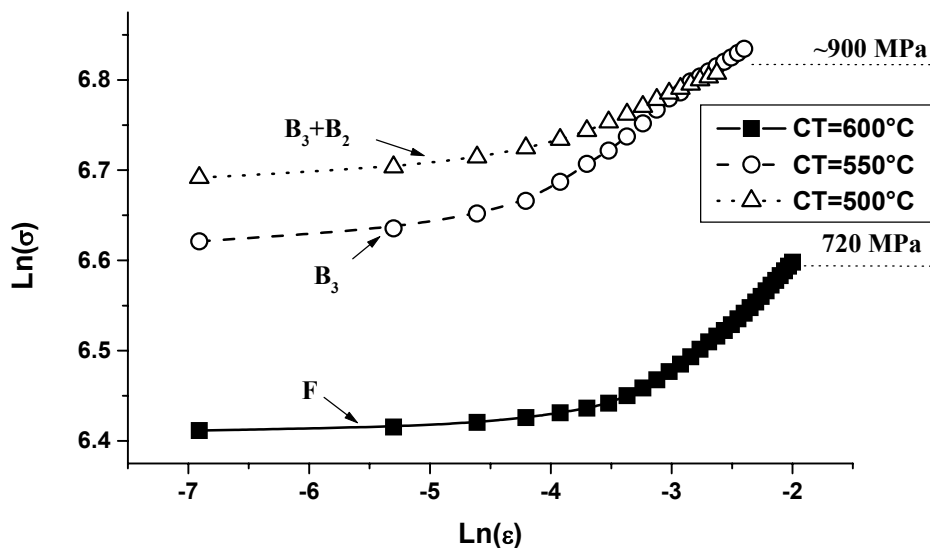
FigureVIII.12: Influence of the microstructure on logarithmic work hardening curves of low-carbon steel compositions. Solid – steel 1 (0.04C-1.5Mn), Open – steel 4 (0.066C-1.5Mn-0.2Mo-B).
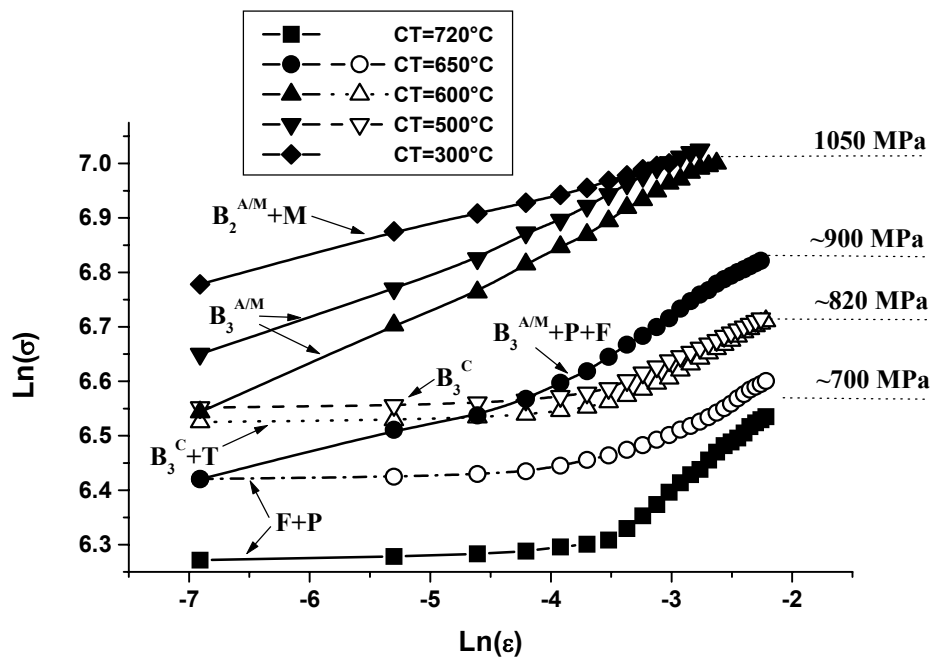
FigureVIII.13: Influence of the microstructure on the work hardening of investigated steels. Open – steel 2 (0.155C-1.5Mn). Solid – steel 6 (0.161C-1.5Mn-0.4Cr-0.2Mo-B). B_2- lath bainitic ferrite, B_3 – granular bainetic ferrite, P-pearlite, T- troostite, M- martensite. Indexes mean type of second phase in bainite: M-martensite, A-austenite, C–carbides.

The decrease of coiling temperature to 600 °C led to a significant increase of the yield stress, tensile strength and work hardening rate in steel 6. Steel 2 showed an increase of stress level, a discontinuous yielding behaviour and a low work hardening when coiled at 600 °C. The stress-strain curve was similar to the one obtained after coiling at 650 °C.

The maximum of strength combined with a lower but still adequate plasticity was found in steel 6 coiled at 300 °C. This resulted from the formation of a bainitic microstructure with martensite.

The influence of the microstructure on the strain hardening is summarized in FigureVIII.12 and FigureVIII.13 giving the ln σ-ln ε curves for the uniform plastic deformation stage. The analysis of strain hardening can be done based on the known properties of microconstituents. The behaviour of polygonal and bainitic ferrite formed in steels during coiling can be presented more correctly by the behaviour of low carbon steels with ferrite or the predominantly bainitic microstructure containing small fractions of second phase. Notice that polygonal ferrite and ferrite strengthened by the precipitations of carbides result in a two stage behaviour (FigureVIII.12). The first stage corresponds to the threshold formation stage and the second corresponds to the ferrite strengthening stage. At uniform elongation the true stress was about 720 MPa.

The MoB alloyed CMn steel 4 coiled at 550 °C with a microstructure consisting of bainitic granular ferrite B_3 with extremely small islands of martensite, showed the similar two stage

behaviour at sufficiently higher stress level and a lower elongation. The presence of lath bainite in the microstructure of steel 4 coiled at 500 °C increased the resistance against the start of plastic deformation and a decreased strain hardening rate, a lower uniform elongation and a lower tensile strength. As a result the microstructure consisting of low carbon bainite of both types B_3 and B_2 with small fraction of martensite islands provided true tensile strength of about 900 MPa.

It is known that the lack of dislocation mobility within the ferritic microconstituents is consistent with the discontinuous yielding behaviour observed in low carbon steels.[12,13,14] The absence of sufficient dislocation mobility in bainitic ferrite can result from the formation of dislocation network during recovery. On the other hand, the observed behaviour implies the absence of mobility of dislocations due to volume change between austenite and martensite formed close to the interphase bainitic ferrite-martensite islands boundary. It is possible that in low carbon steels the C enrichment of the austenite during the bainitic reaction is not significant enough and that martensite is formed at relatively high temperatures. These conditions are sufficient for recovery or aging under slow cooling. Moreover, in steels with a lower carbon content the amount of retained austenite formed during a long holding time in the bainitic transformation region can transform to martensite during the subsequent cooling, but this effect is apparently not sufficient to obtain a continuous yielding behaviour.

Addition of pearlite to the ferrite matrix of steels with a higher carbon content did not affect strongly the strain hardening behaviour. The maximum true stress reached at uniform elongation was about 700 MPa (FigureVIII.13). Change of the ferrite matrix to a bainitic type B_3 microstructure with small disperse islands of second phase, which can be identified as carbides observed in steel 2 after coiling at upper range of bainitic temperatures also resulted in the typical two-stage behaviour of the strain hardening. However, the formation of this microstructure led to lower strength values than were found for the bainite with martensite islands in the steel 6 (FigureVIII.13). The volume fraction of martensite was clearly larger in steel 4 coiled at approximately the same temperatures. The presence of second phase carbides could result in the formation of a more stable recovered matrix. Indeed the existence of the second phase coarse martensite islands containing residual austenite established in the MoCrB added CMn micro-alloyed steel 6 corresponds to a new type of strain hardening. Note that in the steel coiled at 650 °C the presence of some fraction of pearlite with ferrite microconstituent did not lead to clearly two-stage behaviour of strain hardening. The steel in this state demonstrated an intermediate character between the described two-stage behaviour with a yield point elongation and the fully continuous stress-strain curve found in predominantly bainitic microstructures with M/A particles formed at lower coiling temperatures. More likely, the presence of the stage with low strain hardening rate is an effect of the ferrite-pearlite microconstituent. There are two acceptable explanations of a high strain rate continuous hardening found for the microstructures containing M/A islands of second phase:

(a) the formation of a significant fraction of martensite at lower temperatures due to the higher carbon content in the steel or

(b) the presence of retained austenite due to the incomplete bainitic reaction, which induces the formation of numerous mobile dislocations located close to the interphase boundaries.

The behaviour of this multiphase steel can be referred to "dual phase" type in case (a). In comparison, in the steel 6 polygonal ferrite is substituted by bainitic ferrite that provides a higher stress values and lower plasticity. According to the second approach, case (b), the outstanding behaviour is caused by retained austenite in the M/A islands. Thus the high hardening rate is the result of a micro TRIP effect. Alternatively the phenomenon can be a consequence of combined effect of both factors.

The parameters of strain hardening for typical microstructural states of investigated steels presented in TableVIII.3 were obtained by fitting the data to the Hollomon equation:[15]

$$\sigma = C\varepsilon^n \tag{VIII.3}$$

where C is a coefficient equal to stress at strain of 1, n the strain hardening rate. Thus, the magnitude of n is strain dependent. As in most cases two stages were observed, average values of C and n for each stage are presented in the TableVIII.3. Large differences between n_2 and uniform elongation were found for the ferritic microstructure enhanced by fine precipitations and for fine ferrite-pearlite microstructure. This shows that more than two stages of strain hardening exist in these states. For other microstructures a good agreement between n_2 and the uniform strain was observed.

It follows from the data of the TableVIII.3, that the steels with a predominantly ferrite or ferrite-pearlite microstructure can be grouped as steels having a tensile strength of 700-750 MPa and having a clear two-stage strain hardening behaviour with threshold in the $\sigma-\varepsilon$ curve.

A higher value of tensile strength can be reached by the formation of a predominantly bainitic microstructure. The hot rolled multiphase steels with a predominantly bainitic microstructure can be subdivided in steels with a clear two-stage behaviour of strain hardening caused by a yield point elongation in the $\sigma-\varepsilon$ curves (type II) and steels with a continuous $\sigma-\varepsilon$ curve (type III). A high value of the strain hardening rate parameter, n, is typical for the last type even at very low strains. Note that for both groups the transition from granular to lath morphology of bainitic ferrite leads to a decrease of the strain hardening n.

Obviously, the most effective strengthening of steel can be achieved with a microstructure containing granular bainite with a significant amount of second phases in the form of M/A islands. In this state the tensile strength level of about 1100 MPa combined with high strain hardening rate and very adequate elongation were obtained.

TableVIII.3: The parameters of strain hardening for typical microstructures in investigated steels.

Predominant structure	C_1	n_1	C_2	n_2	TS, MPa	Group
Ferrite + carbide precipitates	640	0.0084	910	0.111	730	
Fine ferrite-pearlite + carbide	650	0.0092	940	0.112	740	I
Coarse ferrite-pearlite	560	0.0099	990	0.174	700	
Granular bainite + carbides + troostite	720	0.0076	1070	0.120	825	
Granular bainite + carbides	735	0.0076	1030	0.105	820	II
Granular bainite in low C steels	850	0.013	1180	0.105	930	
Granular and lath bainite in low C steels	880	0.0199	1060	0.062	890	IIa
Granular bainite + M/A islands + some ferrite-pearlite micro-constituents	880	0.0533	1270	0.141	915	III
Granular bainite + M/A islands	-	-	1450-1465	0.094-0.110	1095-1125	
Lath bainite + M/A film-like particles + structural-free martensite	-	-	1300	0.0565	1100	IIIa

VIII.7   Conclusions

The main conclusions of the present chapter are the followings:

1. The relationships between microstructures formed during typical thermomechanical cycles in low C – 1.5 wt.% Mn based high strength micro-alloyed sheet steels and their mechanical properties were examined. The analysis of strain hardening coefficients established the distinction between 3 classes of tensile behaviours corresponding to distinct microstructures. In particular, it was found that a microstructure consisting of bainite with a second phase in the form of martensite-austenite islands had high performance mechanical properties. Continuous yielding, high tensile strength, adequate elongation, low YS/TS ratio and high strain hardening rate were found in this microstructural state. Other microconstituents present in minor amount deteriorated mechanical properties but kept the distinctive mechanical behaviour.

2. The formation of a predominantly bainitic microstructure with austenite-martensite islands in condition simulating standard hot rolled sheet coiling was found in the MoCrB added CMn micro-alloyed steel. This microstructure was formed in this particular steel during the slow cooling of the steel in the temperature range between 550 °C and 650 °C. The study of transformation kinetics revealed that in spite of wide range of coiling start temperature the majority of austenite in this steel transformed in the bainitic region between 550 and 400 °C providing similar properties. The decrease of the coiling start temperature below 550 °C led to a decrease of plasticity due to the formation of the low temperature constituents, lower bainite and martensite.

References

[1] C. Mesplont, T. Waterchoot, S. Vandeputte, D. Vanderschueren, B.C. De Cooman: 41st MWSP Conf. Proc., ISS, Vol.37, 1999, p515.

[2] C. Mesplont, T. Waterchoot, S. Vandeputte, D. Vanderschueren, B.C. De Cooman: Thermomechanical processing of steels Conf. Proc., IOM Communications, UK, May 2000, p.495.

[3] H. de Boer, S. R. Datta, H-J. Kaiser, S.O. Lundgreen, B. Müsgen, H. Schmedders, K. Wick: Stahl und Eisen 115, Nr.2, 1995, p.93.

[4] S. Zalac, T. Siwecki, W.B. Hutchinson, R. Lagneborg: ISIJ International, Vol. 38, No. 10, 1998, p.1030.

[5] Y. Jung, H. Ueno, H. Ohtsubo, K. Nakai,Y. Ohmori: ISIJ International, Vol. 35, No. 8, 1995, p.1001.

[6] P.A. Manohar, T. Chandra, C.R. Killmore: ISIJ International, Vol. 36, No. 12, 1996, p.1486.

[7] T.M. Maccagno, J.J. Jonas, S. Yue, B.J. McCrady, R. Slobodian, D. Deeks: ISIJ International, Vol.34, No.11, 1994, p.917.

[8] F.S. LePera.; J. Metals 32, No. 3, 1980, p.38.

[9] J.Z. Zhao, C. Mesplont, B.C. De Cooman: Z. Metallkd. 92, 4, 2001, p.345.

[10] C.Y. Kung, J.J Rayment: Metall. Trans. A, Vol. 13A, 1982, p.328.

[11] B.L. Bramfitt, J.G. Speer: Metallurgical Transactions A, Vol. 21A, 1990, p.817.

[12] R. Mishra, S. Thompson, T. Hylton, A. Boucek: Metall. Trans. A, Vol. 32A, 2001, p.745.

[13] M.S. Rashid: edited by A.D. Davenport, TMS-AIME, Warrendale, PA, (1977).

[14] E. Vasseur, H. Tsukahara, J. Drillet, E. Pinto da Costa, S. Ribau: 41st MWSP Conf. Proc., ISS, Vol.37, 1999, p.811.

[15] J.H. Hollomon: Trans. TMS-AIME, Vol.162, 1945, p.268.

CHAPTER IX

Microstructure - properties relations in complex phase cold-rolled high strength steels

IX.1 Introduction

The main texture characteristics and the transformation behaviour of the industrial composition hot rolled and coiled at varied coiling temperatures were studied in chapter VII, and its microstructures and properties were detailed in chapter VIII. Starting from hot rolled sheets of the industrial composition with different microstructures and properties, cold rolling simulation were performed in order to reduce the sheet thickness and achieve good mechanical properties.

The present chapter is about the control of microstructure and mechanical properties in cold rolled complex phase steels. Cold rolled sheets cannot be used as such, as the cold deformation causes hardening of the steel and a loss of ductility. Part of the energy of deformation remains stored in the structures of dislocations as elastic energy.[1] Cold rolled complex phase steels are high strength steels and have too little residual ductility. A recrystallizing anneal is thus necessary after cold rolling create a multi-phase microstructure by heating above the Ac_1 temperature.

Industrially, two kinds of thermal treatments can be performed on cold rolled sheet steels:

- batch annealing (BA);

- continuous annealing (CA).

Batch annealing is largely used with fully ferritic steels and it consists in reheating coils under protective atmosphere for several hours in the temperature range of 500 – 850 °C. The reheating rate is usually low (10 °C/h) and the time and temperature of annealing are adjusted to control the recrystallisation and grain growth of ferrite.

Continuous annealing cycles have a much faster reheating rate (10 °C/s) and a shorter annealing time (minutes instead of several hours). The CA process is much more flexible than BA cycles. In multiphase steels such as DP, TRIP and CP steels, complex continuous annealing cycles are used to produce specific microstructures.

Results of batch annealing with different reheating temperatures are presented. Tensile testing on specimen made from annealed plates showed clearly the difference between recrystallised and not recrystallised ferrite. The 50 % recrystallisation temperature was determined.

Most of the work described in the present chapter concerns continuous annealing cycles with a reheating temperature between Ac_1 and Ac_3. With such cycles, complex microstructures were obtained leading to very good tensile performances.

IX.2 Experimental procedure

Blocks with 120 mm length, 60 mm width and 25 mm thickness of industrially produced steel with composition 0.16 wt.% C, 1.6 wt.% Mn, 0.2 wt.% Mo, 0.5 wt.% Cr, 500 ppm Nb, 200 ppm P and 20 ppm B were reheated to 1270 °C, for one hour and hot rolled in 6 passes to a final thickness of 2.5 mm. Three coiling temperatures (CT) were used to produce different microstructures. Ferrite and pearlite were obtained after coiling at 720 °C, and a bainite-martensite microstructure was obtained after coiling at 550 °C. The hot-rolled plates were then cold rolled with 60 % reduction to the final thickness of 1 mm.

Batch annealing simulations were done with 800 mm length and 250 mm width plates in furnace under protective HNX atmosphere.

Continuous annealing cycles were carried out with a laboratory continuous annealing simulator (CASIM) on plates with 650 mm length and 250 mm width.

The phase transformations occurring in the steel during the continuous annealing process were studied by means of dilatometry. At first, a cylindrical sample with 5 mm length and 3.5 mm diameter was reheated to 1200 °C, 2 min then cooled at the rate 300 °C/min to produce a bainite-martensite microstructure. It was then reheated to a temperature between Ac_1 and Ac_3, for 10 min, and cooled at the rate 300 °C/min. Between each inter-critical annealing cycle, the sample was reheated to 1200 °C, to obtain the same starting microstructure. The tests were carried out to estimate the fraction of austenite formed at selected inter critical temperatures and determine the phases formed during cooling. The fraction of phases formed during the continuous annealing cycle has an influence on the tensile properties. It was therefore decided to use cold rolled plates with dimensions 5 mm x 3.5 mm x 1 mm directly in the dilatometer rather than using standard cylindrical samples from the cast steel. As a result, the effects of deformation were taken into account, and the dilatometry results were comparable to the CASIM cycles.

The different phases were observed by light optical microscopy (LOM) and scanning electron microscopy (SEM) after etching with the LePèra etchant.[2] The volume fractions of residual austenite in different cold rolled and annealed samples were determined by means of X ray diffraction and magnetic measurements.

IX.3   Batch annealing

Two different microstructures, *i.e.* ferrite-pearlite and bainite-martensite were obtained after hot rolling and coiling at 720 °C and 550 °C, respectively. Hot rolled plates with 2.5 mm thickness were given a 60 % reduction cold rolling to 1 mm thickness. At first, three annealing cycles shown in Figure IX.1 were used with reheating temperatures 630, 670 and 710 °C, respectively. The purpose of these tests was to produce cold rolled sheets with 800 MPa tensile strength and 15 % elongation. During the annealing, however, the complex bainite-martensite microstructure formed during the coiling at 550 °C was destroyed due to ferrite recrystallisation and carbides precipitation from retained austenite. The sample coiled at 720 °C, initially ferrite-pearlite transformed partially to austenite during the annealing at 710 °C, likely due to Mn rich regions in the initial pearlite. This can be seen in Figure IX.2 in which the bright phases are M/A constituent, either martensite or austenite. In all cases the measured tensile strength in cold rolled and annealed samples was lower than 700 MPa. The total elongation was higher than 15 %. In Figure IX.2, the coarsening of new ferrite grains from deformed zones is clearly seen with increasing reheating temperature.
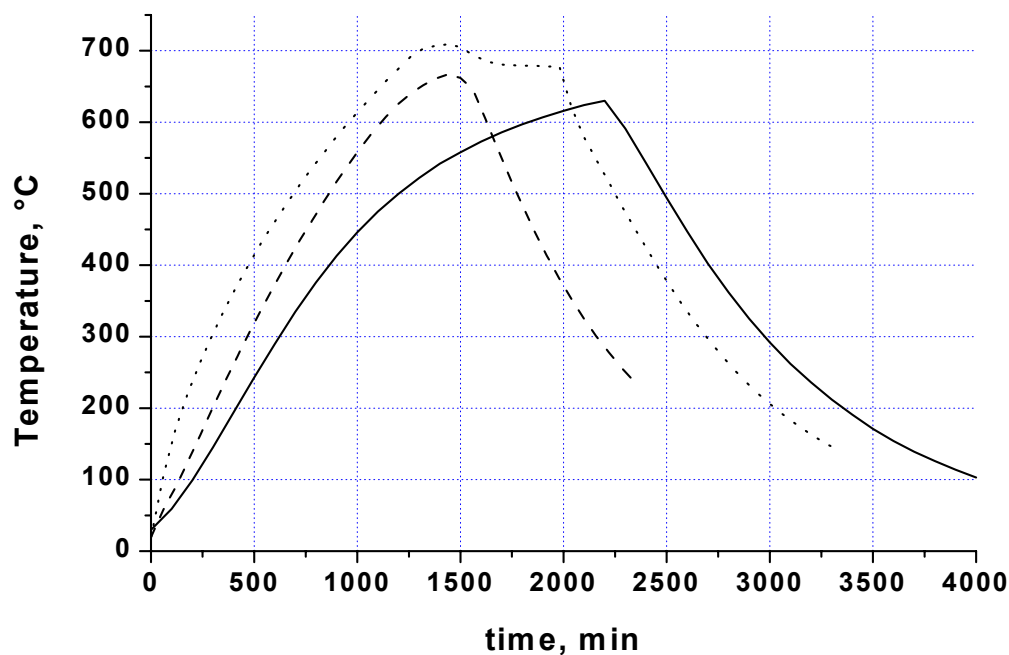
Figure IX.1: Batch annealing cycles.

	CT = 720 °C	**CT = 550 °C**
AT = 630 °C		

AT = 670 °C

AT = 710 °C

20 µm
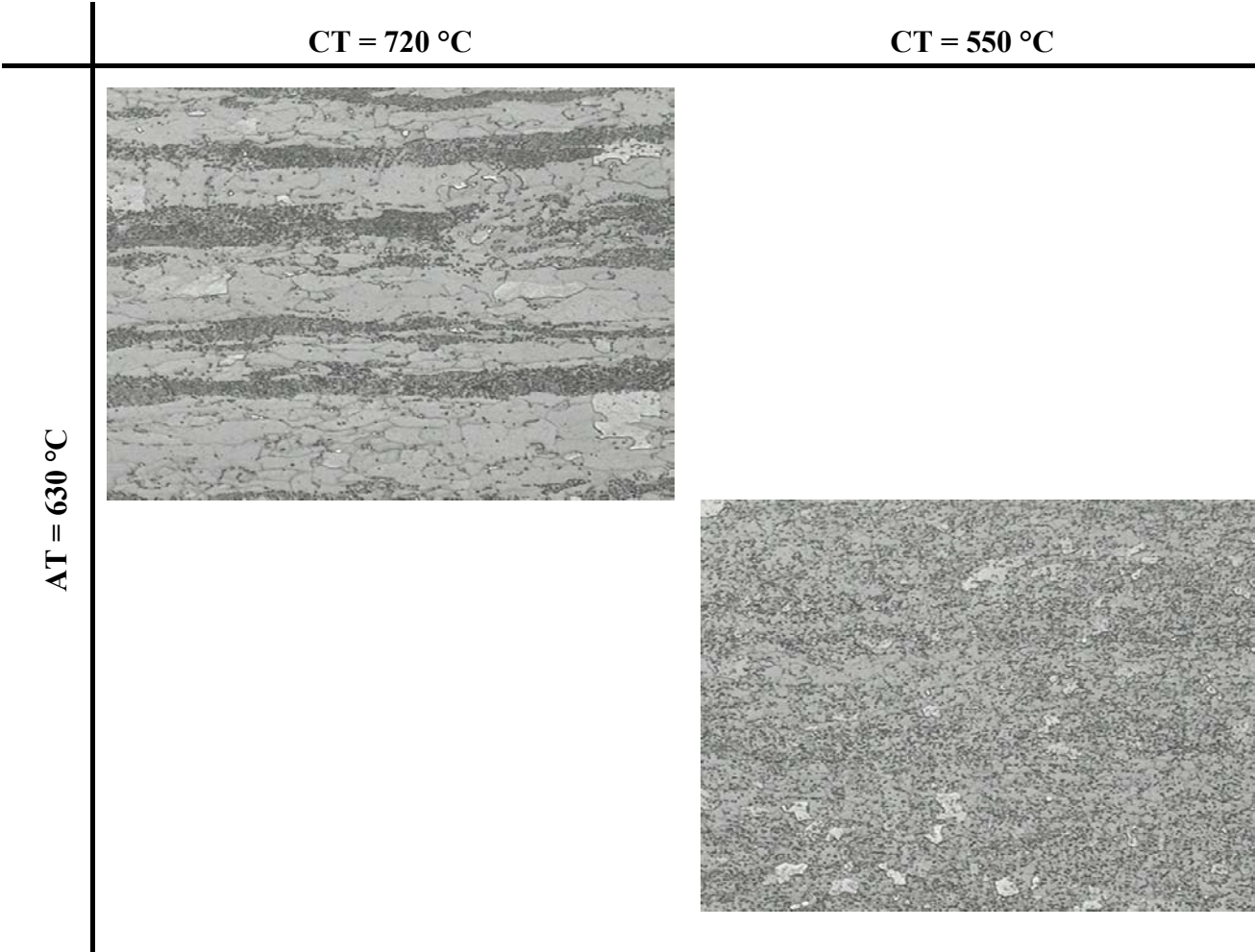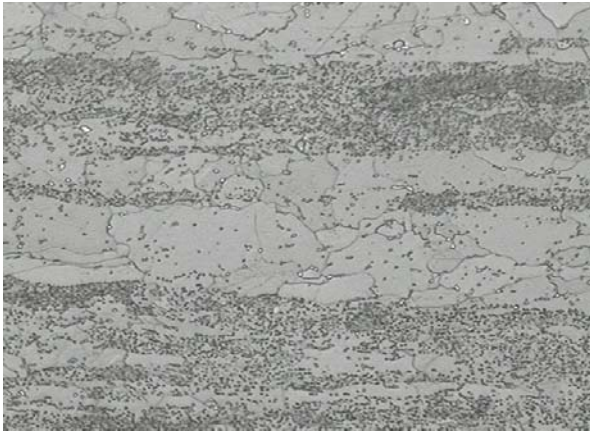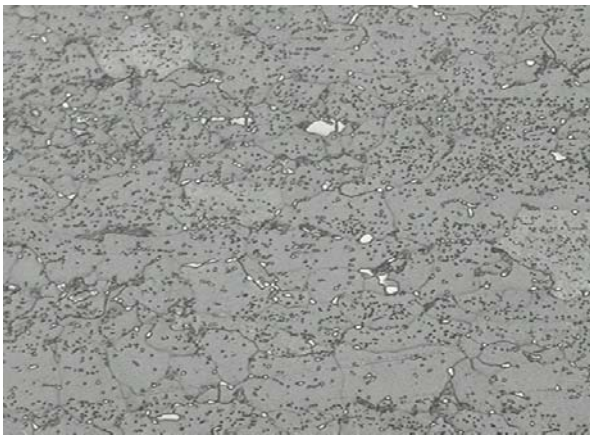
20 µm

Figure IX.2: Microstructures of cold rolled and continuously annealed samples at 630 °C, 670 °C and 710 °C (from top to bottom) hot rolled and coiled at 720 °C (left) and 550 °C (right). CT = Coiling Temperature. AT = Annealing Temperature.

Additional annealing cycles were done with reheating temperatures 600 °C, 570 °C, 530 °C and 480 °C, respectively. The tensile properties of each annealed plate were measured, and the TS *versus* reheating temperature plot of Figure IX.3 shows clearly the recrystallisation temperature range. The temperature at which 50 % recrystallisation occurred was T_{rex} = 585 °C.

Annealing below T_{rex} suppressed the ductility ($A_{tot} < 2$ %) and increased the tensile strength. Annealing above T_{rex} increased the ductility ($A_{tot} > 16$ %) and reduced the tensile strength. Note also the presence of a large threshold (about 3 %) in the strain-stress curves, due to the pinning of dislocations.
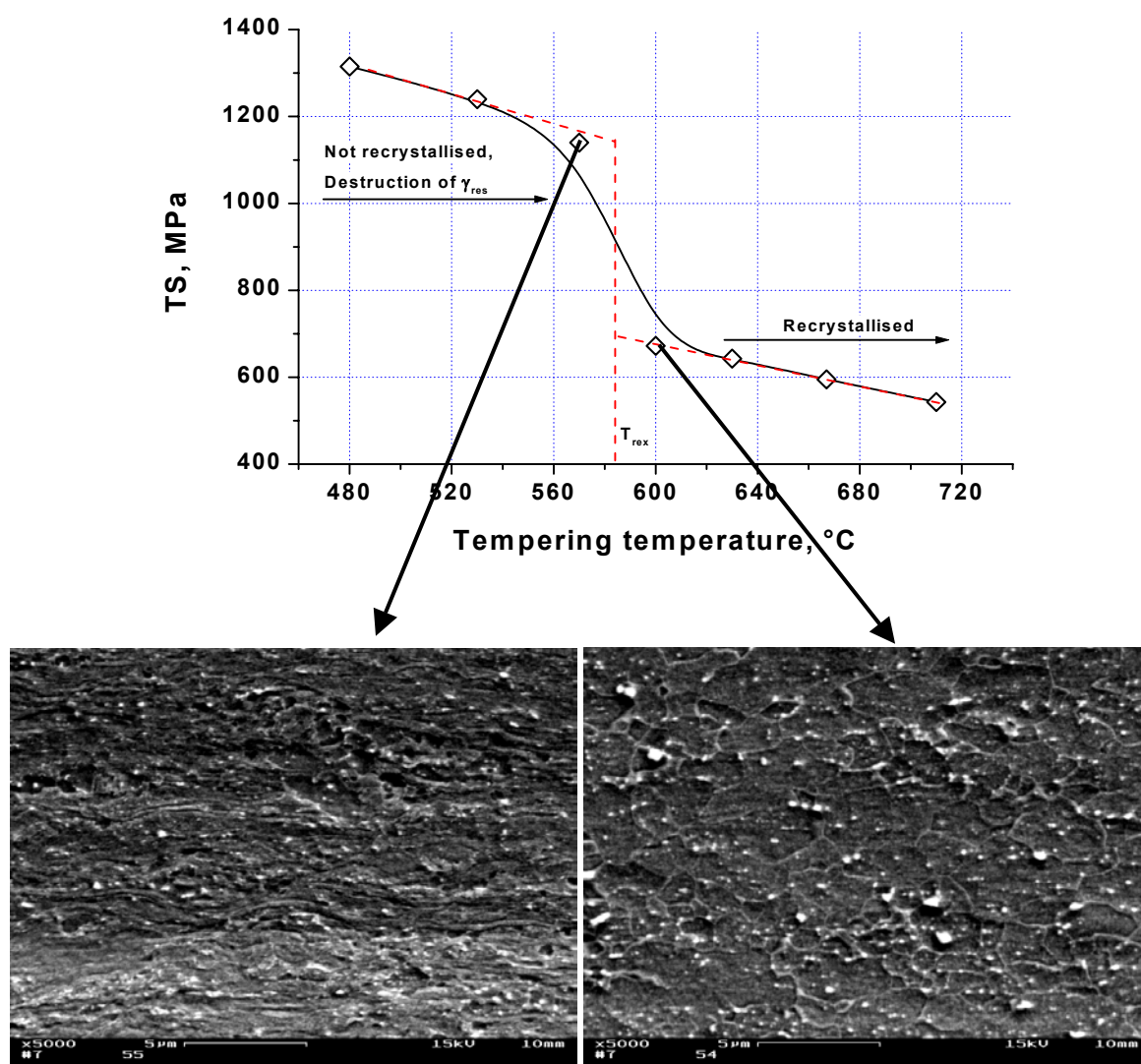
Figure IX.3: TS *vs*. reheating temperature and corresponding microstructures.

IX.4 Continuous annealing: microstructural control

IX.4.1 Dilatometry on cylindrical samples

Figure IX.4 shows the dilatation dl/l_0 of a sample submitted to different CA cycles. It can be seen that the bainite and martensite start temperatures decrease with decreasing annealing temperature. After 10 minutes intercritical annealing (IA), the equilibrium between alpha and gamma phases was almost reached. The cooling curves were analyzed using a program recently developed for dilatometry.[3,4,5] It was assumed after each intercritical annealing temperature that the equilibrium austenite fraction was formed.
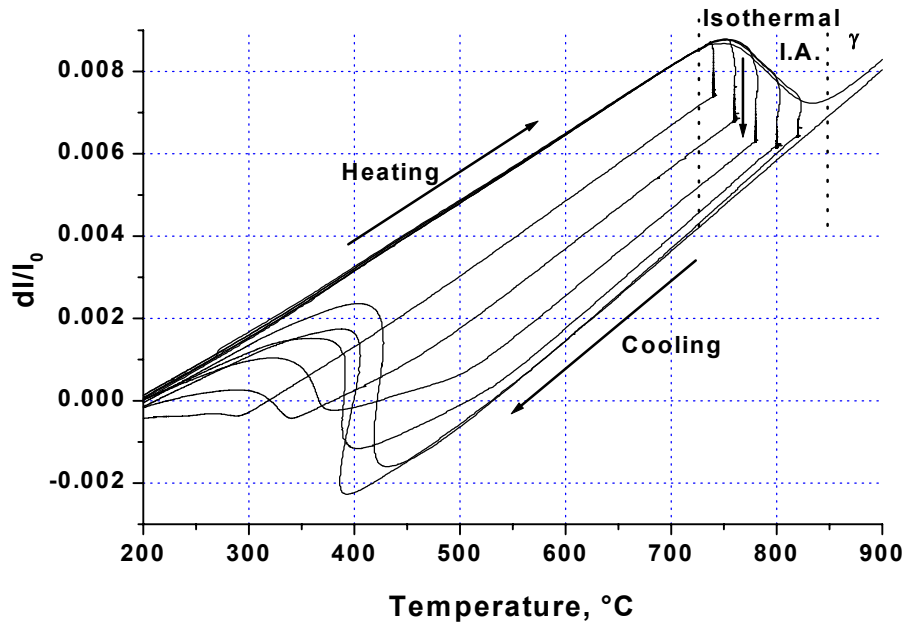
Figure IX.4: Dilatometric curves.

The calculated fractions and measured transformation temperatures for bainite and martensite are shown in Figure IX.5a and 5b for different intercritical annealing temperatures. While the B_s temperature was not much affected by the annealing temperature, lower intercritical annealing temperatures resulted in lower M_s temperatures, as at lower intercritical annealing temperatures the equilibrium partitioning of carbon results to a higher carbon content in austenite.

The M_s temperature was used to estimate the volume fraction of austenite formed during the annealing and its carbon content. From the curves shown in Figure IX.5, the M_s temperature can be determined by fitting the Koistinen-Marburger equation to the dilatometric data obtained experimentally:[6]

$$f_m = 1 - \exp(k(M_s - T)) \tag{IX.1}$$

The empirical formula from Li et al[7] for predicting B_s was used to estimate the carbon content in the austenite before the bainite transformation started:
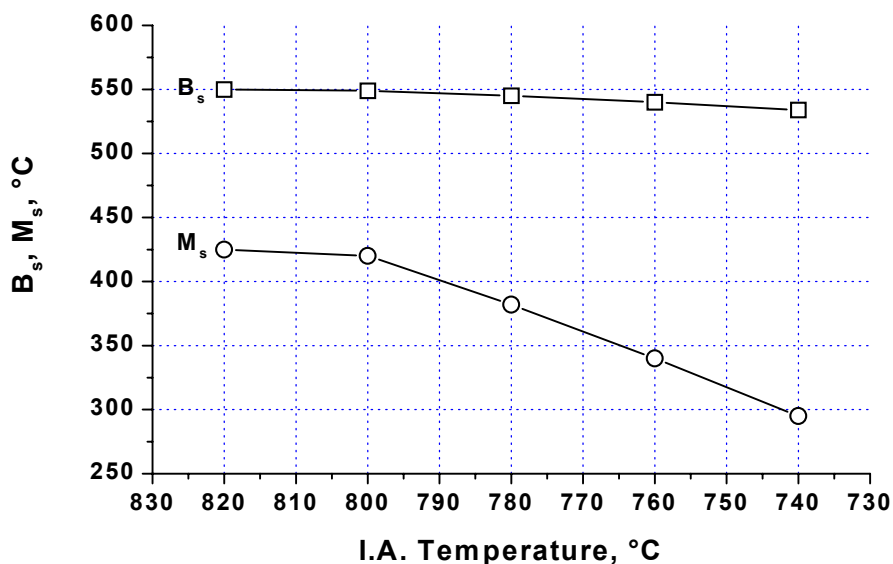
$$B_s(^oC) = 637 - 58wt\%C - 35wt\%Mn - 15wt\%Ni - 34wt\%Cr - 41wt\%Mo \tag{IX.2}$$

Using the measured M_s temperatures, the C content of the parent austenite phase before the martensitic transformation, *i.e.* C_M, the C content of the martensite, was calculated using the Stevens and Haynes equation:[8]

$$M_s(^oC) = 561 - 474wt\%C_M - 33wt\%Mn - 17wt\%Ni - 17wt\%Cr - 21wt\%Mo \tag{IX.3}$$
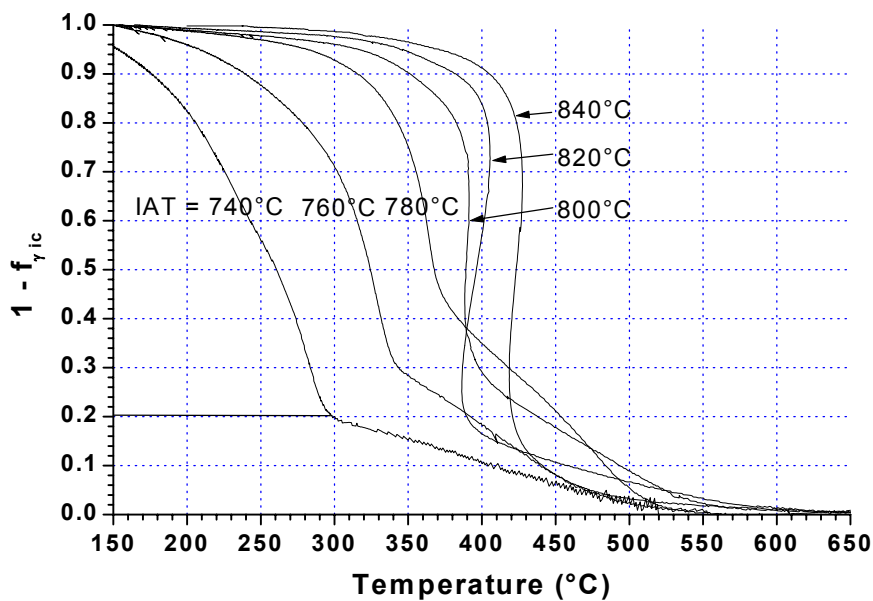
a)

b)

Figure IX.5: a) Fractions of bainite and martensite after I.A., b) M_s and B_s *vs* I.A.T.

It was found that for a CMn steel at cooling rates below 300 °C/min, the carbon content in bainite, C_B, including both C in ferrite and carbides, was the same as the initial carbon content.[9] It was assumed that the C content in the ferrite formed during cooling could not

exceed the solubility limit of C in ferrite, which was $C_\alpha = 0.015$ wt.% for the present steel composition.

Using the balance mass equation, the carbon content in the intercritical austenite was calculated as:

$$C_{\gamma IA} = C_\alpha V_\alpha + C_M V_M + C_B V_B \tag{IX.4}$$

At the annealing temperature, where only ferrite and austenite are present, the austenite fraction was calculated using the mass balance equation:

$$C_0 = C_{\alpha IA} V_{\alpha IA} + C_{\gamma IA} V_{\gamma IA} \tag{IX.5}$$

where C_0 is the total carbon content and $V_\alpha = 1 - V_{\gamma IA}$.

Figure IX.6 illustrates the procedure. After annealing the material for 10 min at 780 °C, the measured B_s and M_s were respectively 545 °C and 382 °C corresponding to a C content of 0.26 wt.% in the parent austenite. 61 vol.% of austenite was formed during intercritical annealing. This austenite decomposed during cooling into 40 vol.% bainite and 60 vol.% martensite. The final microstructure was thus 40 % ferrite, 24% bainite and 36% martensite.
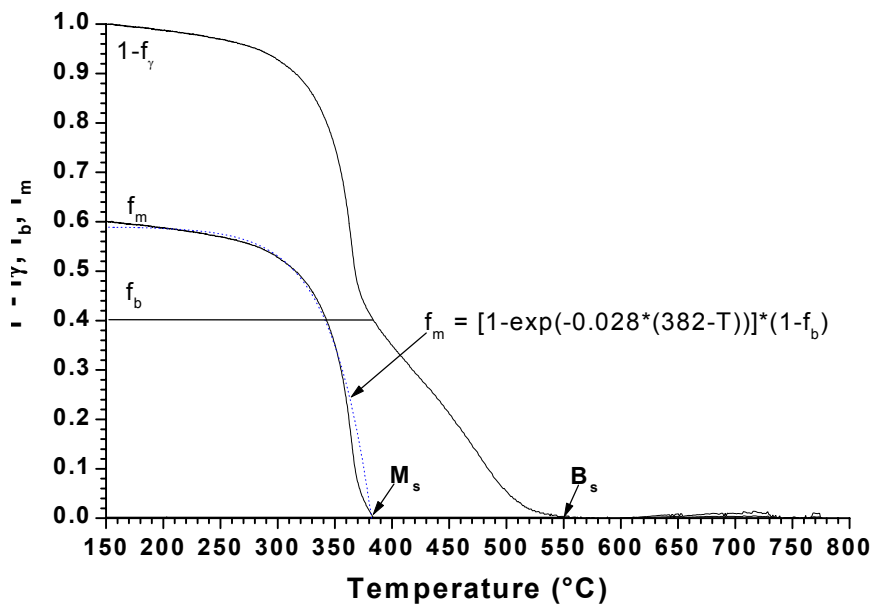

Figure IX.6: Fitting of the martensite formation using the Koistinen equation.[6] I.A.T: 780°C.

Another method to determine the volume fraction of the austenite formed during intercritical annealing was obtained by considering the slopes of the cooling curves. Indeed, the thermal expansion coefficient of a steel is a linear function of the temperature when no phase transformation occurs.[10] If after intercritical annealing the steel is a mixture of ferrite and austenite only, the thermal expansion coefficient at the intercritical temperature, k_{IA}, can be written as:

$$k_{IA} = V_{\gamma IA} k_{\gamma} + V_{\alpha IA} k_{\alpha} \qquad\qquad\qquad (IX.6)$$

The measured values for the thermal expansion coefficient of the α and γ phases were $k_{\alpha} = 16.10^{-6}\ °C^{-1}$ and $k_{\gamma} = 23.10^{-6}\ °C^{-1}$, respectively.

The volume fractions of intercritical austenite obtained with this method were close to those obtained using the M_s temperature, as can be seen in Figure IX.7a.
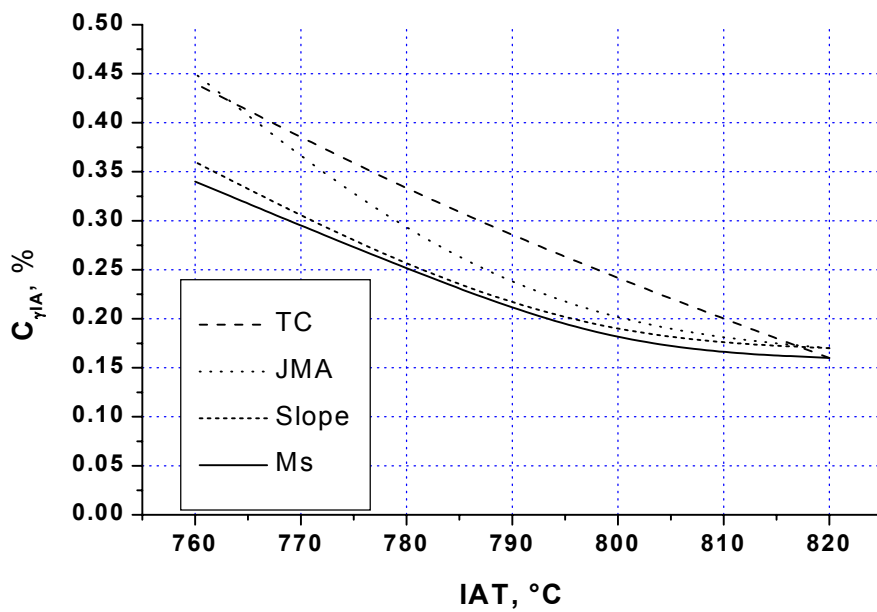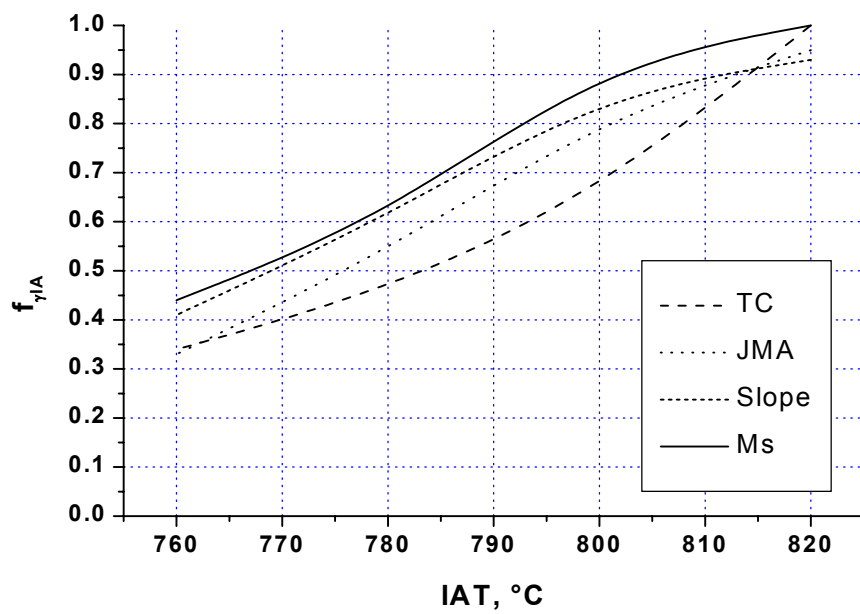
Figure IX.7: a) Austenite fraction as a function of IAT, b) C content in austenite as a function of IAT.

The Figure IX.7a and 7b show respectively the fraction of austenite and its carbon content measured using the two methods just presented, *i.e.* those using the Ms temperature and the slopes of dilatometer curves giving the thermal expansion coefficients, respectively. Two other methods were also used, the fitting to the Johnson Mehl Avrami (JMA) equation described below, and ThermoCalc^{TM} (TC) prediction. More austenite was formed than expected from the pseudo equilibrium FeC diagram calculated using TC. This is not consistent with the increase of Ae_3 usually observed in non-equilibrium conditions during heating[11]. Ac_3 should normally be higher than Ae_3. The morphology of the starting microstructure consisting of bainite, martensite and some austenite acting as nucleation sites may be the reason for the larger amount of intercritical austenite formed.

Finally, the kinetics of austenite formation was studied more in detail. From the curves of Figure IX.4, it was assumed that after annealing 10 min at 840 °C, the microstructure was fully austenitic. Taking the starting time $t_0 = 0$ s at 700 °C, it was possible to follow the progress of austenite formation at different annealing temperatures. It must be noted that the initial microstructure started to transform to austenite during heating from Ac_1 to the intercritical annealing temperature. At each intercritical annealing temperature, the Johnson-Mehl-Avrami (JMA) analysis was carried out by fitting the experimental data to the JMA equation:[12]

$$y = 1 - \exp\left[-(k(T)t)^n\right] \tag{IX.7}$$

where

$$k(T) = A\exp\left(\frac{-Q}{RT}\right) \tag{IX.8}$$

and y is the fraction of austenite formed, t, the time, T, the temperature, A, the frequency factor, Q, the activation energy, $k(T)$, the temperature-dependant rate constant and n, the Avrami exponent. n and k were determined experimentally by modifying equation (IX.7) to:

$$\ln\left(\ln\left(\frac{1}{1-y}\right)\right) = n\ln k + n\ln t \tag{IX.9}$$

As the transformation started during heating, at annealing temperatures above 780 °C, the n and k values obtained for the beginning of transformation were the same. The values of n increased from 2 to 5 between 740 °C and 780 °C.

The measured values of k allowed for the determination of the activation energy Q for the austenite formation between 740 °C and 780 °C; $Q = 326$ kJ/mol was obtained. This value is high in comparison to the activation energy for self-diffusion of gamma iron: $Q = 284$ kJ/mol.[13] An increase of the activation energy is likely due to the presence of alloying elements such as Mo, Nb and B, known to be present at the austenite-ferrite phase boundaries where they cause solute drag-like effects (SDLE).[14]

Figure IX.8 was plotted using equation (IX.9). For each of the annealing temperatures, two linear parts were observed in the double logarithmic plots. The first part corresponds to the austenite formation from C rich regions (martensite in the present sample) during heating and/or holding, while the second part corresponds to the further growth of the austenite in the proeutectoid ferrite.
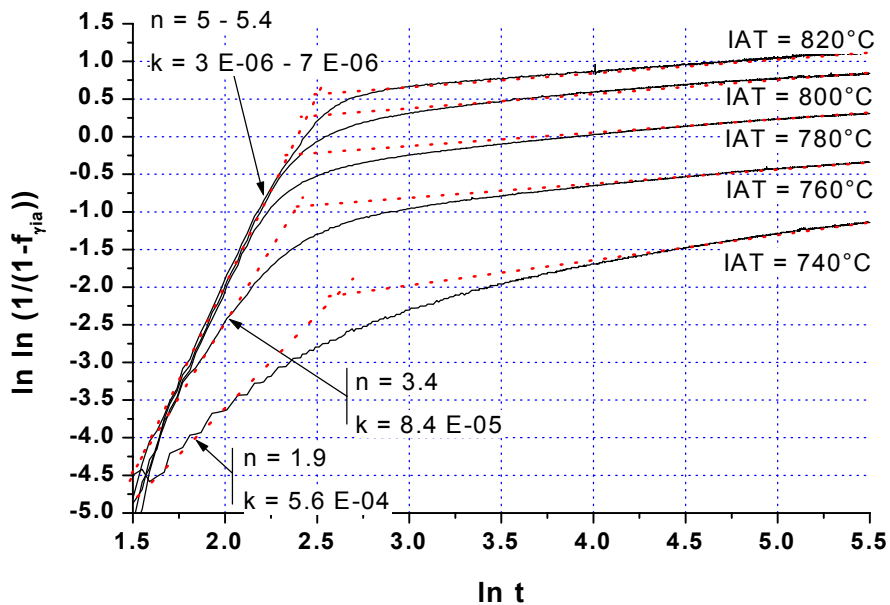

Figure IX.8: Double logarithmic plot according to the JMA equation of the austenite formation during I.A.

This part of the re-austenitisation process has a much slower rate. This behaviour was also observed for TRIP steel during intercritically annealing for their ferrite-pearlite microstructure.[15] The austenite formation during intercritical annealing is dependent on the initial microstructure. The austenite fraction obtained with the JMA analyses were overestimated. Partial recrystallisation of the ferrite during intercritical annealing, leading to an extra decrease in the length of the samples could be a reason for this observation. The fraction of austenite formed was determined using the intersection of the two extrapolated lines of Figure IX.8. The results were close to those obtained with the previous methods, as illustrated in Figure IX.7a and 7b.

IX.4.2 Microstructure predictions in cold rolled sheets

Intercritical annealing experiments were carried out in a dilatometer on cold rolled steel sheets. Due to the non-standard shape of the samples as well as their different starting microstructure, the method using the M_s temperature was used to determine the fraction of intercritical austenite. It can be seen on Figure IX.9 that the decrease in length of the cold rolled plates during annealing was more important than for the cylindrical sample. The difference is clearly due to the shape and the initial microstructure of the samples. In the material coiled at 720 °C, the cold rolled ferrite recrystallised faster than the bainitic ferrite in the plate coiled at 550 °C. It can be seen that after annealing 10 min at 780 °C, the bainitic transformation was suppressed and the M_s temperature was lower in both cold rolled samples than in the cylindrical sample. This implies that less austenite was formed in the case of the

cold rolled steel during intercritical annealing, as its C content was higher. Microstructural observations combined with phase analysis using the M_s method described previously allowed for the determination of the phases volume fractions. 34 and 38 vol.% of austenite was formed in the samples coiled at 550 °C and 720 °C, respectively. The samples were then cold rolled and annealed for 10 min at 780 °C. Other samples were annealed for 10 min at 820 °C. The JMA analysis was carried out to estimate the activation energies for austenite formation in cold rolled plates. It was measured 136 kJ/mol and 276 kJ/mol in the samples coiled at 550 °C and 720 °C, respectively. The lower activation energy in the sample coiled at 550 °C was likely due to the presence of more nucleation sites for the austenite formation. It must be noted that the value of 136 kJ/mol is close to the value of 150 kJ/mol measured in chapter V for the bainite formation during both isothermal holding and continuous cooling CMn steels. It corresponds to the activation energy for carbon diffusion in the austenite. The value of 276 kJ/mol measured in the sample coiled at 720 °C must be compared to the activation energy for self-diffusion of γ-Fe.

This means that in the case of the pearlite decomposition to austenite, the process is controlled by substitutional diffusion, while the bainite decomposition to austenite is controlled by the interstitial C diffusion in the austenite. However, even though the activation energy for the nucleation of intercritical austenite was lower in deformed samples, the growth rate was lower in the cold rolled plates than in the case of the cylindrical sample, which had much larger grain sizes, due to its reheating to 1200 °C between intercritical annealing cycles.
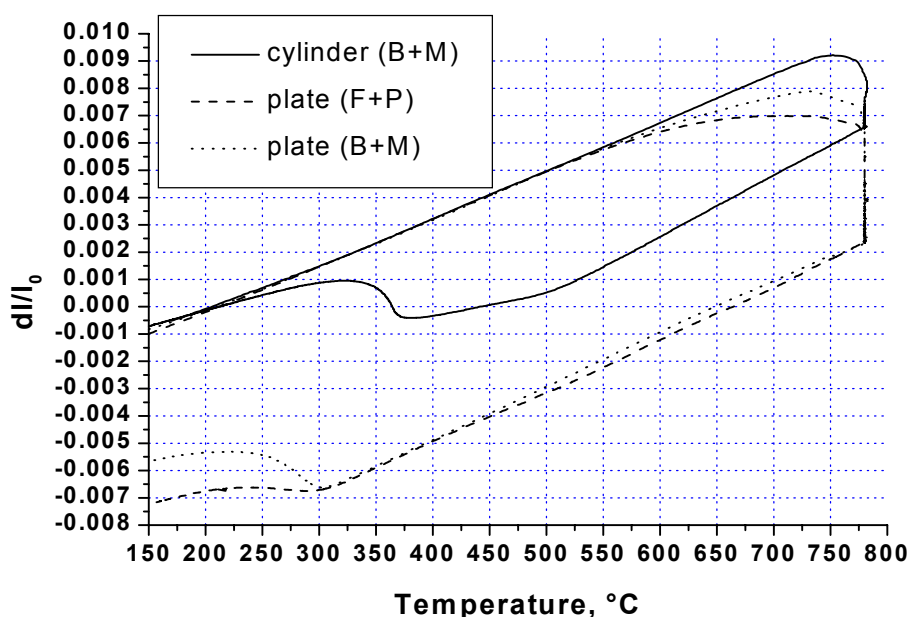

Figure IX.9: Dilatometric curves with intercritical annealing at 780 °C for different initial microstructures.

Figure IX.10 gives the volume fractions of the ferrite, including primary ferrite and ferrite formed during the cooling following the annealing, the austenite formed at the intercritical annealing temperatures, the bainite and the martensite in the final microstructure in the three types of dilatometric samples. It is clear that the kinetics of austenite formation is lower in
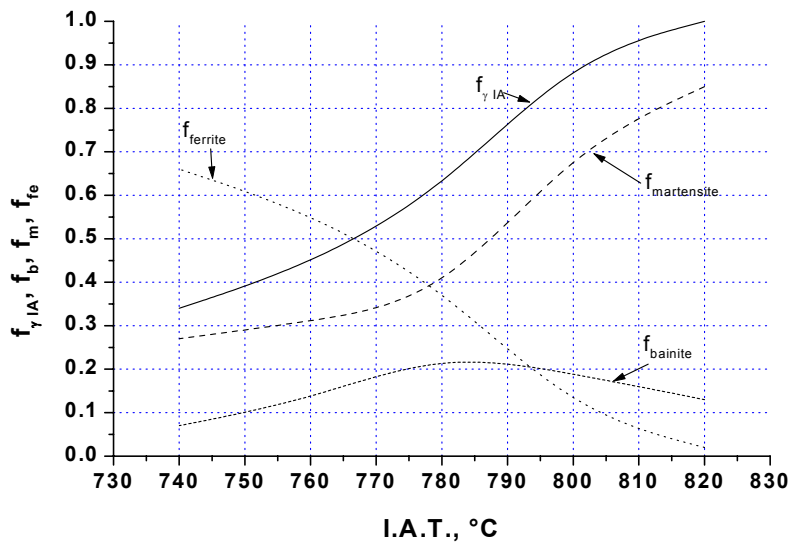
cold rolled plates. The use of such samples instead of standard dilatometer samples seems therefore necessary. The initial microstrucure and the deformation before simulating continuous annealing cycles are to be taken into account.
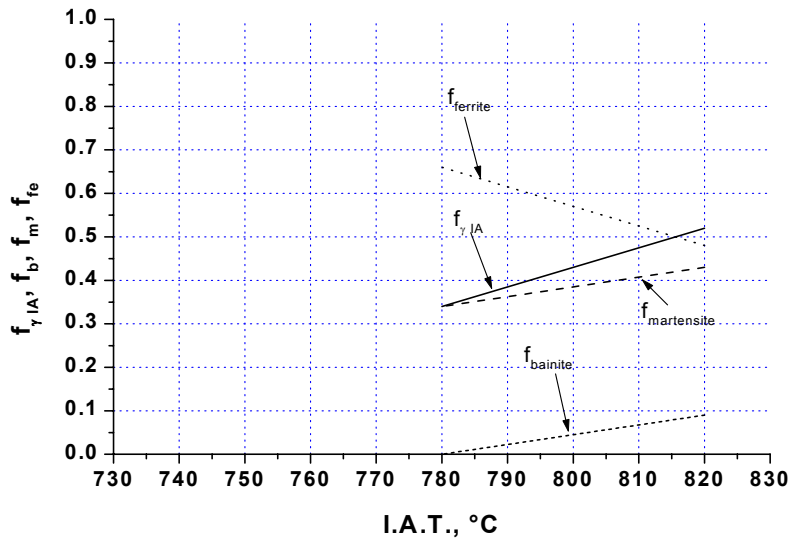
a)
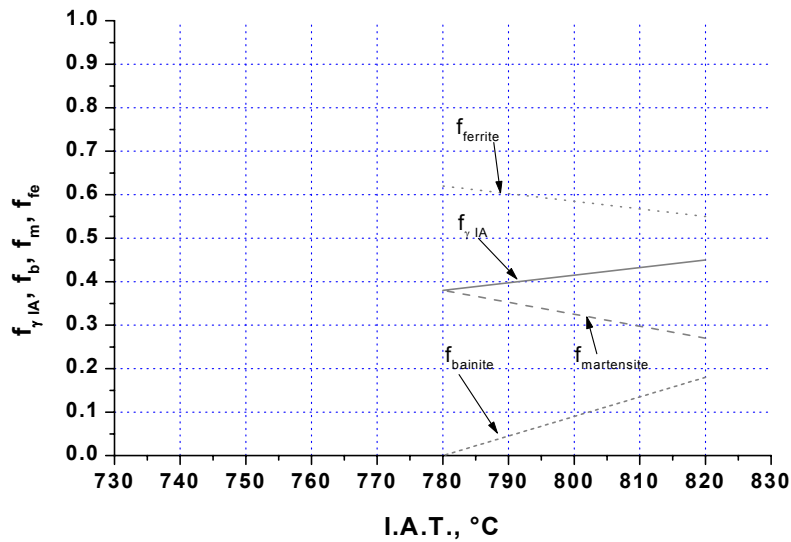
b)

c)

Figure IX.10: Fractions of intercritically annealed austenite and ferrite, and fractions of bainite and martensite formed during subsequent cooling from IAT for a) sheet sample with microstructures F+P, b) sheet sample B+M and c) cylindrical sample B+M (bottom).

It can be seen on the micrographs Figure IX.11 that after the intercritical annealing of 10 min at 820 °C, a cold rolled plate coiled at 720 °C consists of the initial recrystallised ferrite (dark phase), and a mixture of ferrite, bainite and martensite. Annealing a similar sample 10 min at 780 °C lead to a dual phase microstructure of ferrite and martensite. Other simulations using different cooling patterns after the intercritical annealing of the cold rolled plates at different temperatures and times were also carried out. The same cycles were done on larger sheet samples using a continuous annealing simulator. The final complex phase microstructures and the mechanical properties are reviewed in the next paragraphs.
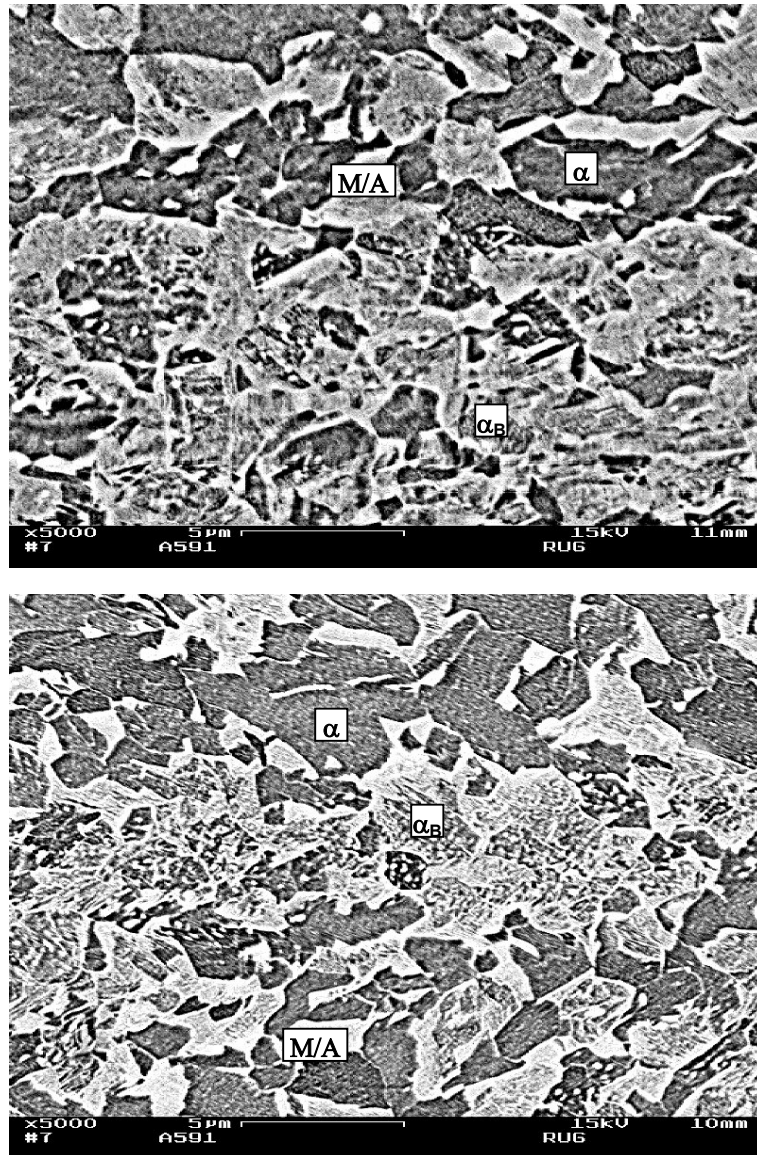

Figure IX.11: SEM micrographs showing the microstructure obtained after annealing cold rolled sheet samples (CT = 720°C) for 10 min at a) 780°C and b) 820°C. Etchant: LePèra.

IX.5 Microstructure-properties relations

The hot rolled plates were cold rolled with 60 % reduction and intercritically annealed in a continuous annealing simulator to obtain microstructures leading to high levels of strength and adequate elongations. Two intercritical annealing temperatures, respectively 780 °C and 820 °C were used. The annealing time was 60 s. Some samples were cooled continuously at different cooling rates to produce a dual phase microstructure and others were cooled to an isothermal holding temperature to favour the bainitic transformation. Microstructures with different volume fractions of ferrite, bainite and martensite were thus produced. In all cases the tensile curves showed a continuous yielding. This is very likely due to the presence of the martensite phase in all the samples. This is consistent with the observation of continuous yielding in dual phase steels with martensite contents of more than about 4 %.[16] Figure IX.12 is an A_{50} *versus* TS graph. Recent tensile tests performed on hot rolled steels with tensile strengths above 800 MPa using A_{80} and A_{50} specimens showed that the measured yield strength, tensile strength and the total elongation were very similar.
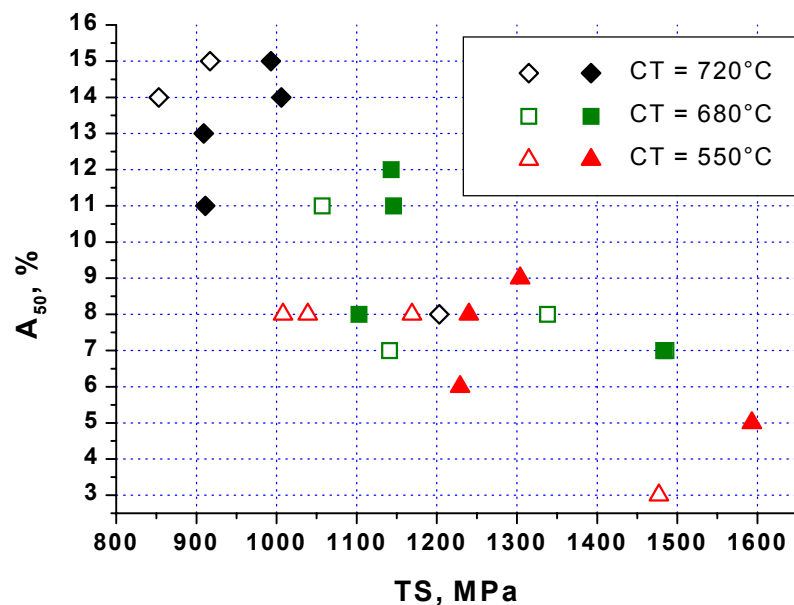

Figure IX.12: Tensile properties of cold rolled complex phase steels intercritically annealed at 780 °C (open symbols) and 820 °C (solid symbols) then cooled using different patterns.

It can be seen on Figure IX.12 that the best elongations were obtained starting from samples coiled at 720 °C, which have a ferrite-pearlite starting microstructure. After the intercritical annealing the ferrite was the softer phase in the material. During tensile testing, ferrite was first deformed and was mainly responsible for the elongation. Its ability to absorb the energy of deformation was higher in the ferrite-pearlite microstructure due to its morphology. The drawback of starting from the ferrite-pearlite was that after cold rolling and annealing, some bands due to the segregation of alloying elements such as Mn in the pearlite were still present and were detrimental for the tensile properties in the transverse direction. It can also be seen that a higher annealing temperature led to both a better strength and a larger elongation (solid symbols in Figure IX.12).

As more austenite was formed at higher intercritical annealing temperature, more M/A constituent was produced during the subsequent cooling, increasing the strength of the material. It has been seen previously that during annealing, the primary ferrite recrystallised and thus accumulated more energy of deformation. This could explain the relatively high values of elongation.

Figure IX.13 shows microstructures obtained after an intercritical annealing at 780 °C and 820 °C, respectively, and an isothermal holding to produce bainite.
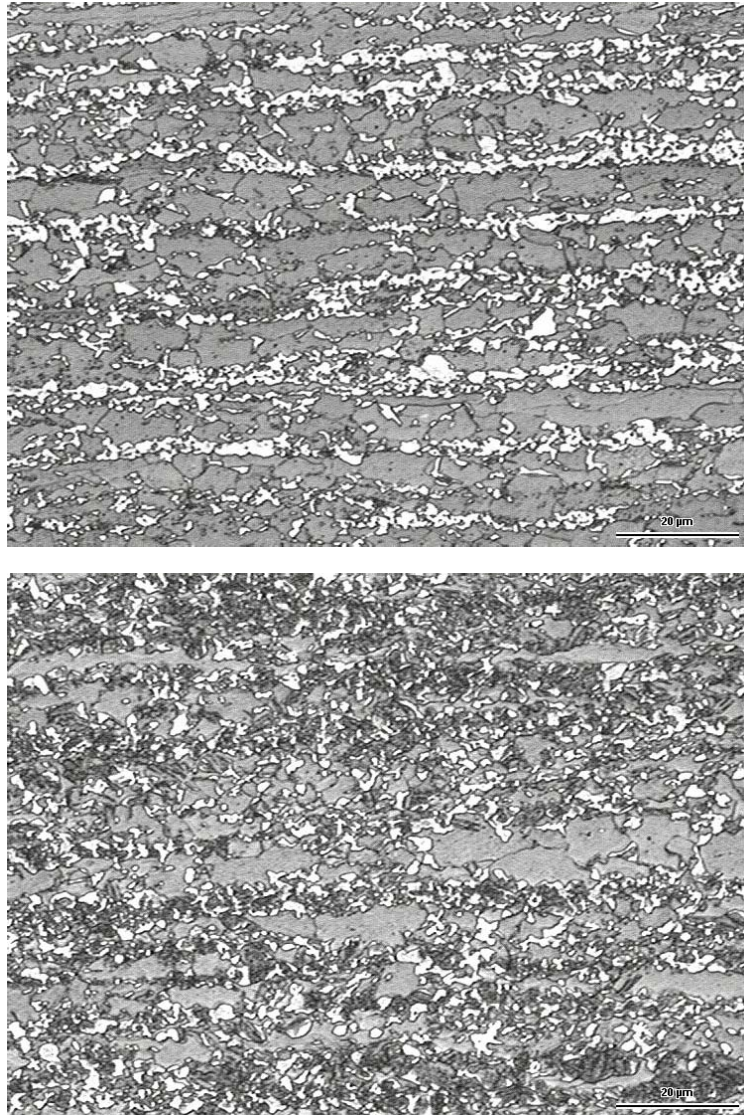

Figure IX.13: Light optical micrographs showing microstructures after continuous annealing cycles on plates coiled at 720 °C. Annealing temperatures: 780 °C (top) and 820 °C (bottom). Etchant: LePèra.

Image analysis on micrographs combined with dilatometer studies were used to determine the volume fractions of each phase after different annealing cycles. The microstructures observed were then plotted in ternary diagrams for different ranges of tensile properties, as shown in Figure IX.14.
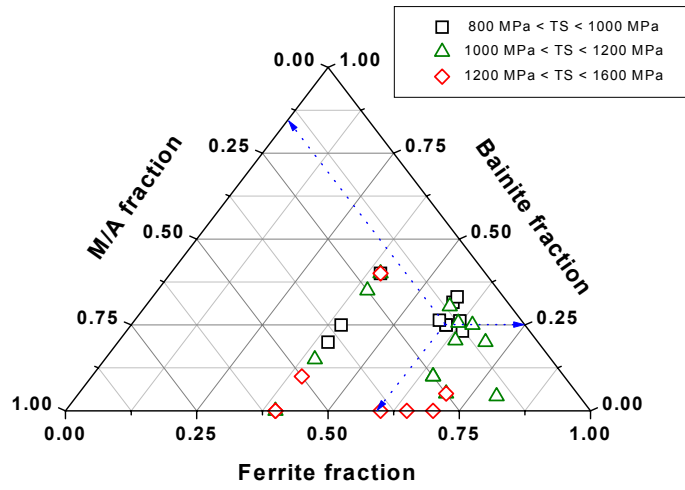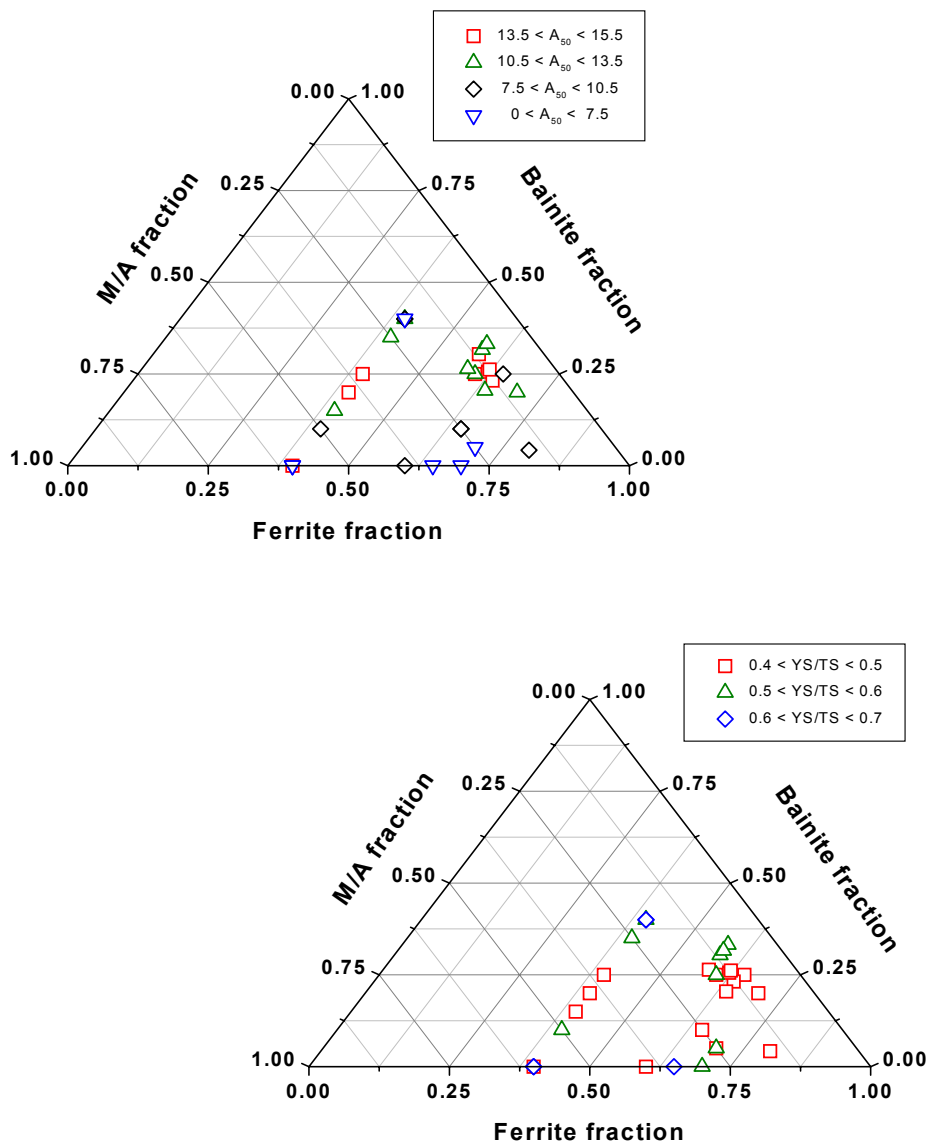
Figure IX.14: Effects of phases content on the tensile strength TS, on the total elongation A_{50} and on the ratio YS/TS.

Using this original method to report the results, it can be seen that the highest tensile strengths were obtained in the steels with the bainite-free microstructures, *i.e.* DP steels. Those had also the lowest elongations. The best compromise between strength and elongation were obtained in steels containing about 25 % bainite. Those CP steels with 15-30 % bainite, 10-50 % martensite/austenite and 50-80 % ferrite had also the lowest YS/TS ratios, which is particularly beneficial for good stretch formability.

IX.6 The M/A constituent

In the three properties graphs shown in Figure IX.14, the microstructure is a mixture of ferrite, bainite and M/A. However, the mixture of martensite and austenite is particularly interesting as sufficient amounts of residual austenite may be responsible for a TRIP effect. Different samples with the industrial composition were thermally treated to produce varied microstructures containing ferrite, bainite and M/A. The resulting samples were observed in SEM after metallographic etching using the method of LePèra. It can be seen in Figure IX.15, that ferrite and bainite could hardly be distinguished. In contrast, the M/A constituent was clearly observed.
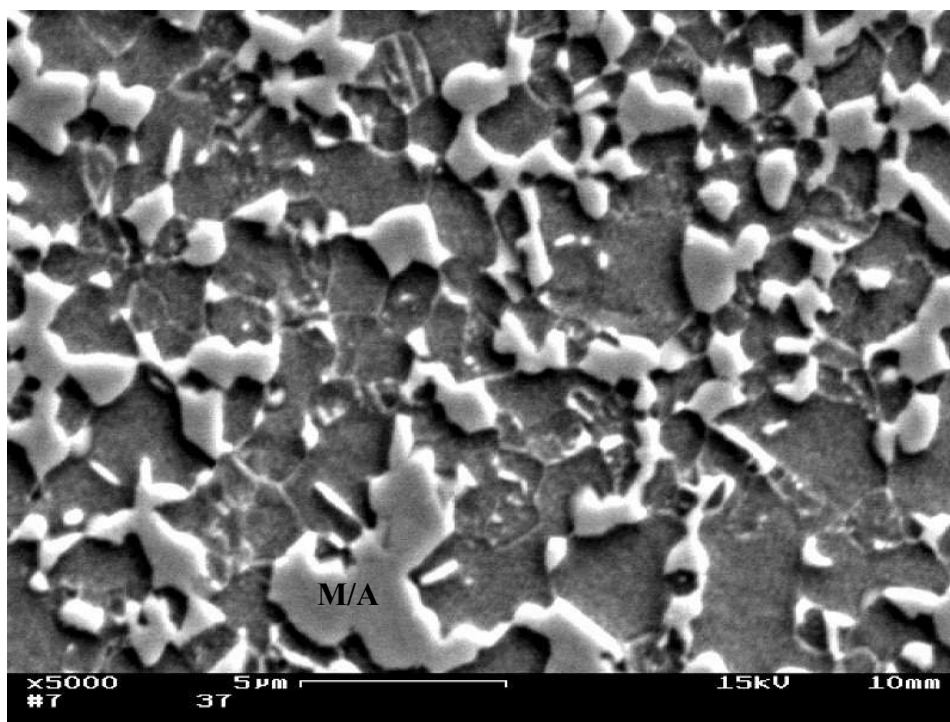

Figure IX.15: SEM Microstructure of cold rolled complex phase steel. CT = 650 °C. IAT = 800 °C. Bainitic transformation at 400 °C. Etching method: LePera.

Using quantitative optical analysis, the fraction of M/A was measured in each sample. The ferrite fraction was calculated from the time and temperature of intercritical annealing by means of the method presented before. The tensile properties were measured on tensile specimen with 80 mm gauge length. The yield strength and tensile strength are plotted as a function of the M/A fraction in Figure IX.16.
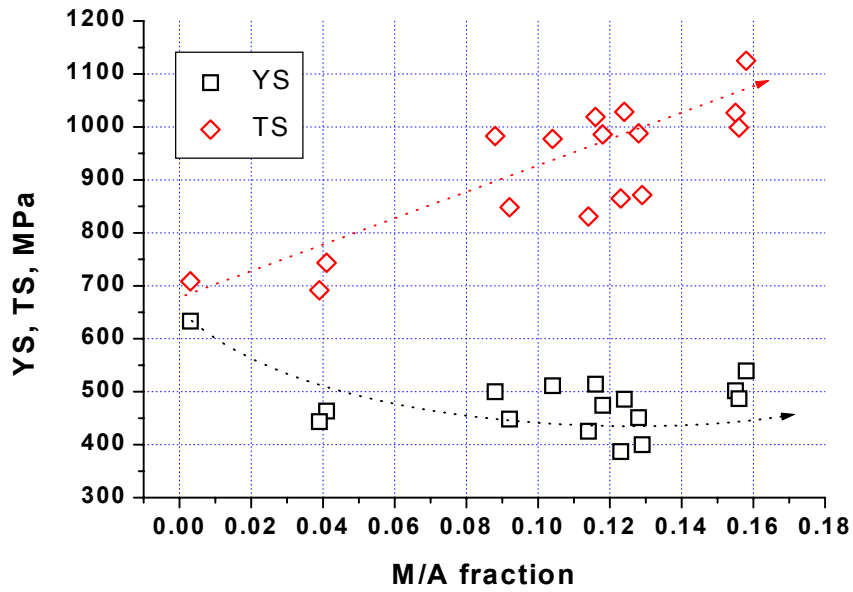
Figure IX.16: YS and TS *vs.* fraction of M/A constituent in cold rolled and annealed CP steel.
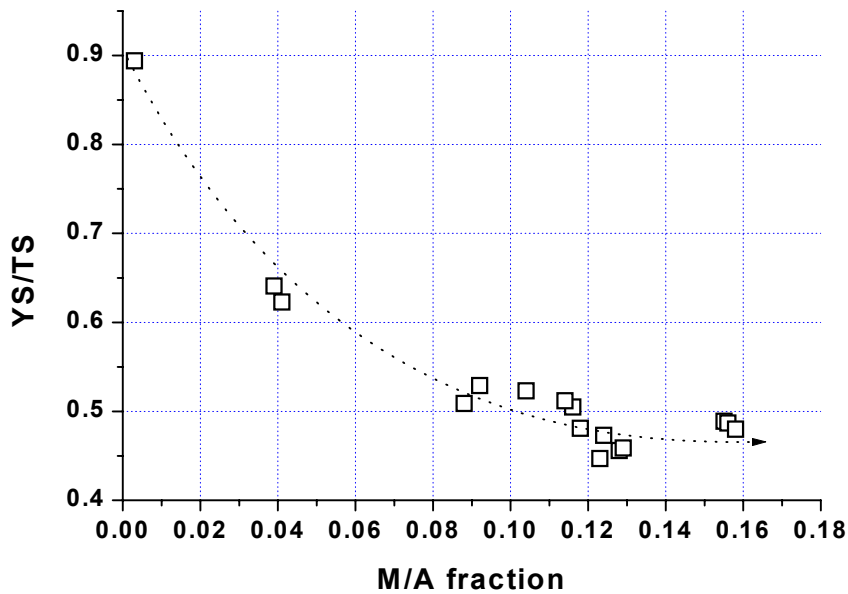

Figure IX.17: Influence of the fraction of M/A constituent on the YS/TS ratio.

It can be seen in Figure IX.16 that the YS is not affected much by the fraction of M/A. On the other hand, TS clearly increases with increasing volume fraction of M/A. As a result, the YS/TS ratio clearly decreases with increasing fraction of M/A as can be seen in Figure IX.17. The YS/TS ratio lower than 0.5, was obtained with microstructures containing more than 0.12 vol.% M/A.

Figure IX.18 shows the evolution of the uniform elongation (UE) and total elongation (TE) with the fraction of M/A. It is clearly seen that the elongation increase with increasing M/A fraction up to a maximum at 0.12. From these results, it is clear that the fraction of residual austenite in M/A influences the elongation. It is very likely that in the martensite-austenite mixture a TRIP effect due to the transformation of residual austenite to martensite occurs. The resulting increase of the strain hardening is the cause of the improved elongation.
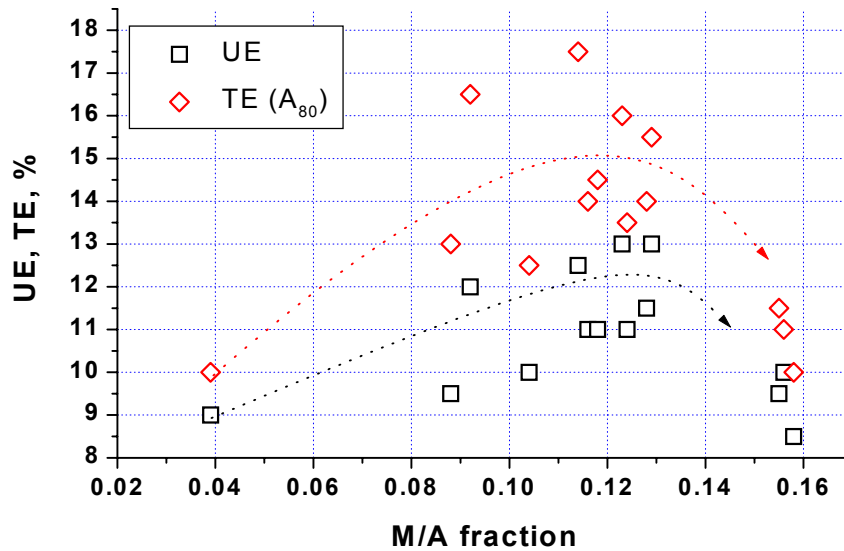

Figure IX.18: Uniform Elongation (UE) and Total Elongation (TE) *vs.* volume fraction of M/A constituent.

Magnetic measurements were carried out to determine the fraction of residual austenite. The carbon content in residual austenite was estimated by means of the equation:

$$C_{\gamma res} = \frac{C_0(1 - f_{\alpha_b}) - 0.02 f_\alpha}{f_{M/A}}$$

(IX.10)

It was assumed that the carbon content in bainite was equal to the initial austenite carbon content $C_o = 0.16$ wt.%. This is based on the findings reported in chapter IV. Figure IX.19 shows the results for the fraction of residual austenite as a function of its carbon content. During the thermal cycle, austenite formed from the initial microstructure, then transformed to bainite and martensite. The intercritical annealing temperature and time determine the fraction and carbon content of intercritical austenite. The intercritical austenite is further enriched in C during the bainitic transformation. The C content in the austenite at the end of the isothermal bainitic transformation determines whether the remaining austenite will transform to martensite or not. The pseudo-binary Fe-C diagram in Figure IX.20 shows the enrichment of austenite in C during the annealing cycle. The experimental results revealed that the highest elongation was obtained for 12 vol.% of M/A constituent with ~5 vol.% residual austenite. The residual austenite is transformed to martensite during straining.
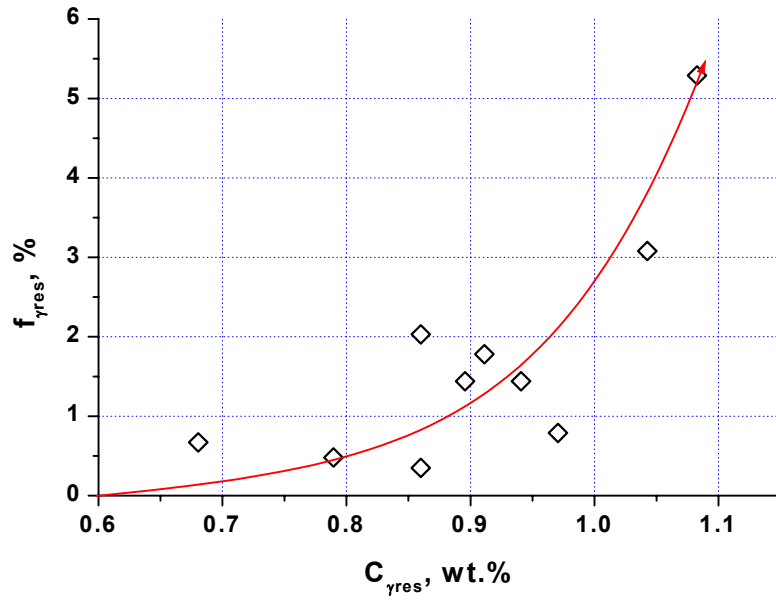
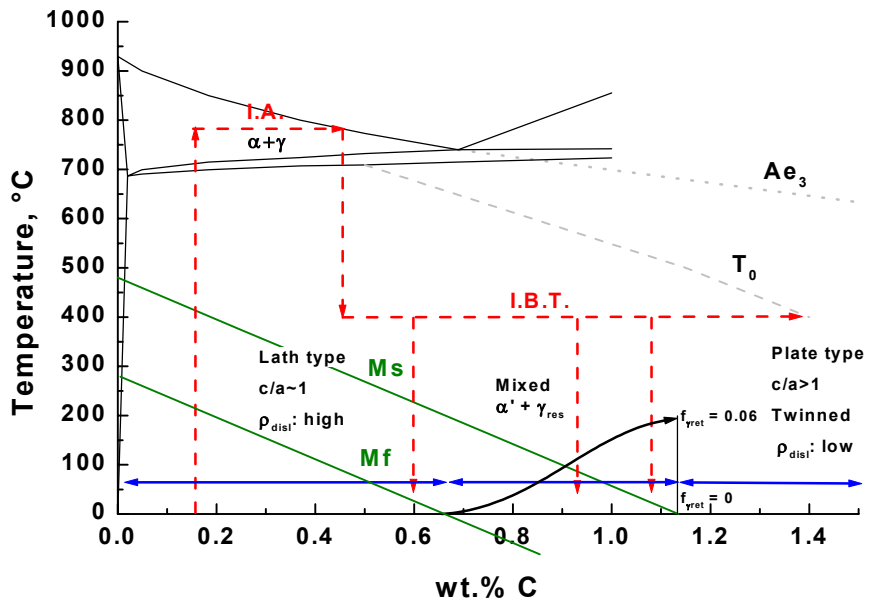**Figure IX.19:** Residual austenite fraction *vs.* carbon content.

Figure IX.20: Pseudo Fe-C diagram showing the variation of C in the austenite during an I.A. cycle.

IX.7   TEM microstructure of cold-rolled CP steel

Thin foils were prepared from cold-rolled complex phase steel with the microstructure shown in Figure IX.15. That cold-rolled Nb-microalloyed CMnMoCrB steel contained a mixture of ferrite (~65 vol.%), bainite (~20 vol.%), and martensite (~15 vol.%). Magnetic measurements and XRD did not detect more than 2 vol.% of retained austenite. The microstructure was observed using a Philips EM 420 Transmission Electron Microscope (TEM) operating at 120 kV. Figure IX.21 shows high dislocations density in the ferritic phase. That phase can either be ferrite coming from the reheating of a dislocated bainitic microstructure, or bainitic ferrite formed during the isothermal bainitic transformation during the annealing cycle. The presence of dislocations can be explained due to the low transformation temperature of bainite in both cases. However, the bainitic ferrite formed during hot-rolling was reheated and likely recovered. If the observed ferritic phase is actually primary bainitic ferrite, the present dislocations are very likely due to the plastic deformation of this phase consequently to the formation of martensite in the close neighbourhood.
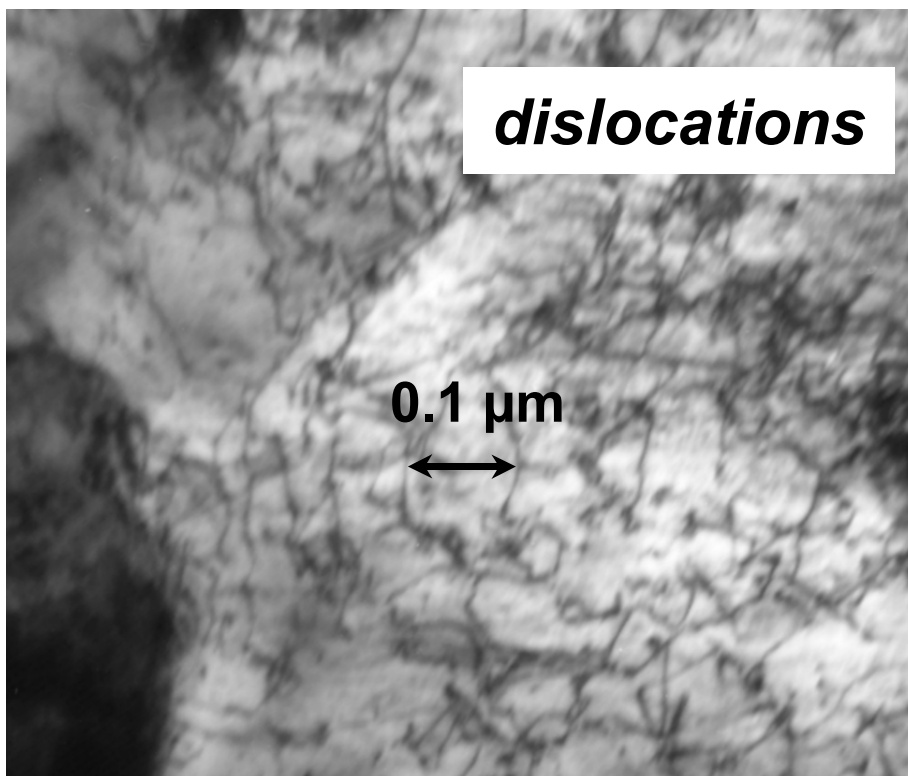

Figure IX.21: TEM micrograph showing high dislocations density in ferritic phase.

As can be seen in Figure IX.22, martensite producing a dark contrast was found between large ferritic zones. In both ferritic and martensitic regions, small precipitates with diameters between 20 and 50 nm were found. Those precipitates are very likely TiCN, TiN or TiC precipitates as they are similar and of the same size order to those observed in chapter VI, Figure VI.5 in CMn steels. The possibility of Nb precipitates must also be envisaged, as Nb is present in the studied steel. A clear identification of those precipitates would require further TEM investigations.
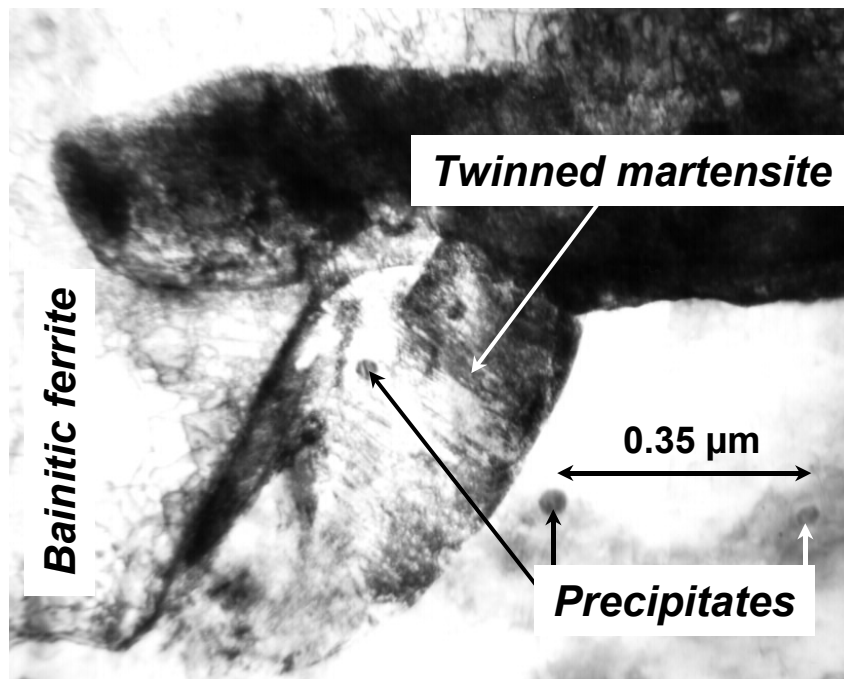
Figure IX.22: TEM microstructure of cold-rolled CP steel.

Figure IX.23 shows a clear twinned martensite, as observed in the hot–rolled sample shown in chapter I. The diffraction pattern shows satellite spots confirming that different crystallographic planes have the same orientation. That martensite, rich in C, was very likely formed during the last step of the annealing cycle, *i.e.* during the cooling to room temperature.

One diffraction spot was selected to obtain the dark field diffraction conditions corresponding to a twin. Figure IX.24 shows clearly that parallel planes are highlighted, corresponding to a same family of diffracting planes.

Figure IX.23: TEM micrograph of twinned martensite in cold rolled sample.

Figure IX.24: Dark field TEM image and corresponding diffraction spot in twinned martensite.

IX.8 Impact testing

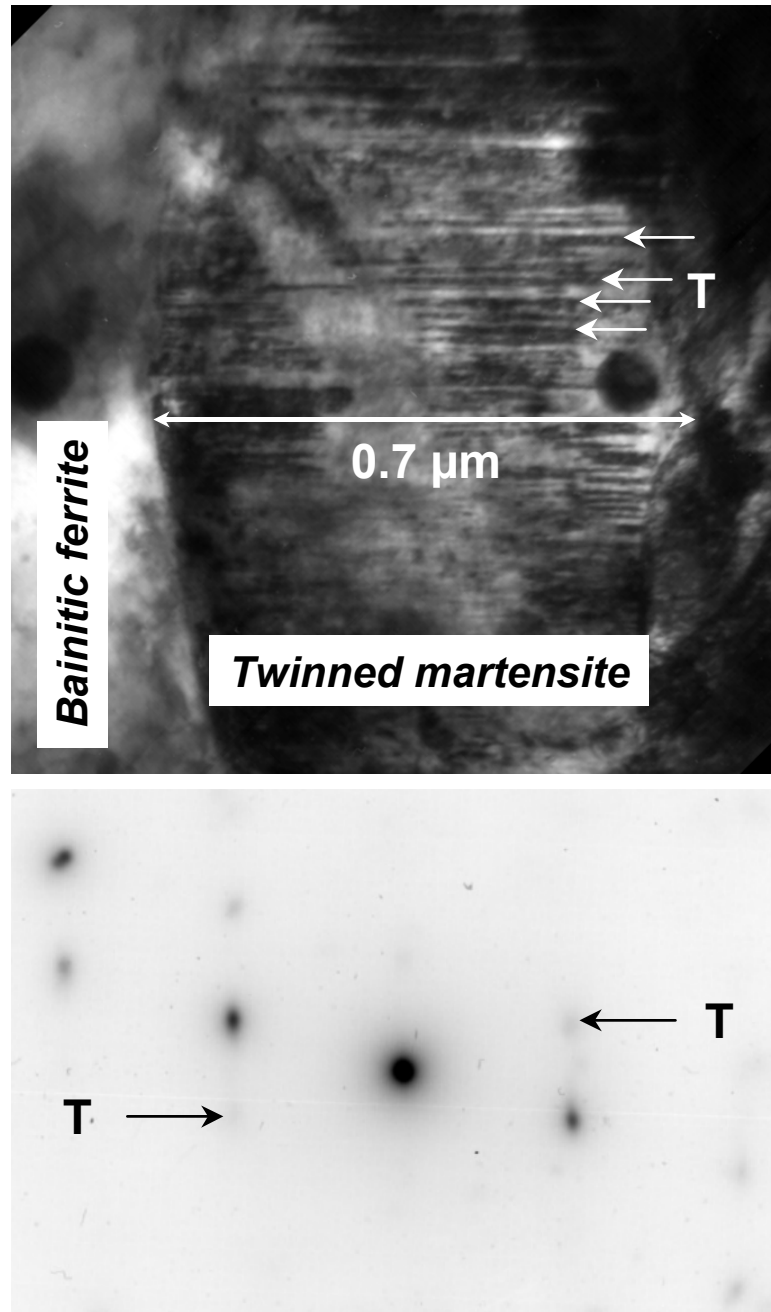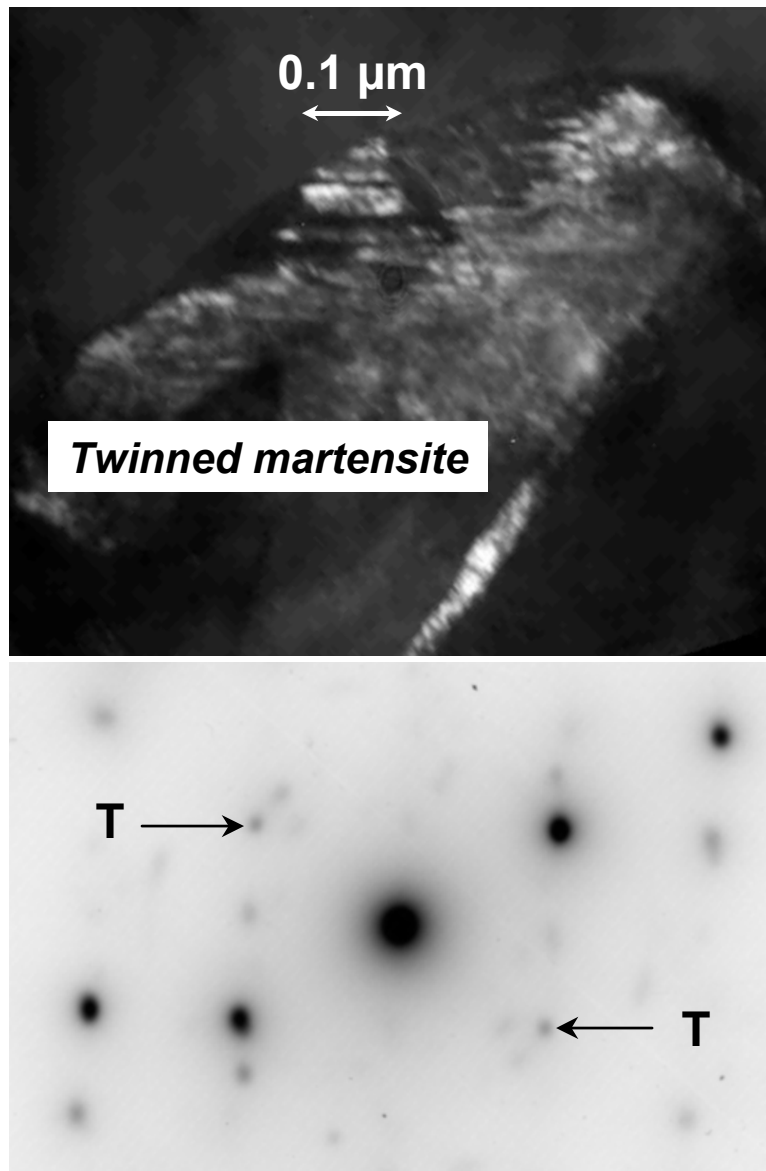High strain rate tensile tests were carried out on a Charpy machine modified for tensile testing and equipped with a force sensor, described in chapter II. The initial impact tension rate was 150 s^{-1}. The effective strain at fracture (ε_{eff}) was calculated as:

$$\varepsilon_{eff} = 2.\sqrt{\varepsilon_2^2 + \varepsilon_2\varepsilon_3 + \varepsilon_3^2} \qquad (IX.11)$$

where ε_2 and ε_3 are the major strains calculated using:

$$\varepsilon_2 = \ln\left(\frac{b_0}{b_f}\right), \varepsilon_3 = \ln\left(\frac{h_0}{h_f}\right) \qquad (IX.12)$$

where h_0, b_0 are the initial cross section dimensions and h_f, b_f the neck size values after fracture.

Specific absorbed energy, total elongation of the specimen and maximum localized strain were measured. The effective stress was calculated as the value providing equivalent absorbed energy at the same elongation.

The comparison between static and impact testing is shown in Figure IX.25. A strong increase of both the total elongation and the tensile strength is observed after impact testing, which means that *e.g.* in case of a crash of a passenger car, using the CP steel would improve the safety. Similar results were observed in TRIP steel alloyed with Al, while in conventional Si-alloyed TRIP steel the elongation was lowered.[17]
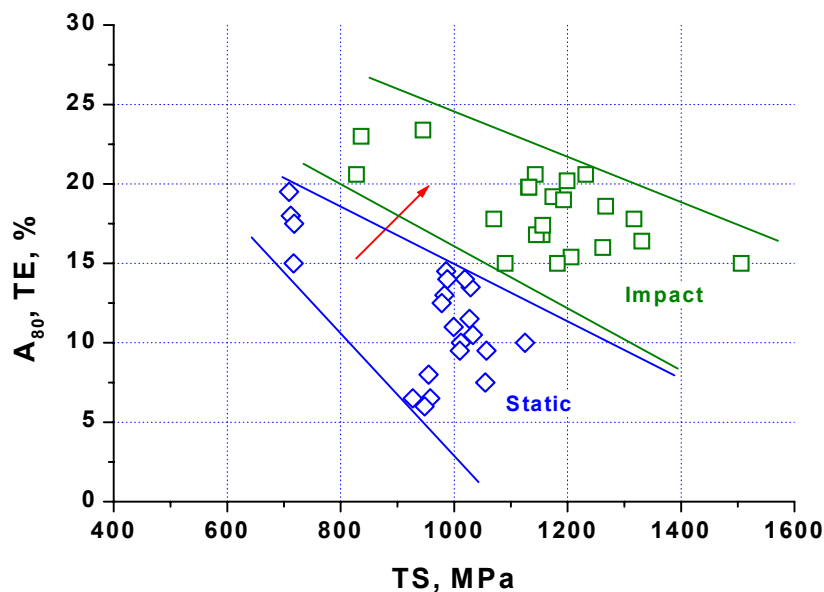
Figure IX.25: Comparison between static and impact tensile tests for the cold rolled CP steel.
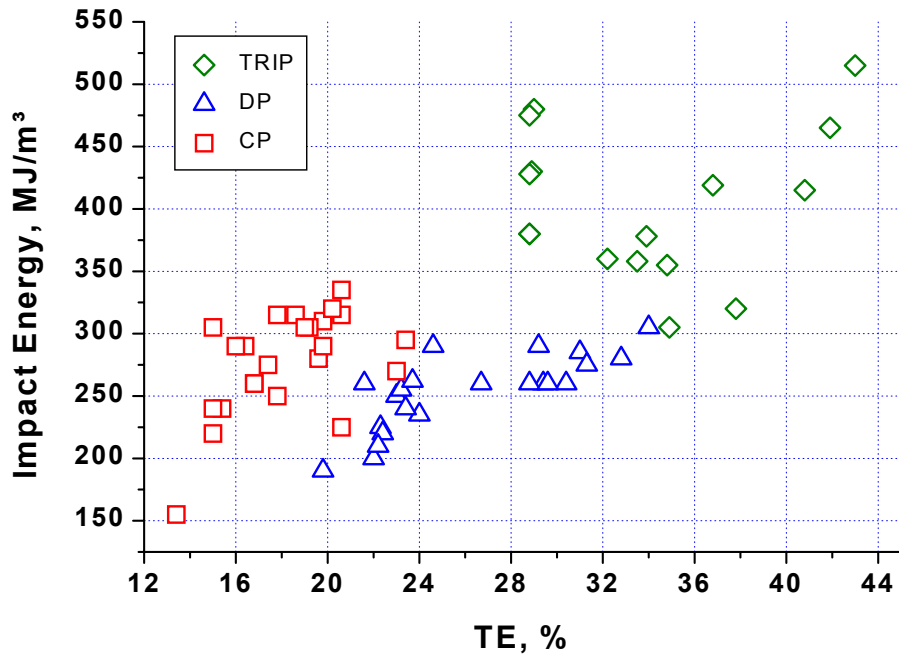
Figure IX.26: Impact energy *vs.* total elongation plot for different HSS grades.
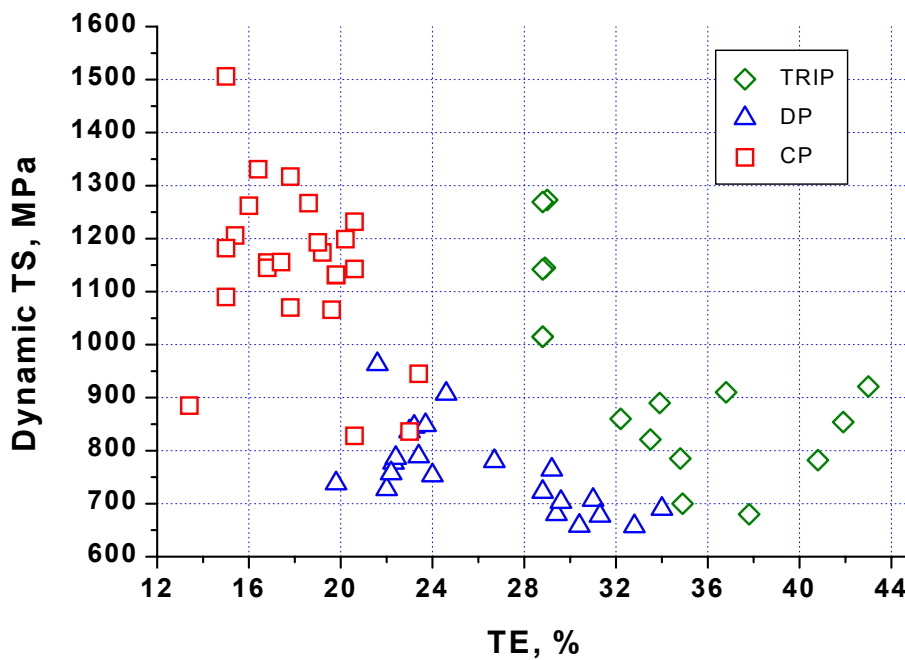
Figure IX.27: Impact tensile stress *vs.* total elongation plot for different HSS grades.

The impact energy and the impact tensile strength as functions of the total elongation are compared in different steel grades, *i.e.* TRIP, Dual Phase (DP) and Complex Phase (CP) steels in Figure IX.26 and Figure IX.27, respectively.

The highest elongation was obtained for TRIP steels, DP steels had an intermediate total elongation and CP had the lowest elongation. The impact energy, however, was higher for CP steels than for DP steels. The tensile strength was much higher in CP steels than in DP and TRIP steels. From these graphs it appears that the TRIP steels have the best crash safety potential. CP steels, however, have to be considered as they have high tensile strength, adequate elongation and good impact energy adsorption.

IX.9 Conclusions

Cold rolled and intercritically annealed CP steel was studied in detail. Batch annealing simulations allowed the determination of the ferrite recrystallisation temperature. It was shown that dilatometry could be done on cold rolled plates to determine the temperatures of phase transformations and the volume fractions of phases formed after continuous annealing simulations. The state of deformation in cold rolled plates was responsible for a decrease in the kinetics of austenite formation during annealing between Ac_1 and Ac_3. Continuous annealing simulations with different cooling patterns were performed on cold rolled plates and the tensile properties were measured. The effects of the different parameters can be summarized as follows:

Initial microstructure - A ferrite-pearlite starting microstructure leads to lower tensile strengths and better elongation after annealing, due to the polygonal shape of ferrite. However, due to the higher decomposition rate of pearlite to austenite than ferrite to austenite, a banded structure is still present after annealing and may be detrimental for the tensile properties in the transverse direction. A bainite-martensite starting microstructure leads to higher strength levels but poorer elongations.

Annealing temperature - Increasing the intercritical annealing temperature leads to the formation of more austenite. Depending on the cooling pattern, more of the hard phases, bainite and martensite, may be formed, increasing the strength level. Larger recrystallised ferrite grains may be responsible for the excellent elongation.

Annealing time - It was shown that the austenite formation was faster at the start of the intercritical annealing. Carbon partitioning was more sluggish. Reducing the annealing time lead to a slightly lower fraction of austenite.

Cooling pattern - The best compromises between high strength and good elongation were obtained for the CP steels with about 63 % ferrite, 25 % bainite and 12 % martensite. It was shown that a thermal cycle with an isothermal bainitic transformation (IBT) at 450 °C was the most efficient.

The M/A constituent was found to be mainly responsible for the improvement of tensile properties, *i.e.* an increase of TS, decrease of the YS/TS ratio and the increase of TE. The residual austenite content in the M/A constituent increased the total elongation very likely due to a TRIP effect.

Finally, impact properties were better than static tensile properties. This implies that CP could be used in crash-sensitive parts of passenger cars.

[1] J-L. Bouteille, C. Brun : in Le Livre de l'Acier, G. Béranger, G. Henry, G. Sanz eds.,1994, p.1327.

[2] F.S. LePera: J. Metals 32, No. 3, 1980, p.38.

[3] J.Z. Zhao, C. Mesplont, B.C. De Cooman: Z. Metallkd. 92, n°4, 2001, p.345.

[4] J.Z. Zhao, C. Mesplont, B.C. De Cooman: ISIJ vol.41, n°5, 2001, p.492.

[5] J.Z. Zhao, C. Mesplont, B.C. De Cooman: Materials Science and Engineering A332, 2002, p.110.

[6] D.P. Koistinen and R.E. Marburger, Acta Metallurgica, Vol. 7, 1959, p.59.

[7] M.V. Li, D.V. Niebuhr, L.Y. Meekisho, D.G. Atteridge: Met. Mat. Trans. B, Vol.29B, June 1998, p.661.

[8] W. Stevens and A.G. Haynes, J. of the Iron and Steel Institute, 183, 1956, p. 349.

[9] C.Mesplont, J.Z. Zhao, S. Vandeputte and B.C. De Cooman: Steel Research 72, 2001, 7, p.263.

[10] G.K.Prior: Materials Forum 18, 1994, p.265.

[11] K.J. Albutt, S. Garber: J. of the Iron and Steel Institute, December 1976, p.1217.

[12] J. Burke: The Kinetics of Phase Transformation in Metals, Pergamon Press, Elmsford, NY, 1965.

[13] D.A. Porter, K.E. Easterling: Phase Transformations in Metals and Alloys, Second Edition, Stanley Thornes (Publishers) Ltd, 2000, p.78.

[14] G.J. Shiflet, H.I. Aaronson: Metallurgical Transactions A, vol. 21A, June 1990, p.1413.

[15] M. De Meyer, J. Mahieu, B.C. De Cooman: « On the Combination of Intercritical Annealing and Isothermal Bainitic Transformation of CMnSi and CMnAlSi TRIP Steels", submitted to Metallurgical Transactions A, 2002.

[16] D.T. Llewellyn and D.J. Hillis: Ironmaking and Steelmaking, Vol. 23, No. 6, 1996, p.471.

[17] I.Y. Pyshmintsev, R.A. Savrai, B.C. De Cooman, O. Moriau : Int. Conf. On TRIP-aided High Strength Ferrous Alloys, B.C. De Cooman, ed., Ghent, Belgium, 19-21 june 2002, p.299.

General conclusions

X.1 Improved method to study multistep phase transformations kinetics from dilatometric data

Due to their thermal expansion and phase transformations, significant volume variations can be measured in steels by means of dilatometry during heating, cooling or isothermal holding. The volume fraction of the parent phase is usually determined from a curve of relative length change as a function of temperature by using the lever rule method. The lever rule is, however, only applicable in the case of a process which involves only one phase transformation as the relation between the amount of formed phase at a certain stage of the transformation and the associated volume change is assumed to be linear. In addition, it does not give any information about the composition of phases. A model was, therefore, developed based on the thermal expansion coefficients to calculate the phase transformation kinetics from a dilatation curve. The model was first validated by comparing its results with the experimental results for a interstitial-free steel which involved only one phase transformation during a cooling from the austenite phase region. The model was then applied to investigate the bainitic transformation using the dilatation curves obtained from a bainitic grade steel. Excellent agreement between the model and the experiments was found.

X.2 Experimental study of multistep phase transformations kinetics during continuous cooling C-Mn steels

Although dilatometry can be used to determine the beginning and the end temperatures of phase transformations, the standard data analysis based on the lever rule is usually not appropriate to determine accurately the different volume fractions of phases when several phases are formed. In addition to the well-known lever rule method, the new method described in chapter III was applied to study the phase transformations in a 0.2C-1.6Mn steel. Calculated volume fractions of phases were compared with microstructural observations and supplemented with hardness measurements. A detailed CCT diagram was obtained. The method was believed to be well suited to study the effects of alloying elements on the austenite decomposition. The bainitic transformation could be analyzed in detail as the model takes into account the carbon partitioning and its considerable enrichment in the bainite. The existence of a critical cooling rate, at which the carbide precipitation is suppressed after the bainite formation, was emphasized.

X.3   Dilatometric study of the effect of soluble boron on the continuous and isothermal austenite decomposition in 0.15C-1.6Mn steel

From the literature study of the reported effects of soluble boron on the phase transformations, it was remarked that soluble boron affected differently the ferrite and the bainite formations. Hence, the mechanism of transformation, diffusive or displacive, seemed to determine how the nucleation rate was affected by soluble boron. It has been suggested that the growth process of ferrite may be slowed down by a solute drag like effect (SDLE) due to the partitioning of alloying elements.

In this chapter, continuous cooling a C-Mn steel containing soluble B from the austenitic region with different cooling rates and isothermal transformation cycles were performed in a dilatometer in order to produce controlled microstructures. The kinetics of ferrite formation during an isothermal holding and a continuous cooling was clearly slowed down by the boron addition. It was observed that no grain boundary nucleation of ferrite occurred in the boron bearing steel. The carbide precipitation was also found to be retarded in the steel containing boron. The kinetics of bainite formation, however, was not influenced by boron additions. The segregation of boron to γ-grain boundaries effectively suppressed the grain boundary nucleation of the ferrite. Ferrite and bainite likely nucleated from TiN precipitates inside the austenite grains. As a result, the microstructures obtained after any heat treatment were morphologically different than the microstructure of the boron free reference steel. Indeed, in the CMnB steel, the formation of the primary ferrite was suppressed, and the upper bainite was acicular ferrite. The interaction between Mn and boron resulted in the enrichment of the austenite in Mn. As a result, after cooling at cooling rates between 6 °C/min and 840 °C/min, the Mn-rich residual austenite zones acted as nucleation sites for the reverse α→γ transformation and resulted in the decrease of the Ac_1 temperature in the CMnB steel.

X.4   Effects of combinations of Mo, Cr and B on phase transformations during continuous cooling

The effects of Cr and Mo on the austenite decomposition during continuous cooling have been studied in CMn steels containing soluble B by means of dilatometry. The combination of Cr, Mo and soluble B produced dual phase bainite-martensite in a wide range of cooling rates, due to transformation stasis during cooling. In the CrMoB alloyed steel, the isothermal bainite transformation at 500 °C was also incomplete. This effect was attributed to a strong SDLE due to local concentration of Cr, Mo and Mn decreasing the mobility of the γ−α interphase boundary. In the MoB steel, Ac_1 was strongly lowered when reheating a bainitic microstructure, likely due to the presence of residual austenite with high substitutional (Mn + Mo) content. That effect was not observed in the Cr containing steels likely due to the carbide forming property of Cr.

Dictra simulations were performed to estimate the partitioning of Cr, Mo and Mn during the austenite decomposition to ferrite. The effect of soluble B was found to be well represented by considering spherical growth from the center of grains, *i.e.* the grain boundary nucleation was suppressed. Using those conditions, Mn was found responsible for the SDLE in the CMnB steel due to its high concentration at the moving interphase boundary. Local equilibrium without partitioning of substitutional elements was predicted in the CrB steel, while in the MoB steel, the transformation likely occurred under paraequilibrium. Mo was clearly responsible for SDLE. In CMn steels, the combination of Cr and Mo with soluble B produced transformation stasis due to a strong SDLE. As a result, with low amounts of alloying elements, complex bainite + martensite microstructures were produced in a wide range of cooling rates.

X.5 Combined dilatometric-crystallographic texture study of the effect of austenite deformation on the phase transformations in a micro alloyed bainitic steel

Local texture measurements were performed using the OIM-EBSD technique on a Nb-alloyed complex phase hot rolled CMnMoCrB steel coiled at CT = 720 °C, 680 °C and 550 °C. The analysis of hot-rolling data showed that no dynamic recrystallisation occurred during the rolling. EBSD Measurements supplemented with XRD showed that up to 11 vol% austenite was retained in the sample coiled at 550 °C. The retained austenite was mainly recrystallised. Dilatometry was performed on samples with different states of deformation in the austenite to see whether the rolling conditions had real implications on the phases transformations. In samples containing deformed austenite, the bainite transformation was strongly retarded due to the combination of small grains size and the presence of microalloying elements such as B responsible for SDLE. As no dynamic recrystallisation of the austenite occurred during the rolling process, static recrystallisation occurred in the course of the phase transformation. As a result, the final microstructure contained metastable recrystallised austenite, and low temperature transformation products such as bainite and martensite, with high densities of immobile dislocations, which are probably responsible for the continuous yielding behaviour observed during tensile testing hot rolled steels coiled at CT below 650 °C. Due to the slow cooling between the end of the rolling and the coiling at 720 °C, the deformed austenite recrystallised statically partially. During the $\gamma \rightarrow \alpha$ transformation, ferrite was formed from both recrystallised and deformed austenite. Due to the segregation of alloying elements, the state of deformation in the austenite was homogeneous and a clear variant selection occurred. Primary ferrite nucleation likely occurred in the deformed austenite with the S orientation. The presence of both the cube and rotated cube texture components in ferrite showed that the recrystallisation of the austenite occurred during the $\gamma \rightarrow \alpha$ transformation. In the ferrite-pearlite bands, the ferrite formed from the S, brass and Goss texture components of the austenite. It was remarkable that a clear α-fiber was present in the ODF, showing that the banding depends on the parent austenite orientation.

In the sample coiled at 680 °C, the faster cooling between the end of rolling and CT did not allow a partial recrystallisation of the austenite, and the primary ferrite formed from deformed austenite with the S and brass texture components. Static recrystallisation of the austenite occurred during the $\gamma\rightarrow\alpha$ transformation, and bainite formed from both deformed austenite with the orientations S brass and Goss, and recrystallised austenite with the cube orientation. The ODF for ferrite had the highest intensities for the texture components resulting from the transformation of the austenite with the brass orientation. Bainite mainly resulted from the transformation of austenite with the Goss orientation. A clear rotation of $\varphi_1 = 30$ ° occurred in the austenite between the ferrite and the bainite formations. The steel coiled at 550 °C consisted of B_3 bainite with M/A islands. In this microstructure the S orientation of deformed austenite did not lead to a clear ferrite texture component. This means that the texturing of the ferrite did not occur due to the recrystallisation of austenite before the bainitic transformation. The bainite was found to form from the brass and Goss orientations of deformed austenite. The residual austenite was mainly recrystallised, with the cube orientation.

X.6 Microstructure, mechanical properties and strain hardening behaviour of hot-rolled C-Mn steels

The relationships between microstructures formed during typical thermomechanical cycles in low C - 1,5 wt.% Mn based high strength micro-alloyed sheet steels and their mechanical properties were examined. The analysis of strain hardening coefficients established the distinction between 3 classes of tensile behaviours corresponding to distinct microstructures. In particular, it was found that a microstructure consisting of bainite with a second phase in the form of martensite-austenite islands had high performance mechanical properties. Continuous yielding, high tensile strength, adequate elongation, low YS/TS ratio and high strain hardening rate were found in this microstructural state. Other microconstituents present in minor amount deteriorated mechanical properties but kept the distinctive mechanical behaviour. The formation of a predominantly bainitic microstructure with austenite-martensite islands in condition simulating standard hot rolled sheet coiling was found in the MoCrB added CMn micro-alloyed steel. This microstructure was formed in this particular steel during the slow cooling of the steel in the temperature range between 550 °C and 650 °C. The study of transformation kinetics revealed that in spite of wide range of coiling start temperature the majority of austenite in this steel transformed in the bainitic region between 550 and 400 °C providing similar properties. The decrease of the coiling start temperature below 550 °C led to a decrease of plasticity due to the formation of the low temperature constituents, lower bainite and martensite.

X.7 Microstructure - properties relations in complex phase cold-rolled high strength steels

Cold rolled and annealed CP steel was studied in detail. Batch annealing simulations allowed the determination of the ferrite recrystallisation temperature. It was shown that dilatometry could be done on cold rolled plates to determine the temperatures of phase transformations and the volume fractions of phases formed after continuous annealing simulations. The state of deformation in cold rolled plates was responsible for a decrease in the kinetics of austenite formation during annealing between Ac_1 and Ac_3. Continuous annealing simulations with different cooling patterns were performed on cold rolled plates and the tensile properties were measured. A ferrite-pearlite starting microstructure led to lower tensile strengths and better elongation after annealing, due to the polygonal morphology of ferrite. However, due to the higher decomposition rate of pearlite to austenite than ferrite to austenite, a banded structure was still present after annealing and may be detrimental for the tensile properties in the transverse direction. A bainite-martensite starting microstructure led to higher strength levels but poorer elongations. Increasing the annealing temperature led to the formation of more austenite. Hence, according to the cooling pattern, more hard phases bainite and martensite were formed, increasing the strength level. More recrystallisation of the ferrite may be responsible for the excellent elongation. It was shown that the austenite formation was faster at the start of the intercritical annealing. Carbon partitioning took more time. Reducing the annealing time led to slightly lower fractions of austenite formed.The best compromises between high strength and good elongation were obtained for the CP steels with about 63 % ferrite, 25 % bainite and 12 % martensite. It was shown that cycles containing a isothermal bainitic transformation (IBT) holding at a temperature at which bainite could be formed were the most efficient. The M/A constituent was found to be mainly responsible for the improvement of tensile properties, *i.e.* increase of TS, decrease of YS/TS and increase of TE. The residual austenite content in the M/A constituent increased the total elongation very likely due to a TRIP effect. Finally, impact properties were better than static tensile properties, meaning that CP could be adequately used in parts of the car that need to absorb energy in the case of crash.

X.8 Further research

The current research on CP steels is still at its beginning as the production of such steels is envisaged. Tracks have been given in this research work to improve the properties of such steels:

- by selecting adequate steel composition, the SDLE could be controlled to obtain desired microstructures;

- the rolling process might be adapted to control the deformation state of austenite and stabilize appreciable amounts of residual austenite;

- the study of the M/A constituent, in particular the residual austenite fraction and its carbon content would lead to the development of complex phase steels able to produce a TRIP effect, thus having improved elongation.

The CP steel developed for the present study was successfully produced industrially in both hot rolled and cold rolled states. However, before being produced in large quantities, customers' requests must be first solved. Those request include coatability, *i.e.* protection against corrosion at low costs, and weldability.

Studies are currently carried out to study the coatability of that CP steel in the Laboratory for Iron and Steelmaking, and weldability is studied at Ocas, the research centre of Sidmar.

Use of the dilatometer to study magnetic transformations in steels

A.1 Introduction

Dilatometry is widely used to study the kinetics of phase transformations in steels. During these experiments dilatometer samples are reheated by means of induction heating to perform thermal cycles. It was found that by induction heating feed-back control signal monitoring not only phase transformations but also magnetic transitions could clearly be detected in a range of Fe alloys. The Induction Power Monitoring Technique (IPMT) makes it possible to observe a rich variety of resistivity and magnetism-related effects in most ferrous alloys. In low carbon steels, the Curie temperature, at which the ferromagnetic-paramagnetic transition occurs, was clearly seen. The effects of alloying elements on the Curie temperature were investigated. The deformation state of the sample could also be characterized. Even the antiferromagnetic-paramagnetic transition in Fe-Mn steels could be clearly observed by IPM. The evidence of premartensitic phenomena during both heating and cooling was found. These pretransformation phenomena are of a fundamental interest in the understanding of phase transformations in shape memory alloys.

A.2 Experimental details

The composition of the steels used for the present study is given in Table A.1.

Table A.1: Studied steels compositions in ppm.

Steel	C	Mn	Si	P	Cr	Mo	Nb	B	Al	Ti
ULC	12	820	50	90	200	-	-	-	220	-
IF	34	9700	70	730	-	-	250	10	430	100
CMn	1900	16400	130	153	230	-	-	-	790	-
CMnB	1400	17200	260	180	260	-	30	35	1200	285
CP	1600	16000	2750	300	5000	1800	500	20	450	300
FeMn14	16	142000	130	143	-	-	-	-	700	-
FeMn21	17	211000	180	148	-	-	-	-	1500	-

The ultra low carbon (ULC) steel was used as a reference sample because of its very low amount of alloying elements. The IF steel, the CMn, the CMnB and the CP (complex phases) steels were used to study the effects of micro alloying and microstructure on the ferromagnetic-paramagnetic transition. Finally, FeMn steels were used to study the antiferromagnetic-paramagnetic transition. Cylindrical samples with 5 mm length and 3.5 mm diameter were used in a Tetha Dilatronic III quench dilatometer. Samples were first reheated at the rate 60 °C/min to 1200 °C, maintained at this temperature 2 minutes, then cooled to room temperature at different cooling rates to produce controlled microstructures. Samples were then reheated at the rate 60 °C/min to 1200 °C.

The experimental details concerning the principle of Induction Power Monitoring (IPM) are given in chapter II.

A.3 Results and discussion

### A.3.1 The Ferromagnetic-paramagnetic transitions

Figure A.1a shows the change in length (dl/l_0) and the feedback signal (output) as a function of the temperature during the reheating at 60 °C/min of the ULC sample. The $\alpha \rightarrow \gamma$ transformation is clearly seen on both the dilatation and the output curves. The output curve gives extra information on the magnetic properties of the sample. It can be seen that at the temperature of 760 °C, which is 10 °C below the Curie temperature in pure iron, the heating power increases suddenly. It is remarkable that in the ULC steel the first order transition ($\alpha - \gamma$ transformation) and the second order transition (magnetic transition) are well separated. Below the Curie temperature T_c, the ferritic sample is ferromagnetic, *i.e.* the magnetic field produced by the induction coil aligns the magnetic domains. The magnetic permeability is high. Hence, the resistivity and the electrical resistance of the sample are high. The resistive sample, traveled by an induced current, is heated easily by Joule effect. The heat energy P is thus low. Above the temperature T_c, the magnetic susceptibility and thus the resistivity drop to a much lower value. As a result, the heat energy increases. More power is indeed necessary to reheat the sample.

The derivative of the dilatation according to the temperature yields the thermal expansion coefficients of α and γ. It can be seen in Figure A.1b, that during the ferromagnetic-paramagnetic transition, the linear dilatation with temperature is slightly affected. It is known that ferromagnetic materials respond mechanically to an impressed magnetic field, changing length slightly in the direction of the applied field. This effect, called magnetostriction seems to be responsible for a very small contraction of the dilatometer sample during the ferromagnetic-paramagnetic transition.

The length change due to magnetostriction does not exceed 0.0001 and is thus difficult to observe by means of dilatometry.
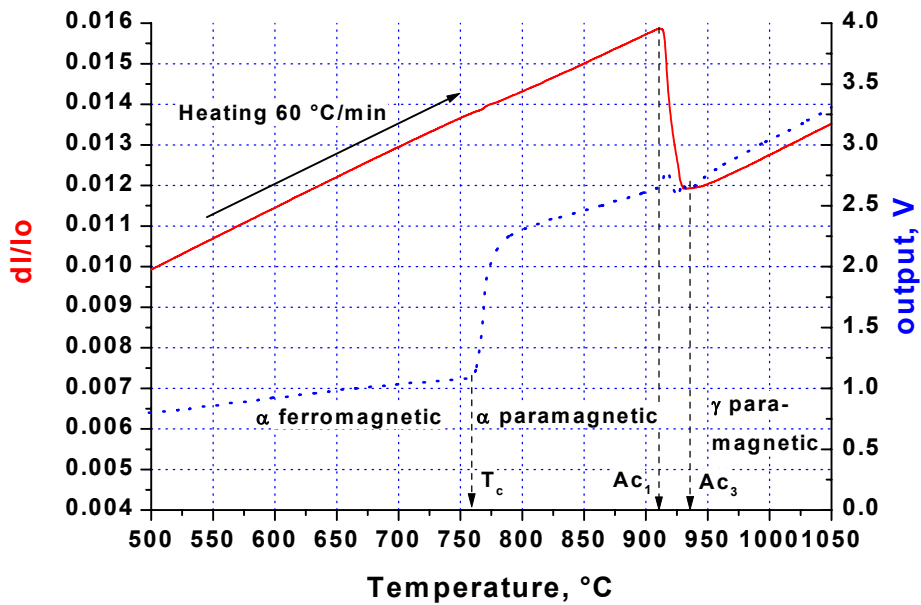
a)
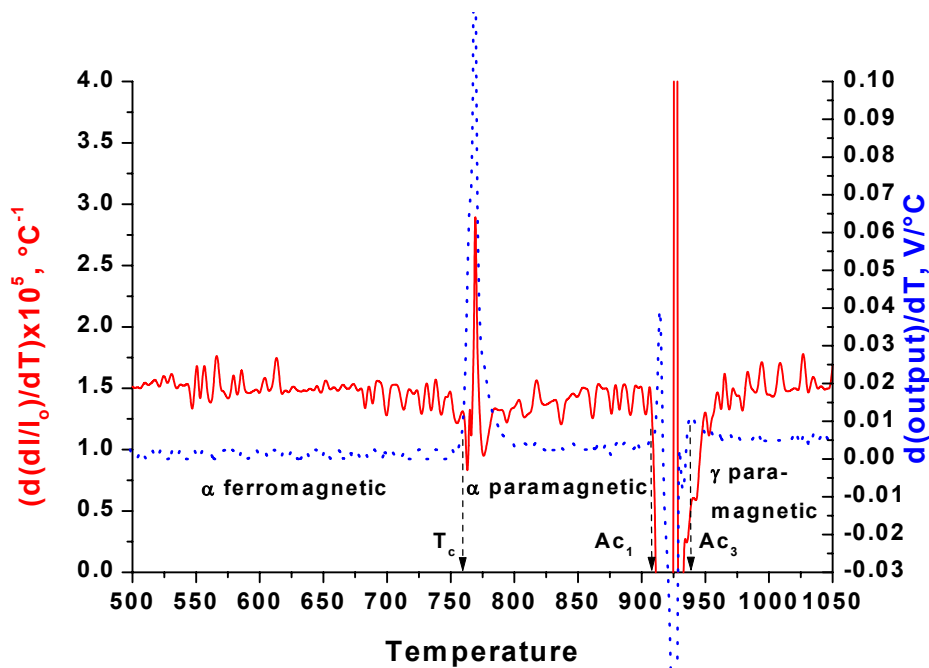
b)

Figure A.1: a) dilatometric curves showing the length change (solid line) and the feed-back signal (dotted line) as functions of the temperature during reheating the ULC steel at 60 °C/min.
b) derivatives of the curves shown in a) *versus* the temperature.

An enlarged area near the Curie temperature is shown in Figure A.2. It can be seen that the transition from ferromagnetism to paramagnetism is gradual. Two temperatures can be determined, respectively the ferromagnetic Curie point θ_f and the paramagnetic Curie point θ_p, which is equal to the constant θ in the Curie-Weiss law:

$$\chi = \frac{C}{T - \theta} \tag{A.1}$$

The difference between θ_p and θ_f is about 20 K in pure iron.[1] The same gap is observed in Figure A.2 for the ULC steel.

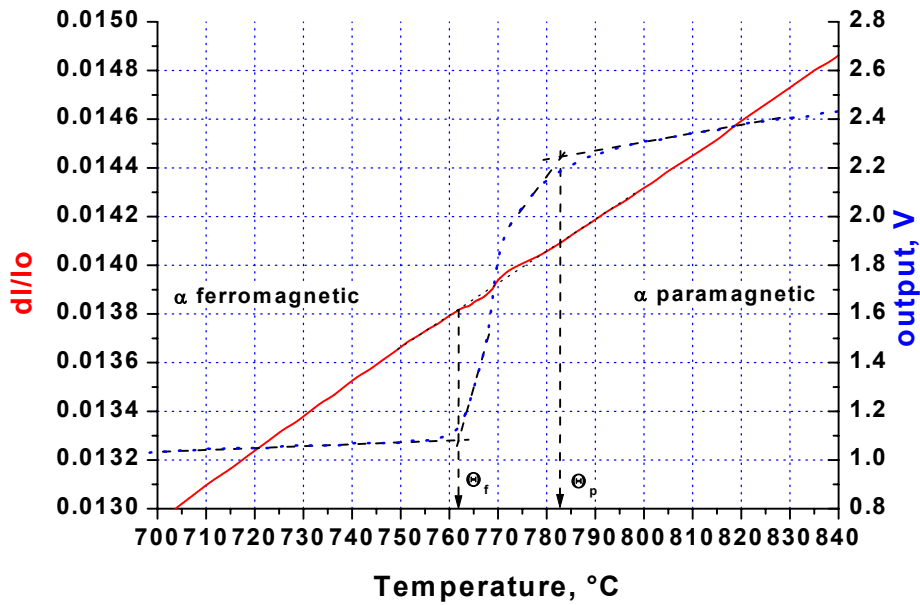**Figure A.2:** Enlarged area near the Curie temperature, showing the paramagnetic Curie point θ_p and the ferromagnetic Curie point θ_f.
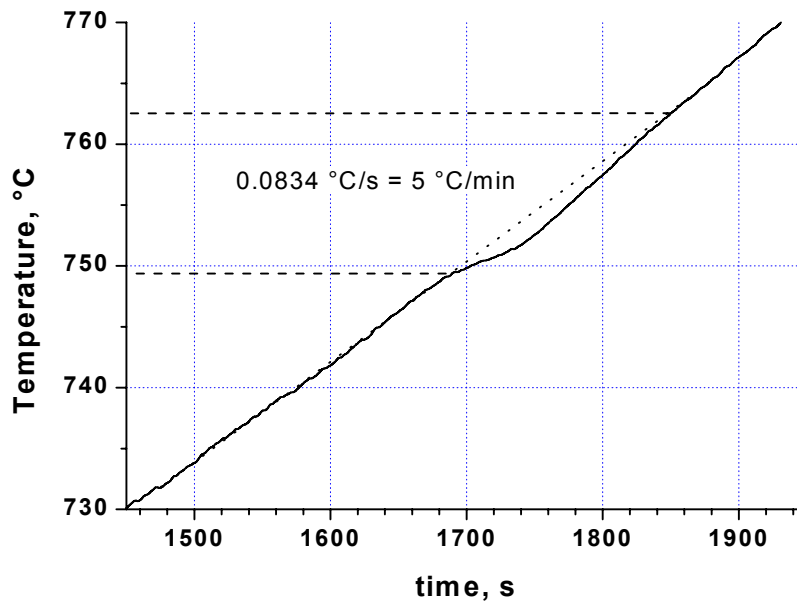

Figure A.3: equivalence time-temperature during heating the IF steel at 5 °C/min. Note the magnetostriction effect.

The dilatation *versus* temperature plot of Figure A.2 shows clearly a contraction followed by a dilatation during the magnetic transition. However, with the heating rate of 60 °C/min, it is likely that the dilatation was due to a kinetics effect induced by the faster reheating of the sample. The IF steel was reheated at the very low heating rate of 5 °C/min, to check whether a contraction or a dilatation occurred independently from the temperature. Figure A.3 is a temperature *versus* time plot. It can be clearly seen that from the beginning of the ferromagnetic-paramagnetic transition a retardation of the reheating occurs. Calorific energy was thus absorbed by the dilatometer sample to fulfill the energy requirement necessary to contract. At the end of the transition, the time-temperature curve is again linear, and no overheat is observed. The extra dilatation observed in Figure A.2 is thus necessary a kinetics effect, as it occurs only at faster heating rates.
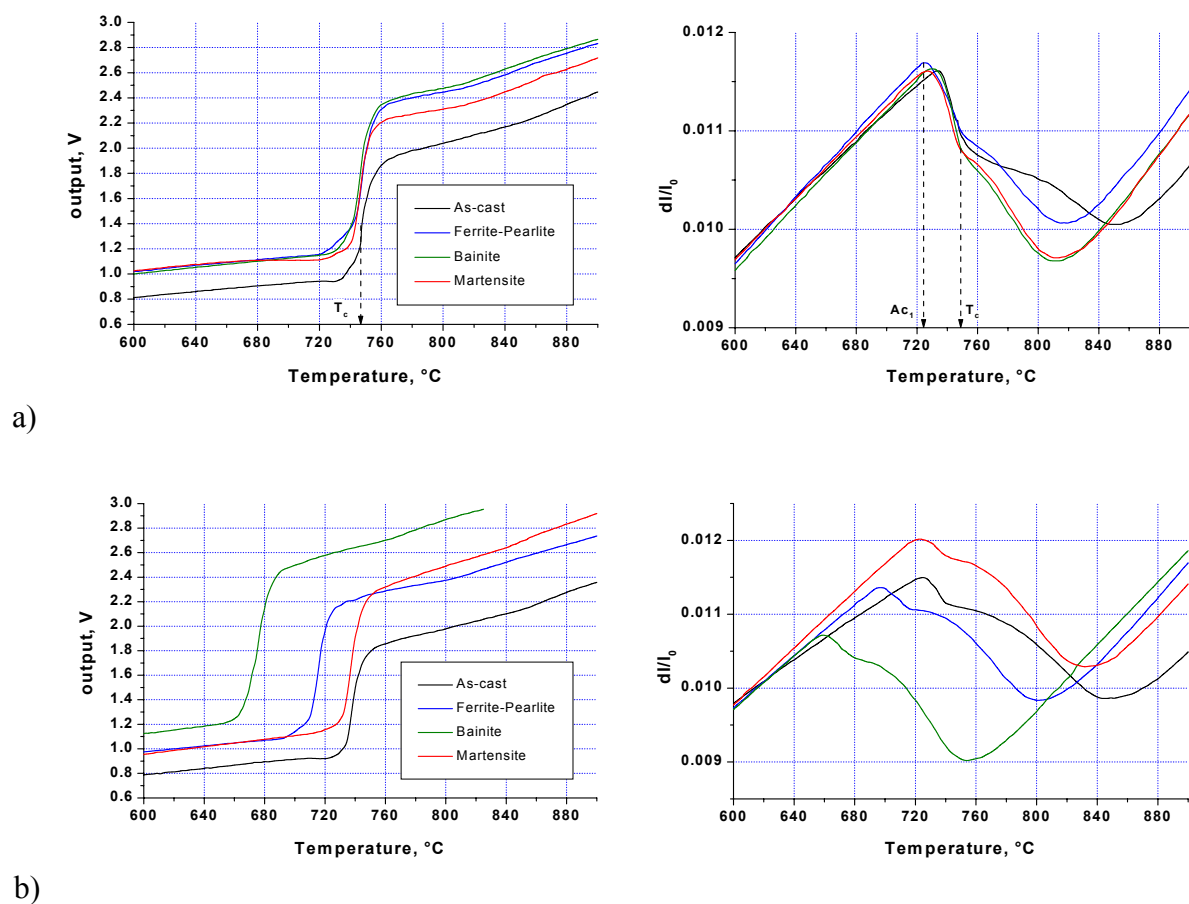

a)

b)

Figure A.4: power versus temperature curves for a) the CMn steel and b) the CMnB steel. The initial microstructure has an influence on the Ac_1 temperature, and consequently on T_c in the B bearing steel.

The presence of about 1 wt.% Mn was found to decrease the Curie temperature from 762 °C in the ULC steel to 749 °C in the IF steel. Note that in the IF steel Ac$_1$ is about 900 °C against 910 °C in the ULC steel. To check the possible influence of alloying elements on the magnetic transitions, CMn based steels with different microstructures were reheated at the rate 60 °C/min. Figure A.4a shows the output curves in function of the temperature. It can be seen that, whatever the microstructure was, the ferromagnetic-paramagnetic transition always occurred at the same temperature of 730 °C. This temperature of 730 °C is also the Ac$_1$ temperature. As the ferromagnetic ferrite transforms to austenite, the magnetic transition must occur simultaneously. It is very likely that the formation of austenite induces the magnetic transition in CMn steels. Figure A.4b shows the output curves of the B bearing CMn steel in function of the temperature. It has been shown in chapter V, that the microstructure formation during cooling is strongly affected by the presence of soluble B in that steel. In particular, in the bainitic microstructure, Mn rich M/A constituents were found. Consequently, Ac$_1$ was found to be lowered during the reheating of this microstructure.[2] The Curie temperature is thus lowered and is determined by Ac$_1$. In the CP steel, microalloyed with Cr, Mo, Nb, Si and B, the different microstructures obtained by varying the cooling rates did not affect the reheating transformation temperature Ac$_1$, neither the ferromagnetic-paramagnetic transition temperature, as shown in Figure A.5.
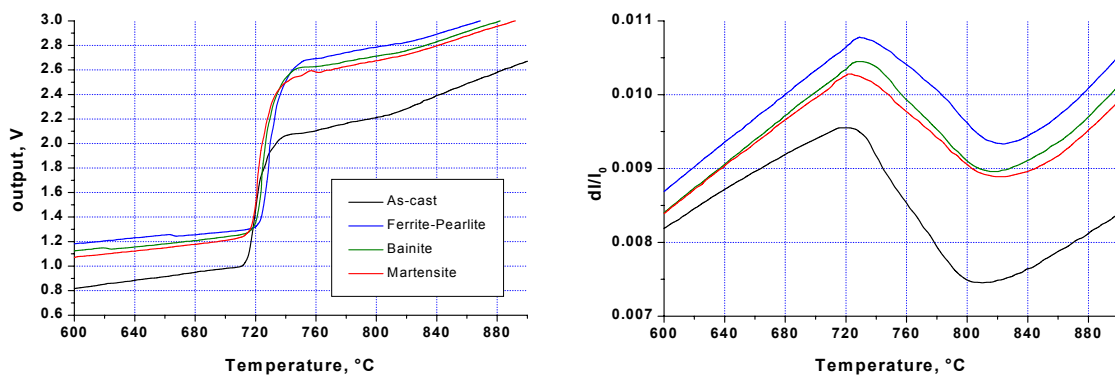

Figure A.5: Complex Phase steel.

However, like in the CMnB steel, residual austenite was present in bainite, but its alloy content did not affect Ac$_1$. In Figure A.4a, A.4b and A.5, it can be clearly seen, that the power necessary to reheat the dilatometer sample was always lower when starting from the as-cast microstructure. According to Matthiessen's law:[3]

$$\rho = \rho_T + \rho_D \tag{A.2}$$

the resistivity is the sum of two terms, the first ρ_T depending only on temperature, and the second ρ_D proportional to the density of reticular defects. As the as-cast sample contains numerous defects due to its machining, its resistivity is certainly higher, thus is its electric resistance higher. The difference between the output curves for the as-cast sample and the other microstructures obtained after several cycles on the same sample is very likely due to the initial defects density.

### A.3.2 *Antiferromagnetic-paramagnetic transition*

Fe-Mn steels are known to exhibit a weak shape memory effect. This effect is due to the reversible $\varepsilon \rightarrow \gamma$ phase transformation that occurs at low temperature. The ε phase is hcp (hexagonal close-packed) and γ is fcc (face centered cubic). The $\varepsilon \rightarrow \gamma$ has been recently studied in Fe-14wt%Mn and Fe-21wt%Mn steels by means of dilatometry and internal friction.[4]

An anomalous decrease in the elastic modulus was observed due to the paramagnetic-antiferromagnetic transition at T_N, the Néel temperature in the Fe-21 wt.% Mn alloy. From the data reported by Cotes et al.[5], the Néel temperatures for the Fe-14 wt.% Mn and the Fe-21 wt.% Mn are calculated to be 7 °C and 87 °C, respectively.

Figure A.6a shows the dilatation curve for the Fe-21 wt.% Mn steel, corresponding to the third reheating and cooling cycle at 60 °C/min. Lu et al.[6] reported an inflection of the lattice parameter of austenite due to magnetostriction associated with the paramagnetic-antiferromagnetic transition. However, such an effect could not be observed in the Fe-21 wt.% Mn with dilatometry. Figure A.6b shows the output curve associated to the full thermal cycle. At the difference from CMn steels in which the magnetic transition was clearly observed, no clear change in the output power associated to a magnetic transition could be seen.

### A.3.3 *Pretransformation behaviour in Fe-Mn steels*

As can be seen in Figure A.6b, a slight increase of the output was observed, during heating and during cooling. This increase, related to a drop of resistivity, is likely due to some crystal arrangement and certainly related to the shape memory effect, as it occurs at temperatures corresponding to M_F (martensite finish) during heating and A_F (austenite finish) during cooling, respectively. However, no change in length was observed at these temperatures, as seen in Figure A.6a. Figure A.6c shows the derivative of the dilatation and the output in function of the temperature. A preaustenitic transformation is seen at a temperature lower than A_s (austenite start). This phenomenon has been studied by several authors for the martensitic transformation in minerals and alloy systems. Its origin is associated to the existence of areas of lattice instability due to local strain.[7] These local areas have been observed by electron-optical microscopy and give rise to a distinctive cross-hatched texture which is familiarly known as "tweed".[8] Up to now, complex and costly techniques such as transmission electron microscopy,[9] electron diffuse scattering[10] and neutron scattering[11] were used to detect the pretransformation or observe the associated tweed microstructure. Using the feedback signal of the induction heating, an indirect measure of the resistivity is done. As resistivity is very likely affected by the density of defects, it is also very likely affected by local strains. The premartensitic and preaustenitic transformations accompanied by local strains apparition need extra energy to occur. The heat energy needed to reheat the sample at those particular temperatures is thus higher. This can be directly seen on the output *versus* temperature curve of Figure A.6c for both heating and cooling.
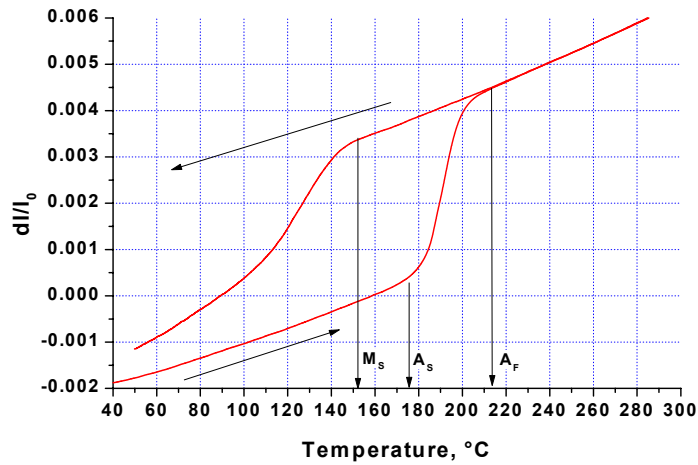
a)
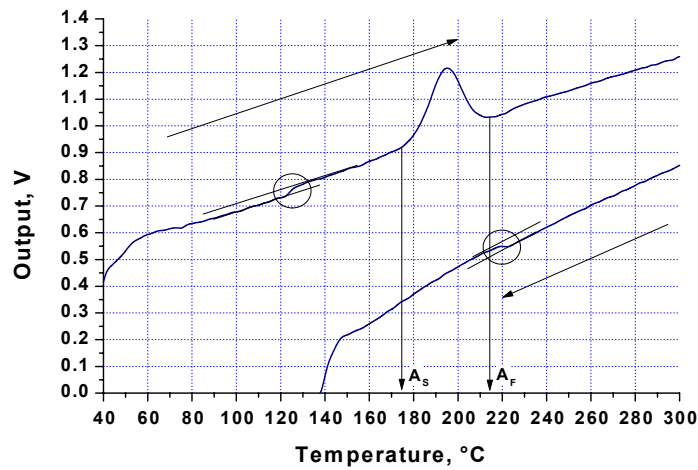
b)
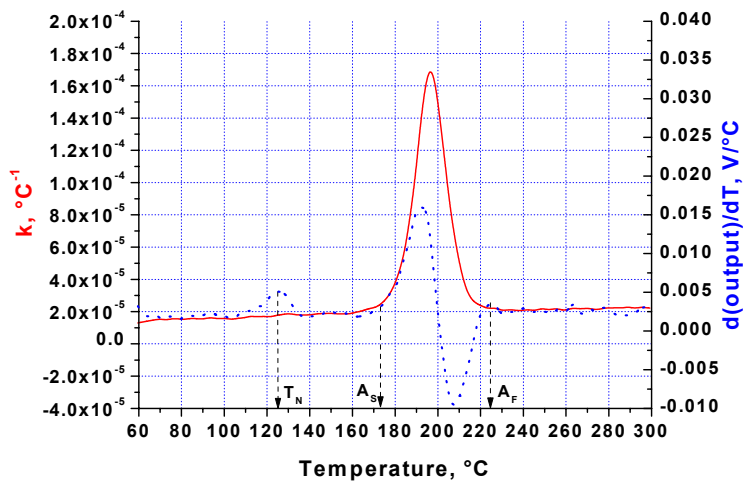
c)

Figure A.6: dilatometric curves showing a) the length change (solid line) and b) the feed-back signal (dotted line) as functions of the temperature during reheating and cooling the FeMn21 steel at 60 °C/min. c) derivatives of the heating curves shown in a) and b) *versus* the temperature.

A.4   Conclusions

The feedback signal corresponding to the power necessary to reheat a dilatometer sample to a desired temperature by means of induction heating has been studied with different iron alloys.

In low C steels, the ferromagnetic-paramagnetic could be clearly observed. In CMn steels, the $\alpha \rightarrow \gamma$ transformation occurring at temperatures below the Curie temperature induced the magnetic transition. The higher deformation state of as-cast samples was found to lower the output power, indicating that a higher density of defects increases the resistivity of the sample.

In Fe-Mn alloys, the antiferromagnetic-paramagnetic transition was not detected. However, premartensitic transformations were clearly seen. Hence new ways appear to study the shape memory effects in such alloys.

References

[1] C.W.Chen, Magnetic properties of metals, p.216.

[2] C. Mesplont, S. Vandeputte, B.C. De Cooman: <u>Z. metallkde</u> 92, No. 4, 2001, p.345.

[3] J. Bénard, A. Michel, J. Philibert, J. Talbot: Métallurgie générale, 2ème édition, Masson, 1984, pp. 32-48.

[4] A.K. De, N. Cabañas, B.C. De Cooman: <u>Z. Metallkde</u> 93, 3, 2002, p. 228.

[5] S. Cotes, M. Sade, A. Fernández Guillermet <u>: Metall. Mater. Trans. A</u>, 26, 1995.

[6] X. Lu, Z. Qin, Y. Zhang, B. Ding, Z. Hu: <u>Scripta mater.</u> 42, 2000, p.433.

[7] B. Verlinden, L. Delay: <u>Metallurgical Transactions A</u>, Vol. 19A, February 1988, p.207.

[8] J. Desmond, C. McConnell: <u>Metallurgical Transactions A</u>, Vol. 19A, February 1988, p. 159.

[9] R. Oshima, M. Sugiyama, F.E. Fujita: <u>Metallurgical Transactions A</u>, Vol. 19A, April 1988, p.803.

[10] T.R. Finlayson, A.J. Morton, P.D. Norman: <u>Metallurgical Transactions A</u>, Vol. 19A, February 1988, p.199.

[11] T.R. Finlayson, H.G. Smith: <u>Metallurgical Transactions A</u>, Vol. 19A, February 1988, p.193.

List of Publications

1. **Development of Complex Phase High Strength Sheet Steel: Current Issues**
B.C. De Cooman, M. De Meyer, T. Waterschoot, C. Mesplont, J. Mahieu and U. Meers
Proceedings High Strength Steels: Processing and Applications (HISPA), 1999, April, Ranchi, pp. 8-19

2. **Development of High-Strength Bainitic Steels for Automotive Applications**
C.Mesplont, T.Waterschoot, S.Vandeputte, D.Vanderschueren and B.C.De Cooman
Proceedings 41st Mechanical Working and Steel Processing (MWSP) Conference, ISS, Oct. 1999, Baltimore, USA, Vol. XXXVII, pp. 515-524

3. **Hot Rolled Bainitic Steels**
C.Mesplont, T.Waterschoot, S.Vandeputte, D.Vanderschueren and B.C.De Cooman
Proceedings Thermo-Mechanical Processing of Steels Conference, IOM Communications, May 2000, London, UK, pp. 495-504

4. **Hot Rolled Bainitic Steels for Automotive Application**
C. Mesplont and B.C. De Cooman
1st FTW Ph.D symposium UG, Dec. 2000, Paper 17

5. **A Model for the Calculation of the Bainitic Phase Transformation Kinetics from Dilatometric Data**
J.Z. Zhao, C. Mesplont, B.C. De Cooman
Z. Metallkd. 92 (4), 2001, pp. 345-350

6. **Kinetics of Phase Transformations in Steels: a New Method for Analysing Dilatometric Results**
J.Z. Zhao, C. Mesplont, B.C. De Cooman
ISIJ 41 (5), 2001, pp. 492-497

7. **Quantitative analysis of the dilatation during an isothermal decomposition of austenites**
J.Z. Zhao, C. Mesplont, B.C. De Cooman
Materials Science and Engineering A332, 2002, pp. 110-116

8. **Calculation of the phase transformation kinetics from a dilatation curve**
J.Z. Zhao, C. Mesplont, B.C. De Cooman
Journal of Materials Processing Technology 129 (1-3), 2002, pp. 345-348

9. **Model for extracting phase transformation kinetics from dilatometry measurements for multistep transformations**
J.Z. Zhao, C. Mesplont, B.C. De Cooman
Materials Science and Technology 18 (10), 2002, pp. 1115-1120

10. **An Improved Method for Determining the Continuous Cooling Transformation Diagram of C-Mn Steels**
C.Mesplont, J.Z. Zhao, S. Vandeputte and B.C. De Cooman
Steel Research, Vol. 72 (7), 2001, pp. 263-270

11. **Microstructure-Properties Relationships in Complex Phase Cold-Rolled High Strength Steels**
C.Mesplont, S.Vandeputte and B.C.De Cooman
Proceedings 43rd Mechanical Working and Steel Processing (MWSP) Conference, ISS, Oct. 2001, Charlotte (NC), USA, pp. 359-371
Also published in Iron & Steelmaker, Vol. 29 (2), 2002, pp. 39-45

12. **Microstructure-Properties Relationships in Complex Phase Cold-Rolled High Strength Steels**
C. Mesplont, S. Vandeputte and B.C. De Cooman
2nd FTW Ph.D symposium UG, Dec. 2001, paper 49

13. **Effect of Austenite Deformation on the Crystallographic Texture during the Transformations in a Microalloyed Bainitic Steel**
C. Mesplont and B.C. De Cooman
Materials Science and Technology, 2002, *in press*

14. **Microstructure and Properties of Hot-rolled High Strength Multiphase Steels for Automotive Application**
I. Yu. Pyshmintsev, C. Mesplont, S. Jacobs and B.C. De Cooman
Steel Research 73 (9), 2002, pp. 392-402

15. **Dilatometric Study of the Effect of Soluble Boron on the Continuous and Isothermal Austenite Decomposition in 0.15C-1.6Mn Steel**
C.Mesplont, S.Vandeputte and B.C.De Cooman
Z. Metallkde 93 (11), 2002, pp. 1108-1118